

Copyright is owned by the Author of the thesis. Permission is given for a copy to be downloaded by an individual for the purpose of research and private study only. The thesis may not be reproduced elsewhere without the permission of the Author.

Deciphering magmatic processes in response to growth and destruction at Taranaki Volcano, New Zealand

A dissertation presented in partial fulfilment of the requirements for the degree of

Doctor of Philosophy in Earth Sciences

at Massey University (Manawatū campus),
Palmerston North, New Zealand

Aliz Zemeny

2021





“Nothing in life is to be feared, it is only to be understood. Now is the time to understand more, so that we may fear less.”

~Marie Skłodowska Curie

Abstract

Taranaki Volcano is an atypical back-arc andesitic stratovolcano located on the Taranaki Peninsula of the North Island in New Zealand. Volcanism started c. 200 kyr ago and the edifice went through at least 14 sector collapse events with the same number of corresponding growth cycles, expanding the surrounding volcanic apron over its lifetime, which presently is populated and farmed. Previous studies focussed on the modern edifice (<14 ka), the tephra deposits (<29 ka), and the volcanoclastic stratigraphy over the 200 kyr volcanic history. However, there is a significant knowledge gap in relation to the evolution of the Taranaki volcanic system during successive edifice growth cycles (i.e. inter-collapse states) and the response of the magmatic system to unloading of the edifice. In order to unravel the subaerial and subvolcanic aspects of these growth cycles, the sedimentary textures, lithologies and stratigraphy of the volcanoclastic mass-flow deposits were investigated in the southwestern sector of the Taranaki ring plain, which provides a nearly continuous stratigraphic record of the time period of c. 65-34 ka that comprises three edifice regrowth phases. Volcanoclastic mass-flow deposits were the focus of this study, providing an opportunity to explore sedimentological and geochemical characteristics of eruptive periods of Taranaki Volcano, as there are no proximal sites available close to the modern edifice. Due to the well-exposed volcanoclastic successions along the coastline of Taranaki Volcano, a classification framework was established for the globally applicable categorization of volcanoclastic mass-flow deposits in ring plain settings. Additionally, the development of the stratigraphic model of the time period c. 65-34 ka highlighted the high frequency of widely distributed volcanic mass-flow events, approximately occurring 4-5 times in every 4-10 kyr. As these deposits encompass the characteristics of eruptive periods, vesicular pyroclasts were analysed in order to investigate the time related aspects of the Taranaki magmatic system during edifice growth cycles. Based on the analysis of 220 lapilli-sized pyroclasts, whole-rock compositions were reproduced by a mixing model, indicating that the volcanic rocks originate from melt-mush mixing processes. The mixing ratios varied within the individual growth cycles and further revealed that the melt-mush ratios define the produced whole-rock compositions, where the assimilant endmember is a primitive mush and the melt endmember is a trachyandesitic ascending melt. The temporal variation of the pyroclast geochemistry showed that within the inter-collapse states (i.e. growth cycles), the range of bulk rock compositions display a broadening pattern over time

towards pre-collapse states. This chemostratigraphic pattern was attributed to edifice loading affecting crustal magmatic processes over time. Whole-rock geochemical results demanded a detailed investigation of the crystal mush, from which Taranaki Volcano is fed, producing the basaltic to trachyandesitic magmas. The textural and chemical analyses of the Taranaki crystal cargo revealed reoccurring and specific crystal patterns and proved the antecrystic origin of the majority of the clinopyroxene, plagioclase and amphibole crystals. The observations highlighted that the Taranaki magmatic plumbing system involved repeated magma recharge, melt-mush mixing and crystal convection processes affecting the produced magmas within the time period of c. 65-34 ka. Crystallisation conditions (i.e. P-T-H₂O) were estimated applying thermobarometric modelling on clinopyroxene and amphibole phenocrysts. Results of the clinopyroxene rim equilibration modelling suggested source depths of approximately 26-12 km (± 7.5), which outline the mid- to lower-crustal regions and further indicate polybaric rim crystallization processes. In addition, hygrometry approximations indicated that within the individual growth cycles, melts with various properties (2.9-3.7 to 3.9-4.8 wt% H₂O) arrived at different regions of the crystal mush at mid-crustal depths. Altogether, textural, chemical and hygrometric analyses outlined the spatiotemporal complexity of the Taranaki magmatic plumbing system and the connected magmatic processes of andesitic volcanism. The interconnected sedimentological and geochemical studies of this research provided an understanding of mid-crustal melt-mush mixing processes producing the Taranaki magmas within a complex, interconnected vertical mush domain affected by the temporal influence of edifice loading and unloading during consecutive edifice growth cycles.

Acknowledgements

In the first instance, I would like to thank my chief-supervisor Jonathan Procter for developing and providing this research, for introducing Taranaki Volcano, the ring plain and the topic of lahars, for being always supportive towards my work and providing all the essential tools, opportunities in order to carry out this project. I am certainly thankful to my co-supervisor Georg Zellmer for fostering my knowledge in geochemistry, for being always there if I needed assistance and for all the helpful discussions that contributed solving the geochemical aenigmas of Taranaki Volcano. I am grateful to my co-supervisors Károly Németh and Shane Cronin for the useful discussions at the start of the project and for the effective supervision over the years and to Anke Zernack for her shared knowledge of the Taranaki mass-flow deposits and their stratigraphy when joining in the last year to the supervisory team. My special thanks to Anja Moebis for introducing me the laboratory, the instruments and for her assistance with sample preparation. Many thanks to Kate Arentsen for organizing my field trips, my travels to Australia, to Japan and to Europe. Thank you Opunake and Taranaki people and farmers for being so friendly and cooperative.

I would like to express my gratitude to Teresa Ubide and John Caulfield (University of Queensland, Australia) for welcoming me to the Centre for Geoanalytical Mass Spectrometry, Radiogenic Isotope Facility (UQ RIF-lab) in Brisbane, for their extraordinary proficiency with the LA-ICP-MS analysis, and for the knowledge in crystal stratigraphy and geochemistry they shared with me during the years. I am also deeply thankful to Ian Smith (Auckland University, New Zealand) for his high-quality expertise in geochemistry of Taranaki Volcano, and for the helpful conversations and guidance over these years.

I cannot signify enough the appreciation towards my friend and high school teacher, Anna Horthy (Sz.I. Gimnázium, Hungary), who introduced my young self to volcanology and Earth sciences and put lots of her energy and effort in order to broaden my scientific knowledge during my teenager years. Örökké hálás leszek!

A special thanks to my MSc. supervisor Prof. Szabolcs Harangi (Eötvös Loránd University, Hungary) for making it possible to be part of the MTA Geochemistry and Petrology Research Group throughout my BSc. and MSc. studies and for guiding my way towards my doctorate.

I am truly grateful to Dr. Orsolya Sztanó (Eötvös Loránd University, Hungary) for being strict about teaching the most important base pillars of geology, sedimentology and field work related logic and thinking during those 5 years. Without your knowledge and wisdom, I couldn't have made this scientific improvement.

I am certainly privileged to get to know exceptional human beings throughout my journey here in NZ. I will always cherish the time and moments we shared and the path we had been walking on together. You know who you are!

My blood, without your existence and sangfroid, I don't know how I could have coped with everything over these years. Nincs nálad jobb tesó, Dönci.

It is impossible to put into words my unmeasurable respect for my parents, who always supported my free thinking and believed in me. Tisztellek mindkettőtöket.

My two incredible superhero grannies! You always knew the answer for everything, and your wisdom washed away each time the foggy thoughts and showed me the way.

What a journey*, my acquaintances [Antalics Brigitta, Jakab Rebeka, Beke Zoltán, Soós Zsuzsa, Csáki Dávid, Pintér Dorina, Péntes Diána + many others]! Köszönöm.

*A kockázatokról és mellékhatásokról olvassa el a betegtájékoztatót, vagy kérdezze meg kezelőorvosát (ha értitek mire gondolok)!

This dissertation is dedicated to my grandfather, Zemeny József.

Table of Contents

Abstract	i
Acknowledgements	iii
Table of Contents	v
List of Tables.....	x
List of Figures	xii
CHAPTER 1 INTRODUCTION	1
1.1 Volcanic growth and collapse cycles.....	1
1.1.1 Interplay between growth cycles and sedimentary processes	3
1.1.2 Volcanic mass-flows and their deposits	4
1.1.3 Post-collapse magmatic response.....	5
1.2 Back-arc magma generation and evolution	6
1.2.1 Andesitic magmatism.....	6
1.2.2 Methods to characterise petrogenesis.....	7
1.2.3 Crystal stratigraphy: a tool to track magmatic processes.....	8
CHAPTER 2 LITERATURE REVIEW	9
2.1 Background Geology	9
2.1.1. North Island.....	9
2.1.2 Taranaki Basin.....	11
2.1.3 Taranaki Volcanic Lineament	11
2.2 Taranaki Volcano.....	12
2.2.1 Stratigraphy	14
2.2.2 The volcanic history of the 65-34 ka period.....	14
2.2.3 Petrology	16
2.2.4 Temporal evolution of the Taranaki magmatic system.....	17
2.3 Research question	20
2.4 Objectives	21
2.5 Thesis Outline.....	24
CHAPTER 3 METHODOLOGY	27

PREFACE

3.1 Terminology 27

3.2 Field Campaign..... 28

3.3 Laboratory Work I – Sedimentology approach 30

 3.3.1 Sample preparation..... 30

 3.3.2 Grain-size distribution and componentry 30

 3.3.3 Petrography 31

3.4 Laboratory Work II – Geochemical approach 32

 3.4.1 Crystal Pattern Classification – CPC 32

3.5 Data Processing – Calculation approach 33

 3.5.1 Modal phase proportions 33

 3.5.2 FC-AFC-FCA and Mixing Modeler..... 33

 3.5.3 Thermobarometry, Hygrometry and Oxygen fugacity modeling..... 33

CHAPTER 4 ELUCIDATING STRATOVOLCANO CONSTRUCTION FROM VOLCANICLASTIC MASS-FLOW DEPOSITS: THE MEDIAL RING PLAIN OF TARANAKI VOLCANO, NEW ZEALAND 38

4.1 Introduction 40

4.2 Taranaki Volcano 41

 4.2.1 Time period 65-34 ka 43

4.3 Terminology 44

4.4 Methods 46

4.5 Volcaniclastic lithofacies..... 46

4.6 Physiographic facies 53

4.7 Lithology 54

 4.7.1 Petrofacies classification..... 54

4.8 Unconformities 57

 4.8.1 Paleochannel systems..... 57

4.9 Distribution, frequency and appearance of lithic-dominated mass-flow deposits 59

4.10 Discussion..... 62

 4.10.1 Proposed classification criteria and coding system for ring-plain volcaniclastic deposits 62

 4.10.2 Eruptive activity during growth cycles: Lithic- and pumice-dominated volcaniclastics..... 62

 4.10.3 Stratigraphic context of growth phases..... 67

PREFACE

4.11 Conclusions	70
Acknowledgements.....	71
CHAPTER 5 THE ROLE OF EDIFICE LOAD ON ANDESITIC MAGMA GENERATION BY MELT-MUSH MIXING AT TARANAKI VOLCANO, NEW ZEALAND	73
5.1 Introduction	75
5.2 Geological setting	76
5.3 Petrogenesis of Taranaki magmas: the development of petrogenetic models....	78
5.4 Stratigraphic background and sample selection.....	80
5.5 Analytical methods	81
5.5.1 Mineral geochemistry and groundmass composition.....	81
5.5.2 Whole-rock major element analysis.....	81
5.5.3 Whole-rock trace element analysis	82
5.6 Results	83
5.6.1 Petrography	83
5.6.2 Mineral compositions.....	83
5.6.3 Major and trace element geochemistry	86
5.6.4 Geochemical stratigraphy.....	91
5.7 Discussion.....	94
5.7.1 The effect of edifice load on successive growth cycles	94
5.7.2 The ‘mid-age’ Taranaki magmatic system.....	95
5.7.3 Melt-phase interaction of Taranaki magmas.....	96
5.7.4 Origin of the ascending intermediate melt	100
5.7.5 Effects of edifice loading and unloading on the mid-age Taranaki plumbing system	101
5.7.6 Mid-age Taranaki in the context of the long-term evolution of its plumbing system	104
5.8 Conclusions	106
CHAPTER 6 MID-AGE TARANAKI ERUPTIVES (NEW ZEALAND) FED BY A COMPLEX MAGMA PLUMBING SYSTEM: INSIGHTS FROM GEOTHERMOBAROMETRY AND CRYSTAL ZONATION.....	109
6.1 Introduction	111
6.2 Geological background.....	113

PREFACE

6.3 Petrology of Taranaki rocks	115
6.4 Methodology.....	116
6.4.1 Material	116
6.4.2 Scanning electron microscope analysis (SEM).....	117
6.4.3 Electron Microprobe Analysis (EMPA).....	117
6.4.4 Laser Ablation Inductively Coupled Plasma Mass Spectrometry (LA-ICP-MS) Analysis	118
6.4.5 Crystal Pattern Classification (CPC).....	119
6.5 Results	121
6.5.1 Petrography and crystal cargo record.....	121
6.5.2 Mineral textures coupled with major oxide chemistry.....	122
6.5.2.1 Plagioclase	122
6.5.2.2 Clinopyroxene	126
6.5.2.3 Titanomagnetite	130
6.5.2.4 Amphibole	130
6.5.3 Mineral trace element chemical zonation.....	131
6.5.3.1 Plagioclase	131
6.5.3.2 Clinopyroxene	133
6.6 Discussion.....	135
6.6.1 Physical setting of crystallisation and the ascending melts.....	135
6.6.1.1 Distinguishing magmas of the growth cycles between c. 65-34ka.	135
6.6.1.2 Geothermobarometric conditions of the investigated mush domain.	137
6.6.1.3 Aspects of the ascending melts.....	147
6.6.2 Crystal cargo characteristics outlined by the CPC	151
6.6.2.1 Interpretation of the crystal patterns (CPs).....	151
6.6.2.2 Overview of the clinopyroxene crystal patterns	153
6.6.2.3 Transect profiles elucidating spatial relationships of the melt-mush interface	155
6.6.2.4 The mid-age Taranaki magmatic plumbing system.....	158
6.7 Conclusions.....	161

PREFACE

CHAPTER 7 TEMPORAL ASPECTS ON THE CRYSTAL-MUSH DOMINATED TARANAKI MAGMATIC SYSTEM DURING SUCCESSIVE GROWTH CYCLES.....164

7.1 Volcaniclastic mass-flow deposits as tools: From subaerial to subvolcanic processes 165

7.2 Integration of the Taranaki petrogenetic models 167

7.3 The recycled crystal cargo: Antecrystic, xenocrystic or a mixture?..... 173

7.4 The spatiotemporal evolution of the Taranaki transcrustal magmatic system 175

7.5 Global applications based on insights from the Taranaki magmatic system..179

CHAPTER 8 CONCLUSIONS.....184

8.1 Accomplished objectives 184

8.2 Future research..... 188

8.3 Epilogue..... 189

REFERENCES..... 190

Appendix A: Supplementary Data of Chapter 4 222

Appendix B: Supplementary Data of Chapter 5 223

Appendix C: Supplementary Data of Chapter 6 224

Appendix D: Supplementary Data of Chapter 7 225

Appendix E: DRC16 Form 226

List of Tables

Table 2.1 Major collapse and mass-flow events with other markers in the Taranaki Region (adapted from Zernack, 2021). ¹⁴C yrs BP presents radiocarbon years before AD1980. Ages (ka) refer to 10³ years before present including calibrated radiocarbon dates BP and chronostratigraphic estimates. Red dashed lines indicate the boundaries of the investigated time period of this study. DA: debris-avalanche; DF: debris-flow 15

Table 3.1 Details of the used models for the thermobarometry and hygrometry calculations. 36

Table 4.1 Stratigraphic overview of the Taranaki ring-plain succession defined by debris avalanche, debris flow deposits and other markers (adapted from Zernack, 2021). ¹⁴C yrs BP presents radiocarbon years before AD1980. Ages (ka) refer to 10³ years before present including calibrated radiocarbon dates BP and chronostratigraphic estimates. Bars indicate the chronostratigraphic boundaries of deposited Kaitakara and Punehu Sands as observed in the ring-plain succession. Dashed lines highlight the stratigraphic position of the deposits of this study 43

Table 4.2 Key markers of the studied time period representing calculated ages from earlier studies (after Zernack et al., 2011 and Tinkler, 2013) along with the direction of collapse, calculated volume and runout distance..... 46

Table 4.3 Categorization of the investigated volcanoclastic mass-flow deposits representing the main sedimentological characteristics, their distinguishing criteria with the representative appearance and their interpretation. Note the connection of textures to certain lithologies and physiographic facies..... 51

Table 4.4 Petrofacies description and classification criteria of the observed medial volcanoclastic mass-flow deposits. Pictures representing the general appearance of lithologies. **A:** lithic-dominated; L, ruler for scale: 17 cm. **B:** pumice-dominated monolithologic; monoP, hammer for scale: 25 cm; **C:** polyolithologic; polyL, person for scale: 170 cm. **D:** lithic and pumice-dominated, LP. **E:** sandy, S, ruler for scale: 10 cm. Semi-quantitative threshold value based on the point counting method calculations on the images for estimating componentry in surface %. 56

Table 4.5 Volume calculations of the Lizzie Bell and the Taungatara Debris Flow deposits based on the mapped thicknesses and lateral distributions observed on the field.58

Table 4.6 Classification criteria of volcanoclastic deposits using the proposed coding scheme that is composed of the lithofacies (1), the physiographic facies (2) and the petrofacies (3) codes. Note that presented coding schemes are examples based on this study. Petrof.: Petrofacies. BAF: Block-and-ash flow. PDC: Pyroclastic density current. HFD: Hyperconcentrated flow deposit; DFD: Debris flow deposit 63

Table 5.1 Stratigraphic overview of the time period c. 65-34 ka based on debris-avalanche and debris-flow deposits and an additional peat marker of the ring-plain succession of Taranaki Volcano (from Zernack et al., 2011; Tinkler, 2013). Age (ka) displays 10^3 years before present including calibrated radiocarbon dates BP and chronostratigraphic estimates.....	81
Table 6.1 Number of mapped clinopyroxene (Cpx) and plagioclase (Pl) crystals from the selected volcanic rocks of the three studied growth phases (GP1, GP2, GP3). P: primitive; T: transitional; E: evolved. Whole-rock compositions after Chapter 5	117
Table 6.2 Crystal pattern classification (CPC) of the analysed plagioclase and clinopyroxene crystals of the GP units. Arrows indicate the order of classification, i.e. from rim to core and from zonation to concentration patterns.....	120
Table 6.3 Clinopyroxene geothermobarometry for GP (1,2,3) igneous rocks of Taranaki Volcano. B T-A: Basaltic trachy-andesite; B: Basalt; TB: Trachy basalt; TA: Trachy andesite. Depth calculated on the basis of the continental pressure gradient of 26.5 MPa/km.....	139
Table 6.4 Amphibole geothermobarometry for GP (1,3) igneous rocks of Taranaki Volcano. TB: Trachy basalt; B T-A: Basaltic trachy-andesite; TA: Trachy andesite. Depth calculated on the basis of the continental pressure gradient of 26.5 MPa/km. Temperature means after Putirka (2016) is calculated using equation 5 and 6.....	143
Table 6.5 H ₂ O wt.% estimations based on the hygrometer developed by Waters and Lange (2015) using average plagioclase rim compositions within each GP along with the clinopyroxene and amphibole geothermobarometers. TB: trachy basalt; B T-A: Basaltic trachy-andesite; B: Basalt; TA: trachy andesite.....	145
Table 6.6 GP1 and GP3 P-T-H ₂ O comparison based on the clinopyroxene and amphibole compositions, the geothermobarometers (Putirka, 2008, 2016; Neave and Putirka, 2017; Ridolfi et al., 2010) and the hygrometer by Waters and Lange (2015).	146
Table 7.1 Stratigraphic resolution of geochemically investigated deposits/volcanic units of selected arc volcanoes in relation to inter-collapse states (i.e. growth cycles). In comparison, the sampled Taranaki inter-collapse volcanoclastic mass-flow deposit packages are indicated for each studied time period outlining the achieved high stratigraphic resolution. DAD: Debris-avalanche deposit.....	182

List of Figures

- Fig. 1.1** *Schematic figure summarising the connections between destructional and constructional periods based on known cyclic behaviour and their characteristics (modified after Stoopes and Sheridan, 1992; Belousov et al., 1999; Walter and Schmincke, 2002; Procter et al., 2009; Zernack et al., 2009); A: Schematic figure of the periods and their main processes within a cycle (adapted from Zernack et al., 2009). B: Detailed outcomes of associated periods of growth and destruction phases. Arrows indicate the connections and order possibilities of periods. 2*
- Fig. 2.1** *A: Main tectonic setting of New Zealand, displaying the relationship of the Australian and Pacific Plates, the Alpine Fault and the connected Trench lines. B: Map of the North Island of New Zealand showing the depth of the subducting slab, the Taupo Volcanic Zone (TVZ) and the location of active andesite stratovolcanoes. C: Onshore part of the Taranaki Basin, which includes the Taranaki Peninsula (TP) and the Taranaki Volcanic Lineament (TVL), the Cape Egmont Fault Zone (CEFZ) to the west and the eastern boundary, marked by the Taranaki Fault. Taranaki Basin adapted from Kamp et al., 2004. Maps: Linz Database; NASA Earth Observatory. 10*
- Fig. 2.2** *Quaternary geological map of the Taranaki Peninsula showing the distribution of debris-avalanche deposits (A); undistinguished debris-avalanche, lahar, fluvial and alluvial deposits (B); pre-Taranaki Maitahi debris-avalanche deposit (C); Young block-and-ash flow deposits of the Maero Fm (D; modified after Neall, 1979; Neall and Alloway, 2004; Alloway et al., 2005)..... 13*
- Fig. 2.3** *Summarised schematic depiction representing the lithospheric cross-section beneath Taranaki Volcano (modified after Zernack et al., 2012b; Price et al., 2016) focused on the magmatic system and the petrogenesis of volcanic rocks based on the previous studies that are presented in the figure (Stewart et al., 1996; Price et al., 1999; Annen et al., 2006; Turner et al., 2008a; Gruender et al., 2010; Zernack et al., 2012b; Price et al., 2016). P Moho: Petrological Moho; S Moho: Seismological Moho; Conrad: Conrad Discontinuity 19*
- Fig. 3.1** *Map of the southern and southwestern sector of the Taranaki ring-plain system indicating the location of the investigated medial coastal region (black dashed line) and the chosen main sites (S1, S2, S3) of the growth phases (GP) along with their estimated stratigraphic timeframe. The stratigraphic context of the representative sites is defined through debris-avalanche deposits (DAD) as chronostratigraphic markers (after Zernack et al., 2011) separating individual growth phases. 29*
- Fig. 3.2** *Selected vesicular pyroclasts exhibiting the four identified colours. A: White B, F: Grey C, D: Dark grey E: Yellow. Black bar for scale: 5 cm. 31*
- Fig. 3.3** *Representative binocular microscopic image of a glomerocryst within a pumiceous volcanic rock sampled from GP2 (sample: LBLHFE-5). 31*

- Fig. 4.1 A:** Location map and main tectonical settings of New Zealand outlining the Taranaki Peninsula (red dashed rectangle: TP; NASA Earth Observatory). **B:** Quaternary Geological Map of the south, south-western part of the ring-plain of Taranaki Volcano on the TP showing the distribution of volcanic and volcanoclastic deposits (LINZ elevation map; modified after Neall, 1979; Neall and Alloway, 2004; Alloway et al., 2005) and the coastal region (black bold line) that was examined during this study along with the chosen reference sites (stars; S1, S2, S3; find coordinates in **Appendix A1**). BAF: Block-and-ash flow deposits. 42
- Fig. 4.2** Representative appearance of the observed volcanoclastic mass-flow deposits. **A:** Massive (MHF) and graded (GHF) hyperconcentrated-flow deposits along with a thin dilute stream-flow (DiSF) deposit layer. Ruler for scale: 1 meter. **B:** Transitional hyperconcentrated-flow (THF) and non-cohesive debris-flow (nCDF; white dashed lines) deposit textures. Ruler for scale: 1 meter. **C:** Channelised debris-flow deposit (ChDF) texture. Person for scale: 170 cm. Note that the pictures of deposits were taken in medial (25.5 – 28 km) distance from the vent. 49
- Fig. 4.3** Two-dimensional cross-section in a flow-perpendicular cut illustrating the physiographic facies as observed on the field. Note that the schematic focuses on a channelization for demonstrative purposes. Arrows indicate the direction of the transportation of volcanoclastic mass-flow deposits and their deposition. 53
- Fig. 4.4** Distribution directions and mapped coastal extensions of lithic-dominated volcanoclastic mass-flow deposits along with the distance from the vent (white circle). Note: Mapped coastal extensions are considered as observed minimal estimations. Grey shaded area outlines the proximal distance - 10 km in diameter - around the edifice. Dashed line indicates the 20 km distance from source, i.e. the proximal – medial distance boundary. 59
- Fig. 4.5** Sedimentological characteristics and point counting results of componentry and grain size of the lithic-dominated and pumice-dominated hyperconcentrated-flow deposits at the representative sites (See **Fig. 1** for locations and **Fig. 4** for lateral extensions). Grain size histograms represent the number of clasts on the Y-axis and grain-size Phi (ϕ) conversion on the X-axis. The coding of mass-flow deposit packages follows the nomenclature introduced in **Table 3** and **4** in relation to texture and lithology. Grain-size and componentry data can be found in **Appendix A1** 61
- Fig. 4.6** Schematic matrix in parameter space outlining the connection between the three main factors that define the studied volcanoclastic deposits: (1) sedimentary texture; (2) petrofacies and (3) physiographic facies. Shaded areas represent the combination of the parameters observed in the coastal successions of the Taranaki ring plain. White areas indicate factor combinations that were not observed on the field. Dashed lines indicate the boundaries of the physiographic facies, whereas thick black lines the boundaries of the petrofacies and thin black lines the boundaries of the sedimentary textures, respectively. The form of the shaded areas is for illustrative purposes and only indicate the connection between

the three main parameters. Based on the linkage of the factors, deposits can be interpreted as rapidly remobilised or other secondary deposits. 64

Fig. 4.7 Summarised general stratigraphic model of Taranaki Volcano between c. 65-29 ka based on the investigated medial volcanoclastic mass-flow deposits. **X axis:** Coastal extension of the field area with the occurring present-day streams (A – A' – B; see field area on **Fig. 1**). **Y axis:** The volcanic cycles, cyclic periods and the connected lithostratigraphic units. Note: All deposit thicknesses outlined are observed average thicknesses (note the scale). Interbedded paleosol layers are not indicated, although they appear mostly in sheet and overbank facies. S1, S2 and S3 representative key sites are marked by black rectangles in the strata with their estimated depositional age. U-shaped components indicate the paleochannel systems that are time-transgressive cutting multiple stratigraphic units..... 69

Fig. 5.1 A: Main tectonical settings of New Zealand. NI: North Island; SI: South Island. **B:** Location map of the Taranaki Volcanic Lineament (TVL) and Taranaki Volcano (Ta) on the North Island along with the Taupo Volcanic Zone (TVZ), Ruapehu (Ru) and Tongariro (To). Green shaded area indicates the Taranaki Region (or Taranaki Peninsula). The dashed lines indicate the depth of the subducting slab (Boddington et al., 2004; Reyners et al., 2006, 2011). **C:** South and south-western portion of the ring plain of Taranaki Volcano with the locations of the sampled mass-flow deposit sites (GP1, GP2, GP3)..... 77

Fig. 5.2 A: Representative BSE image of an antecrystic, patchy zoned, resorbed plagioclase crystal (from GP2; sample LB LHF5-6; crystal PlE) interconnected with a glomerocryst consisting of titanomagnetite and clinopyroxene in a moderately vesicular microcrystalline groundmass. **B:** Glomerocryst consisting of clinopyroxene, plagioclase and titanomagnetite (from GP1; sample KAUHF10-3) emplaced within a moderately vesicular microcrystalline groundmass. **C:** Clinopyroxene antecryst exhibiting resorption surfaces and titanomagnetite inclusions (from GP2; LBLHF2-10 16b, crystal PxA). Gm: groundmass; Pl: plagioclase; Cpx: clinopyroxene; Tm: titanomagnetite..... 84

Fig. 5.3 Plagioclase core and rim compositions of the sampled Taranaki eruptives..... 85

Fig. 5.4 Pyroxene compositional classification of the selected Taranaki eruptives..... 85

Fig. 5.5 A: Total alkali vs. silica classification representing the compositions of the volcanic rocks and groundmasses analysed by EMPA from the GP units. Nomenclature after Le Bas et al. (1986). **B:** K₂O vs. SiO₂ diagram following the classification of Gill (1981) for the mass flow deposit clasts from the three studied GP units..... 86

Fig. 5.6 Major element variation diagrams as a function of SiO₂ abundance (wt.%) for the analysed volcanic rocks of the Taranaki samples..... 88

Fig. 5.7 Trace element variability (ppm) vs SiO₂ content (wt.%) of the sampled volcanic rocks from the GP units. 89

- Fig. 5.8** Primitive mantle- (PM) and chondrite-normalized rare earth element patterns for volcanic rocks of the three studied growth cycles of Taranaki Volcano. Normalising values are from Sun and McDonough (1989). 91
- Fig. 5.9** Schematic illustration of the chemical stratigraphy of mass-flow packages within the time period c. 65-34 ka comprising the investigated three growth-phases (GP units) of Taranaki Volcano. Grey scales indicate the compositional variability of a measured element within a sampled mass-flow package. Mean values of element concentrations are indicated by the dark shades, whereas the lighter is the scale, the less frequent is the given composition. Note that the number of vesicular pyroclast samples of each mass-flow package is between 5 and 30, whereas the number of analysed crystals is between 5 and 20. Ages on the left of the stratigraphic columns are maxima based on the stratigraphic context of the sampled deposits. DAD marks the debris-avalanche deposits separating the GP sequences. It is important to note that the time between the deposition of the DADs and GP units cannot be determined, thus the right-side stratigraphic figure is presented for visualization purposes only, i.e. the thickness is not for scale. Question mark indicates the stratigraphically uncertain mass-flow packages and their selected clasts, that based on their major and trace element compositions ('GP2 or GP3' in Fig. 5, 6 and 7) were grouped to the GP2 sequence 93
- Fig. 5.10** Mixing modelling results of the GP sample suites represented by major element Harker diagrams. Red hexagon indicates the melt compositions, whereas white star represents the assimilated compositions in each plot. Dashed lines exhibit the mixing lines calculated by equations obtained from Powell (1984) and Ersoy and Helvacı (2010). Blue field represents amphibole compositions, orange field clinopyroxene compositions and green field plagioclase compositions. The grey shaded area highlights the Median Batholith compositions (gabbro, gabbro-diorite and diorite data from Mortimer et al., 1997; Price et al., 2011). Results are represented as the function of K₂O for better illustrative purposes. 98
- Fig. 5.11** Melt inclusion (clinopyroxene and plagioclase) and groundmass compositions measured by EMPA and groundmass compositions calculated by modal phase proportions of the GP sample suites represented by total alkalis as the function of SiO₂. Dashed lines indicate the possible compositional area of melt mixing. GM: Groundmass; Amph: Amphibole; Cpx: Clinopyroxene; Plag: Plagioclase. 101
- Fig. 5.12** Model of andesitic magma evolution and mid- to upper-crustal processes beneath Taranaki Volcano in relation to the influence of major collapse events. The "Inter-collapse" scenario is considered to follow a "post-collapse" end-member, as eruptives deposited immediately following collapse could not be sampled as part of this study. Edifice loading through time is building up to the pre-collapse scenario. The shaded area on the viscosity vs. crystallinity diagram (after Lejeune and Richet, 1995) indicates the viscosity range of the generated magmas at inter-collapse (crystallinity of sampled rocks between 35 – 60 vol%) and pre-collapse states. PE: Edifice load from Watt (2019). Lower Crust – mantle boundary is from Sherburn and White (2005) and Stern et al. (2006). Rock types beneath the edifice after Mortimer et al. (1997), Gruender et al. (2010) and Price et al. (2011). 102

- Fig. 5.13** Major and trace elemental comparison of inter-collapse (clasts of the GP units; 65-34 ka), pre-collapse (clasts of Te Namu DAD ~34 ka, Rama DAD ~40 ka and Otakeho DAD ~55 ka) and early-system (clasts of Okawa and Motunui DAD; >105 ka) compositions as a function of SiO₂ and K, respectively (pre-collapse and early-system composition data from Zernack et al., 2012b). Dashed lines indicate the SiO₂ (for major elements) and K (for trace elements) compositional boundary between pre- and inter-collapse chemistry 106
- Fig. 6.1 A:** Map of New Zealand indicating the Taranaki Peninsula (yellow rectangle) as the focus area of the study. **B:** The North Island indicating the Taupo Volcanic Zone (TVZ), the Taranaki Volcanic Lineament (TVL) and the location of the field area (yellow rectangle) within the south and southwestern part of the ring plain. Stratigraphic context of the three investigated growth-phases (GP) is represented with the illustrative position of the sampled GP sites along with the investigated number of clinopyroxene (Cpx) and plagioclase (Pl) crystals. The debris-avalanche deposits are indicated in-between the growth cycles (DAD) outlining the collapse events within the time period 65-34 ka. 114
- Fig. 6.2** Main textural and compositional features of plagioclases of the pumiceous and scoriaceous samples from GP1, 2, 3. **A:** Flat profiles. **B:** Small-scale oscillatory zoning and discordancy oscillatory zoning indicated by the arrow. The average anorthite (An) contents of oscillatory zones are also indicated. **C:** Patchy-textured core with resorption/dissolution textured mantle. The average An content of cores are indicated by the arrow. **D:** Large-scale sieve-textured mantle. The average sieve-texture compositions as indicated. **E:** Multiple sieve-textured resorption surfaces. Numbers indicate the order of resorption events. Yellow dashed lines highlight the resorption surfaces. 124
- Fig. 6.3** Anorthite content of plagioclase mottled cores and patches analysed from the GP units..... 125
- Fig. 6.4** Core, mantle and rim anorthite compositions of each GP unit plagioclase analysis..... 125
- Fig. 6.5** Pyroxene crystals representing the main textural characteristics. **A:** Patchy-zoned cores outlined by the yellow arrows along with the Mg# value range. **B:** Thin and thick oscillatory zoning indicated by the arrows. Mg# content range of Mg#-rich mantles as indicated. **C:** Flat profiles with Fe-Ti oxide association. 127
- Fig. 6.6** Mg# compositions for core, mantle and rim of each GP unit clinopyroxene analyses. Inset: General Cpx SiO₂ wt.% compositions as a function of Mg#... 129
- Fig. 6.7** Minor element (Al-Na) zonation within a clinopyroxene phenocryst. White line indicates the path of data extraction from the crystal map using CellSpace.... 129
- Fig 6.8 A:** Amphibole (outlined by yellow arrow) with patchy zoning forming a glomerocryst with a clinopyroxene. **B:** Amphibole with decompression rim (indicated by the arrow) accompanied by titanomagnetite..... 131

Fig. 6.9 The main types of trace elemental distributions within plagioclase phenocrysts. Type 1: Li enrichment within rims. Sample from GP1: KAUHF10-3_2PL. Type 2: Ba enrichment within rims. Sample from GP3: TAULHF4-5_plA. Type 3: Sr enrichment in the mantle region. Sample from GP3: TAULHF1-20_plA. White lines indicate the path of data extraction from the crystal map by CellSpace. Red arrows indicate data extraction from resorbed surfaces. 132

Fig. 6.10 Representative trace element zonation types of clinopyroxenes showing the most characteristic trace elemental compositional distribution patterns. Type 1: Cr-rich cores. Type 2: Oscillatory zonation of trace elements. Type 3: Cr-rich mantle. Type 4: Minor oscillatory zoned rims slightly enriched in mildly incompatible elements. White lines indicate the path of data extraction from the crystal maps by CellSpace..... 134

Fig. 6.11 Titanomagnetite MgO wt.% compositions of the GP unit clasts as a function of TiO₂ wt.% showing different magmas of the growth cycles. Three distinct groups in GP2 (I., II., III.) and two separate groups within GP3 (I. and II.) can be identified. Dashed arrow indicates time. The numerals I. – III. indicate mass-flow packages from older to younger..... 136

Fig. 6.12 A: Pressure - temperature equilibration for amphiboles and clinopyroxenes from the GP volcanic rocks of Taranaki Volcano based on the Putirka (2016), Neave and Putirka (2017), Ridolfi et al. (2010) geothermobarometers. For amphiboles, geobarometer uncertainty with respect to temperature is ± 22 °C, for pressure is a maximum of ± 61 MPa and for H₂O wt.%, is an average of ± 0.7 (Ridolfi et al., 2010). Maximum and average uncertainties are indicated by the length of the cross signs, respectively. Neave and Putirka (2017) geothermobarometer 1SEE for T is ± 42 °C (Eq. 33; Putirka, 2008) and for P is ± 0.96 kbar (Neave and Putirka, 2017; Jd-in-clinopyroxene barometer), respectively. See all geothermobarometer uncertainties summarized in **Chapter 3, Section 3.5**. Equilibration range for amphiboles of Taranaki volcanics and xenoliths after Price et al. (2016). Equilibration range for xenoliths of MB after Gruender et al. (2010) and Gründer et al. (2006). TBS: Sediments of the Taranaki Basin. Dashed lines indicate the transition between TBS-Median Batholith and Median-Batholith – mid- to lower-crust. Crust/mantle boundary is from Sherburn and White (2005) and Stern et al. (2006). **B:** Calculated H₂O wt.% melt contents for amphiboles and clinopyroxenes using the hygrometer of Waters and Lange (2015). Melt water content 1SEE is 0.35 wt.% coupled with T 1SEE of ± 42 °C after Neave and Putirka (2017; Eq. 33). Average H₂O wt.% for Taranaki magmas after Price et al. (2016). 141

Fig. 6.13 Temporal stratigraphic illustration of the GP2 volcanoclastic mass-flow packages and the clinopyroxene equilibration conditions of their sampled pyroclasts (results after the thermobarometer by Neave and Putirka (2017). Black arrow indicates time. Time break corresponds to the presence of paleosol between the volcanoclastic deposits. The age-range is considered as a maximum for GP2. 147

Fig. 6.14 A: Schematic representing the different ascending magmas of GP1, GP2 and GP3 over time (indicated by black arrow) based on the hygrometry (after Neave

and Putirka, 2017) and geothermobarometry P - T - H_2O estimations (for details see **Section 6.1**). Viscosity vs crystallinity after Lejeune and Richet (1995) indicating the viscosity ranges of generated magmas during edifice growth cycles. Arrows show trachyandesitic melt ascent with water contents as indicated. **B**: Zoomed in spatial illustration of the melt-mush interface and the generated Mg# zoning profiles of clinopyroxenes due to the low- T mush incorporation into high- T melts.149

Fig. 6.15 Clinopyroxene rim equilibration estimations (Neave and Putirka, 2017) as the function of SiO_2 wt.% of the whole rocks. Dashed lines indicate a representative range of increasing T with increasing SiO_2 considering the rock types of the volcanics, i.e. from basaltic to trachytic compositions. Neave and Putirka (2017) geothermobarometer ISEE for T is ± 42 °C (Eq. 33; Putirka 2008). Collected samples as the following: Basalt: LB LHF4-12; Trachy-basalt: KAUHF9-3, KAUHF10-3, TAUHFO.5; Basaltic trachy-andesite: LBLHF2-16b, LBLHF5-6, TAULHF2-17; Trachy andesite: TAULHF1-20. 150

Fig. 6.16 Mg# and Al_2O_3 variation transects within individual crystals of GP the units. Mg# indicated by yellow circles; Al_2O_3 content highlighted by black circles. **A**, **B**: Normal and reverse zoned pyroxene phenocrysts from two different samples (KAUHF10-3 and KAUHF9-3) of GP1 unit. **C**, **D**: Single (**C**) and multiple (**D**) Mg# change within clinopyroxene phenocrysts towards the rims. The crystals are originated from the same pumiceous rock sample of GP2 (LBLHF5-6). **E**: GP2 clinopyroxene phenocryst (TAU HFO.5 PxA) with flat profile outlining a significant Mg# change within its mantle. **F**: Small size clinopyroxene from a GP3 sample (TAULHF4-5) with flat profiles representing noteworthy Mg# decrease within its inner rim. 156

Fig. 6.17 Schematic illustration of the vertical plumbing system architecture at Taranaki Volcano in post-collapse state. MB: Median Batholith. Eq.: Equilibration. Cpx rim eq.: Clinopyroxene rim equilibration values by this study with dashed lines indicating the error (ISEE) after Neave and Putirka (2017). Amphibole eq.: Amphibole equilibration values by this study. Dashed lines show error (ISEE) after Ridolfi et al. (2010). TBS: Taranaki Basin Sediments. Crust/mantle boundary is from Sherburn and White (2005) and Stern et al. (2006). Hexagons indicate incorporated crystal residues and their crystal patterns (CPs) observed by the CPC in this study. Note that the vertical representation of different CPs is only illustrative to highlight that both spatial and temporal factors acted on the investigated crystal cargo within different segments of the plumbing system. Thus, the emplacement of CP hexagons may vary due to the different ascending melt characteristics (see **Fig. 13 A** for different melt emplacement depths). Inset of hexagon shows the general concept of crystal incorporation to ascending melts (black arrow) by melt:mush mixing. 160

Fig. 7.1 Integrated petrogenetic model of Taranaki Volcano considering timescales and cyclic edifice growth and collapse induced magmatic response. **A**: Inter-collapse petrogenetic model proposed by this study and its inclusion in the combined model (see details in **Chapter 5** and **6**). **B**: The long-term temporal evolution model after Zernack et al. (2012b) and Turner et al. (2008a) in agreement with the hot zone model of Annen et al. (2006). **C**: MgO vs SiO_2 and **D**: K_2O vs SiO_2 of the analysed

*Taranaki volcanic rocks indicating significant differences over time. Fanthams Peak and Summit/Staircase data after Stewart et al. (1996); DAD and early system data after Zernack (2009) and Zernack et al. (2012b); GP1,2,3 data after this study. Datasets provided in **Appendix D1** 172*

Fig. 7.2 A: Amphibole and clinopyroxene pressure and temperature equilibration estimates based on early (debris avalanche deposit clasts) and mid-age system (pumice and scoria clasts) volcanics of Taranaki Volcano. Thermobarometry models after Ridolfi et al. (2010) and Neave and Putirka (2017) and hygrometry model of Waters and Lange (2015) were used. Amphibole geobarometer ISEE is ± 22 °C, for pressure is ± 61 MPa and for H₂O wt.% is an average of ± 0.7 (Ridolfi et al., 2010). Clinopyroxene thermobarometer ISEE for T is ± 42 °C (Eq. 33; Putirka 2008) and for P is ± 0.96 kbar (Neave and Putirka, 2017). **B:** Calculated H₂O wt.% melt contents for amphiboles and clinopyroxenes using the hygrometer of Waters and Lange (2015). Melt water content ISEE is 0.35 wt.% coupled with T ISEE of ± 42 °C after Neave & Putirka (2017; Eq. 33). Average H₂O wt.% for Taranaki magmas after Price et al. (2016). Early system clinopyroxene (n=19), plagioclase and amphibole (n=148) compositions after Zernack et al. (2012). Equilibration range for amphiboles of Taranaki volcanics after Price et al. (2016). Crust/mantle boundary is from Sherburn and White (2005) and Stern et al. (2006). Uncertainties (ISEE) are indicated by the length of the cross signs..... 177

CHAPTER 1

INTRODUCTION

1.1 Volcanic growth and collapse cycles

Stratovolcanoes, within any tectonic setting, are highly unstable structures and tend to fail, generating large landslides (Ui, 1983; Siebert, 1984). The term sector collapse was developed to describe structural failures of the cone that involve the central conduit and summit of the edifice (e.g., Ui, 1983; Siebert, 1984; Siebert et al., 1987). On the other hand, smaller mass movements affecting flanks may be termed as flank collapse. The long-term behaviour of composite and stratovolcanoes is represented by growth (construction) phases followed by collapse (destruction phases) events (**Fig. 1.1 A**), which result in a recurring cyclic pattern on timescales that range from a few hundred to tens of thousands of years (Belousov et al., 1999; Tibaldi, 2004, Zernack et al., 2009, 2011; Zernack and Procter, 2021). There appears to be a natural height limit for edifice growth and at that point the structure becomes unstable. The average maximum size of stratovolcanoes lies between 2000 – 2500 m (Davidson & de Silva 2000). After the destruction event, mass-flow events change the landscape and the sedimentation processes (Procter et al., 2009).

The number of edifice failures identified at long-lived volcanoes depends on the exposure and preservation of the volcanoclastic record and volcanic debris-avalanche deposits (VDADs). VDADs have been described from volcanoes in various settings: (i) in subduction zone settings (Ui et al., 1986a, b; Vallance et al., 1995; Capra et al., 2002; Silver et al., 2009), (ii) at intraplate ocean islands (Moore et al., 1989; Carracedo, 1994; Masson et al., 2002; Watt et al., 2020) or (iii) at small cinder cones (Németh et al., 2011; Delcamp et al., 2012). Edifice failures at frequently collapsing volcanoes exhibit a semi-regular recurrence pattern involving a wide range of volumes (e.g. Zernack and Procter, 2021) and over 300 events with estimated volumes of $>1 \text{ km}^3$ have been documented worldwide from >200 volcanoes (e.g. Watt, 2019). In subduction settings, most documented collapses involve volumes between $1\text{-}5 \text{ km}^3$ (Watt, 2019 and references therein). However, the complex interplay of factors contributing to destabilisation (i.e. edifice volume, height, diameter, internal structure, influencing hydrothermal systems, mechanical strength of rocks and deposits) and the timing along with the nature of trigger events play an important role for the size and frequency of collapse (Zernack et al., 2012a; Zernack and Procter, 2021).

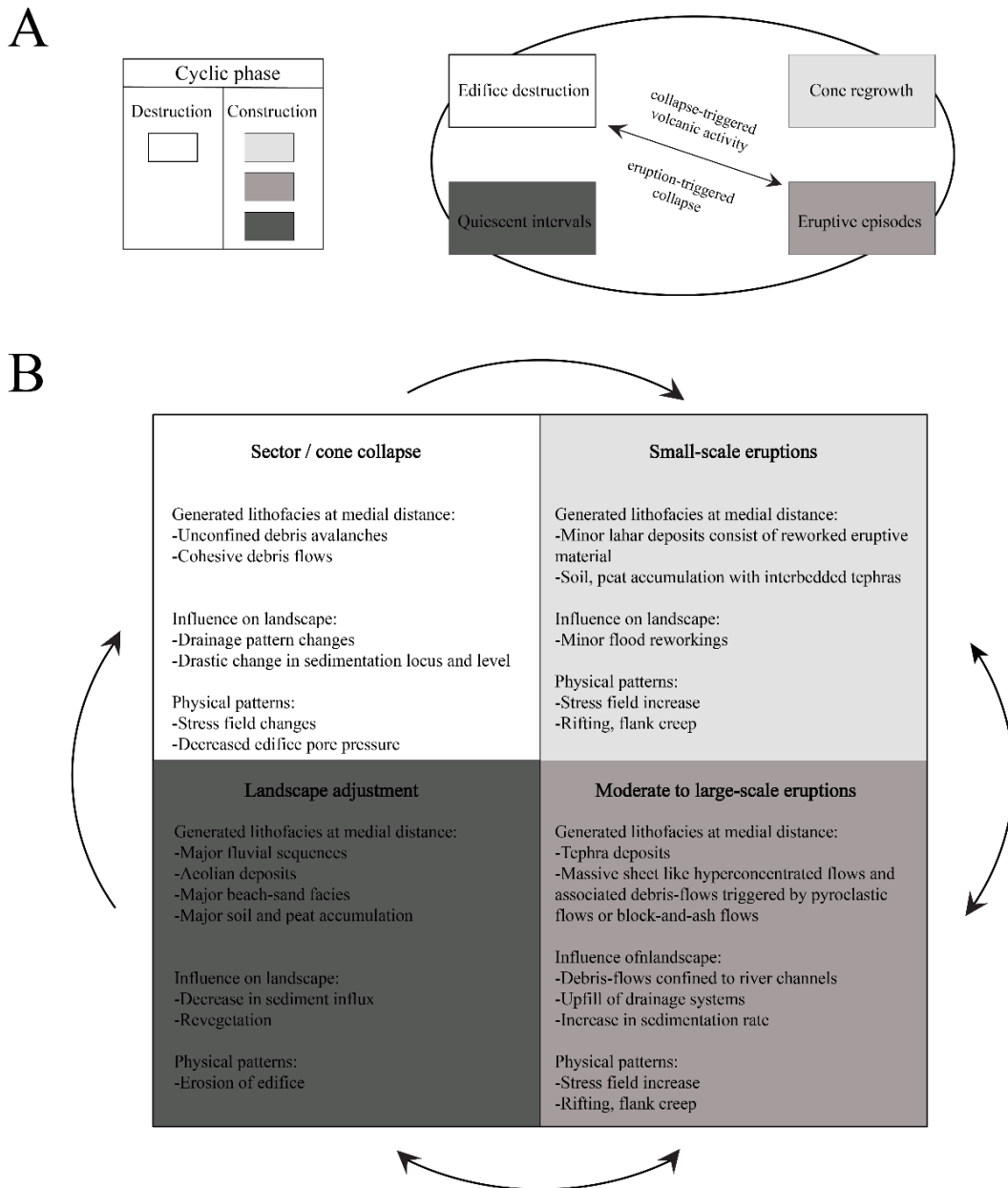


Fig. 1.1 Schematic figure summarising the connections between destructional and constructional periods based on known cyclic behaviour and their characteristics (modified after Stoope and Sheridan, 1992; Belousov et al., 1999; Walter and Schmincke, 2002; Procter et al., 2009; Zernack et al., 2009); **A**: Schematic figure of the periods and their main processes within a cycle (adapted from Zernack et al., 2009). **B**: Detailed outcomes of associated periods of growth and destruction phases. Arrows indicate the connections and order possibilities of periods.

A high frequency of cyclic collapse and subsequent edifice growth has been attributed to a high magma supply rate, whereas volcanoes characterised by low eruption rates typically display a low number of failures with long intervals between events or smaller volumes of collapses. Failure frequencies along with the volumes vary strongly (Zernack and Procter, 2021 and references therein) ranging from minor landslides (10^2 - 10^3 m³)

every few months to the largest events involving volumes of 5000 km³ (Moore et al., 1989) and return periods of 10⁴-10⁵ years (McGuire, 2003). Volcanoes such as Shiveluch (Russia) exhibit VDA return intervals of 0.6-2 kyr with volumes of 1-2.5 km³, whereas Colima displays collapse event frequencies of 1.1-8.5 kyr with VDA volumes of 0.4-35 km³ compared to Taranaki Volcano, with return intervals of 2-2.5 kyr and volumes of 1-7.5 km³ (Zernack and Procter, 2021 and references therein).

Deposition

Volcanic ring plains or volcanoclastic aprons contain the most complete record of volcanic activity and thus provide insights into the history of the edifices through sedimentary signatures of the volcanoclastic successions. The term ‘ring plain’ is defined as a circular area surrounding a volcanic edifice (Davidson and de Silva, 2000). The rounded map-view outline only occurs in the absence of other volcanoes or mountains close to the edifice that could form barriers to the distribution of the deposits (Smith, 1991). Ring-plain successions are progressively built up through the deposition of syn- and post-eruptive volcanoclastics, minor eruption-related or primary deposits and reworked (secondary) materials (Palmer and Neall, 1991; Smith, 1991; Cronin et al., 1996; Davidson and De Silva, 2000; Donoghue and Neall, 2001; Borgia and van Wyk de Vries, 2003) along with the background sedimentation and deposition of non-eruptive material (i.e. fluvial, aeolian, paleosol or peat). Therefore, the ring-plain depositional system offers the most complete sedimentological record on the cyclic behaviour of long-lived composite volcanoes (Procter et al., 2009; Zernack et al., 2009; Zernack et al., 2011; Zernack, 2021; Zernack and Procter, 2021).

1.1.1 Interplay between growth cycles and sedimentary processes

During edifice growth, volcanoclastic successions within the ring plain contain a range of volcanoclastic and sedimentary deposits that exhibit diverse textures and fabrics, along with various compositions, lithologies, grain sizes and thicknesses. All of these deposits represent time windows within the history of a volcano providing information on sedimentary and eruptive processes: (i) major poly lithologic volcanoclastic mass-flow deposits mostly in channel lithofacies along with interbedded fluvial deposits suggest cone regrowth or dome-building periods, (ii) individual tephra deposits, interbedded tephra layers within soils or debris-flow deposits with minor fluvial sequences in channel

lithofacies indicate larger eruptive periods, (iii) massive, monolithologic lahar deposits in sheet lithofacies may be derived from reworked block-and-ash flow events and possible connected eruptive activity (**Fig. 1.1 B**), (iv) major paleosol and fluvial successions, and beach sands suggest quiescence intervals with revegetation and landscape stability with less sediment influx to the environment (**Fig. 1.1 B**; Zernack et al., 2009; Zernack, 2021). Volcaniclastic mass-flow deposits encompass primary and/or secondary clasts, the former representing eruptive products of the source region, whereas the latter might originate from fluvial deposits or incorporation along the flow path (Scott, 1988a, b; Pierson et al., 1990; Major et al., 2005).

1.1.2 Volcanic mass-flows and their deposits

The different types of observed mass flows represent different generation and transport mechanisms. The term '*lahar*' (Smith, 1986) and volcanic mass-flow both describe a rapidly flowing mixture of rock debris and water, excluding normal stream flow, from a volcano, indicating the origin of the flow and including a wide spectrum of sediment/water ratios. They describe:

- Flow rheologies from dilute Newtonian flows through to normal stream flows (>20% by volume sediment).
- Variable hyperconcentrated flows with characteristic, measurable yield strength with sediment concentrations between 20-60 vol% (Beverage and Culberston, 1964) or 11-57 vol% (Pierson and Scott, 1985).
- Cohesive or non-cohesive debris flows that are highly concentrated, comprising >60 vol% of solid fraction (Costa, 1984; Pierson and Costa, 1987; Smith and Lowe 1991; Cronin et al., 2000a, b; Major et al., 2005; Pierson, 2005).

These flows were classified also by rheology (viscoplastic model: Johnson, 1970); matrix strength (Rodin and Johnson, 1976); buoyant lift (Costa, 1984; Lowe, 1982) and dispersive pressure (Bagnold, 1954). Volcaniclastic mass flows can be primary (syn-eruptive or eruption-triggered), secondary (post-eruptive or meteorologically triggered; Vallance, 2000; Thouret, 2005) or reprocessed (Sohn and Sohn, 2019). Based on the proportion of clay-sized particles, two types are distinguished: (1) cohesive (clay-rich, >3-5%) and (2) non-cohesive (<3-5% clay-sized particles; Scott et al., 1995).

They can be generated in several ways (Neall, 1976a, b): The most common events are eruption-triggered lahars, developed by transformation of water-rich tephra jets

(Lorenz, 1974a, b), ejection of crater-lake water (Scrivenor, 1929; Nairn et al., 1979; Cronin et al., 1996; Thouret et al., 1998) or direct melting of ice and snow (Pierson and Scott, 1985; Major and Newhall, 1989; Pierson et al., 1990; Pierson and Janda, 1994), as well as by de-watering and liquefaction of debris-avalanche deposits or their direct transformation (Scott, 1988; Capra et al., 2002). Lahars can also be triggered by rainfall (Rodolfo, 1989; Hodgson and Manville, 1999; Manville et al., 2000; Lavigne and Thouret, 2002; Barclay et al., 2007) during the eruption sequence or thousands of years later (Pareschi et al., 2000; Zanchetta et al., 2004; Scott et al., 2005) or by crater lake breakout floods (Manville and Cronin, 2007; Kilgour et al., 2010) and by other failures (Capra and Macias, 2002; Manville et al., 2009).

1.1.3 Post-collapse magmatic response

Sector collapses involve a rapid redistribution of a large portion of a volcanic edifice, resulting in pressurization and failure condition changes, that influence the magmatic plumbing system at depth. The changed subaerial physical conditions and their subvolcanic effects result in changes in the magmatic processes, and thus in eruptive mechanisms, eruption rates and/or erupted magma compositions. As sector collapse is a significant event during stratovolcano development, systematic variations in volcanic outputs following a collapse may be connected to the maturity of the magma reservoir, the subvolcanic plumbing system and the growth of the overlying edifice (e.g. Watt, 2019 and references therein). Studies of intraplate and arc volcanoes worldwide have highlighted that post-collapse volcanic activity can be associated with a change in magma composition and/or eruptive behaviour. In arc settings, composite volcanoes display different responses to collapse events as indicated by chemical changes of their eruptives, such as:

- More evolved magmas being erupted following collapse, i.e. at Shiveluch or Tungurahua (e.g. Belousov et al., 1999; Hall et al., 1999; Gorbach et al., 2013).
- Post-collapse volcanic activity characterised by a shift to more mafic compositions, i.e. at Fuego de Colima (Stoopes and Sheridan, 1992; Capra and Macias, 2002), Antuco (Costa and Singer, 2002), Pelée (Boudon et al., 2013; Germa et al., 2011), Chimborazo (Samaniego et al., 2012), Soufrière Hills (Watt et al., 2012; Cassidy et al., 2015) or at Stromboli (Tibaldi, 2001).

- Post-collapse absence of significant upper-crustal storage in contrast to pre-collapse evolved compositions, i.e. at Planchon (e.g. Tormey, 2010) or at Parinacota (e.g. Hora et al., 2007, 2009; Jicha et al., 2015).

Variations and changes in pre- and post-collapse erupted compositions indicate the complex and diverse processes that operate beneath volcanoes and affect the produced magma chemistry over time. Subvolcanic effects of edifice collapse that are able to influence arc magma compositions during subsequent edifice growth cycles are thought to be associated with mid- to upper-crustal processes. These might involve melt-mush or magma mixing and their ratios, wall-rock assimilation, crustal transit timescales, magma ascent and stalling and their timescales and the P-T conditions acting on mineral phase stabilities (e.g. Watt, 2019). Additionally, edifice regrowth and connected increasing influence of edifice loading are thought to promote upper-crustal storage, manifested as a return to more evolved compositions over time. However, the opportunities to study such geochemical patterns at individual volcanoes are often limited due to the lack of exposures, dating uncertainties and/or the poorly resolved or coarse stratigraphic resolution gained in the field.

1.2 Back-arc magma generation and evolution

1.2.1 Andesitic magmatism

Subduction-induced magma generation processes at convergent plate margins are primarily threefold: (1) due to subduction the generated corner flow induces mantle decompression (Sisson and Bronto, 1998; Elkins-Tanton et al., 2001; Hasegawa and Nakajima, 2004; Wiens et al., 2008; Marschall and Schumacher, 2012); (2) co-development of partial melting of the mantle wedge and H₂O-rich liquids originating from slab dehydration (Nichols and Ringwood, 1973; Ringwood, 1974; Hawkesworth et al., 1979; Tatsumi and Eggins, 1995; Schmidt and Poli, 1998; Ulmer, 2001; Grove et al., 2002; Zheng et al., 2016) and (3) melting of the subductive slab (Morris, 1995; Peacock et al., 1994).

Subduction-related andesitic magmas originate from the mantle wedge above subducting slabs and are further affected by the combination of several magmatic processes acting during ascent through the lithosphere (i.e. differentiation by fractional crystallisation or partial melting of older crust; Gill, 1981; Grove and Kinzler, 1986; Müsselwhite et al., 1989; Rogers and Hawkesworth, 1989; Müntener et al., 2001, Grove

et al., 2002, 2003; Smith and Leeman, 1987; Atherton and Petford, 1993; Tepper et al., 1993; Rapp and Watson, 1995; Chappell and White, 2001). These mantle-derived magmas primarily react with the sub-arc lithosphere in deep-crustal “hot-zones” (Hildreth and Moor bath, 1988; Price et al., 2005; Annen et al., 2006; Reubi and Blundy, 2009), followed by dominant fractional crystallisation (open and/or closed) while they ascend through the crust. The storage and plumbing systems of these melts are complex and characterised by the combination of several processes that can alter over time: (i) fractional crystallisation (FC; Bowen, 1928; Gill, 1981; Grove et al., 2003); (ii) assimilation fractional crystallisation (AFC; Grove and Kinzler, 1986; Graham and Hackett, 1987); and (iii) magma mixing (Eichelberger, 1978; Clyne, 1999; Tepley et al., 2000). Andesites that are erupted from these multi-level storage and plumbing systems are composite mixture of crystals and melts developed and derived from a variety of crustal and mantle sources (Davidson et al., 2005).

1.2.2 Methods to characterise petrogenesis

Andesitic eruptives represent magmas that have been derived by the complex processes mentioned above. Several approaches were used worldwide to decipher the pathways of petrogenetic modes and characterise the magmatic plumbing system, including (1) whole-rock major and trace element analysis coupled with isotopic geochemistry for stratigraphically controlled time-frames or eruptive episodes (Gamble et al., 1999; Price et al., 1999; Dungan et al., 2001; Gertisser and Keller, 2003; Rouchon et al., 2008; Price et al., 2012; Oyan et al., 2016;); (2) analysis of the degassing and crystallisation record (Blundy and Cashman, 2001; Rutherford and Devine, 2003); (3) trace element and isotope analysis of phenocrysts (Humphreys et al., 2006; Davidson et al., 2007); (4) geochemical analyses of xenoliths enclosed in andesitic eruptives (Graham, 1987; Graham et al., 1992; Heliker, 1995; Costa, 2000; Turner et al., 2003; Gruender et al., 2010; Stamper et al., 2014; Smith, 2014; Price et al., 2016); and (5) crystal stratigraphy techniques conducted on geochemically zoned phenocrysts to determine reservoir characteristics, mush-melt interactions, plumbing system features and potential eruption triggers (Costa and Chakraborty, 2004; Davidson et al., 2007; Blundy and Cashman, 2008; Putirka, 2008; Costa and Morgan, 2010; Ganne et al., 2018; Ubide and Kamber, 2018; Ubide et al., 2019).

1.2.3 Crystal stratigraphy: a tool to track magmatic processes

Plumbing system and crystal cargo investigations aim to use new analytical techniques on minerals, such as crystal stratigraphy, which is applied to decipher information on plumbing system and crystal cargo evolution and processes leading to volcanic activity. Crystal zonations deliver insights into differentiation processes, timescales of magma ascent or volatile element contents and magma mixing histories within a magmatic plumbing system (Humphreys et al., 2006; Blundy and Cashman, 2008; Arienzo et al., 2010; Masotta et al., 2013; Ubide and Kamber, 2018).

Pyroxene and plagioclase minerals are exceptionally useful to decrypt information of these processes due to their slow lattice/elemental diffusion rates, which allows the development of compositional zonations of certain major, minor and trace elements during specific conditions. Clinopyroxene phenocrysts record the most detailed history of recharge events, timescales from recharge to eruption and pressure - temperature conditions (Mollo et al., 2015a, b; 2018; Putirka, 2008; Perinelli et al., 2016; Ubide and Kamber, 2018; Petrone et al., 2018), while plagioclase crystals are used to assess magmatic storage conditions and processes, ascent rates and eruptive events (Blundy et al., 2006; Ginibre et al., 2007; Ginibre and Wörner, 2007; Ruprecht and Wörner, 2007; Shea and Hammer, 2013).

CHAPTER 2

LITERATURE REVIEW

2.1 Background Geology

The geological and tectonic setting of New Zealand is controlled by the subduction of the Pacific Plate under the Australian Plate, which formed an active convergent boundary that extends from the Tonga-Kermadec Trench through the Hikurangi Trench (Hikurangi Trough) to the Puysegur Trench (**Fig. 2.1 A**). The Tonga and Kermadec Arcs lie within oceanic crust (Cole, 1982), where the dip of the Benioff zone is 28-30° down to a depth of c. 100 km beneath the volcanoes. The Benioff zone then steepens from 40-57° beneath the Tongan-Islands to 55-71° beneath the Kermadec Islands (Sykes, 1966; Isacks and Barazangi, 1977) and 50-70° beneath New Zealand (Adams and Ware, 1977; Ewart et al., 1977). The Hikurangi Trench is formed within continental crust (Cole, 1982) and defines the southernmost extension of the Tonga-Kermadec Trench, where converging plate motion decreases from c. 70 mm yr⁻¹ to c. 40 mm yr⁻¹ from N to S (Walcott, 1987; Parson and Wright, 1996; Beavan et al., 1999). The Hikurangi Plateau (as the subducting oceanic plateau remnant) to the east of the North Island has variable crustal thicknesses and thus, collisional resistance to subduction, resulting in a forced clockwise rotation (Wallace et al., 2004, Rowan and Roberts, 2005; Nicol and Wallace, 2007). The subduction becomes more oblique south of the Hikurangi Trench where it transforms into a strike-slip fault system, which controls the tectonic features of the South Island (van Dissen and Yeats, 1991).

2.1.1 North Island

Beneath the North Island, the Pacific Plate is subducted into the mantle to a depth of 100 km below the continental crust of the Australian Plate, which is approximately 40 km thick beneath Ruapehu in the central part of North Island (**Fig. 2.1 B**; Reyners et al., 2006). To the west beneath the Taranaki Region, the depth of the subducting slab increases to c. 250 km (Boddington et al., 2004; Reyners et al., 2006). The Taupo Volcanic Zone (TVZ) is the southern expression of the Tonga-Kermadec subduction system (**Fig. 2.1 B**) and the main source of atypical arc volcanism on the North Island (Wilson et al., 1995; Cole, 1979, 1986).

The TVZ is one of the most productive rhyolitic magmatic system worldwide caused by the anomalously high total crustal heat flux of 2600 MW/100 km (Hochstein, 1995),

which is more than seven times the norm (Wilson, 1995). The TVZ encompasses (a) an active volcanic arc containing volcanoes from White Island to the Tongariro Volcanic Centre (TgVC) that are associated with andesite-dacite rock types and (b) an extending back-arc basin in the central part of the North Island where rhyolites dominate (Wilson et al., 1995, 2009; Rowland et al., 2010).

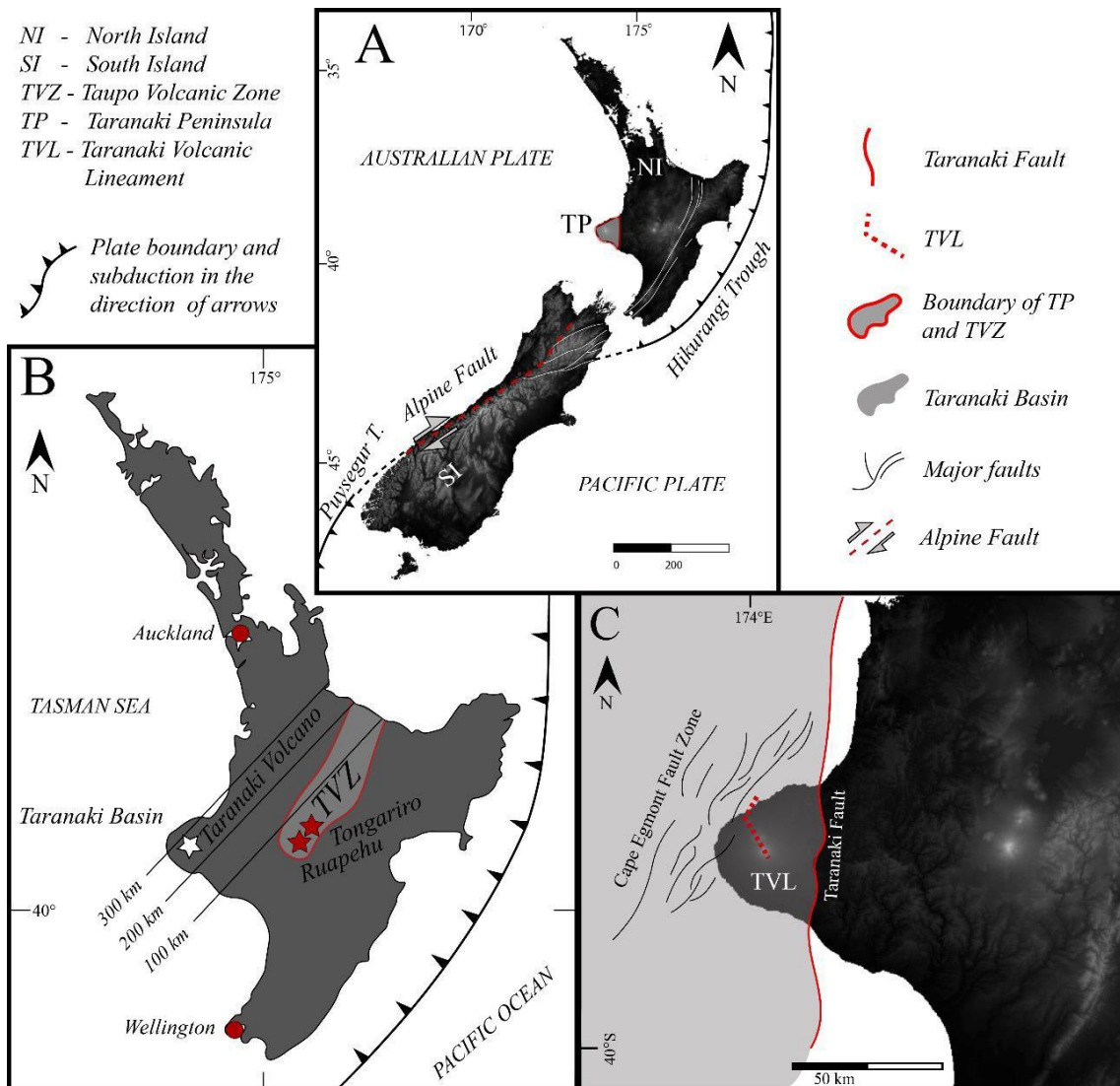


Fig. 2.1 A: Main tectonic setting of New Zealand, displaying the relationship of the Australian and Pacific Plates, the Alpine Fault and the connected Trench lines. **B:** Map of the North Island of New Zealand showing the depth of the subducting slab, the Taupo Volcanic Zone (TVZ) and the location of active andesite stratovolcanoes. **C:** Onshore part of the Taranaki Basin, which includes the Taranaki Peninsula (TP) and the Taranaki Volcanic Lineament (TVL), the Cape Egmont Fault Zone (CEFZ) to the west and the eastern boundary, marked by the Taranaki Fault. Taranaki Basin adapted from Kamp et al., 2004. Maps: Linz Database; NASA Earth Observatory.

The TgVC comprises Ruapehu, Tongariro and Ngauruhoe (Donoghue et al., 1995; Cronin and Neall, 1997; Hobden et al., 2002). The central TVZ is subdivided into four volcanic centres: Taupo, Maroa, Okataina, and Rotorua Volcanic Centres characterised

by rhyolitic and silicic volcanism and associated minor andesitic and high-Al basalt volcanism (Wilson et al., 1995). The most western area of the North Island, which is connected to subduction-related volcanic activity, is the Taranaki Basin (**Fig. 2.1 B, C**). It contains the Taranaki Peninsula that is located 130 km west of the TVZ.

2.1.2 Taranaki Basin

The Taranaki Basin (**Fig. 2.1 C**) is cut by several active and inactive Quaternary faults. The Cape Egmont Fault Zone (CEFZ) to the west of the peninsula subdivides the basin into two regions, the tectonically inactive Western Stable Platform and the active Eastern Mobile Belt dominated by extension- and compression-related tectonic processes (King, 1991; King and Thrasher, 1996). The Taranaki Fault (**Fig. 2.1 C**; TF) marks the eastern boundary that vertically offset the basement by 6 km and has accommodated a dip-slip displacement of 12-15 km since the Late Cretaceous (King and Thrasher, 1996; Nicol et al., 2004). The Taranaki Basin was formed during the extension and faulting of the basement associated with the opening of the Tasman Sea in the middle Cretaceous. The basin was subsequently filled with 5-10 km thick sedimentary sequences consisting of limestone, coal, silt- and sandstones of Late Cretaceous to Pleistocene age (King and Thrasher, 1996). The basin (100 000 km²) overlies a basement of calc-alkaline metamorphic and plutonic rocks that belong to the Median Tectonic Zone (MTZ; Mortimer et al., 1997). The Taranaki Peninsula, also known as the Taranaki Region, represents the onshore component of the Taranaki Basin. The deeper basement geology of the Taranaki Region is considered to be part of the Median Batholith (Mortimer et al., 1999), which is overlain by Cenozoic sedimentary rocks, such as coals, limestones, silt- and sandstones that are covered by an up to 300 m-thick volcanoclastic succession derived from the Taranaki Volcanic Lineament (TVL; King and Thrasher, 1996; Knox, 1982; Muir et al., 2000; Gaylord and Neall, 2012; Reilly et al., 2015).

2.1.3 The Taranaki Volcanic Lineament (TVL)

The Taranaki Volcanic Lineament (**Fig. 2.1 C**) trends northwest-southeast (King and Thrasher, 1996; Neall, 1979; Neall et al., 1986; Neall, 2003) and is the expression of Quaternary volcanism of the western part of the North Island. The volcanoes are located about 400 km west of the trench, and c. 250 km above the Wadati–Benioff zone (Adams and Ware, 1977; Boddington et al., 2004; Reyners et al., 2006) and overlie 25 – 35 km thick continental crust (Stern and Davey, 1987). They form a chain that become

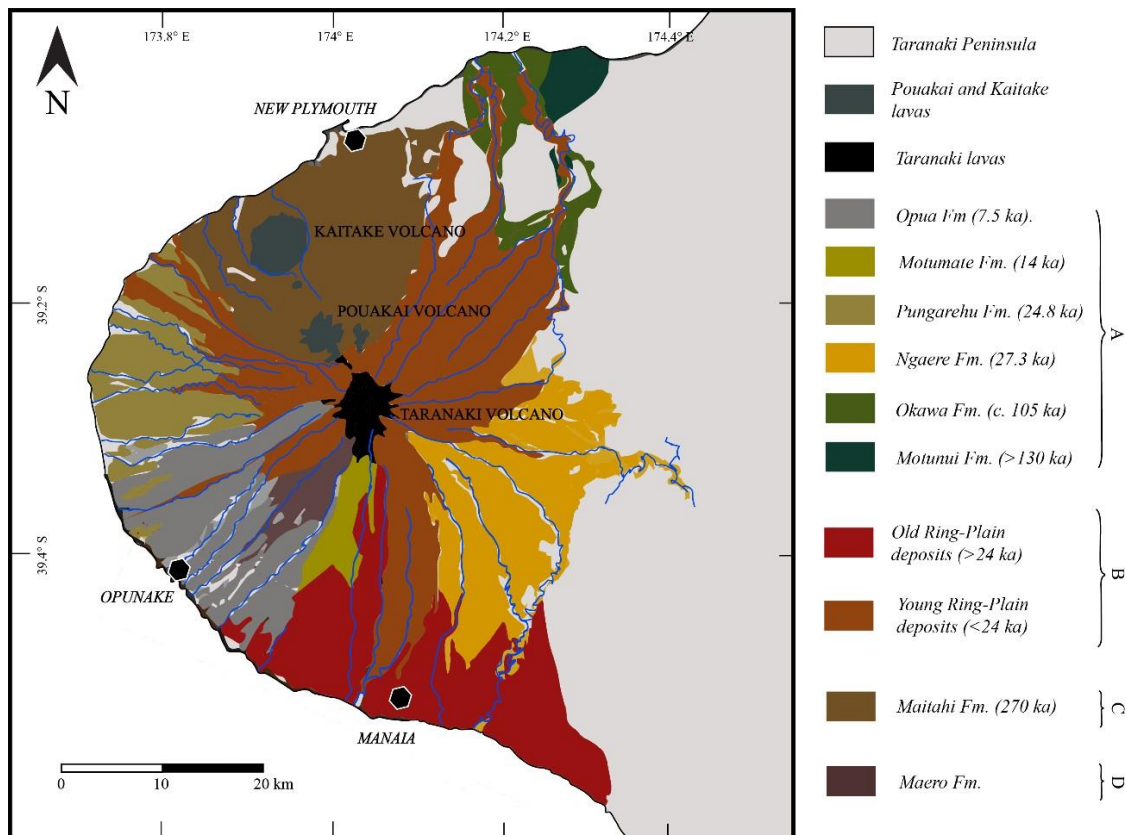
progressively younger from the NNW to the SSE and are distinct from andesitic volcanism of the TVZ (Neall et al., 1986): (a) Sugar Loaf Islands and Paritutu (*1.7 Ma*; Neall, 1979), (b) Kaitake Volcano (*0.57 Ma*; Neall, 1979), (c) Pouakai Volcano (*0.25 Ma*, Neall, 1979) and (d) Taranaki Volcano (formerly known as Egmont Volcano; *0.2 Ma*; Zernack et al., 2011). Volcanism has migrated in a southeast direction (Neall, 1979; Neall et al., 1986), which is almost perpendicular to the orientation of the TVZ lineament. The Sugar Loaf Islands are remnants of older cumulodomes offshore and the onshore volcanic spike Paritutu, representing dykes and spines (Arnold, 1959; Grant-Taylor, 1964a, b), was K-Ar dated at 1.7 Ma (Stipp, 1968). Kaitake Volcano was active at c. 575 ka (Stipp, 1968). Ten kilometres to the SE, the deeply eroded andesitic edifice of Pouakai Volcano (Neall, 2003) rises up to 1,399 m above sea level. Volcanism at this centre started at c. 670 ka (Neall, 2003) and ended with a destruction event that generated the Maitahi debris avalanche at c. 210-250 ka (**Fig. 2.2**; Gaylord et al., 1993; Gaylord and Neall, 2012). The youngest and most southerly andesitic edifice of the TVL is Taranaki Volcano. The areas surrounding Taranaki Volcano and the older edifices on the peninsula comprise deposits derived from collapse episodes (or destruction phases) and intercalated volcanoclastic and reworked deposits predominantly sourced from Taranaki Volcano (Neall, 1979; Alloway et al., 2005; Zernack et al., 2009, Zernack, 2021).

2.2 Taranaki Volcano

Taranaki Volcano (2,518 m above sea level) is the youngest member of the TVL and the second highest mountain of the North Island (Neall et al., 1986) after Ruapehu Volcano (2,797 m). Volcanism started at least 130 kyrs ago (Neall et al., 1986; Alloway et al., 2005), however, based on recognition of a c. 200 ka old debris-avalanche deposit, the Mangati Formation, an earlier inception of volcanic activity was suggested by Zernack et al. (2011). The latest known eruption occurred between 1785 and 1860 A.D. (Platz et al., 2012).

The modern Taranaki edifice is an almost perfectly shaped stratovolcano that is made up of lavas and pyroclastic deposits that are mainly younger than 14 ka (Neall, 1979; Turner et al., 2011). The eruptive history of the past 10 kyrs (Neall et al., 1986) is characterised by sub-Plinian eruptions and effusive events (Alloway et al., 1995; Damaschke et al., 2017a, b; Torres-Orozco et al., 2017a, b), which produced alternating layers of pyroxene-andesite and hornblende-andesite lavas and fragmental volcanic

deposits, including tephra-fall units, scoria-rich pyroclastic-flow deposits and juvenile-, lithic-rich block-and-ash-flow deposits. These deposits represent only a small amount (~12 km³) of the total volume of erupted material (Neall et al., 1986; Zernack et al., 2012a). The symmetric shape of the cone is broken by three lava domes on its lower flanks: (1) The Dome (900 m above sea level) and (2) Skinner Hill (1100 m above sea level), located on the northern flank and (3) the two Beehive domes (800 - 900 m) on the southern flank, which are in a NNE-trending alignment with the satellite vent of Fanthams Peak. The cone is surrounded by a 1,000 km² volcanoclastic ring plain, made up of >150 km³ of debris-avalanche, other volcanoclastic mass-flow and fluvial deposits (**Fig. 2.2**; Neall et al., 1986; Alloway et al., 2005; Procter et al., 2009; Zernack et al., 2011; Zernack, 2021). The western to southern Taranaki coast is characterised by cross-sectional successions of the <105 ka medial ring-plain, while the oldest Taranaki-sourced debris-avalanche deposits (DADs) are found in the north eastern ring-plain sector and along the northeastern coast (Alloway et al., 2005). To the north, the eroded remnants of Pouakai and Kaitake Volcanoes formed a physiographic barrier to mass-flows derived by Taranaki Volcano.



◀**Fig. 2.2** Quaternary geological map of the Taranaki Peninsula showing the distribution of debris-avalanche deposits (A); undistinguished debris-avalanche, lahar, fluvial and alluvial deposits (B); pre-Taranaki Maitahi debris-avalanche deposit (C); Young block-and-ash flow deposits of the Maero Fm (D; modified after Neall, 1979; Neall and Alloway, 2004; Alloway et al., 2005).

2.2.1 Stratigraphy

The stratigraphy of Taranaki Volcano can be subdivided into two categories: (1) the modern edifice succession and (2) the older ring-plain deposits (**Table 2.1**; Neall, 1979; Neall et al., 1986; Alloway et al., 1995, 2005; Zernack et al., 2009, 2011; Zernack, 2021). At least 14 large-scale and several minor collapse events were identified in the last 200 kyr of volcanic activity at Taranaki Volcano (Zernack et al., 2009, 2011) and these deposits are represented in its surrounding ring plain (**Fig. 2.2**) that extends 25-45 km onshore from the present summit.

Edifice failures occurred on average every 8 kyr, with five collapses recognised in the last 30 kyrs (Zernack et al., 2011). Although the frequency of collapse events are minimal estimations based only on the recognised and mapped debris-avalanche deposits (Zernack et al., 2012a). The volcanoclastic sequences comprise mass-flow deposits that are exposed in cross-sectional cliffs along the coastline representing medial facies at distances between 20-45 km from source. Proximal mass-flow sites are here considered to be <15 km and distal distributions are typically >50 km (c.f. Scott et al., 1995; Waythomas et al., 2000; Major et al., 2005). The southwestern ring-plain system consists of debris-avalanche units, volcanoclastic mass-flow deposit sequences, fluvial deposits, paleosol / peat-dominated accumulations, aeolian sands and rarely tephra deposits. These deposits exhibit a range of transport and emplacement mechanisms, environmental conditions and associated volcanic influences that can be connected to particular periods within repeated growth and collapse cycles of Taranaki Volcano (Palmer and Neall, 1991; Zernack et al., 2009; Zernack, 2021; Zernack and Procter, 2021).

2.2.2 The volcanic history of the 65-34 ka period

The previously used term “Composite Formations” (Grant-Taylor and Kear, 1970; Neall, 1979) referred to deposit sequences that make up the c. 80 – 50 ka and 38 – 30 ka southern and southwestern sectors of the ring plain and include debris-avalanche, volcanoclastic mass-flow (or lahar) and alluvial deposits. The identification of the “Stratford and Opunake lahars” was carried out during the initial mapping of the Taranaki region (Hay, 1967) and later studies described these formations in more detail with the

Stratford Fm. occupying the area to the east of Manaia and the Opunake Fm. occurring between Opunake and Manaia (Grant-Taylor and Kear, 1970).

Subsequent studies recognised individual debris-avalanche deposits (Palmer and Neall, 1991; Palmer et al., 1991) and redefined their dispersal (Neall and Alloway, 2004). The most recent studies concluded that at least three major collapse events happened during the here studied interval of 65-34 ka (**Table 2.1**; Zernack et al., 2011):

<i>DA deposits</i>	<i>DF deposits</i>	<i>Other key marker</i>	^{14}C yrs BP	<i>Age (ka)</i>
<i>Opua</i>		<i>Oakura Tephra</i>	$6,570 \pm 110^c$	7.5^c $c. 7.8^c$
<i>Motumate</i>				14^{ac}
		— <i>Katikara Sands</i> — <i>Okato Tephra</i>		$c. 27.3-15.1^c$ $c. 19.2^c$
<i>Pungarehu</i>				$20,776 \pm 170^a$
<i>Ngaere</i>			$23,400 \pm 400^e$	27.3
<i>Te Namu</i>			$29,074 \pm 399^a$	34^a
		<i>Hihiwera Peat</i>		$36.9-34.4^a$
<i>Rama</i>	<i>Ihaia</i>		$31,522 \pm 381^a$	36.9^a
		<i>Rotoehu Tephra</i>	$<44,330 \pm 1,757^b$	$c. 45-40^a$ 45.1^f
	<i>Young Kaupokonui</i>			$c. 50-45^a$
<i>Otakeho</i>			$>44,330 \pm 1,757^b$	$c. 55-50^a$
	<i>Punehu</i>			$60-55^a$
	<i>Old-Kaupokonui</i>			$60-55^a$ $c. 60^a$
<i>Tokaora</i>		— <i>Punehu Sands</i>		$c. 80-60^a$
<i>Waihi</i>				
<i>Waingongoro</i>				$c. 75^a$ $c. 80^a$
		— <i>Puketapu buried forest</i> — <i>Manaia Lignite</i>		$c. 80^g$ $c. 80^g$
<i>Oeo</i>				$c. 90-85^a$
		<i>Inaha Marine Bench</i>		100^h
<i>Okawa</i>				$c. 105^i$
		<i>Rapanui Marine Bench</i>		127^h
<i>Motunui</i>				$>130^i$
<i>Mangati</i>				$c. 200^i$
		<i>Ngarino Marine Bench</i>		210^h

^a Zernack et al. (2011), ^b Tinkler (2013), ^c Neall (1979), ^d Vandergoes et al. (2013), ^e Alloway et al. (1995), ^f Danišič et al. (2012), ^g McGlone et al. (1984), ^h Pillans (1983), ⁱ Alloway et al. (2005)

Table 2.1 Major collapse and mass-flow events with other markers in the Taranaki Region (adapted from Zernack, 2021). ^{14}C yrs BP presents radiocarbon years before AD1950. Ages (ka) refer to 10^3 years before present including calibrated radiocarbon dates BP and chronostratigraphic estimates. Red dashed lines indicate the boundaries of the investigated time period of this study. DA: debris-avalanche; DF: debris-flow.

(i) the collapse event that produced the Otakeho debris-avalanche deposit at ~55 kyrs ago; (ii) the failure resulting in the emplacement of the Rama debris-avalanche deposit c. 40 kyrs ago; and (iii) the generation and deposition of the Te Namu debris-avalanche deposit 34 kyrs ago. Two additional key markers are recognised in the target sequence: (1) the Hihiwera Peat with converted calendar ages of $34,227 \pm 0,283$ kyr (Zernack et al., 2011), $38,679 \pm 1,097$ kyr (McGlone et al., 1984) and $39,735 \pm 1,443$ kyr (Grant-Taylor and Rafter, 1963) at various locations; and (2) the Ihaia debris-flow deposit (DFD) with a calibrated age of $36,896 \pm 0,417$ kyrs (Table 2.1; Zernack et al., 2011).

2.2.3 Petrology

The first classification for Taranaki rocks was given by Gow (1968) based on ferromagnesian phenocryst assemblages, recognising 5 types of rocks: augite andesite; augite – hornblende andesite (augite > hornblende); augite – hornblende andesite (augite ~ hornblende); augite – hornblende andesite (augite < hornblende); augite – olivine andesite (modal olivine up to 7%). Later on, this classification was updated by adding new mineral phases such as plagioclase and biotite (Neall et al., 1986; Stewart et al., 1996; Price et al., 1999). Igneous rocks of Taranaki are mainly andesites and basaltic-andesites with minor basalts (Price et al., 1992). The most common rock type is augite – hornblende andesite (augite > hornblende). The main phenocryst phases are plagioclase, clinopyroxene, hornblende, Fe-Ti oxides (titanomagnetites with additional ilmenite), minor olivine and orthopyroxene (Neall et al., 1986; Stewart et al., 1996; Zernack et al., 2012). Accessory minerals that occur rarely are apatite and zircon (Neall et al., 1986). Crustal xenoliths are abundant and classified as peridotite, pyroxenite, amphibolite, gabbro, diorite and meta-sediments mainly originating from the Median Batholith basement (Price et al., 1992; Gruender et al., 2010).

Geochemically, Taranaki rocks are classified as high-K, low-Si andesites (Gill, 1981) with magmas becoming progressively enriched in potassium and silica over time (Stewart et al., 1996; Price et al., 1999, 2005, 2016; Zernack et al., 2012b). Taranaki eruptives are highly evolved based on $Mg\# < 53$ and low whole-rock Cr and Ni contents (Price et al., 1999). Trace element abundances are characterised by significant enrichment of large ion lithophile elements (LILE; such as Rb, Sr, Cs, Ba) and light rare elements (LREE) compared to high field strength elements (HFSE; Ta, Nb, Zr; Price et al., 1992, 1999, 2005). Typical arc-signatures such as depletion of Nb relative to La and enrichment of Pb

and Sr relative to Ce are characteristic features as well. These signatures indicate low-degree partial melts from a depleted mantle source (Price et al., 1999). Isotopes of Taranaki rocks exhibit a narrow trend of $^{143}\text{Nd}/^{144}\text{Nd}$ and $^{87}\text{Sr}/^{86}\text{Sr}$ ratios (Price et al., 1992, 1999, 2005; Zernack et al., 2012), similar to evolved basalts and basaltic andesites from the TVZ (Price et al., 1992).

2.2.4 Temporal evolution of the Taranaki magmatic system

A broad range of studies have characterised the temporal evolution as well as early and mature stages of the tectono-magmatic system beneath Taranaki Volcano, based on geochemical examination of young tephra fall deposits, block-and-ash flow deposits and lavas or older clast assemblages from debris-avalanche deposits (Platz et al., 2007a; Turner et al., 2008a; Zernack et al., 2012b; Damaschke et al., 2017a, b). The current model of the Taranaki magmatic storage and plumbing system is shown in **Fig. 2.3**, which also summarises the most important statements of the respective studies:

- Stewart et al. (1996) developed a model for the high-K magmatic system outlining the petrogenesis of Taranaki magmas in three stages: (i) High-Al basaltic melts react with fractionated and wall-rock mafic minerals in the lower crust. (ii) The rising basaltic andesite magmas begin to melt amphibole in wall-rocks, generating K_2O -rich liquids resulting in the temporal increase of potassic magmas. (iii) At shallow depths, the magma is stored and becomes zoned by melt segregation, generating a hydrous upper part or fluid-rich ‘cap’. Fractionation of amphibole drives the melt composition from andesitic to dacitic. Therefore, the residual melt will crystallise further plagioclase around xenocrysts and phenocrysts.
- A general model was constructed by Price et al. (1999) explaining the evolution of andesitic and rhyolitic magmatic systems, which highlights the differences and similarities between Taranaki and Ruapehu magmas (Price et al., 1999). Geochemical contrasts were attributed to the different slab contribution beneath Taranaki Volcano, a more depleted mantle wedge component and distinct parental magma compositions. The evolutionary trends of the two magmatic systems were explained by differences in crustal thickness and heat flow.
- A further conceptualised model by Price et al. (2005), Gruender et al. (2010) and Zernack et al. (2012b) proposed that magmas feeding into the plumbing system were primarily generated in a lower crustal “hot zone”, based on the model

established by Annen et al. (2006). Their concept corroborates basaltic magma modification through fractional crystallisation (FC) and assimilation (AFC) of the partially melted lower crust. This small-scale “hot zone” is generated due to repeated primitive melt intrusions into the lower crust raising the geothermal gradient. As a result of the developed hot zone, larger parts of the lower crust were melted interacting with fractionating primitive magmas, which lead to the development of progressively more K-rich and LILE-enriched compositions over time. This complex model is used to explain the genesis of Taranaki magmas, and the evolution of magmas and the subvolcanic plumbing system.

- A ‘recharge model’ was proposed by Turner et al. (2008a) for the young Taranaki eruptives suggesting a mature, two-staged upper magma system (>10 ka) based on the investigation of phenocryst assemblages of plagioclase, pyroxene, amphibole and titanomagnetite. The model states that the upper-level reservoir (5 – 7 km) of Taranaki Volcano was recharged by a similar, but hotter and more volatile-rich magma. It is corroborated by patchy plagioclase, amphibole and clinopyroxene cores, which suggest decompression resorption processes and the resorption of high-Ti titanomagnetites. The model suggests that these mineral phases were crystallised at depth and upon ascent, each phase was resorbed due to decompression-driven superheating, followed by volatile dissolution and decompression crystallisation.
- Recently, Price et al. (2016) have reconstructed a lithospheric cross-sectional model beneath Taranaki Volcano based on xenoliths, assuming that (1) primary basaltic magmas from lithospheric and or mantle sources were underplated, stored within, and over time, interacted with the lower crust forming a MASH (Hildreth and Moor bath, 1988) or deep crustal “hot-zone” (Annen et al., 2006). (2) The lower crustal wall rocks were melted and suffered assimilation. (3) The mantle-derived magmas went through fractional crystallisation and ascended to shallower depths, over time building up a complex, multi-level magma storage and plumbing system (Gruender et al., 2010; Zernack et al., 2012b), which became progressively more fractionated with evolved magmas. Crustal level processes, direct crustal input and their complexity were argued to play an important role throughout the generation of andesitic suites beneath the volcano.

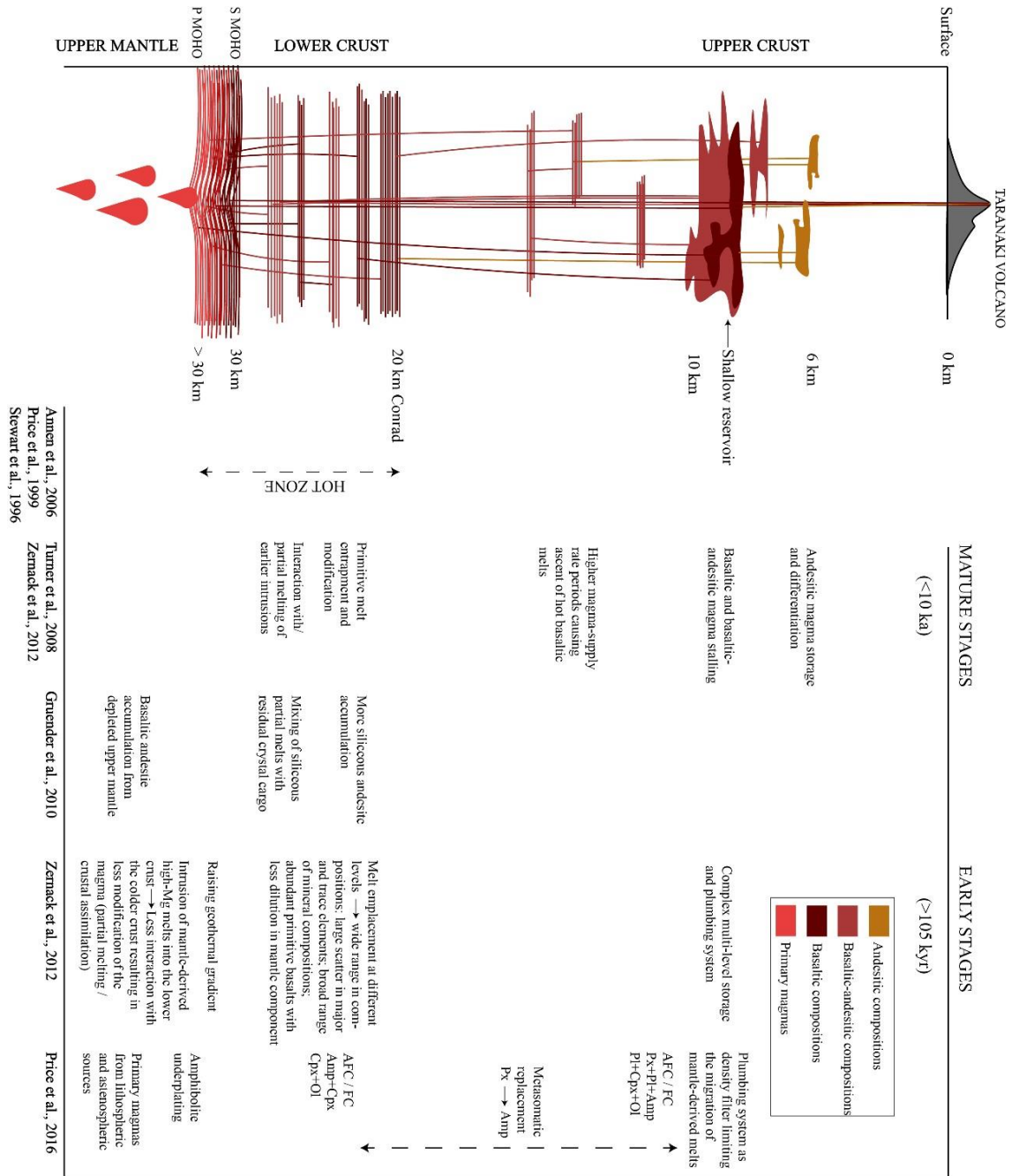


Fig. 2.3 Summarised schematic depiction representing the lithospheric cross-section beneath Taranaki Volcano (modified after Zernack et al., 2012b; Price et al., 2016) focused on the magmatic system and the petrogenesis of volcanic rocks based on the previous studies that are presented in the figure (Stewart et al., 1996; Price et al., 1999; Annen et al., 2006; Turner et al., 2008a; Gruender et al., 2010; Zernack et al., 2012b; Price et al., 2016). P Moho: Petrological Moho; S Moho: Seismological Moho; Conrad: Conrad Discontinuity.

2.3 Research question

Individual long-lived stratovolcanoes can experience repeated edifice growth interspersed by catastrophic sector collapse events. During edifice growth cycles (i.e. construction or growth phases), dome collapses or flank collapses of stratovolcanoes can be triggered by a variety of mechanisms and pose a significant risk to the population and infrastructure close to the volcano. However, the processes of alternating collapse and re-growth operate over long-time scales and such cyclic behaviour is often overlooked as most of the time the evidence of such phases is buried or eroded (e.g. Zernack et al., 2012a). Due to more complete exposure, studies often concentrate on the Holocene geologic record, an interval which is too brief to interpret long-term cyclic characteristics of a volcano (e.g. Siebert et al. 1995; Belousov et al. 1999; Waythomas & Miller 1999; Reid et al. 2001; Zernack et al., 2011). While collapse events and the produced debris-avalanche deposits have been reported and investigated at many volcanoes worldwide, for most volcanoes only one major collapse event is recorded. Repeated debris avalanches have been described from several long-lived stratovolcanoes globally, e.g. Colima (Stoopes and Sheridan, 1992), Rainier (Vallance and Scott, 1997), Shiveluch (Belousov et al., 1999) or Taranaki Volcano (Procter et al., 2009, Zernack et al., 2009, 2011).

New Zealand has several long-lived stratovolcanoes, such as Taranaki and Ruapehu Volcanoes, and Tongariro as a complex volcano, that exhibit long-term records of growth and destruction cycles providing a unique opportunity for detailed hazard analysis. The observed high frequency of volcanic mass-flow events throughout growth cycles pose a significant hazard for the nearby population, because they are able to inundate large areas (>25 km from source). In the case of Taranaki Volcano, mass flows and debris avalanches could potentially impact the extensive drainage network, reaching significant parts of the region (Neall, 1976a, b; Zernack et al., 2009; Procter et al., 2009). Earlier studies provided knowledge on the magmatic processes, the temporal evolution and the volcanic eruptive history of the young (<24 ka) and old (>105 ka) Taranaki volcanic system. However, the time-period of 65-34 ka has not been studied in detail, therefore this study aims at closing this knowledge gap.

A fundamental question that arises is how does the magmatic system respond to consecutive collapse and regrowth of Taranaki Volcano? Furthermore, how does the magmatic plumbing system behave during individual edifice re-growth cycles and how is this reflected on the sedimentary and geochemical characteristics of the produced

volcaniclastic mass-flow deposits? Can these deposits be used to construct a petrogenetic model that assesses the temporal changes of the magmatic system throughout growth phases and what are the best approaches in the field and the laboratory? Do the magmatic sources and processes vary over short timescales at Taranaki Volcano and do these variations provide evidence of an influence by the increasing edifice load conditions over time.

In order to address these questions, this study will investigate and characterise the sedimentology, lithology, stratigraphy and geochemical variability of volcaniclastic mass-flow deposits throughout several consecutive growth cycles that are exposed in the medial Taranaki ring plain with a nearly continuous stratigraphic record.

2.4 Objectives

This research intends to explore and elucidate, from subaerial to subvolcanic scales using sedimentological and geochemical perspectives, the temporal driving forces and processes operating at stratovolcanoes during growth cycles. This aim may be reached by investigating stratigraphically localised volcaniclastic deposits as edifice growth indicators in order to zoom into the eruptive products they deposited to discover the space-time conditions of the Taranaki magmatic plumbing system at depth, the connected characteristics of andesitic magmatism and its response to edifice growth over time.

The below presented objectives were set as the main stepping stones of this research in the light of the following aspects:

- Taranaki Volcano underwent at least 14 collapse events throughout its ~200 ka lifetime and the modern edifice has already reached a structurally unstable condition.
- The observed volcaniclastic mass flows travelled more than 30 km from source, and thus had significant impact on medial areas (25-30 km), which are now populated and intensively farmed.
- Our insufficient knowledge of the Taranaki volcanic system during growth cycles is inadequate for accurate future hazard assessments.
- The unique volcaniclastic record provides an opportunity to gain insights into the andesitic magmatism of an atypical arc system during consecutive growth cycles, which may significantly improve our present-day knowledge on this topic.

Five principal objectives were developed as follows:

Objective 1: Investigating sedimentological, lithological and stratigraphic properties and relationships of volcanoclastic mass-flow deposits in the southwestern sector of the Taranaki ring plain.

Volcanoclastic mass-flow deposits at Taranaki Volcano are exceptionally well-exposed due to continuous coastal erosion and uplift of the ring plain succession. This provides access into time-windows, which are buried and/or eroded at more proximal (<20 km) sites of the modern edifice. The southwestern sector of the ring plain is unique in that the exposed debris-avalanche and volcanoclastic mass-flow deposit sequences along with fluvial sediments, aeolian deposits and paleosols display a nearly continuous stratigraphic timeframe between c. 65-34 ka. The range of volcanoclastic deposits, their different sedimentary textures, lithologies and paleotopographic relationships record the volcanic history of Taranaki Volcano.

Thus, the classification of these well-exposed volcanoclastic mass-flow deposits based on their broad range of observed facies variations may provide robust information to develop a classification criteria specifically attributed to volcanoclastic deposits, which can be applied globally in ring-plain settings. The classification further acts as a foundation for establishing a more detailed stratigraphic model for the time period c. 65-34 ka, by elucidating the nature of sedimentary and volcanic processes, while broadening our knowledge on the complex evolution of the Taranaki ring plain system and stratigraphy.

Objective 2: Geochemical fingerprinting of consecutive Taranaki growth cycles based on the nearly continuous stratigraphic succession from c. 65-34 ka.

The aim is to target specific volcanoclastic mass-flow deposits that indicate a direct relationship with eruptive periods during individual growth cycles for sampling their eruptive products. Major and trace element whole-rock analysis of the sampled volcanic clasts allows the geochemical characterisation of the individual growth cycles within the studied time period and potential temporal variations. This provides the basis for developing a petrogenetic model for inter-collapse (i.e. growth cycle) conditions of Taranaki Volcano.

The eruptive sample suite can further be subjected to geochemical analyses of the mineral assemblages (such as plagioclase, clinopyroxene, Fe-Ti oxides and amphiboles) as a tool for investigating the geochemical characteristics of the Taranaki crystal cargo

between c. 65-34 ka. The result will be compared to what is known about the early system (>105 ka) to gain insights into the temporal evolution of the Taranaki magmatic plumbing system. Furthermore, a geochemical comparison of studied debris avalanche deposit clast assemblages and growth cycle eruptives may unravel geochemical signatures that indicate the response of the Taranaki magmatic system to repeated edifice collapse and regrowth.

Objective 3: Determining crystallisation conditions and characterising ascending melts during individual growth cycles.

The P-T-H₂O conditions of crystallisation and the ascending melts can be determined based on the mineral geochemical data derived in Objective 2. Geothermometry, geobarometry and hygrometry modelling will be undertaken to develop a better understanding of the vertically complex plumbing system beneath Taranaki Volcano, the characteristics of melts mobilised at depth and the overall response of the magmatic system to frequently occurring edifice collapse and subsequent regrowth. The results will be compared to datasets from earlier studies, to reveal similarities or discrepancies in relation to crystallisation conditions within the Taranaki magmatic plumbing system.

Objective 4: Crystal stratigraphy of texturally and chemically complex mineral phases to unravel recurring patterns within the Taranaki crystal cargo.

The whole-rock compositional results obtained in Objective 2 will provide the basis for further investigating textural and chemical patterns in the observed mineral phases of the Taranaki crystal cargo. Crystal stratigraphy will be used on selected plagioclase and clinopyroxene crystals from each studied growth cycle. Applying this technique allows the exploration of multiple elemental variations (i.e. zonations) within a complex crystal by mapping the entire crystal surface. Choosing a range of whole-rock compositions and analysing the comprised crystals, may unfold specific links or uncoupling between the bulk-rock and mineral assemblage geochemistry. Crystal stratigraphy will not only provide information on the observed crystal patterns and their recurrence but may also expose chemical signatures of specific major and/or trace elements within certain regions of the crystals. These can be linked to unique magmatic processes and their spatiotemporal variation within the vertically extended Taranaki magmatic plumbing system.

Objective 5: Temporal aspects of the Taranaki magmatic system and the development of an integrated model for inter-collapse states.

Conclusively, the data and new knowledge obtained in Objectives 1-4 will provide the foundation for developing a revised Taranaki petrogenetic model in the light of growth and collapse cycles, which will be tuned to the early models. This will significantly improve our present-day understanding of the spatiotemporal variation of mid-crustal processes at back-arc volcanoes and their response to edifice growth cycles.

2.5 Thesis Outline

This dissertation is comprised of submitted or planned to be submitted manuscripts. Therefore, repetition, to a certain extent, is present between chapters, mainly connected to the introductory sections describing the geological and petrological aspects of Taranaki Volcano. This chapter dealt with a summarized introductory on the topics this research gains insights into, and is followed by Chapter 2, providing a geological and petrological background to Taranaki volcanism. Chapter 3 introduces the methods applied in this research, the connected terminology, and the used models.

The core of this study comprises the following chapters. Chapter 4 deals with the field work related observations, classification development and reconstructed stratigraphy of the volcanoclastic mass-flow deposits in the Taranaki ring plain. Chapter 5 builds upon the information collected on the field and intends to investigate the temporal geochemical variation of Taranaki volcanic rocks during consecutive growth cycles. Melt-mush mixing is proposed as the dominant magmatic process on which edifice loading has a significant effect over time towards pre-collapse states. The subject of Chapter 6 involves the crystallization conditions (i.e. P-T-H₂O) of the Taranaki crystal cargo observed within the collected pyroclasts (i.e. the amphiboles and clinopyroxenes) of the individual growth cycles and further encompasses the exploration of the plagioclase and clinopyroxene chemical zonation patterns, for which the crystal pattern classification framework was developed.

As the final parts of the thesis, the focus of Chapter 7 includes the synopsis of the volcanoclastic mass-flows as multitools, the discussion on the newly developed Taranaki petrogenetic model and the origin of the recycled crystal cargo. Further, it introduces the comparison between the early system (>105 ka) and mid-age system (65-34 ka) in the light of the physical conditions of crystallization and emplaces the findings of this

research on an international level. The closing Chapter 8 consists of the short summary of the objectives that were targeted and achieved by this study and provides implications for future research.

CHAPTER 3

METHODOLOGY

3.1 Terminology

This research builds on different sedimentological, lithological and volcano-sedimentological descriptions and concepts, which have been developed by a range of previous studies that also defined specific nomenclature. The terminology used in this study is introduced and summarised below.

General terms: The term Taranaki Volcano corresponds to the edifice, whereas other terms used in this study (such as Taranaki magmatic system, Taranaki phenocrysts, Taranaki melts, etc.) are all referred to Taranaki Volcano. The terms “lahar” and “volcanic mass-flow” are here used for gravity-driven flows of high-concentration mixtures containing water and solid particles, wood or ice and other debris (such as epiclasts after Fischer, 1961) that originate from volcanoes (e.g. Vallance 2000; Vallance and Iverson, 2015). Volcaniclastic deposits are produced, transported and deposited by volcanic and sedimentary processes, comprising diverse particles that underwent various fragmentation, transport and depositional procedures (Fisher and Schmincke, 1984; Cas and Wright, 1987; McPhie et al., 1993; White and Houghton, 2006; Manville et al., 2009; Sohn and Sohn, 2019). In this study, the term “volcaniclastic mass-flow deposit” encompasses all deposits that comprise volcanic debris (e.g. McPhie et al., 1993; White and Houghton, 2006), which are typically deposited by volcanic mass-flows. The different types of volcaniclastic mass-flow deposits are described in detail in **Chapter 4**. Primary volcaniclastic deposits are understood as deposits that did not involve interim storage and this study follows the terminology of White and Houghton (2006). Secondary (i.e. reworked) volcaniclastic deposits are constituted as volcaniclastic particles created through or after volcanic eruption and were deposited by volcanic processes, but they underwent “reworking” by typical sedimentological mechanisms before lithification (e.g. Sohn and Sohn, 2019). A pyroclast in this study is defined as a volcanic rock that was formed by explosive volcanic fragmentation, using the classification of Fischer (1961). The “ring plain” was coined by Cronin and Neall (1997) and Davidson and de Silva (2000) and describes a geometrically well-defined volcaniclastic apron that surrounds a volcanic edifice.

Grain-size terminology: Grain-sizes of the investigated volcaniclastic mass-flow deposits were determined by applying the classification of Wentworth (1922). The grain

size terminology for volcanoclastic deposits used here follows the nomenclature developed by White and Houghton (2006) that connects the terminology by Fischer (1961) with a deposit-origin focus (Cas and Wright, 1987) while integrating the scale for grain-size determination of Wentworth (1922).

Componentry terminology: The studied volcanoclastic mass-flow deposits are comprised of remobilised juvenile and lithic components, such as recycled pumice, scoria and dense clasts and individual crystals, that were defined following the component classification of White and Houghton (2006). Pumiceous and scoriaceous pyroclasts, or in this study collectively referred to as vesicular pyroclasts, exhibit similar characteristics (with respect to vesicularity, phenocryst and/or microcryst content), especially in the case of the eruptive products of Taranaki Volcano. However, when feasible, pumice and scoria clasts are distinguished by their colour with pumices typically being white or light grey and rarely yellow (e.g. McPhie et al., 1993; Jackson et al., 2005), whereas scoriae are commonly dark grey or black in colour (e.g. Taddeucci et al., 2015).

3.2 Field Campaign

Field observations involved detailed mapping of the south and southwestern sector of the medial (25-30 km from source) ring plain succession over a c. 30 km-long stretch of coastline between the townships of Opunake and Manaia (**Fig. 3.1**). This involved using the debris-avalanche stratigraphy for chronostratigraphic control and to identify the boundaries of growth cycles between collapse events. Additional marker beds, such as the Hihiwera Peat and the Ihaia debris-flow deposit recognised by earlier studies (Zernack et al., 2011), helped further define the timeframes of volcanic mass-flow deposition in the southwestern ring-plain sector.

Stage 1. *Deposit classification*

Volcanoclastic mass-flow deposits were identified based on lithological and sedimentological features and by their stratigraphic position with respect to marker beds. A classification system was established based on clear distinction-criteria derived from specific sedimentary features of the volcanoclastic mass-flow deposits, as well as varying petrofacies, i.e. lithological variation of comprised clast assemblages, and physiographic facies (reflecting the influence of the paleotopography; see detailed description in **Chapter 4**).

Stage 2. *Key sections*

Stratigraphic columns were recorded and measured at selected key sections (**Appendix**

A2) along the coastline, which provided the best detailed exposure of the volcanoclastic mass-flow deposits over the studied time period (c. 65-34 ka). These key sections were also used to develop the classification scheme mentioned above in Stage 1. The deposits were described and characterised in lateral exposure to record depositional changes mainly perpendicular to the source and rarely parallel to the flow direction.

Stage 3. Stratigraphic model

The coastal cross-section of the volcanoclastic mass-flow deposits was mapped by establishing the stratigraphy of individual deposit packages and analysing facies variations over the studied 30 km-long stretch of shoreline. The location of paleochannels was recorded and their age range was estimated (**Appendix A2**). These erosional unconformities proved to be helpful markers and tools for reconstructing the volcano-sedimentological history of the investigated time period.

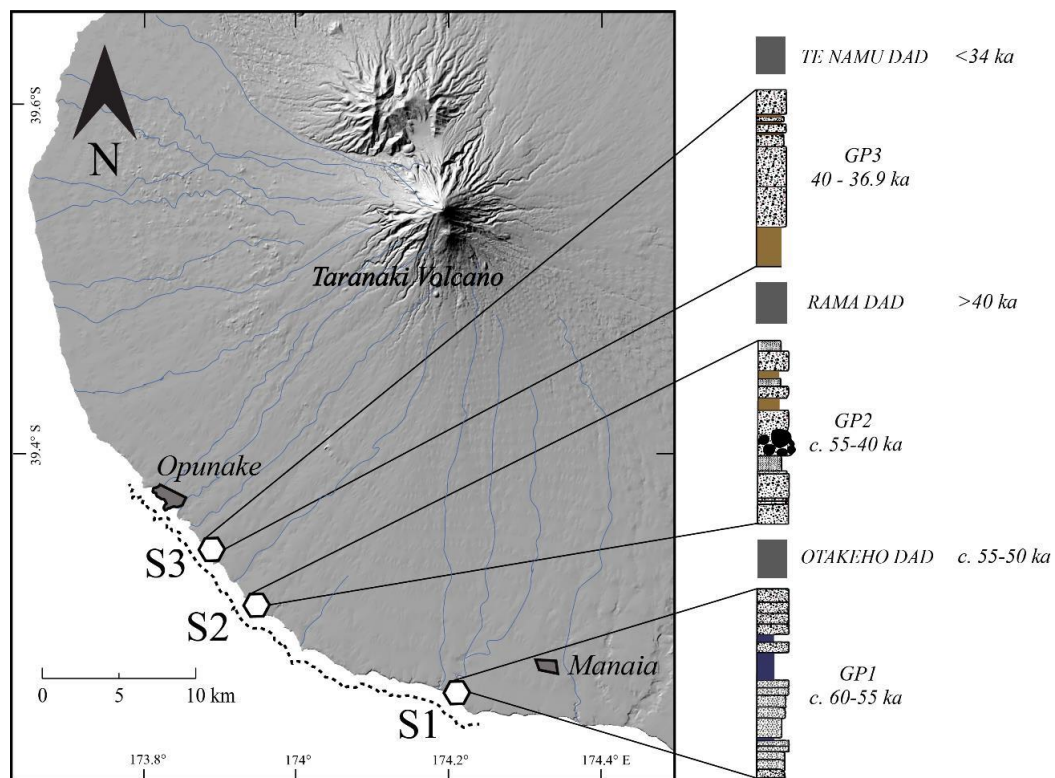


Fig. 3.1 Map of the southern and southwestern sector of the Taranaki ring-plain system indicating the location of the investigated medial coastal region (black dashed line) and the chosen main sites (S1, S2, S3) of the growth phases (GP) along with their estimated stratigraphic timeframe. The stratigraphic context of the representative sites is defined through debris-avalanche deposits (DAD) as chronostratigraphic markers (after Zernack et al., 2011) separating individual growth phases.

The interpretation and classification of deposits was based on and linked to the research of Stage 1 and 2, respectively. Combining all observations, a stratigraphic model

was developed for the volcanic history of Taranaki Volcano between 65-34 ka.

Stage 4. Selection of outcrops for further analysis

After unravelling the ring-plain stratigraphy, widely distributed lithic- and pumice-dominated volcanoclastic mass-flow deposits that represent specific volcano-sedimentary conditions during edifice growth cycles were targeted for sampling and further geochemical analysis. For this purpose, key sections that contained the highest number of lithic- and pumice-dominated mass-flow deposit packages with interbedded paleosols or fluvial deposits were chosen as they hold the most complete volcanoclastic and sedimentary record of individual growth phases (GPs; locations of S1, S2, and S3 and timeframes are indicated in **Fig. 3.1** and coordinates can be found in **Appendix A1**).

3.3 Laboratory Work I – Sedimentology approach

3.3.1 Sample preparation

Collected samples include coarse-lapilli or rarely bomb-sized pumice and scoria clasts from each volcanoclastic mass-flow deposit (10 – 20 clasts from each mass-flow package; **Fig. 3.2**; see sample locations and connected stratigraphy in **Appendix B3**). Individual clasts were cleaned and cut in half. Part (1): Petrographic thin sections (~50-100 µm thick) were prepared for petrology and following analyses. The greater thickness was chosen due to the fragile texture of the rocks. However, further analyses required additional thin section preparation with a standard thickness of ~35 µm. Part (2): Ultrasonic bath was used to clean more the rest of the samples (n = 220) thoroughly. After drying, outer parts of the samples were cut, then the inner parts (minimum 10 – 15 clasts from each layer) were prepared for further geochemical analysis.

3.3.2 Grain-size distribution and componentry

Selected mass-flow deposit packages were subjected to grain-size and componentry analysis (**Appendix A1**) using the point counting method. Two photographs of each layer were taken of an area between 300 x 300 – 1000 x 1000 mm that comprised general macroscopic features of certain deposit textures. Grids of 1 x 1 cm size were used on the photographs in order to classify the clasts by lithology and size (e.g. Karátson et al., 2002).

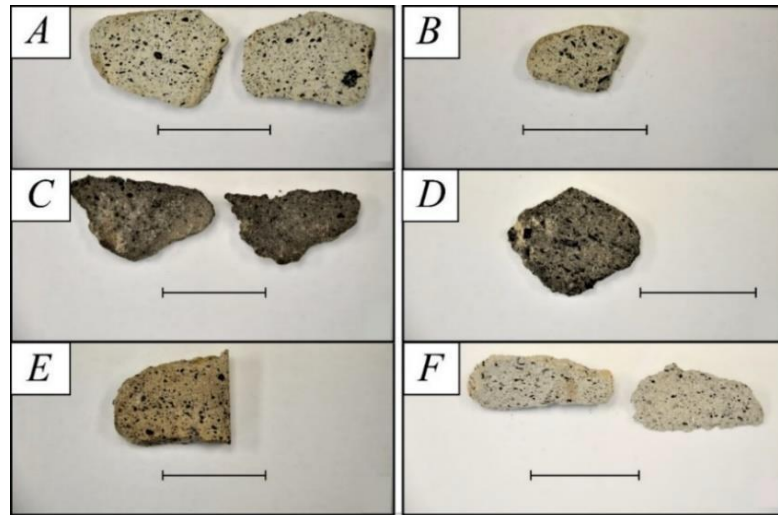


Fig. 3.2 Selected vesicular pyroclasts exhibiting the four identified colours. **A:** White **B, F:** Grey **C, D:** Dark grey **E:** Yellow. Black bar for scale: 5 cm.

3.3.3 Petrography

General petrographic analyses were carried out in order to describe the main rock textures and mineral phases using a polarising microscope (Nikon Eclipse) with integrated digital camera at Massey University, Palmerston North (**Fig. 3.3**). Mineral assemblages and matrix characteristics were investigated and grouped. Proportions of minerals to groundmass were calculated using ImageJ software for phase discrimination. Microlites were classified as groundmass.

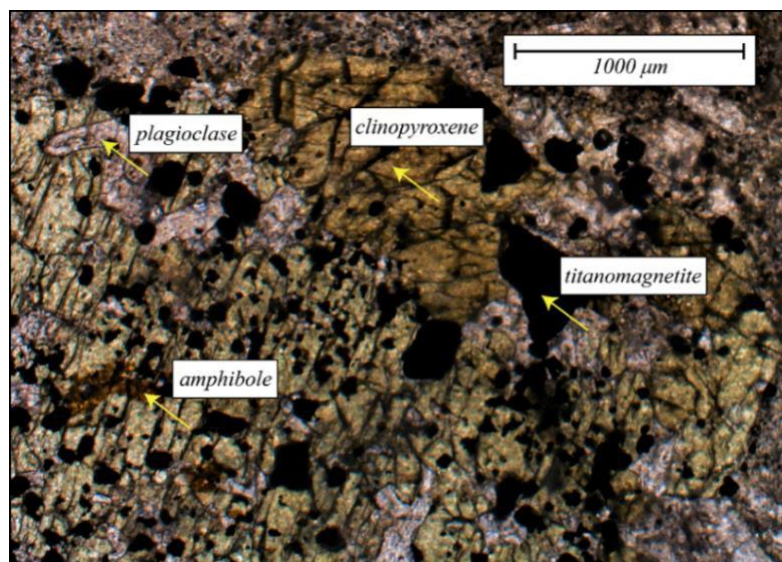


Fig. 3.3 Representative binocular microscopic image of a glomerocryst within a pumiceous volcanic rock sampled from GP2 (sample: *LBLHFE-5*).

3.4 Laboratory Work II – Geochemical approach

Please note, that detailed descriptions of the geochemical methodologies that were used can be found in Chapter 5 and 6, under the Methodology and Analytical methods sub-chapters, respectively.

3.4.1 Crystal Pattern Classification - CPC

The CPC tool was developed after the acquisition of complex plagioclase and clinopyroxene crystal maps. The aim of this classification system was to combine the nomenclature and application of crystal regions and the textural and chemical zonation profiles to enable better and more consistent interpretation of the produced datasets. The classification system characterises the observed textural and chemical patterns of different areas of a crystal to assess the processes affecting the explored mineral. The advantage of such a framework is that it efficiently exposes multiple elemental distribution patterns within a complex single crystal, which contributes to a better understanding of diverse magmatic processes. Based on the findings of this study, the CPC is highly recommended as a tool for future research that involves multiple elemental chemical zonation and distribution investigations on Taranaki phenocrysts or at other volcanoes globally. For further description see **Chapter 6**.

3.5 Data Processing – Calculation Approach

3.5.1 Modal phase proportions

Mineral phase, void/bubble and groundmass proportions of the investigated clasts from three GP units have been calculated using ImageJ software on thin section photographs (**Appendix B1**). Using these estimated ratios and whole-rock compositions, the melt (“starting/parental”) and mineral (“assimilant”) compositions were re-calculated for representative clasts of the individual GPs. The calculated melt compositions provided better approximations than the EMPA spot analyses carried out on the microcrystalline groundmass.

3.5.2 FC-AFC-FCA and Mixing Modeler

Whole-rock compositions have been reproduced using the modeller by Ersoy and Helvacı (2010), which incorporates fractional crystallisation (FC), assimilation fractional crystallisation (AFC), fractional crystallisation and assimilation (decoupled; FCA) and mixing processes. A relevant equation adapted from Powell (1984) is used for the mixing modeller, which is expressed as

$$C_m = X(C_a - C_b) + C_b$$

where C_a , C_b and C_m are the concentration of an element in magma a, in magma b, and in a mixed magma that is a product of magmas a and b (Ersoy and Helvacı, 2010), while X is the degree of mixing.

Two modelling strategies were applied (see details in **Appendix B1; Chapter 5**): (1) Assimilant composition (average chemical composition of the Median Batholith) has been added to the modelling of Price et al. (2016) along with selected “parental basaltic” compositions of three clasts from each sampled growth phase. (2) Modal phase proportion calculations provided melt and mush composition estimations for each individual growth phase. Therefore, calculated melt contents were used as “starting” and mush contents as “assimilant” compositions in the modeler.

3.5.3 Thermobarometry, Hygrometry and Oxygen fugacity modeling

EMP spot analyses of plagioclase, clinopyroxene and amphibole phenocrysts of the individual GPs have been used to estimate possible crystallisation conditions and ascending melt characteristics of the Taranaki plumbing system over the investigated time

period. For this purpose, several models were applied (additional properties can be found in **Table 3.1**; along with detailed descriptions and modelling procedures in **Chapter 6**):

- (1) The amphibole geobarometer developed by Ridolfi et al. (2010; Eq. 4) offers an equation to predict pressures and builds on the Al index provided for the H₂O_{melt} estimation:

$$P = 19.209e^{(1.438Al_T)}$$

- (2) The amphibole geobarometer by Putirka (2016) is an advanced, recalibrated version of the Putirka (2008) geobarometer. In this study, the preferred Eq. 7a is used, which is more precise at higher temperatures:

$$P \text{ (kbar)} = -30.93 - 42.74[\ln(D_{Al}) - 42.16[\ln(X_{Al_2O_3}^{liq})] + 633[X_{P_2O_5}^{liq}] + 12.64[X_{H_2O}^{liq}]] + 24.57[Al^{amp}] + 18.6[K^{amp}] + 4.0[\ln(D_{Na})]$$

where Al^{Amp} and K^{Amp} are the numbers of the cations in amphibole (calculated on the basis of 23 O atoms). All liquid composition terms are hydrous mole fractions of the indicated oxides, and the partition coefficient terms (i.e. D_{Al} or D_{Na}) use respective hydrous mole fractions for the liquid.

- (3) The amphibole geothermometer defined by Ridolfi et al. (2010; Eq. 1) adds a silicon index (Si*) to the formula, which is expressed as

$$T = - 151.487Si^* + 2.041$$

where $Si^* = Si + \frac{[4]Al}{1.5} - 2[4]Ti - \frac{[6]Al}{2} - \frac{[6]Ti}{1.8} + \frac{Fe^{3+}}{9} + \frac{Fe^{2+}}{3.3} + \frac{Mg}{26} + \frac{B\ Ca}{5} + \frac{B\ Na}{1.3} - \frac{A\ Na}{15} + \frac{A\ []}{2.3}$

- (4) The clinopyroxene geothermometer that is applied in this study uses Eq. 33. from Putirka (2008), as it is still the most accurate clinopyroxene-liquid thermometer established, based on the Jd-DiHd (Jadeite - Diopside + Hedenbergite) exchange of 1174 hydrous and anhydrous experimental data:

$$\frac{10^4}{T(K)} = 7.53 - 0.14 \ln \left[\frac{X_{Jd}^{cpx} X_{CaO}^{liq} X_{Fm}^{liq}}{X_{DiHd}^{cpx} X_{Na}^{liq} X_{Al}^{liq}} \right] + 0.07 \ln (H_2O^{liq}) - 14.9 (X_{CaO}^{liq} X_{SiO_{1.5}}^{liq}) -$$

$$0.08 \ln (X_{TiO_2}^{liq}) - 3.62 (X_{NaO_{0.5}}^{liq} + X_{KO_{1.5}}^{liq}) - 1.1 (Mg\#^{liq}) - 0.18 \ln (X_{EnFs}^{cpx}) -$$

$$0.027 P(kbar)$$

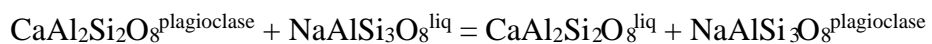
where *DiHd* and *EnFs* are the clinopyroxene components, namely diopside + hedenbergite and enstatite + ferrosilite. These clinopyroxene components are calculated using the strategy of Putirka et al. (2003).

- (5) The clinopyroxene geobarometer developed by Putirka (2003, 2008) was refined and reformulated by Neave and Putirka (2017). The model is defined by Eq. 1, which is a more reliable Jd-in-clinopyroxene barometer to predict pressure estimates, based on 113 hydrous and anhydrous experiments:

$$P(kbar) = -26.27 + 39.16 \frac{T(K)}{10^4} \ln \left[\frac{X_{Jd}^{cpx}}{X_{NaO_{1.5}}^{liq} X_{AlO_{1.5}}^{liq} X_{SiO_2}^{liq}} \right] - 4.22 \ln (X_{DiHd}^{cpx})$$

$$+ 78.43 X_{AlO_{1.5}}^{liq} + 393.81 (X_{NaO_{0.5}}^{liq} X_{KO_{0.5}}^{liq})$$

- (6) The clinopyroxene geothermobarometers mentioned above are dependent on H₂O, thus they require the H₂O_{melt} content, which can be obtained by using the thermobarometers in combination with the hygrometer of Waters and Lange (2015). This hygrometer is a recalibrated, advanced version of the model of Lange et al. (2009), based on 107 hydrous and anhydrous phase-equilibration experiments. It provides more constraint standard error estimates on the equilibrium exchange reaction of the anorthite (CaAl₂Si₂O₈) and albite (NaAlSi₃O₈; **Table 3.1**) components between crystalline plagioclase and magmatic liquid:



Hygrometry models for melt water-content estimations were carried out by two approaches: (i) Ridolfi et al. (2010) model using Al content in amphiboles as it is mainly

sensitive to the water content of the melt; (ii) Putirka (2008; 2016) and Neave and Putirka (2017) pyroxene-liquid thermobarometers (using clinopyroxene rim compositions) coupled iteratively with the plagioclase-liquid hygrometer by Waters and Lange (2015; using An compositions of the plagioclase rims).

(7) The amphibole hygrometer defined by Ridolfi et al., (2010; Eq. 3) is based on the development of an octahedral Al index that relates to the Al sensitivity in amphibole to the melt water-content. It is expressed as:

$$H_2O_{melt} = 5.215^{[6]}Al^* + 12.28$$

$$\text{where } [6]Al^* = [6]Al + \frac{[4]Al}{13.9} - \frac{Si+[6]Ti}{5} - \frac{C Fe^{2+}}{3} - \frac{Mg}{1.7} + \frac{B Ca+A []}{1.2} + \frac{ANa}{2.7} - 1.56K - \frac{Fe\#}{1.6}$$

(8) Oxygen fugacity approximation by Ridolfi et al. (2010; Eq. 2) is used for the calculation of a magnesium index improving the NNO-equation in the model. It is expressed as

$$\Delta NNO = 1.644Mg^* - 4.01$$

$$\text{where } Mg^* = Mg + \frac{Si}{47} - \frac{[6]Al}{9} - 1.3[6]Ti + \frac{Fe^{3+}}{3.7} + \frac{Fe^{2+}}{5.2} - \frac{B Ca}{20} - \frac{A Na}{2.8} + \frac{A []}{9.5}$$

MODEL	MINERAL PHASE (and additional region)	COUPLED WITH	COMBINED WITH OTHER MODEL	EQUATION	ERROR (1SE)
Ridolfi et al. (2010)	amphibole			Eq. 1 (T), 2 (NNO), 3(H ₂ O), 4(P) (Ridolfi et al. 2010)	±22 °C (T) + ±0.61 kbar (P) + ±0.7 (H ₂ O wt%)
Putirka (2016)	amphibole	groundmass/melt	Waters and Lange (2015)	Eq. 5 (T) + Eq. 7a (P) (Putirka, 2016)	±30 °C (T) + 2 kbar (P)
Putirka (2008)	clinopyroxene rim	groundmass/melt	Waters and Lange (2015)	Eq. 30 (P) + Eq. 33 (T) (Putirka, 2008)	±42 °C (T) + 1.6 kbar (P)
Neave and Putirka (2017)	clinopyroxene rim	groundmass/melt	Waters and Lange (2015)	Eq. 1 (P); Neave and Putirka, 2017) + Eq. 33 (T; Putirka, 2008)	±42 °C (T) + 0.96 kbar (P)
Waters and Lange (2015)	plagioclase rim	clinopyroxene P-T groundmass/melt	Holland and Powell (1992)	Eq. 14 (Waters and Lange, 2015)	0.35 wt% H ₂ O

Table 3.1 Details of the used models for the thermobarometry and hygrometry calculations.

CHAPTER 4

ELUCIDATING STRATOVOLCANO CONSTRUCTION FROM VOLCANICLASTIC MASS-FLOW DEPOSITS: THE MEDIAL RING PLAIN OF TARANAKI VOLCANO, NEW ZEALAND

This chapter has been published as:

Aliz Zemeny, Jonathan Procter, Károly Németh, Georg F. Zellmer, Anke V. Zernack and Shane J. Cronin (2021) Elucidating Stratovolcano Construction from Volcaniclastic Mass-Flow Deposits: The Medial Ring Plain of Taranaki Volcano, New Zealand – *Sedimentology*, DOI: 10.1111/sed.12857

Supplementary Data for this Chapter can be found in **Appendix A**.

Chapter Contributions:

- ◆ **Aliz Zemeny:** Conceptualization, Formal analysis, Investigation, Methodology, Resources, Supervision, Visualization, Writing (original draft), Writing (review & editing)
- ◆ **Jonathan Procter:** Conceptualization, Funding acquisition, Project administration, Resources, Supervision, Writing (review & editing)
- ◆ **Károly Németh** Writing (review & editing)
- ◆ **Anke V. Zernack:** Writing (review & editing)
- ◆ **Georg F. Zellmer** Writing (proofreading)
- ◆ **Shane J. Cronin:** Discussion on conceptualization, Supervision

Abstract

Long-lived stratovolcanoes display a thick volcanic apron surrounding the edifice. This sedimentary succession incorporates the majority of the deposits from both growth and destruction phases of a volcanic massif. The ring plain of Taranaki Volcano (>200 ka) is composed of volcanoclastic mass-flow deposits that are exceptionally well-exposed along its coastal-cliff shoreline, at 20-30 km distance from the edifice. Overall, the volcanoclastic deposits in the southern and south-western sector record three growth phases (65-34 ka) which can be investigated due to access and stratigraphic control of ring-plain section. Each cyclic growth phase is represented by a sequence of mass-flow deposits. Lithostratigraphic units or repeated packages with similar properties were identified in order to understand the depositional sequences. The mass-flow units within these growth phases can be described by three criteria subdivided into 9 distinct sedimentological textural types (e.g. massive, graded, etc.), 5 different lithological types (e.g. lithic-dominated, poly lithologic, etc.) and 3 main physiographic facies types (sheet, overbank, channel). The mass-flow deposits can then be further categorized through a classification scheme by assigning these three criteria. Widely distributed lithic-dominated hyperconcentrated-flow deposits were recognized, which are thought to be directly or indirectly associated with eruption-fed events (remobilised from block-and-ash flows) providing evidence for eruptive activity occurring on a 4 – 10 kyr cycle. Therefore, we propose classification criteria for mass-flow deposits in volcanic ring plains using a developed three-part coding system. The study also aims to clarify the order of sedimentary and volcanic events by establishing a stratigraphic model for the investigated time-period offering a better understanding for future research.

Keywords: Taranaki Volcano/Egmont, volcanoclastic deposit, mass-flow, ring plain, edifice growth, classification

4.1 Introduction

Andesitic stratovolcanoes exhibit a tendency for periodic edifice growth (construction phases) interspersed by sector or flank collapses (destruction phases) that are evidenced by the deposition of debris-avalanche deposits (DAD; Voight et al., 1981; Crandell et al., 1984; Siebert, 1984; Ui et al., 1986b; Vallance et al., 1995; Glicken, 1996; Van Wyk de Vries and Francis, 1997; Capra et al., 2002; Waythomas and Wallace, 2002; Concha-Dimas et al., 2005; Shea et al., 2008; Zernack et al., 2009; Gaylord and Neall, 2012; Zernack and Procter, 2021). Thus, debris-avalanche deposits as edifice failure indicators terminate and separate individual growth cycles of long-lived stratovolcanoes. Eruptive periods are characterised by the regrowth of the volcanic edifice through effusive and explosive volcanic activity. Volcanic activity during edifice rebuilding is not constant and the depositional processes affect different sectors of a volcanic apron (ring plain) surrounding a volcanic edifice at different times, while others record simultaneous periods of quiescent. As an outcome of this naturally occurring cyclic behaviour mass-flow deposits, reseedimented pyroclastic deposits and occasionally fluvial and aeolian deposits build up the landscape-forming regions of the volcanoclastic apron throughout edifice regrowth, involving timescales of 0.1 to 10 kyr (Scott et al., 1995; Belousov et al., 1999; Tibaldi, 2001; Zernack et al., 2011; Zernack and Procter, 2021). Ring-plain successions are progressively constructed through the deposition of syn- and post-eruptive volcanoclastics, minor eruption-related or so-called primary deposits and secondary materials (Palmer and Neall, 1991; Smith, 1991; Cronin et al., 1996; Davidson and De Silva, 2000; Donoghue and Neall, 2001; Borgia and van Wyk de Vries, 2003; Zernack, 2021). These deposits provide a complete and detailed lithostratigraphic and chronostratigraphic long-term record of eruptive activity and sedimentary events (Palmer and Neall, 1991; Smith, 1986, 1991; Cronin et al., 1996; Cronin and Neall, 1997; Davidson and De Silva, 2000; Donoghue and Neall, 2001; Németh and Martin, 2007; Zernack et al., 2011; Zernack, 2021) and are important for calculating and mitigating the impacts of volcanic hazards (Pierson et al., 2014).

Landscape-forming events (i.e. fluvial reseedimentation, soil accumulation) have occurred over the lifespan (c. 200 kyr; Zernack et al., 2011) of this stratovolcano, leading to the accumulation of a thick volcanoclastic apron around the present-day massif (Palmer and Neall, 1991). Collapses of Taranaki Volcano occurred in different directions, resulting in different-age segments within the ring-plain (Grant-Taylor, 1964b; Neall,

1979; Palmer and Neall, 1991; Zernack et al., 2011). Earlier studies focused on both the younger eruptives and older deposits: depositional sequences of the modern edifice (<14 ka; Neall, 1979; Platz et al., 2007a, 2012; Turner et al., 2011) and younger deposits exposed in the ring plain have been investigated to understand the last c. 30 kyr of volcanic activity (Neall, 1979; Neall et al., 1986; Alloway et al. 1995, 2005; Procter et al., 2009; Damaschke et al., 2017a, b; Lerner et al., 2019). Prior this time period, older units (>30 ka) have been studied in coastal cliff exposures in south-west and south Taranaki Volcano due to coastal erosion and uplift of the Taranaki Peninsula (Pillans, 1983). Previous investigations have included a regional mapping project and sedimentological (Neall et al., 1986; Palmer and Neall, 1991; Zernack et al., 2009) and stratigraphy-based work (Zernack et al., 2011), correlating the exposed debris-avalanche deposits and reconstructing the older volcanic history. Earlier studies also provided a lithofacies classification (Palmer and Neall, 1991) and categorized these lithofacies by clast features, textures, thicknesses, and geometries of the deposits.

This study presents a comprehensive sedimentological and lithological framework and sedimentary facies classification of the medial (20-30 km from source) volcanoclastic deposits within the ring plain of Taranaki Volcano. The stratigraphic model further aims to clarify sedimentological and volcanic processes throughout the studied growth phases, establishing the order of events within the volcanoclastic apron. The facies analysis takes into account lithologies associated with each deposit and also connects facies to each sedimentological texture. Therefore, linkage of lithological classification to source areas is improved by pointing out unique lithological identifiers within the deposits. This classification also attempts to provide information on the possible trigger mechanisms of the volcanoclastic mass flows. Overall, the developed framework assists in clarifying transport, depositional processes and possible origin of mass flows providing a well-defined model for rapidly changing environments in a ring-plain system.

4.2 Taranaki Volcano

Taranaki Volcano is located on the Taranaki Peninsula in the North Island, New Zealand (**Fig. 4.1 A**). Volcanic activity started more than 130 kyr ago (Alloway et al., 2005). However, based on an old debris-avalanche deposit (Mangati Fm.), an earlier onset of c. 200 ka was suggested by Zernack et al. (2011). The almost perfectly shaped cone (~15 km³; Procter et al., 2009) is composed of lava and pyroclastic deposits that are

younger than 14 kyr (Neall, 1979; Turner et al., 2011). The volcanic edifice is surrounded by an almost circular, volumetrically larger ring plain containing >150 km³ of volcanoclastic material, characterised by debris-avalanche, mass-flow (hyperconcentrated-flow, debris-flow) and fluvial deposits (Fig. 4.1 B; Neall et al., 1986; Procter et al., 2009; Zernack et al., 2009). The south-western ring plain provides sedimentary records extending back at least 100 kyrs (Neall, 1979; Palmer and Neall, 1991). At least 14 large collapse events occurred within the lifespan of Taranaki Volcano, represented by debris-avalanche deposits within the ring-plain record suggesting one major sector collapse or slope failure in every 10-14 ka (Zernack et al., 2011). Construction phases in between these collapse events are represented by mass-flow deposits interbedded with fluvial, paleosol or peat-dominated sequences, dune sands and occasional tephra layers (Palmer and Neall, 1991; Zernack et al., 2009).

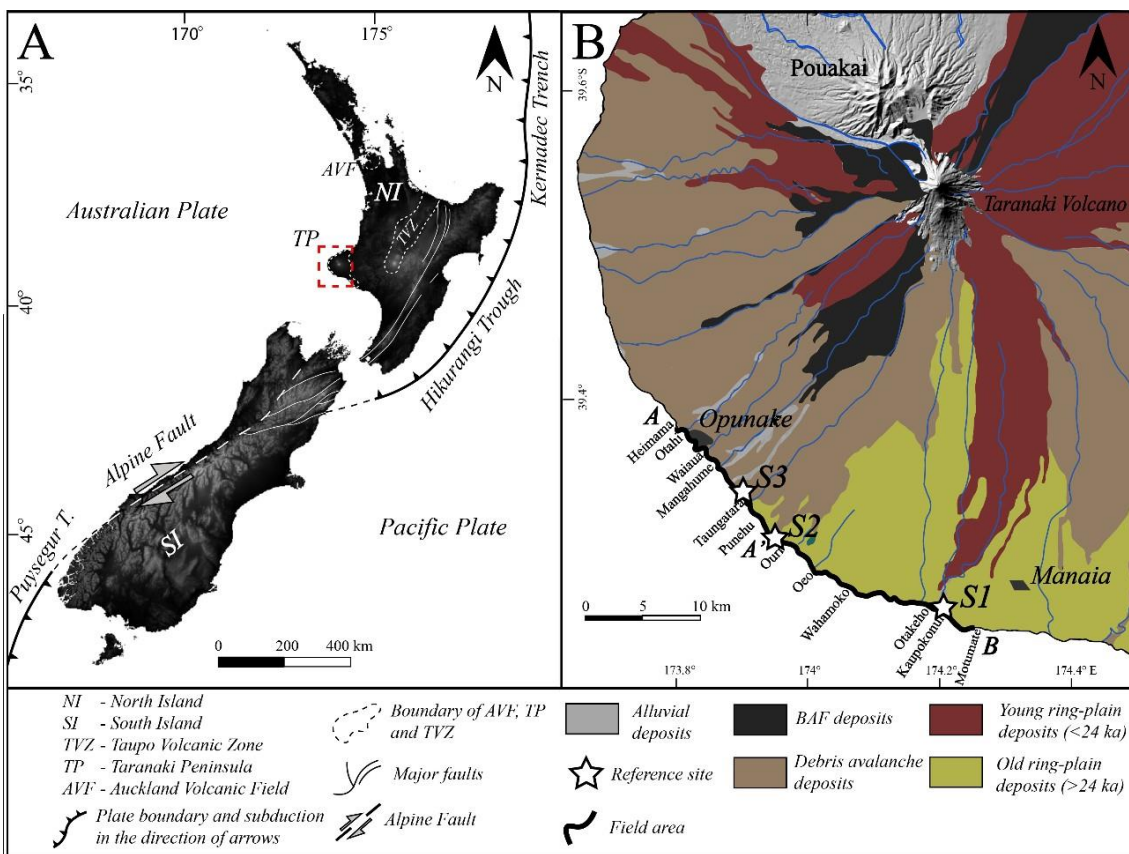


Fig. 4.1 A: Location map and main tectonical settings of New Zealand outlining the Taranaki Peninsula (red dashed rectangle: TP; NASA Earth Observatory). **B:** Quaternary Geological Map of the south, south-western part of the ring-plain of Taranaki Volcano on the TP showing the distribution of volcanic and volcanoclastic deposits (LINZ elevation map; modified after Neall, 1979; Neall and Alloway, 2004; Alloway et al., 2005) and the coastal region (black bold line) that was examined during this study along with the chosen reference sites (stars; S1, S2, S3; find coordinates in **Appendix A1**). BAF: Block-and-ash flow deposits.

4.2.1 Time period 65-34 ka

The stratigraphy of Taranaki Volcano can be divided into two main categories, the modern edifice successions and the older ring-plain deposits (**Table 4.1**; Neall, 1979; Neall et al., 1986; Alloway et al., 1995, 2005; Zernack et al., 2009, 2011; Zernack, 2021). Studies by Neall (1979), Neall et al. (1986), Gaylord et al. (1993), Neall and Alloway (2004) and Procter et al. (2009) provide geological mapping and stratigraphy of mass-flow deposits in the ring plain. Recent studies included the identification of 14 large debris-avalanche deposits (Zernack et al., 2009), their ages, with associated redefinition of their distribution (Zernack et al., 2011).

<i>Debris avalanche deposit</i>	<i>Debris flow deposit</i>	<i>Other marker</i>	^{14}C yrs BP	<i>Age (ka)</i>
<i>Opua</i>			$6,570 \pm 110^c$	7.5^c
		<i>Oakura Tephra</i>		<i>c. 7.8^c</i>
<i>Motumate</i>				14^{ac}
		<i>Katikara Sands</i>		<i>c. 27.3-15.1^c</i>
		<i>Okato Tephra</i>		<i>c. 19.2^c</i>
<i>Pungarehu</i>			$20,776 \pm 170^a$	24.8^a
		<i>Kawakawa Tephra</i>		25.4^d
<i>Ngaere</i>			$23,400 \pm 400^e$	27.3
<i>Te Namu</i>			$29,074 \pm 399^a$	34^d
		<i>Hihiwera Peat</i>		$36.9-34.4^a$
	<i>Ihaia</i>		$31,522 \pm 381^a$	36.9^a
<i>Rama</i>			$<44,330 \pm 1,757^b$	<i>c. 45-40^a</i>
		<i>Rotoehu Tephra</i>		45.1^f
	<i>Young Kaupokonui</i>			<i>c. 50-45^a</i>
<i>Otakeho</i>			$>44,330 \pm 1,757^b$	<i>c. 55-50^a</i>
	<i>Punehu</i>			$60-55^a$
	<i>Old-Kaupokonui</i>			$60-55^a$
<i>Tokaora</i>				<i>c. 60^a</i>
		<i>Punehu Sands</i>		<i>c. 80-60^a</i>
<i>Waihi</i>				<i>c. 70^a</i>
<i>Waingongoro</i>				<i>c. 75^a</i>
		<i>Puketapu buried forest</i>		<i>c. 80^a</i>
		<i>Manaia Lignite</i>		<i>c. 80^g</i>
<i>Oeo</i>				<i>c. 90-85^a</i>
		<i>Inaha Marine Bench</i>		100^h
<i>Okawa</i>				<i>c. 105ⁱ</i>
		<i>Rapanui Marine Bench</i>		127^h
<i>Motunui</i>				$>130^i$
<i>Mangati</i>				<i>c. 200ⁱ</i>
		<i>Ngarino Marine Bench</i>		210^h

^a Zernack et al. (2011), ^b Tinkler (2013), ^c Neall (1979), ^d Vandergoes et al. (2013), ^e Alloway et al. (1995), ^f Danišik et al. (2012), ^g McGlone et al. (1984), ^h Pillans (1983), ⁱ Alloway et al. (2005)

Table 4.1 Stratigraphic overview of the Taranaki ring-plain succession defined by debris avalanche, debris flow deposits and other markers (adapted from Zernack, 2021). ^{14}C yrs BP presents radiocarbon years before AD1980. Ages (ka) refer to 10^3 years before present including calibrated radiocarbon dates BP and chronostratigraphic estimates. Bars indicate the chronostratigraphic boundaries of deposited Kaitakara and Punehu Sands as observed in the ring-plain succession. Dashed lines highlight the stratigraphic position of the deposits of this study.

Initial “ring-plain” mapping of Taranaki Volcano by Hay (1967) identified the “Stratford and Opunake lahars”, followed by studies based on distinguishing their differences (Grant-Taylor and Kear, 1970). These composite units make up the coastal regions of the south and south-western part of the ring plain comprising laharic, debris-avalanche and alluvial deposits that accumulated c. 80 – 50 ka and 38 – 30 ka (Grant-Taylor and Kear, 1970; Neall, 1979). Subsequent studies described three debris-avalanche deposits within the Stratford Formation and one within the Opunake Formation (Palmer and Neall, 1991). They were redefined by Neall and Alloway (2004), clarifying their distribution in the southern sector and showing that the main dispersal of the Stratford Formation is to the east of Manaia, whereas the Opunake Formation is situated between Opunake and Manaia (**Fig. 4.1 B**). Therefore, the medial volcanoclastic succession in south-west Taranaki comprises at least three major collapse events between 65-34 ka: (i) the collapse event that produced the Otakeho debris-avalanche deposit c. 55; (ii) the Rama debris-avalanche c. 40 ka; and (iii) the Te Namu debris-avalanche deposit c. 34 ka. Two important markers of the studied time period were also recognized in the strata: (1) Radiocarbon dates of Hihiwera Peat from various locations provide converted calendar ages of $34,227 \pm 0,283$ ka (Zernack et al., 2011), $38,679 \pm 1,097$ ka (McGlone et al., 1984) and $39,735 \pm 1,443$ ka (Grant-Taylor and Rafter, 1963); (2) Wood samples from the Ihaia debris-flow deposit (DFD) were dated at $36,896 \pm 0,417$ ka (calibrated age; **Table 1**; Zernack et al., 2011).

4.3 Terminology

Volcaniclastics are formed and produced by volcanic and sedimentary processes, and consist of diverse particles that underwent various fragmentation, transport and depositional procedures (Fisher and Schmincke, 1984; Cas and Wright, 1987; McPhie et al., 1993; White and Houghton, 2006; Manville et al., 2009). Primary volcanoclastic deposits are defined by their process of emplacement (Cas and Wright, 1987; McPhie et al., 1993; White and Houghton, 2006) or by the mode of fragmentation of the particles (Fisher, 1961, 1966; Schmid, 1981). Volcaniclastics created through volcanic processes that underwent “reworking” by typical sedimentary mechanisms can be termed secondary deposits, or, as in this study they have been further described through their emplacement modes, e.g. fluvial. Sohn and Sohn (2019) suggested using the term “reprocessed” for describing a category of syn-eruptive volcanoclastic deposits. In general, reprocessed

volcaniclastic deposits were originated directly from a volcanic eruption and were deposited by non-volcanic means. The term “reworked” encompasses a broader range of sedimentological processes (e.g. Sohn and Sohn, 2019), thus being irrespective of the exact reworking modes.

Lahars or volcanic mass flows are discrete, rapid, gravity-driven flows of saturated, high-concentration mixtures containing water and solid particles of rock, wood or ice and other debris that originate from volcanoes (Vallance 2000; Vallance and Iverson, 2015). Primary mass flows are triggered during eruptions by various eruption-related mechanisms, whereas secondary mass flows are most commonly triggered by post-eruptive processes such as erosion or gravity. However, syn-eruptive rainfall might also initiate mass-flow events. Debris avalanches are rapid, dry or wet, gravity-driven granular mass flows generated by sector collapses or large-volume landslides producing horseshoe-shaped collapse scar (Ui et al., 1983, 1986a, b; Pierson and Costa, 1987) within the edifice. Debris-avalanche deposits may contain both debris derived from the source and debris eroded and incorporated during flow (Crandell et al., 1984; Palmer and Neall, 1989; Palmer and Walton, 1990; Glicken, 1991; Palmer and Neall, 1991; Zernack, 2021) commonly display a non-graded and very poorly sorted texture and contain angular to sub-angular clasts ranging in grain size from a few centimetres to several tens of metres or larger (Ui, 1983; Siebert and Glicken, 1987; McPhie et al., 1993). Volcaniclastic debris flows are defined as rapidly flowing, non-Newtonian fluids with high yield-strength produced by sediment-concentrations around 60-80 wt% (Costa, 1984; Pierson and Costa, 1987; Smith and Lowe, 1991; Iverson, 1997; Cronin et al., 2000; Major et al., 2005; Pierson, 2005) from a volcano. The resulting deposits are poorly sorted and composed of particles ranging from clay to large boulder size. Clast-supported matrix is characteristic, although matrix-supported framework may occur rarely (Smith, 1986). They are commonly non-graded, with sharp or rarely erosive contacts (Fisher, 1961; McPhie et al., 1993). Hyperconcentrated flows contain sediment concentrations intermediate between debris flow and stream flow (20-60 wt% of solid fraction; Beverage and Culberston, 1964; Smith, 1986; Pierson and Costa, 1987). Their deposits typically display normal grading with clast-supported texture and are often poorly-to-moderately sorted.

The ring-plain system, hosting the above-detailed volcaniclastic mass-flow deposits, corresponds to a geometrically well-defined volcaniclastic apron that surrounds a volcanic edifice (Cronin and Neall, 1997; Davidson and de Silva, 2000). Hence, the

rounded shape only occurs if there is no other volcano or mountain present as a natural barrier, which can influence the distribution of the deposits (Smith, 1991).

4.4 Methods

Sedimentological descriptions of mass-flow deposits were conducted examining the continuous lateral sequences of coastal cross-sections in the southern and south-western sectors of the medial ring-plain (**Fig. 4.1 B**). Previous mapping of peats, debris-flow and debris-avalanche deposits (**Table 4.2**; Zernack et al., 2011) and their estimated ages provided chronostratigraphic control of the studied mass-flow deposits and allowed for the identification of unconformities in the coastal cliffs. Field campaigns were also carried out in valleys inland, which provided outcrops parallel to the transportational and depositional directions. Reference sites were chosen in order to best describe the lateral distributions of hyperconcentrated-flow deposits from each growth-phase, namely succession 1 (S1), succession 2 (S2) and succession 3 (S3; see locations in **Fig. 4.1 B**; coordinates in **Appendix A1**). Point counting based on image analysis was used for grain size and componentry examination (**Appendix A1**; 2 photographs / layer; photograph dimensions minimum 50 x 50 cm, maximum 1 x 1 m) on specific clast populations of hyperconcentrated-flow deposits and the results are expressed in surface % (i.e. surf. %; for analysed clast numbers and components see **Fig. 4.5**). Grain-size determination and componentry calculation was obtained using a mm grid on the images. Grain sizes of the investigated volcanoclastic clasts were defined using the classification after Wentworth (1922). Extrapolated volume measurements were based on the mapped horizontal extension of the debris-flow deposits, the average thicknesses and the estimated distance from source. The calculated volumes are approximate estimations.

Debris avalanche deposit	Debris flow deposit	Other marker	¹⁴ C yrs BP	Age (ka)	Direction of collapse	Calculated / estimated volume (km ³)	Runout distance (km)
Te Namu			29,074 ± 399 ^a	34 ^a	SW	1.5 - 2	26+
		Hihiwera Peat		36.9-34.4 ^a			
	Ihaia		31,522 ± 381 ^a	36.9 ^a	SW	0.1 - 0.2	25+
Rama			<44,330 ± 1,757 ^b	c. 45-40 ^a	S	4.5 - 5	34+
	Young Kaupokonui			c. 50-45 ^a	S	0.1 - 0.2	30+
Otakeho			>44,330 ± 1,757 ^b	c. 55-50 ^a	S	2 - 2.5	32+

^a Zernack et al. (2011), ^b Tinkler (2013)

Table 4.2 Key markers of the studied time period representing calculated ages from earlier studies (after Zernack et al., 2011 and Tinkler, 2013) along with the direction of collapse, calculated volume and runout distance.

4.5 Volcanoclastic lithofacies

The exposed successions represent a wide range of textural, sedimentological and lithological features with variable geomorphologies and geometries reflecting various sediment-water ratios of the volcanic mass-flows, unsteady environmental factors and different physiographical conditions. The sedimentary texture characteristics, their distinction criteria and the connected depositional processes compose observed the lithofacies associations. They are summarized and interpreted in **Table 4.3**.

Graded hyperconcentrated-flow deposits (**Fig. 4.2 A**; GHF / iGHF) often show normal or reverse-to-normal grading. The thickness of layers can vary between 20 cm and 2 m. The units often have fine graded base with an upper division consisting of medium sand to coarse-sand sized and rarely very fine-pebble sized clasts. The coarse main central body comprises very fine to medium, angular or sub-angular, rarely rounded pebble sized clasts with non-graded, massive texture. The interclast matrix consists of sand and individual phenocrysts (millimetre sized amphibole and pyroxene crystals). The very top of these layers is overlain by a very-fine to medium-sand sized, thin (c. 1 – 5 cm) layer.

Massive hyperconcentrated-flow deposits (MHF; **Fig. 4.2 A**) are non-graded, tabular and mostly exhibit basal contacts that seem to be non-erosive. Their thickness varies between 20 cm and 2.5 m. They consist of coarse-sand to coarse-pebble sized clasts in a fine-to-coarse sand-sized matrix. The matrix is characterized by a high amount of sand and individually occurring mineral crystals (millimetre-sized amphiboles and pyroxenes). Clasts are mostly angular to sub-angular in shape.

Dilute stream flow (DiSF; **Fig. 4.2 A**) may form through the transition from hyperconcentrated flows that were controlled by topography. However, the resulting deposits are also present as individual beds, enclosed by sheet-like deposits. They often consist of overlapping broad channel structures containing alternating low-angle cross-stratified or cross-bedded lenses of fine-to-coarse sized sands (few cm) and fine-to-medium sized pebbles (up to 5 cm). The beds are typically moderately to well-sorted. Their stratigraphic position indicates that they are likely runout-pulses associated with hyperconcentrated flows as they overlie or grade into underlying hyperconcentrated-flow deposits. Laterally, they texturally transform into more chaotic transitional hyperconcentrated flow deposits (THF).

THF deposits (**Fig. 4.2 B**) are moderately to well sorted, contain fine-to-coarse sand-sized particles and are typically stratified, with low-angle cross bedding or horizontal to wave-bedding. Often, rounded coarse-sand sized and fine-pebble sized pumice clasts and

elongated lenses of sand and or fine-to-coarse pebble sized pumice fragments occur. The matrix is comprised of fine-to-coarse sand. The thickness of the deposit packages varies strongly, depending on the substrate and channels they were deposited in. Their intersectional geometries are lenticular with erosive basal parts, and they can form steep or overlapping channel morphologies.

Non-cohesive debris flow deposits (nCDF; **Fig. 4.2 B**) consist of fine-pebble to boulder-sized, angular or rounded volcanic lithics with a lower amount of fine-to-coarse sand matrix. The bottom portion of the deposit was produced by a faster, sand-size hyperconcentrated-flow pulse due to the sieving of fine particle fraction by water. The top of the deposit can contain finer grained layers of THF textures due to the deposition of the runout parts of the same flow.

Transitional debris-flow deposits (TDF) are different from channelized deposits in that their grain size ranges mostly from coarse-pebble to boulder size (0.5 – 1 meter). The coarse base is not erosional and sometimes the deposits transform continuously into finer grained, moderately to poorly sorted and often bedded hyperconcentrated-flow units. The deposit represents one individual flow event that deposited coarse, angular to rounded pebbles to boulders at the bottom and a very coarse, sand-sized to medium-pebble sized pulse at the top.

Thinly or crudely bedded hyperconcentrated-flow deposits (tBHF/cBHF) typically have variable thickness c. 5 cm – 1 m. They display lenticular spatial geometry with non-graded textures of sub-angular to well-rounded clasts.

Grain size usually varies from very coarse-sand to medium-pebbles within a fine-to-medium sand-sized matrix. The matrix contains high amounts of sand with individually occurring crystals (amphibole, pyroxene). Coarse to very-coarse pebble-sized fragments are characteristic with rare cobbles. Coarser fragments often appear in discontinuous thin beds. Individual beds are intercalated with thin (1-10 cm thick) fine grained sandy beds. The observed lateral extent of packages of this type of deposit might reach hundreds of meters and they are frequently eroded by subsequent debris flows.

Cohesive debris-flow deposits (CDF) differ not just in grain size but also in clay content (> 5%; Vallance and Scott, 1997) from nCDF, channelized debris flow deposits (ChDF) or TDF textures. Their observed lateral extent may reach tens of meters. Thickness of the deposit packages varies from 0.5 to 3 m.

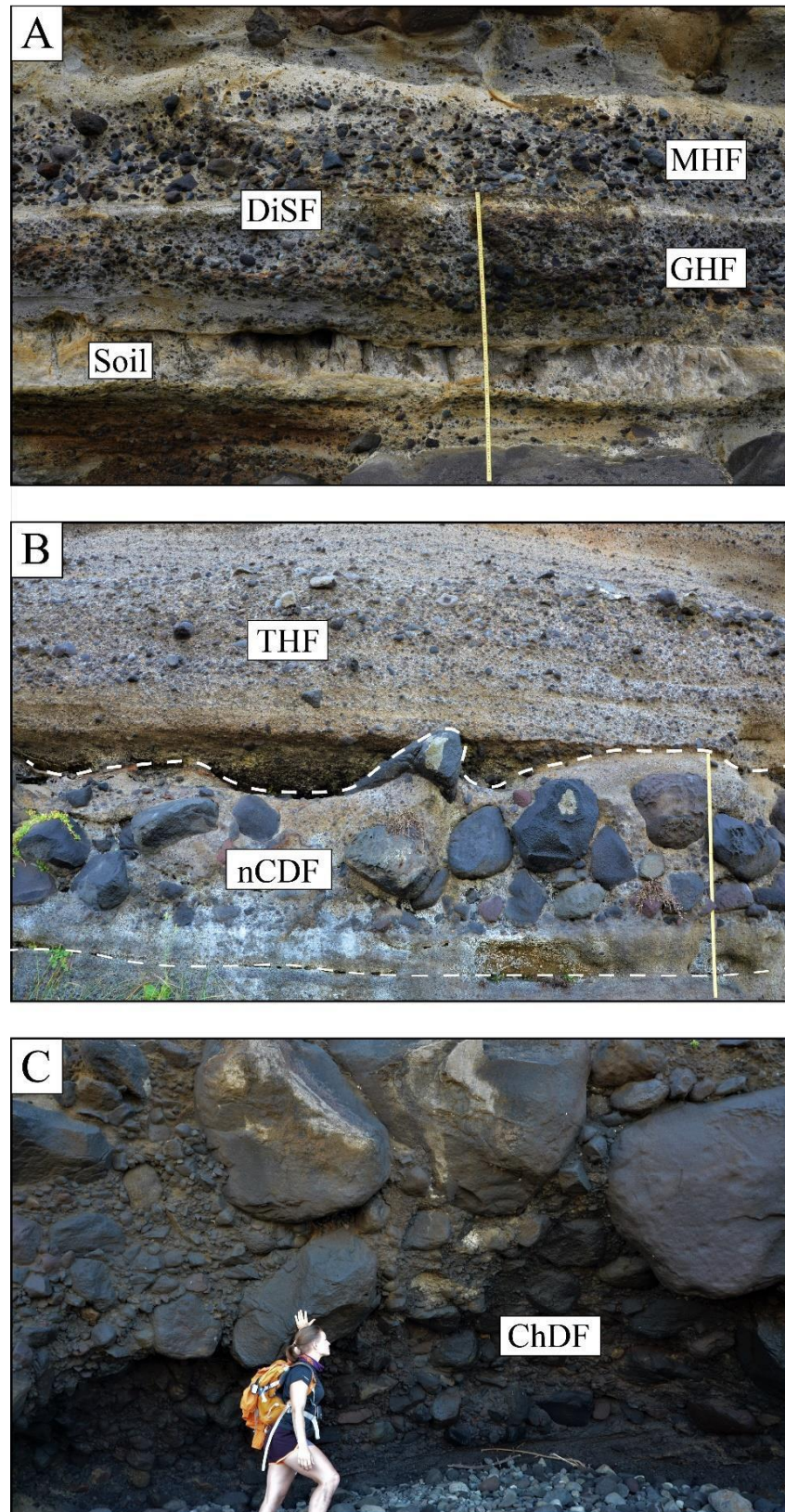


Fig. 4.2 Representative appearance of the observed volcaniclastic mass-flow deposits. **A:** Massive (MHF) and graded (GHF) hyperconcentrated-flow deposits along with a thin dilute stream-flow (DiSF) deposit layer. Ruler for scale: 1 meter. **B:** Transitional hyperconcentrated-flow (THF) and non-cohesive debris-flow (nCDF; white dashed lines) deposit textures. Ruler for scale: 1 meter. **C:** Channelised debris-flow deposit (ChDF) texture. Person for scale: 170 cm. Note that the pictures of deposits were taken in medial (25.5 – 28 km) distance from the vent.

Texturally they consist of fine-pebble to coarse-pebble sized rounded to subrounded clasts in a very fine to fine-sand sized clay-rich matrix.

ChDF (**Fig. 4.2 C**) deposits are non-graded, lack internal stratification and they often have a thin, matrix-supported base (Scott, 1988a; Vallance, 2000; Zernack, 2021). Boulders are rounded to angular and may reach diameters of 1 to 3 m. Rounded boulders may indicate fluvial origin, whereas angular or sub-angular clasts represent either older debris-avalanche material that has been reworked or the deposit can contain ripped-up clasts that consist of hyperconcentrated-flow deposits. The sedimentological textures of ChDF can vary depending mostly on the paleo-topography and transportation direction: (i) Channelized deposits may have a coarse-sand to very fine pebble-sized top division that represents the last portion of the flow. Normal grading also occurs in moderately to poorly sorted hyperconcentrated-flow deposits (see also Cronin et al., 2000). (ii) In cross-sections parallel to the transportation axis, the texture of the debris-flow deposit may be chaotic due to the physical properties of the flow and/or the topography. In this case, the texture may display TDF, THF or NSF characteristics. (iii) They may exhibit erosive, lenticular shapes in two-dimensions. In a flow-transverse cross-sectional cut, they horizontally often grade into thinner, coarse-to-fine-pebble grained deposits that are more wide-spread in overbank dimensions. The deposit gets better sorted and becomes finer grained with increasing distance from the channel.

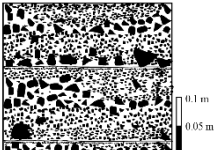
TEXTURE code	KEY CRITERIA		DEPOSITIONAL PROCESS code	Physiographic Facies [code]	Petrofacies code	INTERPRETATION (flow mechanisms and deposition)
	Sedimentary characteristics	Geometry/Boundary/Distribution				
GRADED G/iG	Clast-to-matrix supported coarse main body. Matrix supported finer and or bottom division. Normal graded, inversely-graded, normal-to-inversely graded. Very fine to medium-pebbles, coarse-sand sized matrix. Angular to sub-angular, rarely rounded fragments. Bombs might appear.	Tabular with non-erosive boundaries. From hundreds of meters to kilometers.	Hyperconcentrated flow HF	Sheet [SH]	L	Hyperconcentration is achieved when matrix strength and/or dispersive pressure contribute, to the same extent as fluid turbulence, to the separation of particles. (Beverage and Culberston, 1964; Costa, 1988; Coussot and Meunier, 1996; Benvenuti and Martini, 2002) iGIF lithofacies can be generated when a turbulent fluidal flow expands over a surface resulting in a two-phase flow, where a more concentrated, coarser grained bottom flow-layer moves slower than the upper turbulent division of the flow carrying suspended load. (i.e. gravity transformation; Fisher, 1983) Matrix strength domination during deposition results in massive texture.
	Thickness: 20 cm - 2 m					
MASSIVE M	Clast-to-matrix supported with sandy matrix. Massive, non-graded, poorly to moderately sorted. Coarse-sand to pebble sized clasts in fine-to-coarse sand sized matrix. Angular to sub-angular clasts with sub-rounded or rounded pumice.	Tabular with non-erosive boundaries. From hundreds of meters to kilometers.	Hyperconcentrated flow HF	Sheet [SH]	L polyL	
	Thickness: 20 cm - 2,5 m					
DILUTE Di	Clast-supported. Massive to thinly or crudely bedded, often horizontally laminated, cross or wavy bedded, or low-angle cross-stratified, rarely normal-graded. Poorly to well sorted. Very fine to coarse grained sands with fine to medium-pebble sized pumice clasts that mostly occur in lenses. Rounded sand sized sand and pumice, sub-angular pebble to boulder sized clasts.	Lenticular and/or tabular with often erosive boundaries. From tens of meters to hundreds of meters.	Stream flow SF	Sheet [SH] Overbank [OB] Channel [CH]	S	Low sediment concentration due to the lack of flow strength. Turbulence plays an important role during transport where sediments are transported as suspended load or bed load. DiSF deposits indicate runoff facies of hyperconcentrated flow deposits. They also may represent transitions in distal facies from sheet to overbank and channel topographies. (Pierson and Costa, 1987; Costa, 1988)
	Thickness: 4 cm - 3 m					
TRANSITIONAL T	Clast-to-matrix supported. Non-graded, low-angle cross bedding or stratification, horizontal, cross or wave-bedding. Moderately to well sorted layers or pulses. Alternating layers of fine-to-medium pebble sized lithics with low amount of sandy matrix and fine to coarse-sand sized, massive pulses of sand beds that represent dilute flows. Fine to coarse-sand sized to medium-pebble sized clasts. Rounded or sub-angular clasts.	Lenticular, steep, rarely tabular and usually overlapping with erosive boundaries. From tens of meters to hundred meters.	Hyperconcentrated flow HF	Sheet [SH] Overbank [OB] Channel [CH]	S polyL LP	THF deposits represent transition between hyperconcentrated flows and stream flows during deposition. This modification may occur due to the role of particles in a sediment-water mixture where the sediment concentrations are lower than those of to achieve actual hyperconcentration, i.e. hyperconcentrated flow characteristic. Matrix strength/dispersive pressure < fluid turbulence. (Benvenuti and Martini, 2002 and references therein)
	Thickness: 20 cm - 1 m					

Table 4.3 Categorization of the investigated volcaniclastic mass-flow deposits representing the main sedimentological characteristics, their distinguishing criteria with the representative appearance and their interpretation. Note the connection of textures to certain lithologies and physiographic facies.

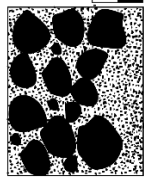
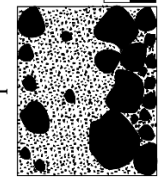
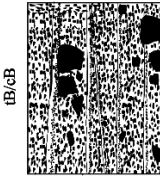
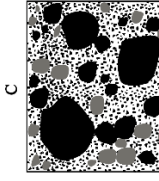
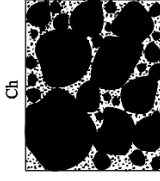
 <p>NON-COHESIVE nC</p>	<p>Clast-to-matrix supported texture with sandy matrix. Massive, non-graded, non-stratified, very poorly to poorly sorted. Often exhibiting a fine-to-coarse grained sandy bottom portion. Medium- to boulder sized clasts with low amount of coarse-sand sized matrix. Angular to rounded pebbles.</p> <p>Thickness: 0.5 m - 3 m</p>	<p>Tabular with rarely erosive boundaries. From tens of meters to a maximum of a hundred meter.</p>	<p>Debris flow DF</p>	<p>Sheet [SH] Overbank [OB] Channel [CH]</p>	<p>polyL</p> <p>nCDF deposits indicate flow mechanisms during deposition where clast interactions are the main influencing factors along with the role of turbulence contributing to the non-graded, massive textural appearance. (Schultz, 1984; Giordano et al., 2002)</p>
 <p>TRANSITIONAL T</p>	<p>Clast-supported bottom and matrix supported upper division. Layers are non-graded and moderately to poorly sorted. Alternating layers of medium-to-coarse pebble sized lithics with low amount of sandy matrix and coarse-pebble to boulder sized layers. Base comprises of coarse-pebble to boulder sized clasts, which is overlapped by coarse-sand sized, non-stratified region. The top of the deposit mostly contains coarse-pebble to boulder sized grey, dark grey and black fragments.</p> <p>Angular to sub-angular fragments, rarely rounded pebbles.</p> <p>Thickness: 0.5 m - 2.5 m</p>	<p>Tabular with non-erosive boundaries. From tens of meters to hundred meter.</p>	<p>Debris flow DF</p>	<p>Sheet [SH] Overbank [OB] Channel [CH]</p>	<p>polyL</p> <p>The clast-supported lower division of the TDF is deposited from a turbulent cohesive portion of the flow, whereas the upper matrix-supported part is deposited by cohesive freezing. The TDF deposit exhibits the modification of the flow, where turbulence is smothered by flow deceleration. Thus, larger clasts are deposited from suspension first. (Lowe, 1982)</p>
 <p>THIN / CRUDELY-BEDED TB/CB</p>	<p>Clast-to-matrix supported, rarely clast supported. Massive, non-graded, moderately to poorly sorted beds. Planar and cross bedding. Commonly occurring lenses of coarse-pebble pumices and planar run-out sand beds. Very coarse-sand to medium-pebble sized clasts in fine to medium-sand sized sandy matrix. Sub-angular to rounded clasts.</p> <p>Thickness: 5 cm - 1 m</p>	<p>Lenticular with rarely erosive boundaries. Hundreds of meters.</p>	<p>Hyperconcentrated flow HF</p>	<p>Channel [CH]</p>	<p>polyL</p> <p>Lenticular, bedded TB/CBIF deposits represent pulses of mass flows and deposition in confined conditions. Massive inner texture indicates the dominance of the matrix strength influencing factor of the flow. The deposit might be generated by the confinement of debris flows into the valley (i.e. palaeo-channel) resulting in dilution (i.e. surface transformation; Fisher, 1983) and additional increasing turbulence.</p>
 <p>COHESIVE C</p>	<p>Clast-to-matrix supported with high amount (> 5 wt. %) of clay in matrix. Massive, non-graded, very poorly to poorly sorted. Fine-pebble to coarse-pebble sized dense to vesicular lithic clasts and weathered pumices suspended in very fine to fine-sand sized mixture of clay and sand matrix. Sub-angular and sub-rounded fragments and rounded, well-rounded pumice clasts.</p> <p>Thickness: 0.5 m - 2 m</p>	<p>Lenticular with non-erosive boundaries. Tens of meters.</p>	<p>Debris flow DF</p>	<p>Channel [CH]</p>	<p>LP</p> <p>Dominant sustaining mechanisms are matrix strength and matrix density generating CDF deposits (Lowe, 1982). They can be derived from the collapse of hydrothermally altered volcanic edifice (Vallance and Scott, 1997; Capra and Macías, 2000; Vallance and Iverson, 2015). They may represent syn-eruptive materials or could be transformed and confined from proximal debris avalanche deposits (Minami et al., 2019).</p>
 <p>CHANNELIZED Ch</p>	<p>Clast-supported. Massive, non-graded, very poorly to extremely poorly sorted. Coarse-pebble to boulder sized fragments, in a medium to coarse-sand sized matrix. Angular to rounded clast morphologies.</p> <p>Thickness: 1 m - 6 m</p>	<p>Channel-confined with extremely erosive boundaries. Tens of meters to hundred meters.</p>	<p>Debris flow DF</p>	<p>Channel [CH]</p>	<p>polyL</p> <p>Debris-flow deposition occurs due to the grain-contact friction and bed friction concentrated along the flow perimeter where high pore-fluid pressure is absent. Clast interaction plays an important role within the flow mechanism due to the confining conditions during deposition. (Major and Iverson, 1999)</p>

Table 4.3 Continued.

4.6 Physiographic facies

Physiographic facies are associations that correspond to different physiographic factors (i.e. limitations of paleo-topography), which affect the transportation of mass flows (i.e. sediment influx rates or water content changes) influencing the depositional environment. The term is here used to distinguish three main types that affect the sedimentological textures, lateral extensions and geometries of mass-flow deposits (**Fig. 4.3**): (i) Sheet [SH] facies association indicates materials deposited broadly on landscapes with relatively plain and flat morphology. (ii) Overbank [OB] facies describes the medial parts of channel geometries or runout facies of hyperconcentrated flows. (iii) Channel [CH] facies corresponds to proximal parts of channel geometries confining the flows and thereby affecting their depositional conditions and structural features of the resulting deposits. Moreover, paleosol and peat accumulations are present as interbedded associations. Plain facies represents fluvial deposition, whereas shore facies specifies near-coast environments with the appearance of aeolian sediments interbedded with reworked mass-flow and fluvial deposits.

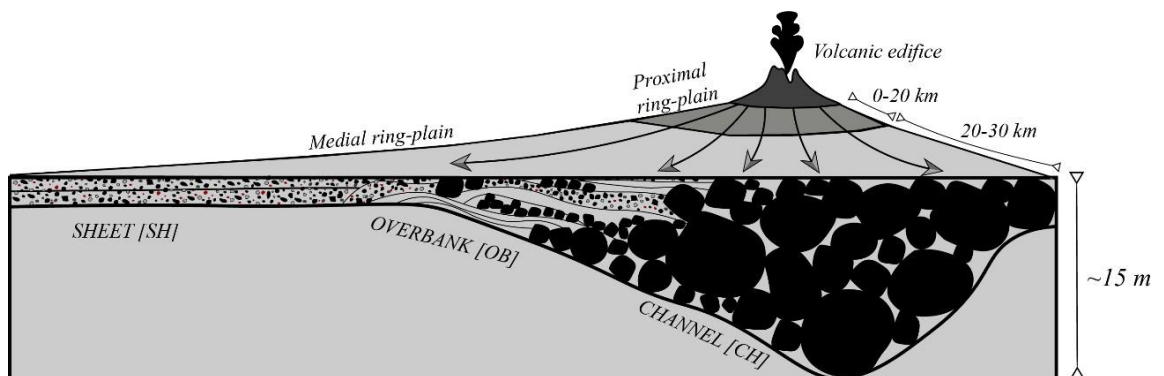


Fig. 4.3 Two-dimensional cross-section in a flow-perpendicular cut illustrating the physiographic facies as observed on the field. Note that the schematic focuses on a channelization for demonstrative purposes. Arrows indicate the direction of the transportation of volcanoclastic mass-flow deposits and their deposition.

Observed physiographic facies are linked to the examined lithofacies in **Table 4.3**. In general, iGHF/GHF and MHF lithofacies distributions are laterally traceable in sheet physiographic conditions for kilometres and their textures often show transitions between each other. Complex DiFS lithofacies are common in every physiographic environment. Additionally, THF lithofacies seem to be connected to physiographic facies change, i.e. channel to overbank or from overbank to sheet. Therefore, this lithofacies can be observed in every facies similarly to DiSF. These repeated facies changes result in the observed chaotic transitional textures. THF deposits are horizontally variable and can transform into DiSF with distance from channels or into MHF or iGHF/GHF from overbank to sheet

physiographic facies. nCDF deposits probably were not formed by channelization, but rather developed due to varying water/sediment ratios during the passage of the flow. These conditions allowed them to appear in overbank to sheet physiographic facies, whereas CDF deposits stratigraphically appear beneath debris-avalanche or debris-flow deposits and show connection to channel topographies, where tBHF/cBHF and ChDF deposits similarly occur.

4.7 Lithology

Observed volcanic rocks were classified by their lithological characteristics and by their occurrence in the deposits. The described petrofacies assemblages are introduced in **Table 4.4** and are connected to the investigated lithofacies in **Table 4.3**. Macroscopically observed colour differences were considered as possible deviation in composition and/or in density. Lithological components were defined as the following: white, grey or yellow pumiceous clasts and red or black coloured scoriaceous clasts (vesicular volcanic fragments) as recycled juveniles (White and Houghton, 2006); black, dark grey and grey lava rock fragments (dense nonvesicular fragments) and black, dark grey and grey glassy volcanic fragments as lithics (White and Houghton, 2006). In addition, accidental lithoclasts and individually occurring crystals (amphibole and pyroxene phenocrysts) have also been identified within the matrix of the mass-flow deposits.

4.7.1 Petrofacies classification

Lithic-dominated lithology (L) corresponds to mainly dense and glassy, angular to subangular lava rock fragments, dome rock fragments and scoriaceous clasts (>50%) with c. 5-25% abundance of pumiceous clasts (**Table 4.4 A**). Dominant dense lithics are grey or dark grey in colour. Red colour also occurs in minority for scoriaceous assemblages. Pumice clasts are vesicular or microvesicular appearing mainly in white, grey and rarely in yellow colour.

Pumice-dominated monolithologic petrofacies (monoP) contains pumice clasts (>70%) that are rounded or subrounded in shape (**Table 4.4 B**). Occasionally occurring red scoria and accidental lithoclasts may be present. Pumice clasts are generally fresh to moderately weathered. Their colour is mainly white and grey or yellow. The lithology is further comprised of medium-to-coarse lapilli sized scoria or pumice bombs (after Fisher, 1961), often having a breadcrust appearance.

Poly lithologic petrofacies (polyL) exhibits clasts that can be subdivided into scoria, dome and lava rock fragments, glassy volcanic fragments, accidental lithoclasts (5-25%) and rarely pumiceous clasts (<5%). The components exhibit at least three colours (black, grey, red) that share the same size and shape patterns (**Table 4.4 C**).

Lithic- and pumice-dominated petrofacies (LP) is mainly composed of scoriaceous and pumiceous lithologies (>50%). They are recognizable in overbank and rarely in sheet lithofacies in the coastal successions. The majority of clasts are rounded pumices and mainly dark grey and black coloured scoria and occasionally rounded to sub-rounded lava rock fragments with differing vesicularity. Red coloured scoria may occur rarely. Lithic- and pumice-dominated debris flow deposits (LPDF) are compositionally similar to LPHF deposits but differ in texture. The main lithologies are pumice, black scoria and dark grey lava rocks. Pumice clasts range from coarse-sand to small-pebble size, whereas scoria and lava rocks are small-to-medium pebble sized (**Table 4.4 D**). Both lithologies are rounded, rarely subrounded in shape. Minor amounts of accidental lithoclasts or red coloured, vesicular scoria may occur. The matrix contains high amounts of clay and sand. Stratigraphically, this lithology usually appears below debris-avalanche or debris-flow deposits.

The sand-dominated lithology (S; **Table 4.4 E**) comprises major amounts of sand (>50%) with commonly occurring lithoclasts (>5%) and occasional pumiceous fragments (5-10%). The lithoclasts are subangular, whereas pumice clasts are rounded to subrounded in shape.

<i>Petrofacies, code</i>	<i>Description</i>	<i>Semi-quantitative threshold value</i>	<i>Previous studies</i>	<i>Interpretation of this study</i>
<i>Lithic-dominated</i> L	<i>Lithology:</i> Mainly occurring lithics with major presence of pumice clasts. <i>Colour:</i> Dark grey, grey lithics with minor red and dark grey scoria, yellow lithoclasts and often occurring white, grey and yellow pumice clasts. <i>Clast shape:</i> Angular to subangular lithics and scoria, rounded to subrounded pumices.	Lithics: >50% Pumice: 5-25% Accidental lithoclast: <5%	Macroscopically lithic-rich deposits are thought to represent block-and-ash-flow material as the result of dome-collapse events (Platz et al., 2007a; Zernack et al., 2009; Zernack, 2021).	The petrofacies specifies particular events connected to dome collapses (generated block-and-ash flows). This petrofacies occurs in multiple hyperconcentrated-flow deposits, thus exhibiting a periodic depositional pattern throughout the studied growth phases.
<i>Pumice-dominated Monolithologic</i> monoP	<i>Lithology:</i> Major abundance of pumice with lithics and rarely occurring lithoclasts. <i>Colour:</i> White, grey and yellow pumice clasts. Dark grey, grey and red lithics, minor red scoria and yellow lithoclasts. <i>Clast shape:</i> Rounded to subrounded pumices, subangular lithics.	Pumice: >70% Accidental lithoclast: <5%	Monolithologic pumice deposits are thought to represent deposited materials that are originated from remobilised tephra falls after explosive sub-Plinian eruptions or from connected pyroclastic flows (Schmincke, 1967; Waitt et al., 1983; Pierson and Scott, 1985; Scott, 1988a; Cronin et al., 1997; Waythomas et al., 2000; Zanchetta et al., 2004; Major et al., 2005; Zernack et al., 2009).	The lithology refers to the clasts and also to the matrix of the observed deposits. Macroscopically occurring pumice fragments may differ in colour that is thought to indicate density or geochemical difference. The petrofacies implies volcanic activity and they are considered as syneruptive material that was deposited by the assistance of water and confined pyroclastic flows of the same volcanic event.
<i>Polyolithologic</i> polyL	<i>Lithology:</i> Major amount of accidental lithoclasts and scoria with minor amount of pumice fragments with often occurring weathered fragments. <i>Colour:</i> Dark grey, grey and red lithics, yellow, red lithoclasts, white and grey pumiceous clasts and red scoria. <i>Clast shape:</i> Angular to subangular lithics, rounded to subrounded scoria and pumiceous clasts.	Accidental lithoclast: 5-25% Pumice: <5%	Earlier studies suggested that polyolithologic volcanoclastic deposits in ring-plain environments could not indicate eruptional activity, hence, they represent run-out of facies of mass-flows in quiescence periods (Zanchetta et al., 2004; Zernack et al., 2009; Zernack, 2021).	The presence of diverse lithologies in the deposits deputizes reworked origin, thus indicating significant remobilisation processes that mostly occur in quiescence periods, when sediment-influx rates are high.
<i>Lithic- and pumice-dominated</i> LP	<i>Lithology:</i> Double-like abundance of pumiceous or scoriaceous clasts with minor lithics. <i>Colour:</i> Dark grey, grey lithics and scoria and white or grey pumiceous clasts with minor occurrence of red scoria and accidental lithoclasts. <i>Clast shape:</i> Sub-rounded to rounded lithics and scoria, rounded to well-rounded pumiceous clasts.	Lithics and pumice: >50% Accidental lithoclast: <5%	(Zernack et al., 2009)	The bimodal petrofacies characteristic of the observed deposits may indicate the linkage between possible eruption triggered events and the transported material. Moreover, it was only mappable stratigraphically beneath debris-avalanche deposits that might assume a connection to volcanic activity prior collapse events.
<i>Sand-dominated</i> S	<i>Lithology:</i> Major amount of sand with commonly occurring lithoclasts and pumice clasts. <i>Colour:</i> Dark grey, grey lithics with minor red scoria, yellow lithoclasts and white or grey pumice clasts. <i>Clast shape:</i> Subangular lithics, rounded to subrounded pumices.	Pumice: 5-10% Accidental lithoclast: >5%	(Zernack et al., 2009)	Sandy lithology with occurring lithoclasts and pumiceous clasts represents reworked origin and might indicate runoff facies of mass-flow events or reworked stream-flow deposits.



Table 4.4 Petrofacies description and classification criteria of the observed medial volcanoclastic mass-flow deposits. Pictures representing the general appearance of lithologies. **A:** lithic-dominated; L, ruler for scale: 17 cm. **B:** pumice-dominated monolithologic; monoP, hammer for scale: 25 cm; **C:** polyolithologic; polyL, person for scale: 170 cm. **D:** lithic and pumice-dominated, LP. **E:** sandy, S, ruler for scale: 10 cm. Semi-quantitative threshold value based on the point counting method calculations on the images for estimating componentry in surface %.

4.8 Unconformities

Large-scale (up to hundreds of meters in lateral section) erosional unconformities were identified as paleochannel systems that were filled by several debris- and hyperconcentrated-flow deposits. Small-scale (a few tens of meters of lateral extent) unconformities occurred as minor channelizations following mainly the present-day stream locations/drainage pattern. This landscape-pattern indicates that the direction and distribution of streams in the last 65-34 ka shared similarities with the ones today, although several other minor channelizations appeared elsewhere in the ring plain over time.

4.8.1 Paleochannel systems

Kaupokonui paleochannel system

The Kaupokonui paleochannel system formed c. 80-55 ka ago, based on its stratigraphic position in relation to the estimated age of sand dune generation (Puketapu Sands) and the Otakeho DAD by Zernack et al. (2011). The lateral extent of the paleochannel is approximately a few hundred meters, involving the present-day position of Kaupokonui Stream (see stream emplacements in **Fig. 4.1 B**). Outcrops along the coastal cliffs are buried or obscured by streams and sand dunes. The lateral changes of the Otakeho debris-avalanche and fluvial deposits followed the topography of the channel, indicating that it pre-dated the collapse event.

Lizzie Bell paleochannel system

The Lizzie Bell paleochannel system was filled by several debris flows producing an approximately 500 m wide paleochannel system at Ouri stream (**Fig. 4.1 B**). The bottom key marker bed is the Otakeho DAD that provides a maximum age of ca. 55 ka. Although, there is no key marker that would constrain the minimum age of the paleochannel, based on the DAD distributions (Zernack et al., 2011; Zernack, 2021), it is considered that its deposits were produced before the Rama DAD was deposited, c. 40 ka ago. The top of the sequence contains a series of paleosols that might be of similar age to the Hihiwera Peat (Zernack, 2021). In this study, the deposit – produced by an extremely erosive debris flow – is referred to as the Lizzie Bell Debris-flow deposit (Lizzie Bell DFD), which is considered to represent one single mass-flow event filling up a large portion of the

paleochannel. Its measured distribution and calculated extrapolated volume are provided in **Table 4.5**.

Taungatara paleochannel system

The Taungatara paleochannel system was filled up c. 40 and 34 ka ago based on the dated Te Namu and Rama DAD marker beds (Zernack et al., 2011) at Taungatara stream (**Fig. 4.1 B**). The observed lateral extent of the channel is c. 300 m, but due to the lack of significant outcrops, it may be up to 400 m wide. Mapped debris-flow deposits suggest one mass-flow event filled the channel through several successive flows, as indicated by the lack of intercalated soil accumulation and thin (from cm to a meter) stream flow and transitional hyperconcentrated flow units between the erosive debris-flow deposit packages. The deposit is referred to as the Taungatara Debris-flow deposit (Taungatara DFD; **Table 4.5**). At well-exposed locations, ripped-up clasts of hyperconcentrated-flow deposits can be found in its matrix.

<i>Debris flow deposit</i>	<i>Mapped lateral extent (m)</i>	<i>Average thickness (m)</i>	<i>Distance from source (km)</i>	<i>Estimated minimum volume (km³)</i>
<i>Lizzie Bell DFD</i>	<i>200</i>	<i>3</i>	<i>28</i>	<i>0.02 - 0.05</i>
<i>Taungatara DFD</i>	<i>400</i>	<i>3.5</i>	<i>26.5</i>	<i>0.05 - 0.1</i>

Table 4.5 Volume calculations of the Lizzie Bell and the Taungatara Debris Flow deposits based on the mapped thicknesses and lateral distributions observed on the field.

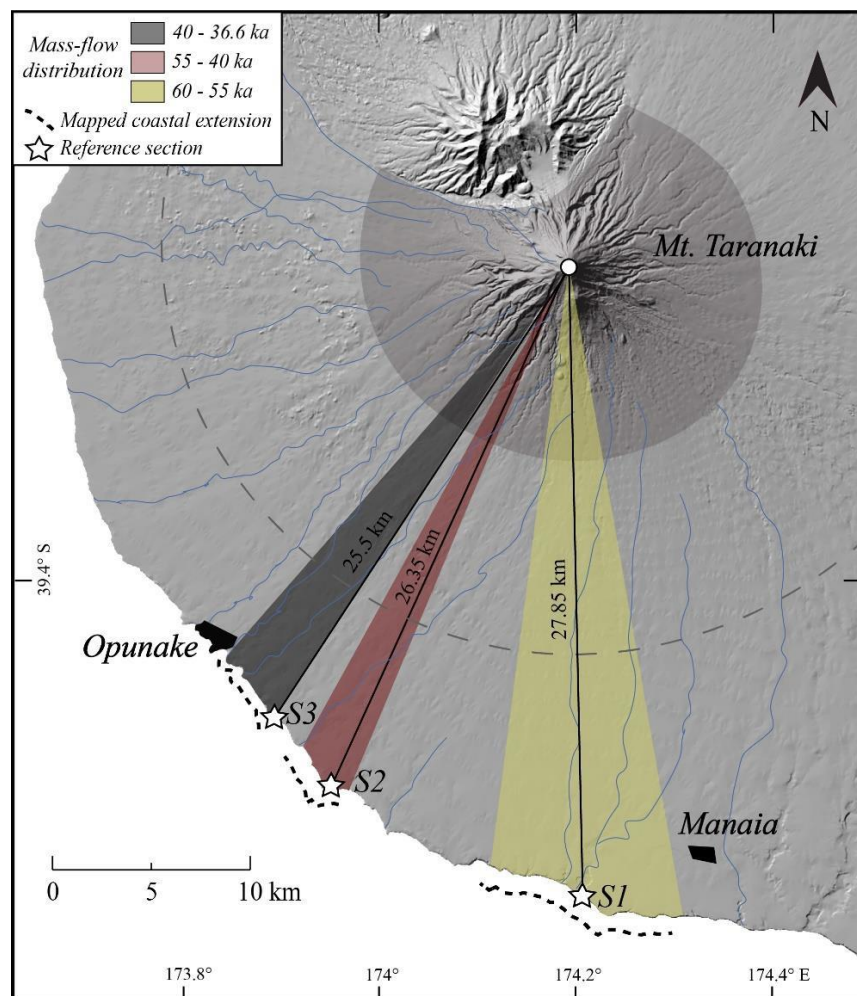
Opunake paleochannel systems

The Opunake paleochannel (A) is at least 1.5 km wide and distributed mainly between Otahi and Waiaua Streams (**Fig. 4.1 B**). It was filled by several pulses of channelized mass-flows (ChDFs, CDFs and nCDFs), resulting in a minimum of 5 observed major unconformities in the paleochannel. The channel system was active between –36.9–24.8 ka as constrained by the Pungarehu DAD and Hihiwera Peat as upper and lower marker deposits in the strata. Another channelization occurred through several mass-flow events that formed a second, younger Opunake paleochannel (B), with an age range between 24.8 and 7.5 ka (age of markers based on Zernack et al., 2011; Zernack, 2021). The lateral distribution of individual mass-flow deposits that filled the channel is approximately 250 meters.

4.9 Distribution, frequency and appearance of lithic-dominated mass-flow deposits

All three construction phases of the studied time period (65-34 ka), in-between the collapse events indicated by DADs, contain widely distributed lithic-dominated hyperconcentrated-flow deposits mappable (**Fig. 4.4**) along the shoreline. The 4 units of the deposit packages in the construction phase between 60 – 55 ka can be traced for more than 8.5 km in the south sector of the ring-plain (see location of representative site S1 in **Fig. 4.4**). In the following growth phase (55-40 ka), at least three lithic-dominated mass-flow packages were deposited to the south – southwest (key site S2 in **Fig. 4.5**), with a lateral mapped extent of more than 3 km. This was followed by at least four units in the next construction phase (40 – 36.9 ka), for which the depositional direction moved south-west, trackable for more than 2.5 km along the coastal cliff sections (key site S3 in **Fig.**

4.4). The depositional orientation or main dispersal axis of the lithic-dominated hyperconcentrated flows share similarities with the direction of DAD deposition with time, i.e. from south to west.



◀**Fig. 4.4** Distribution directions and mapped coastal extensions of lithic-dominated volcanoclastic mass-flow deposits along with the distance from the vent (white circle). Note: Mapped coastal extensions are considered as observed minimal estimations. Grey shaded area outlines the proximal distance - 10 km in diameter - around the edifice. Dashed line indicates the 20 km distance from source, i.e. the proximal – medial distance boundary.

A periodic pattern can be observed as fluvial deposits (in reference site S1) and soil accumulations (in reference sites S2 and S3; **Fig. 4.5**) are present between the studied mass-flow sequences, indicating regularly occurring time-breaks in volcanoclastic deposition (thicknesses range between 20 cm and 2 m; **Fig. 4.5**) during each growth phase. In general, the observed mass-flow packages indicate a recurrence time of a minimum of 3 to 5 mass-flow events every approximately 4 – 10 kyr in each construction phase. The estimations are based on the dated marker deposits (**Table 4.2**) and the soil and fluvial deposits as time-break indicators between the mass-flow sequences and are considered minimum approximations.

Pumice-dominated monolithologic hyperconcentrated-flow units are composed of main clast sizes of -4ϕ , whereas lithic-dominated hyperconcentrated flow deposits consist of clasts with sizes ranging between -3ϕ to -5ϕ (**Fig. 4.5**). The former deposits dominantly contain pumice clasts (45 – 97 surf. %) with minor presence of varicoloured dense lava rock and scoriaceous fragments. Based on point counting analysis of representative sites, lithic-dominated hyperconcentrated-flow deposits in each studied construction phase contain grey, black and red coloured, dense to vesicular volcanic rock fragments in majority (75 - 95 surf. %), in which grey lava rock fragments dominate (25 – 50 surf. %). Pumiceous clasts are also present as the second or third major lithology with 5 – 25 surf. % in the mass-flow deposit packages (**Fig. 4.5**). Accidental lithoclasts are present in minority (0 – 5 surf. %).

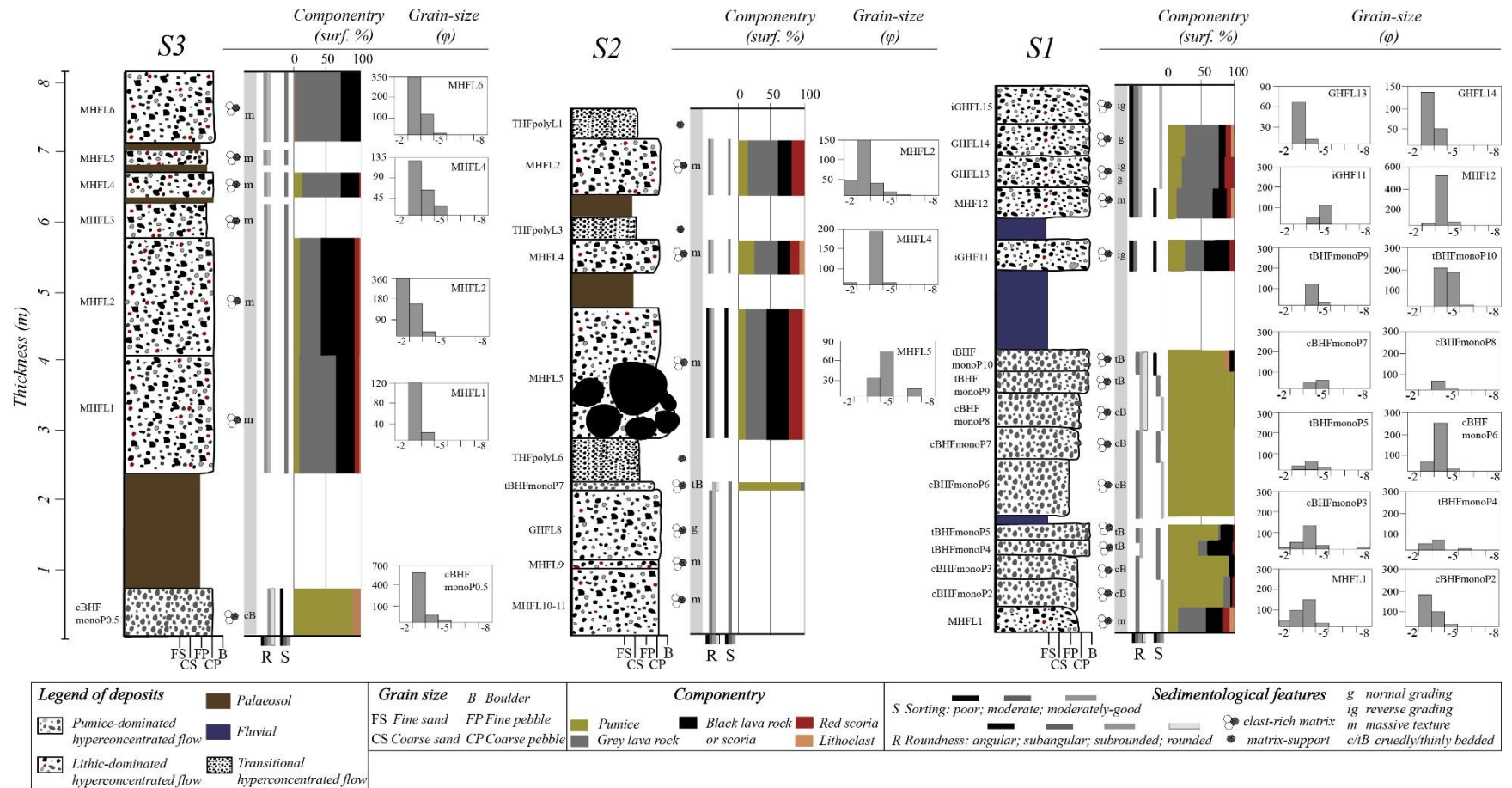


Fig. 4.5 Sedimentological characteristics and point counting results of componentry and grain size of the lithic-dominated and pumice-dominated hyperconcentrated-flow deposits at the representative sites (See **Fig. 1** for locations and **Fig. 4** for lateral extensions). Grain size histograms represent the number of clasts on the Y-axis and grain-size Phi (ϕ) conversion on the X-axis. The coding of mass-flow deposit packages follows the nomenclature introduced in **Table 3** and **4** in relation to texture and lithology. Grain-size and componentry data can be found in **Appendix A1**.

4.10 Discussion

4.10.1 Proposed classification criteria and coding system for ring-plain volcanoclastic deposits

The ring-plain depositional system of Taranaki Volcano preserves the detailed events of volcanic evolution in the coastal-cliff successions, exposed by marine erosion. As a nearly continuous stratigraphic sequence of construction phases is evident, these cross-sectional successions are representative sites to categorize the volcanoclastic deposits. Therefore, a classification criterion using the medial (20-30 km in distance from source) mass-flow deposits could be established (**Table 4.6**).

The classification matrix aims to interconnect the sedimentological, geometric and lithological features of the deposits and their relationships based on field observations leading to a schematic framework. Lithofacies characteristics along with the physiographical emplacement of the deposits and the connected petrofacies were introduced above (see **Table 4.3** and **Table 4.4**) and their codes are combined to compose the code schemes (1 + [2] + 3) characterizing each lithofacies (**Table 4.6**). Considering the three-part coding system, the syneruptive or inter-eruptive (i.e. post-eruptive) origin of the volcanoclastic deposits can be interpreted, which then allows the subcategorization of the deposits using the terms as reworked (White and Houghton, 2006), reprocessed (Sohn and Sohn, 2019) or rapidly remobilised, respectively. The illustration of a criterion matrix exemplifies how volcanoclastic mass-flow deposits can provide information on volcanic histories, which can be deciphered from a ring-plain system. Additionally, this study deals with secondary deposit subcategorization, the classification matrix can thus be used on primary volcanoclastics of volcanoclastic mass-flow deposits.

4.10.2 Eruptive activity during growth cycles: Lithic- and pumice-dominated volcanoclastics

A nomenclature for describing volcanoclastic deposits in ring-plain settings is essential. Careful consideration needs to be given to ensure that the nomenclature accurately represents and differentiates the lithology and emplacement mechanisms. The term “rapidly remobilised” is proposed to describe syn-eruptive volcanoclastic deposits or material that was erupted and initially emplaced by pyroclastic density currents (PDC) or dome-collapse (block-and-ash flow) events. These deposits then immediately or at some time afterwards (hours to weeks) were transported in the form of volcanoclastic

mass flows through the interaction with water to be deposited medially or distally. The phrase “rapidly remobilised” implies both the relatively short time passed between volcanic activity and initial emplacement before being remobilised by water and transported further. The exact time interval between the initial event and further transportation cannot be determined. However, based on the distributional and lithological observations of the deposits, the time window between emplacement and remobilisation is suggested to be on a scale of hour to weeks. Additionally, “rapidly remobilised” deposits are proposed to be classified as a subtype of secondary volcanoclastic deposits due to the sedimentological key criteria that would designate non-volcanic processes. Thus, this distinction allows the compatible usage of the different secondary deposit subcategories, such as reworked (White and Houghton, 2006), reprocessed (Sohn and Sohn, 2019) and “rapidly remobilised”, respectively.

Mapping the mass-flow deposits in the coastal cliff successions highlighted the complex structure of the medial ring-plain. Considering the variability of mass-flow sequences during construction phases, stratigraphic correlations can only be made if marker beds are present.

LITHOFACIES 1			PHYSIOGRAPHIC FACIES 2	PETROF. 3	CODING SCHEME	VOLCANICLASTIC ORIGIN		SECONDARY DEPOSIT SUBCATEGORY
TEXTURE	CODE	EMPLACEMENT PROCESS			1 + [2] + 3	SYNERUPTIVE	INTER-ERUPTIVE	
<i>Graded/inversely graded</i>	iG / G	Hyperconcentrated flow ^{1 2 4} HF	SHEET [SH]	L	GHF[SH]L MHF[SH]L	BAF		<i>Rapidly remobilised</i>
<i>Dilute</i>	Di	Stream flow ² SF	SHEET [SH]	S	DiSF[OB]S		HFD	<i>Reworked</i>
<i>Transitional</i>	T	Hyperconcentrated flow ^{1 2 4} HF	OVERBANK [OB]	polyL	TiHF[OB]polyL		DFD	<i>Reworked</i>
<i>Non-cohesive</i>	nC	Debris flow ^{2 3 4} DF	CHANNEL [CH]	polyL	nCDF[CH]polyL		DED	<i>Reworked</i>
<i>Transitional</i>	T	Debris flow ^{2 3 4} DF	CHANNEL [CH]	polyL	TDF[OB]polyL		DFD	<i>Reworked</i>
<i>Thinly/crudely bedded</i>	tB / cB	Hyperconcentrated flow ^{1 2 4} HF	CHANNEL [CH]	monoP	tBHF[CH]monoP	PDC		<i>Rapidly remobilised</i>
<i>Cohesive</i>	C	Debris flow ^{2 3 4} DF	CHANNEL [CH]	LP	CDF[CH]LP	PDC		<i>Rapidly remobilised</i>
<i>Channelized</i>	Ch	Debris flow ^{2 3 4} DF	CHANNEL [CH]	polyL	ChDF[CH]polyL		DFD	<i>Reworked</i>
Tephric soil / Peat		In-situ				Tephra fall	Soil accumulation	
Massive / Bedded		Fallout						
Horizontal-bedding / Cross-stratification		Fluvial	PLAIN				Flood	
Imbrication of clasts		Fluvial	SHORE				Wind	
Cross-bedding		Aeolian						

¹ Beverage and Culbertson, 1964, ² Pierson and Costa, 1987, ³ Costa, 1984, 1988, ⁴ Smith, 1986

Table 4.6 Classification criteria of volcanoclastic deposits using the proposed coding scheme that is composed of the lithofacies (1), the physiographic facies (2) and the petrofacies (3) codes. Note that presented coding schemes are examples based on this study. Petrof.: Petrofacies. BAF: Block-and-ash flow. PDC: Pyroclastic density current. HFD: Hyperconcentrated flow deposit; DFD: Debris flow deposit.

Correlating individual flow units using traditional chronostratigraphic techniques was entirely impractical in channel and overbank settings. Therefore, the developed sedimentological, lithological and facies classification highlights the connection between the three main factors that define medial (<30 km from vent) mass-flow generation, transportation and deposition: (i) the occurrence of certain sedimentological textures (that mirror transportation processes), (ii) comprised clast lithologies (which point out origin relationships) and (iii) physiographic facies conditions (defining particular transportational and depositional physiography-limitations).

Considering the three factors and their dependence on each other, mass-flow deposit features were placed into a matrix representing their linkage in parameter space. Thus, mass-flow deposit characteristics were able to be classified in relation to their origin due to the groups they created (**Fig. 4.6**).

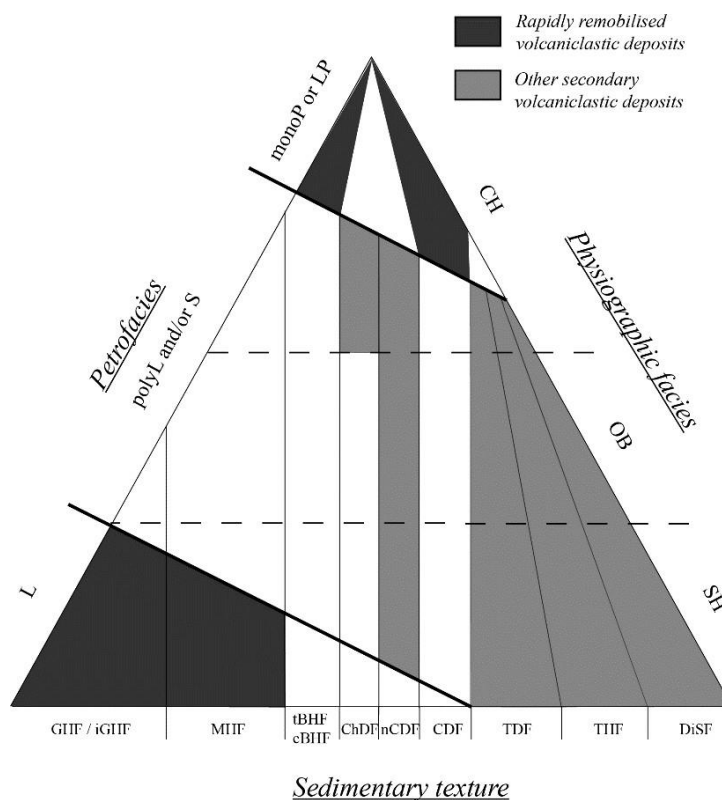


Fig. 4.6 Schematic matrix in parameter space outlining the connection between the three main factors that define the studied volcaniclastic deposits: (1) sedimentary texture; (2) petrofacies and (3) physiographic facies. Shaded areas represent the combination of the parameters observed in the coastal successions of the Taranaki ring plain. White areas indicate factor combinations that were not observed on the field. Dashed lines indicate the boundaries of the physiographic facies, whereas thick black lines the boundaries of the petrofacies and thin black lines the boundaries of the sedimentary textures, respectively. The form of the shaded areas is for illustrative purposes and only indicate the connection between the three main parameters. Based on the linkage of the factors, deposits can be interpreted as rapidly remobilised or other secondary deposits.

Four main clusters were distinguishable from which two groups are considered as “rapidly remobilised” volcanoclastic mass-flow deposits (that are directly or indirectly related to volcanic eruptions) and two groups that are associated with non-eruptive processes resulting in the deposition of other secondary deposits.

Rapidly remobilised volcanoclastic mass-flow deposits

Lithic-dominated deposits are widespread, traceable packages. They blanket the landscape laterally up to a 9 km wide segment of the medial ring plain (20-30 km from source; see lateral distributions in **Fig. 4.4**), indicating possible (small-scale) dome collapse events initiated mass-flow events reaching medial (<30 km; possibly distal, >30 km) run-out distances. These widely distributed lithic-dominated volcanoclastic mass-flow deposits are considered to represent periodically occurring explosive and effusive events and they are present in each of the investigated construction phases of Taranaki Volcano.

These deposits typically have MHF or iGHF/GHF textures with similar grain sizes (between -3 and -5 ϕ). While volcanic lithics dominate, the second major lithology is pumiceous or scoriaceous (5 to 25 surf. %) with the matrix containing individual crystals. Earlier observations noted that monolithologic BAF deposits containing crystals in their matrix imply syn-eruptive dome failure (Tahurangi BAF deposit; Platz et al., 2012). According to the amount of pumiceous or scoriaceous clasts in these deposits and the presence of crystals in the matrix, the origin of the units could be connected to eruptive activity. Therefore, the deposits may represent block-and-ash-flow material resulting from dome-collapse events that occurred frequently during the history of Taranaki Volcano (Platz et al., 2007a). Macroscopically, multicoloured clasts share similar mineral assemblage features. However, it is problematic to describe the exact origin of these deposits due to the lack of proximal outcrops. Additionally, these deposits suggest a relationship to small to moderate-scale dome collapses after or during pumice-forming eruptions and the syn-eruptive origin of these lithic-dominated deposits can be suggested. Moreover, recent studies validate the hypothesis that volcanoclastic mass-flow deposits are remobilised run-out facies of dome collapses (connected PDCs). They state that PDCs could reach 24 km distance from the source at Taranaki Volcano (the Warea Formation; Lerner et al., 2019), 9 km farther than it was previously determined. Thus, the observed minimum run-out distances of the deposits of this study are between 25 – 28 km (**Fig.**

4.4), supporting the idea that syn-eruptive volcanic materials are able to get remobilised relatively fast after volcanic activity with the interaction of water.

Pumice-dominated monolithologic hyperconcentrated flows and lithic- and pumice-dominated debris flows deposited channel lithofacies with bedded or cohesive textures (using the coding system, the former is termed *tBHF[CH]monoP* and the latter *CDF[CH]LP*). The former deposits are characterised by enrichment in pumice clasts with high amounts of pumiceous breadcrust bombs. The latter display a unique assemblage of lithologies of pumice and volcanic lithics in a clay-rich matrix. Both deposits have a high amount of sandy matrix and are confined to channels. Despite the wide distribution of lithic-dominated deposits, pumice-dominated monolithologic hyperconcentrated-flow deposits were found mostly in channel facies or close to channels. Their mapped lateral extent was a few hundred meters on average indicating relatively confined conditions. Pumice-clast characteristics are similar to those found in lithic-dominated deposits, i.e. grey colours dominate, with rare yellow clasts. Macroscopically, *tBHF[CH]monoP* deposits represent explosive eruption products that were remobilised from tephra falls or from PDCs accompanying sub-Plinian eruptions (Pierson and Scott, 1985; Scott, 1988b; Cronin et al., 1997; Waythomas and Miller, 1999; Zanchetta et al., 2004; Major et al., 2005). This is corroborated by the large number of breadcrust bombs found in these deposits, which also suggest immediately remobilised origin. Moreover, pumice-rich beds suggest direct or indirect relations to pumice-forming eruptions, where PDC deposits are subsequently mobilized into debris flow, then to hyperconcentrated flows in valleys confining the deposits (Pierson, 1986; Major and Iverson, 1999; Cronin et al., 2000a, b).

Other secondary deposits

Polyolithologic deposits occur in all lithofacies representing diverse sedimentological conditions. Mixed lithologies correspond to secondary origins. Furthermore, deposits that contain these lithologies often transform into transitional textures and cannot be traced laterally. The transitional (T) and dilute (Di) textures in most cases indicate runout facies of mass-flows reaching medial distance from the source and thus, their origin cannot be determined. Voluminous, erosive debris-flow events producing ChDF deposits may originate from dome or flank collapse events, which were confined to paleoriver-channels, where they transformed into poorly to extremely-poorly sorted, clast-supported deposits with low amounts of sandy matrix. The erosive nature of confined ChDF is also

proved by rip-up clasts made of hyperconcentrated flow deposits within the matrix (i.e. in the matrix of the Taungatara Debris-flow deposit). The occurrence of rip-up clasts has been observed in debris avalanche deposits as a textural characteristic (Zernack et al., 2009) suggesting that the Taungatara Debris-flow deposit may be connected to and represents the runout facies of a small-scale collapse event.

4.10.3 Stratigraphic context of growth phases

The development of the sedimentological and lithological classifications provided a detailed picture of the volcanoclastic deposits and their stratigraphic position. The establishment of a stratigraphic model (**Fig. 4.7**) offers a better understanding of the sedimentary processes in the ring plain and the volcanic history of Taranaki Volcano within the studied time period (see **Fig. 4.1 B** for cross-section A – A' – B). We propose using the same term for growth phases within a volcanic cycle of Taranaki Volcano following the appellation of the DAD deposits (Zernack et al., 2011), e.g. Rama Growth Phase and Rama Destruction Phase was terminated by the collapse and deposition of the Rama DAD. Based on the observed and categorized deposits, three volcanic cycles are defined by the strata (**Fig. 4.7**):

Otakeho Volcanic Cycle

The oldest construction phase in the studied timespan (c. 65 – 55 ka), is dominated by aeolian deposits with interbedded tephra units and reworked fluvial deposits containing high amounts of reworked pumice. Following this period, pumice-dominated hyperconcentrated-flow deposits are present referred to as Kaupokonui hyperconcentrated-flow deposits (**Fig. 4.7**) indicating eruptive activity. Above these sequences, widely distributed lithic-dominated volcanoclastic hyperconcentrated-flow deposits with interbedded fluvial deposits are exposed. The occurrence of these deposits indicates alternating behaviour of eruptive periods and non-activity. The volcanic cycle is completed with the collapse event producing the Otakeho DAD.

Rama Volcanic Cycle

Following the Otakeho collapse event, the coastal cliffs reveal widely distributed hyperconcentrated-flow sequences on the southern shoreline with interbedded soil layers and frequently occurring minor channelization of reworked deposits. These observations

are interpreted as representing alternating processes of small-scale eruptive or effusive activity (i.e. cone regrowth), frequent sedimentation and quiescence. The Lizzie Bell Paleochannel System indicates a confined debris-flow deposit (Lizzie Bell DFD; **Fig. 4.7**) that may be linked to a small-scale flank collapse event. After these sequences of deposits, the same pattern that was previously observed in the Otakeho growth phase is recognizable as alternating layers of widely distributed hyperconcentrated-flow deposits and soils representing eruptive and quiescent periods. A possible hiatus in the stratigraphy is suspected, indicated by the emplacement of the Rama DAD, which is not present above deposits at Lizzie Bell Paleochannel. The growth phase is followed by the collapse event producing the Rama DAD, distributed to the south (Zernack et al., 2011).

Te Namu Volcanic Cycle

This growth phase is characterised by several chaotic, uncorrelatable THF and TDF textured deposits often interbedded with fluvial deposits or tephric soils. Peat accumulation is present in the south-western coastal cliffs, but their distribution is scattered. This is followed by several THF deposits and the Taungatara paleochannel, which was filled by several minor debris flows followed by the major mass-flow event producing the Taungatara debris-flow deposit (**Fig. 4.7**). Minor channelization of mass-flow deposits on the WSW ring plain is characteristic for this time period. Following the paleochannel filling, several widely distributed hyperconcentrated-flow deposits were emplaced. Above these sequences, the Ihaia debris-flow deposit is found overlain by Hihiwera Peat in the WSW sector. This was followed by the complex filling of the Opunake paleochannel system. Fluvial reworking in the WSW occurred prior to the collapse event that produced the Te Namu DAD and completed this volcanic cycle.

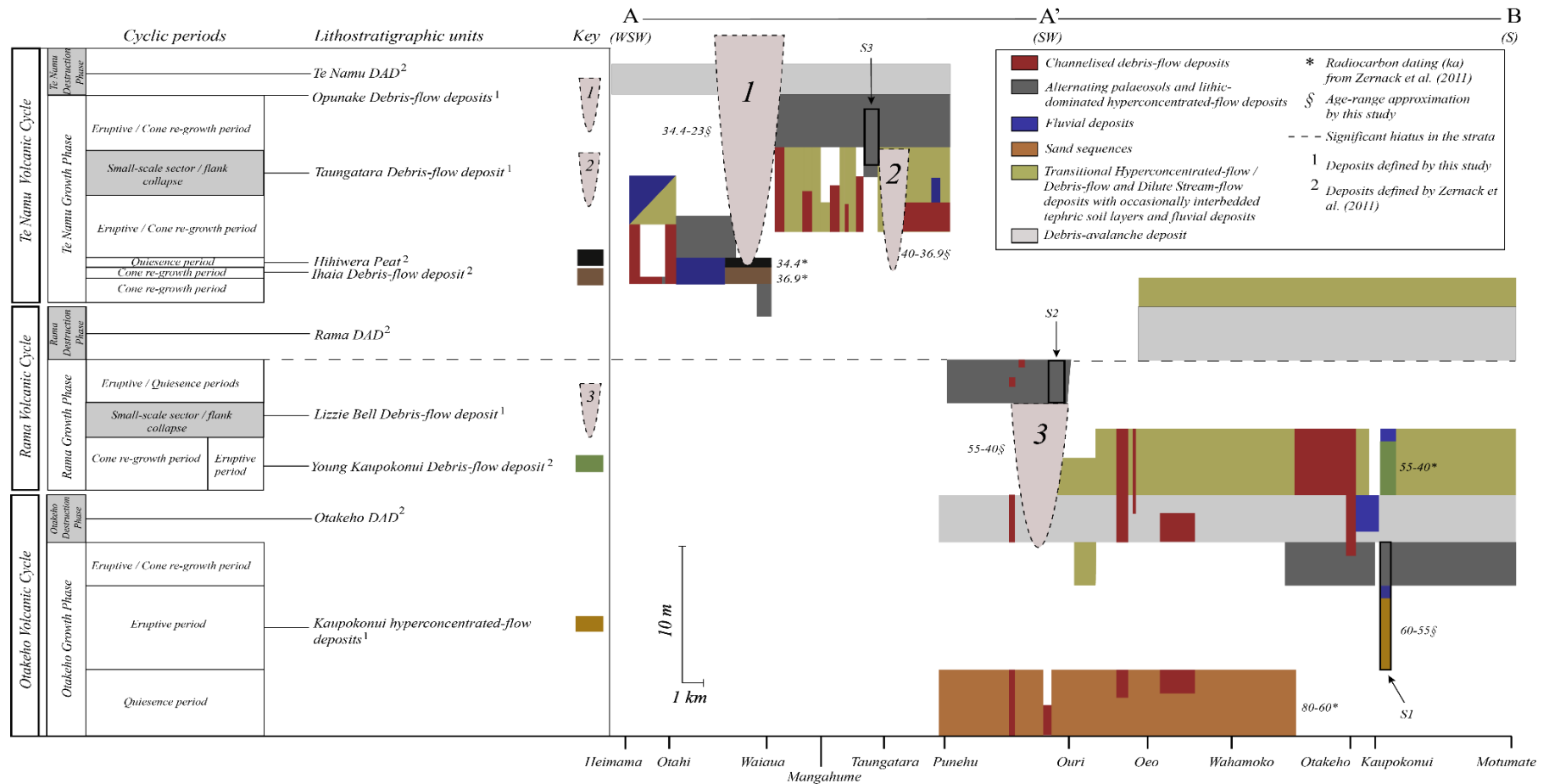


Fig. 4.7 Summarised general stratigraphic model of Taranaki Volcano between c. 65-34 ka based on the investigated medial volcanoclastic mass-flow deposits. **X axis:** Coastal extension of the field area with the occurring present-day streams (A – A' – B; see field area on **Fig. 1**). **Y axis:** The volcanic cycles, cyclic periods and the connected lithostratigraphic units. Note: All deposit thicknesses outlined are observed average thicknesses (note the scale). Interbedded paleosol layers are not indicated, although they appear mostly in sheet and overbank facies. S1, S2 and S3 representative key sites are marked by black rectangles in the strata with their estimated depositional age. U-shaped components indicate the paleochannel systems that are time-transgressive cutting multiple stratigraphic units.

4.11 Conclusions

Between c. 65-34 ka, Taranaki underwent a minimum of three major collapse events. The field survey further revealed two debris-flow deposits (i.e. the Taungatara and the Lizzie Bell DFDs) that are possibly produced and deposited by additional small-scale but significant landslides and/or flank collapse events reaching medial (<30 km; and possibly distal) sectors. The associated growth cycles during this time period are characterised by eruptive and quiescence periods resulting in the deposition of particular volcanoclastic mass-flow deposits and the formation of soils. The periodically alternating nature defines a significant frequency of a minimum c. 3 to 5 mass-flow events per 4 – 10 kyr period in each construction phase. This frequently occurring phenomena provides additional information on mitigating volcanic risks at stratovolcanoes in the future. Moreover, taking into account rapidly remobilised widely distributed or channel confined, distantly transported volcanoclastic mass flows during or shortly after volcanic activity accentuates the reassessment of hazard mapping at Taranaki Volcano.

The introduction of the term “rapidly remobilised” for a subcategory of secondary volcanoclastic deposits has been proposed to distinguish specific syneruptive volcanoclastic material that was remobilised through water interaction and deposited within the medial-distal ring-plain regions shortly after eruptive activity. The identification of these either widely distributed, lithic-dominated, massive or graded hyperconcentrated flow deposits or channel-confined, pumice-dominated monolithologic, bedded hyperconcentrated flow deposits is important for evaluating the volcanic hazards from mass-flow deposition in medial ring-plain settings during volcanic unrest. The recognition of similarly distributed and remobilised deposits in other ring-plain systems might help improve the risk mitigation at composite stratovolcanoes in back-arc settings.

The developed classification criteria and coding scheme built on the sedimentary texture, physiographic facies and petrofacies framework aims to classify the diverse volcanoclastic mass-flow deposits within a medial ring-plain setting with relation to the rapidly changing environment and eruptive activity. The usage of such coding system is suggested when dealing with volcanoclastic mass-flow deposits stratigraphically at both nearly continuous and incomplete depositional sequences within ring-plain environments at stratovolcanoes.

Additionally, the stratigraphic model for the investigated volcanoclastic sequences with the connected unconformities contribute to the development of a more detailed volcanic history. Although volcanoes have different volcanic apron settings, we assume that the mass-flow deposit criteria presented provide a contextual framework and can generally applied to elucidate the long-term history of volcanic and non-volcanic events in ring-plain settings. Therefore, the presented classification scheme may improve the identification and classification of volcanoclastic mass-flow deposits globally.

Acknowledgements

The authors would like to thank to the George Mason Charitable Trust for providing financial assistance contributing to field surveys and data processing. We thank the New Zealand Natural Hazards Platform and the Resilience to Natures Challenge support for funding this research through the respective research programs of “Quantifying exposure to specific and multiple volcanic hazards” and “Āhea riri ai ngā maunga puia? When will the volcanoes get angry?”.

CHAPTER 5

THE ROLE OF EDIFICE LOAD ON ANDESITIC MAGMA GENERATION BY MELT-MUSH MIXING AT TARANAKI VOLCANO, NEW ZEALAND

This chapter is going to be submitted to the Journal of Petrology as:

Aliz Zemeny, Georg F. Zellmer, Teresa Ubide, Ian E.M. Smith, Jonathan Procter, Al-Tamini Tapu, Anke V. Zernack (2021) The role of edifice load on andesitic magma generation by melt-mush mixing at Taranaki Volcano, New Zealand

Supplementary Data for this Chapter can be found in **Appendix B**.

Chapter Contributions:

- ◆ **Aliz Zemeny** (Massey University, New Zealand): Conceptualization, Sampling, Formal analysis, Investigation, Methodology, Resources, Supervision, Visualization, Writing (original draft), Writing (review & editing)
- ◆ **Georg F. Zellmer** (Massey University, New Zealand): Methodology, Visualization, Supervision, Writing (review & editing)
- ◆ **Teresa Ubide** (The University of Queensland, Australia) Formal analysis (EMPA), Resources, Supervision, Writing (review & editing)
- ◆ **Ian E.M. Smith** (The University of Auckland, New Zealand): Analysis valuation (LA-ICP-MS), Resources, Supervision, Writing (review & editing)
- ◆ **Jonathan Procter** (Massey University, New Zealand): Funding acquisition, Project administration, Resources, Supervision
- ◆ **Al-Tamini Tapu** (The University of Queensland, Australia): Formal analysis (EMPA), Data processing, Image production (BSE)
- ◆ **Anja Moebis** (Massey University, New Zealand): Introduction to the XRF analysis and assistance with sample preparation
- ◆ **Anke Zernack** (Massey University, New Zealand): Discussion on stratigraphy, Writing (proofreading)
- ◆ **Károly Németh** (Massey University, New Zealand): Writing (proofreading)

Abstract

Many andesitic stratovolcanoes are characterized by cycles of edifice growth interrupted by collapse events. The long-term record of the evolution of such magmatic systems is mainly preserved in the deposits of the volcanic apron surrounding the active cone. Taranaki Volcano in New Zealand provides an unusually detailed example of these processes due to excellent coastal ring-plain and young cone exposures. In this study, we investigate the magmatic system through three consecutive growth phases by sampling a detailed, stratigraphically controlled selection of volcanic clasts from volcanoclastic mass-flow deposits in the medial ring-plain. The clasts from three growth phases (GP1 – 65-55 ka; GP2 – 55-40 ka; GP3 – 40-34 ka) differ in bulk composition and form geochemically distinct trends on variation diagrams. These trends can be modelled by mixing of trachyandesitic melts and a mafic crystal mush illustrating cyclical melt-mush mixing processes throughout the growth-phases. The degree of melt-mush mixing varies within and between the GP units, and is responsible for variable bulk rock compositions. Chemostratigraphic variability within each growth cycle exhibits widening of compositional ranges over time. Thus, melt-mush mixing proportions in the mid- to upper-crustal reservoir become more variable with increasing edifice load indicating increasing subvolcanic magmatic activity. Overall, the data obtained from the Taranaki volcanic system elucidate the mid- to upper-crustal magmatic processes and reservoir conditions throughout growth cycles, demonstrating the top-down control of volcanic edifice loading on the magmatic plumbing system and the subvolcanic magmatic processes operating.

Keywords: Taranaki Volcano/Egmont, melt-mush mixing, andesitic magmatism, back-arc, edifice load, petrogenesis

5.1 Introduction

Magma generation in subduction zones is determined primarily by partial melting in the mantle wedge where primary mafic magmas are generated by a combination of addition of H₂O-rich liquids released from the subducted slab (Nichols and Ringwood, 1973; Ringwood, 1974; Hawkesworth et al., 1979; Gill, 1981; Arculus and Powell, 1986; Tatsumi et al., 1986; Davies and Stevenson, 1992; Tatsumi and Eggins, 1995; Schmidt and Poli, 1998; Ulmer, 2001; Grove et al., 2002; Forneris and Holloway, 2003; Gaetani and Grove, 2003; Grove et al., 2012; Zheng et al., 2016) and mantle decompression produced by subduction-induced corner flow (Sisson and Bronto, 1998; Elkins-Tanton et al., 2001; Hasegawa and Nakajima, 2004; Wiens et al., 2008; Marschall and Schumacher, 2012). Intermediate and silicic magmas in these environments are thought to be generated by three main processes: (i) In the crust or uppermost mantle by the differentiation of primary mafic magmas by crystal fractionation (Gill, 1981; Grove and Kinzler, 1986; Müsselwhite et al., 1989; Rogers and Hawkesworth, 1989; Müntener et al., 2001, Grove et al., 2002, 2003). (ii) Partial melting of older crustal rocks (Smith and Leeman, 1987; Atherton and Petford, 1993; Tepper et al., 1993; Rapp and Watson, 1995; Chappell and White, 2001). (iii) Silicic melt generation by the melting of silica-excess pyroxenite, which may be generated in the wedge through silica flux from the subducted slab (Straub et al., 2011). Additionally, crustal assimilation and mixing of melts and crystals from different sources (Grove et al., 1988, 1997; Müsselwhite et al., 1989; DePaolo et al., 1992) is the basis for the development of assimilation and fractional crystallization (AFC; DePaolo, 1981) and mixing, assimilation, storage and hybridization (MASH; Hildreth and Moorbath, 1988) models. The primary processes of magmatic evolution in arc volcanoes are thus crustal anatexis, magma mixing and crystal fractionation (Price et al., 2012; Lee and Bachmann, 2014) overprinting the compositions of primitive magmas produced by processes arising from the subduction of oceanic crust.

Fundamental to an understanding of the way that magmatic systems work is an examination of their temporal evolution on both short- and long-term scales. Variations in magma chemistry in andesitic volcanoes occur over a range of timescales in the evolution of an individual volcano (Newhall, 1979; Gill, 1981). The temporal magmatic behaviour of volcanoes in arc settings has been studied globally (Elburg and Foden, 1998; Gertisser and Keller, 2003; Reubi and Nicholls, 2004; Pearce and Stern, 2006; Rouchon et al., 2008; Oyan et al., 2016; Rawson et al., 2016). In this paper we examine in detail a

temporal window in the evolution of an atypical andesitic arc system, Taranaki Volcano in the western North Island, New Zealand.

To date, several studies have examined the evolution of magmatic systems during edifice growth, and the effects and connection to recurring cone/sector collapse events (Belousov et al., 1999; Capra and Macias, 2002; Petrone et al., 2009; Samaniego et al., 2012; Watt et al., 2012; Gorbach et al., 2013; Vezzoli et al., 2014; Cassidy et al., 2015; Day et al., 2015; Karstens et al., 2019; Watt, 2019, Watt et al., 2019). Research has highlighted that there is an intrinsic relationship between surface loading and the change or re-development of mid- to upper-crustal magma reservoirs and thus, a potential magmatic response to large-scale sector collapses along with the modification in eruption rate, style of eruption or geochemical compositions of the pre- and post-collapse eruptive products (Geist et al., 2002; Galipp et al., 2006; Carracedo et al., 2007; Longpre et al., 2009; Manconi et al., 2009; Boulesteix et al., 2012; Hildner et al., 2012; Cassidy et al., 2015; Tost et al., 2016).

Taranaki Volcano surmounts a young active andesitic magmatic system that has been investigated in some detail in recent times (Stewart et al., 1996; Price et al., 1999, 2016, 2020; Zernack et al., 2012b). The present study examines the behaviour and temporal evolution of the Taranaki Volcano magmatic system within the context of periodic growth cycles. For the investigation of edifice growth phases, lithic-dominated and pumice-dominated volcanoclastic mass-flow deposit material was collected, based on the well-characterized ring-plain stratigraphy of Taranaki Volcano (**Chapter 4**; Zernack et al., 2011) providing information on the magmatic system at depth.

5.2 Geological setting

The Pacific Plate is subducted beneath New Zealand's North Island (**Fig. 5.1 A**) into the mantle at the Hikurangi Trench with a depth of 100 km below Mt. Ruapehu (central part of North Island; Reyners et al., 2006; **Fig. 5.1 B**). Taranaki Volcano, is the southernmost and youngest member of the Taranaki Volcanic Lineament (TVL; **Fig. 5.1 B**; King and Thrasher, 1996; Neall, 1979; Neall et al., 1986; Neall, 2003) located about 400 km west of the trench, lying some 180 km behind the active volcanic front (Cole, 1982). It is c. 180 - 250 km above the Wadati–Benioff zone (Adams and Ware, 1977; Boddington et al., 2004; Reyners et al., 2006), situated on 25 – 35 km thick continental crust (Stern and Davey, 1987). Previous studies have identified a group of xenoliths

(gabbros and ultramafic hornblendites and hornblende pyroxenites) that are thought to have originated at or near the crust/mantle boundary (Gruender et al., 2010).

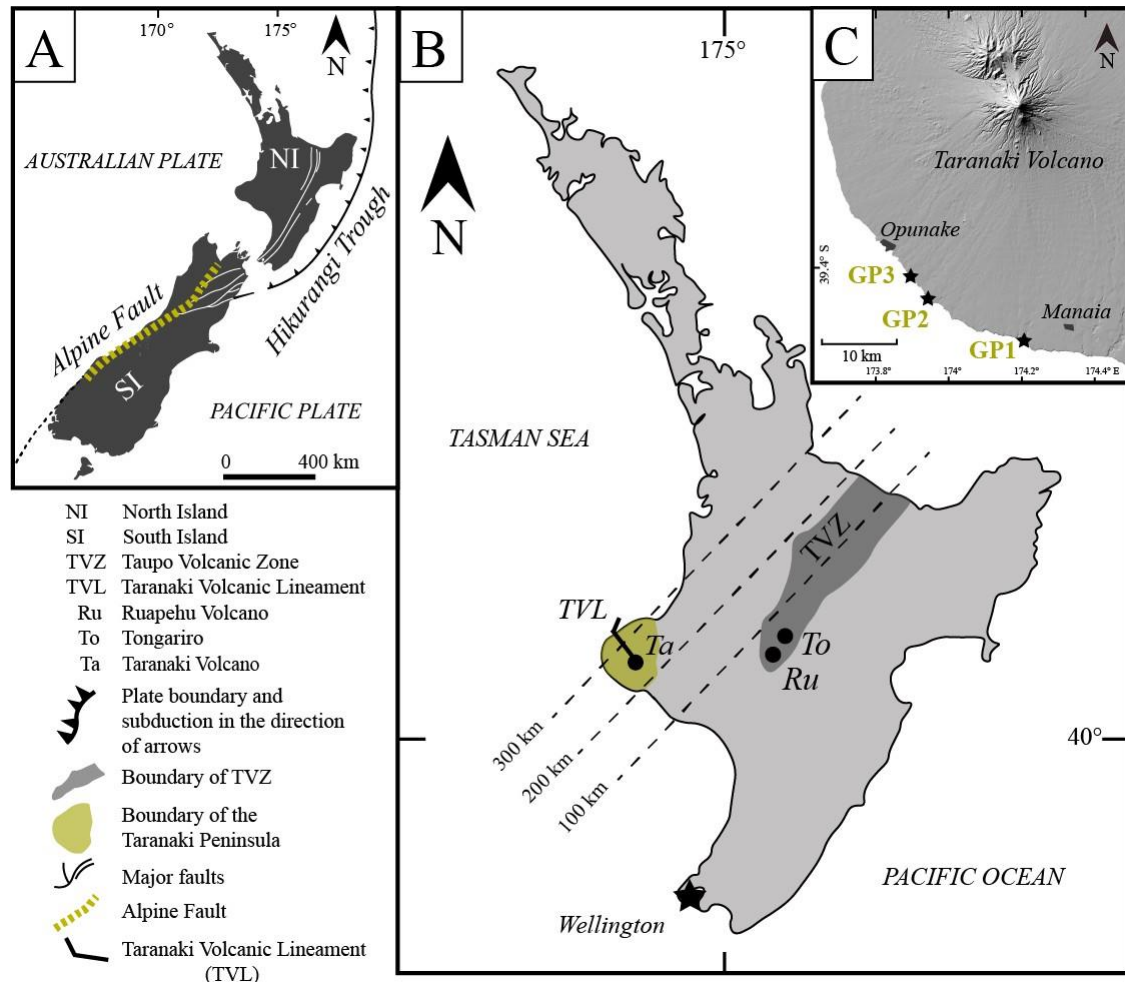


Fig. 5.1 **A:** Main tectonical settings of New Zealand. NI: North Island; SI: South Island. **B:** Location map of the Taranaki Volcanic Lineament (TVL) and Taranaki Volcano (Ta) on the North Island along with the Taupo Volcanic Zone (TVZ), Ruapehu (Ru) and Tongariro (To). Green shaded area indicates the Taranaki Region (or Taranaki Peninsula). The dashed lines indicate the depth of the subducting slab (Boddington et al., 2004; Reyners et al., 2006, 2011). **C:** South and south-western portion of the ring plain of Taranaki Volcano with the locations of the sampled mass-flow deposit sites (GP1, GP2, GP3).

The mid- to lower-crustal rocks at greater than 6–7 km depth belong to the Median Tectonic Zone and are composed of mafic hornfels, metagabbros and amphibolitic gneisses, whereas the lower part of the magmatic plumbing system is interpreted as gabbroic cumulates of Cretaceous age (Mortimer et al., 1997; Gruender et al., 2010). A xenolith suite preserved in rocks erupted from the volcano was investigated using the Al-in amphibole geobarometer (Hollister et al., 1987; Gruender et al., 2010), showing that

rocks of the Median tectonic zone lie between 12 - 7 km depth. Additionally, geophysical subvolcanic basement research (Sherburn and White, 2005; Sherburn and White, 2006) determined a zone of higher heat flow beneath the volcano extending from the lower crust at 25 km up to 10-7 km depth, which was described as a zone containing melt. The geophysical transition at 10-7 km depth also constrains the upper limit of magma assembly beneath the volcano (Sherburn and White, 2005). The transition between these and the approximately 6 km-thick overlying Pleistocene to Eocene sandstones and mudstones of the Taranaki Basin is clearly defined by various geophysical methods (Sherburn and White, 2006; Infante-Paez and Marfurt, 2017).

Volcanic activity at Taranaki started more than 130 ka ago (**Fig. 5.1 C**; Alloway et al., 1995, 2005). However, an earlier onset of volcanic activity of c. 200 ka was suggested by Zernack et al. (2011). The modern constructional edifice is composed of lavas and pyroclastic deposits that are younger than 14 ka (Neall, 1979; Turner et al., 2011). The cone is surrounded by an almost circular, volumetrically much larger ring-plain containing >150 km³ of volcanoclastic successions, characterised by debris-avalanche, mass-flow (hyperconcentrated flow, debris flow) and fluvial deposits (Neall et al., 1986; Procter et al., 2009; Zernack et al., 2011; Zernack, 2021). The southwestern ring-plain provides sedimentary records extending back to 100 kyr (**Fig. 5.1 C**; Neall, 1979; Palmer and Neall, 1991). At least 14 large collapse events occurred during the lifespan of Taranaki Volcano, represented by debris-avalanche deposits (DAD) within the ring-plain record, suggesting that one major sector collapse or slope failure occurred every 10 – 14 kyr (Zernack et al., 2011). Over the past four decades, the magmatic system beneath the volcano has been studied in terms of comparisons with other andesite volcanoes of the central North Island (Price et al., 1992, 1999, 2005; Stewart et al., 1996), and focussing on the lavas younger than 10 kyr along with the present-day cone (Price et al., 1992; Stewart et al., 1996; Platz et al., 2007a, b; Turner et al., 2008a), the overall debris-avalanche deposits tracing the temporal evolution of the 200 ka Taranaki system (Zernack et al., 2012b), the overall xenolith suite (Price et al., 2016) and the tephra record of the last <29 kyr (Damaschke et al., 2017a, b). In addition, recent study investigated the melt genesis at Pouakai Volcano in the light of the evolution of the TVL (Price et al., 2020).

5.3 Petrogenesis of Taranaki magmas: the development of petrogenetic models

Earlier studies developed magma generation and evolution models based on geochemical investigation of older pumice and rock clasts from debris avalanche

deposits, younger fall deposits, block-and-ash flow deposits and from lava flows. The earliest model was produced for high-K arc magmas at Taranaki Volcano by Stewart et al. (1996), emphasizing petrogenesis in three stages: (1) High-Al basaltic melts reacting with fractionated magmas and wall-rock mafic minerals. (2) Rising basaltic magmas melting amphibole in wall-rocks, generating K₂O-rich liquids that cause the temporal increase of potassium concentrations in magmas. (3) At shallow depths, the magma is stored and becomes zoned by melt segregation. The hydrous upper part constitutes of a fluid-rich 'cap' that fractionates amphibole, driving melt composition from andesitic to dacitic, thus triggering further the crystallization of plagioclase in the residual melt around xenocrysts and phenocrysts.

Later, a general model was constructed for the evolution of andesitic and rhyolitic magmatic systems that explained the reasons of differences and similarities between Taranaki and Ruapehu magmas (Price et al., 1999). They suggested that geochemical contrasts between these two systems originated through differences in slab contributions and mantle wedge depletion, resulting in distinct parental magma compositions. Evolutionary trends of the different parental magmas were thought to be controlled by differences in crustal thickness.

Further, Price et al. (2005), Gruender et al. (2010) and Zernack et al. (2012b) suggest that magmas feeding into the plumbing system were initially processed in a lower crustal "hot zone", a model that was developed by Annen and others (2006). This model is based on the concept of basaltic magma modification in the crust through a combination of fractional crystallisation (FC), combined with assimilation (AFC), and partial melting of lower crustal intrusive rocks. Repeated primitive melt intrusions into the lower crust create a small-scaled "hot-zone" (Annen et al., 2006) by raising the geothermal gradient, where mantle derived magmas are underplating and reactivating an evolving lower crust. As the hot zone matures, larger parts of the lower crust are melted, increasing interaction with fractionating primitive magmas over time, generating progressively more K-rich and LILE-enriched compositions.

Focusing particularly on young Taranaki eruptives, Turner et al. (2008a) further proposed a two-stage magmatic system of storage, crystallization and fractionation for the late-stage magmatic system (<10 ka). Recently, Price et al. (2016) examined xenoliths from Taranaki, concluding that crustal level processes, direct crustal input and their complexity played an important role throughout the generation of andesitic suites beneath

the volcano. They reconstructed a lithospheric cross-sectional model beneath Taranaki Volcano assuming that (i) primary basaltic magmas (originated from lithospheric and/or mantle sources) were underplated, stored in, and over time interacted with the lower crust forming a MASH (Hildreth and Moorbath, 1988) or a deep crustal “hot-zone” (Annen et al., 2006). (ii) The lower crustal wall rocks were melted, suffered assimilation, and the mantle-derived magmas experienced fractional crystallization, and (iii) over time, ascended to shallower depths building up a complex, multi-level magma storage and plumbing system (Gruender et al., 2010; Zernack et al., 2012b), which became progressively more fractionated, with more evolved magmas residing at shallower crustal levels beneath the volcano.

5.4 Stratigraphic background and sample selection

The southern and western sector of the Taranaki ring plain features deposits that represent collapse events (destruction phases) and mass-flow deposits that represent edifice construction (growth phases; Neall, 1979; Alloway et al., 2005; Zernack et al., 2009, Zernack, 2021). With no available outcrops at proximal sites, the coastal cliff successions at medial distances from the vent (25 – 30 km from the edifice) provide the only opportunity to explore the characteristics of older edifice growth cycles. Within the time span between 65 and 34 ka, three construction phases define the volcanic history of Taranaki Volcano. These are the Otakeho growth phase, in this study referred to as *GPI* (ca. 65-55 ka), the Rama growth phase (*GP2*; ca. 55-40 ka) and the Te Namu growth phase (*GP3*; ca. 40-34 ka; Zernack et al., 2009, 2011; **Chapter 4; Table 5.1**). Sampling for this study targeted as many pumice-dominated and lithic-dominated mass-flow deposit sequences within each growth cycle as possible (see **Appendix B3 for exact stratigraphic positions of the samples**; see sampling locations in **Fig. 5.1 C**) in order to obtain a record of the development and evolution of the magmatic system. However, not all of mass-flow deposits within the growth phases could be sampled and the exact stratigraphic position of three mass-flow packages are not as well-constrained as the remaining sequence. Thus, sampled clasts from these deposits are labelled as “GP2 or GP3”, as they might be part of either GP2 or GP3. Systematic sampling of hyperconcentrated flow deposits was limited to vesicular pyroclasts that represent the closest relationship to primary products within these rapidly remobilised volcanoclastic mass-flow deposits (**Chapter 4**).

<i>Debris-avalanche deposit</i>	<i>Debris-flow deposit</i>	<i>Other marker</i>	<i>Age (ka)</i>	<i>Direction of collapse</i>	<i>Calculated / estimated volume (km³)</i>	<i>Runout distance (km)</i>
<i>Te Namu</i>			34 ^a	<i>SW</i>	1.5 - 2	26+
		<i>Hihiwera Peat</i>	36.9-34.4 ^a			
	<i>Ihaia</i>		36.9 ^a	<i>SW</i>	0.1 - 0.2	25+
<i>Rama</i>			^b c. 45-40 ^a	<i>S</i>	4.5 - 5	34+
	<i>Young Kaupokonui</i>		c. 50-45 ^a	<i>S</i>	0.1 - 0.2	30+
<i>Otakeho</i>			^b c. 55-50 ^a	<i>S</i>	2 - 2.5	32+

^a Zernack et al. (2011), ^b Tinkler (2013)

Table 5.1 Stratigraphic overview of the time period c. 65-34 ka based on debris-avalanche and debris-flow deposits and an additional peat marker of the ring-plain succession of Taranaki Volcano (from Zernack et al., 2011; Tinkler, 2013). Age (ka) displays 10³ years before present including calibrated radiocarbon dates BP and chronostratigraphic estimates.

5.5 Analytical methods

5.5.1 Mineral geochemistry and groundmass composition

Electron Microprobe Analysis (EMPA; **Appendix B1**) was undertaken on prepared thick sections (ca. 50 - 100 µm) of the sampled volcanic rocks from the three investigated growth phases (GP1, GP2, GP3). Mineral chemical studies focussed on plagioclase, clinopyroxene, Fe-Ti oxide and hornblende phenocrysts, and on the groundmass, using a JEOL JXA 8200 electron microprobe equipped with five wavelength-dispersive spectrometer (WDS) at the Centre for Microscopy and Microanalysis (CMM) of University of Queensland, Brisbane, Australia. Analytical conditions were a fully focused beam (c. 2×2 µm interaction surface), accelerating voltage of 15 kV, a beam current of 15 nA and a counting time for all elements of 10 s on the peak and ±5 s on each of two background positions. Calibration standards were obtained on the energy spectrum at the analytical conditions using wollastonite (Si-TAP and Ca-PET), orthoclase (K-PET), albite (Na-TAP and Al-TAP), chromite (Fe-LIF and Cr-PET), spessartine garnet (Mn-LIF), Durango F-apatite (P-PET), rutile (Ti-PET), P140 olivine (Mg-TAP) and Ni-olivine (Ni-LIF). Precision for major elements ranges between 1 – 5% at an accuracy of 1 to 3%. Precision for minor elements displays 2 to 9% and accuracy of 4 to 13%. Secondary standards were measured to monitor accuracy using Springwater olivine, Kakanui augite, Lake Co feldspar, and VG2 glass. The ZAF method was used for matrix correction.

5.5.2 Whole-rock major element analysis

A total of 220 pieces of medium lapilli-sized (after Fisher, 1961), variably vesicular porphyritic clasts were collected during the field campaign. The volcanic rocks were selected visually based on their visible vesicularity and colour. The samples were cleaned in an ultrasonic bath and then prepared for major element analysis by X-Ray fluorescence

(XRF) spectroscopy (**Appendix B1**). The outer parts of the rocks were removed, and the central portions were first crushed in a jaw crusher and then milled to fine powders using a tungsten carbide ring mill. Trace element contamination occurring during the crushing procedure is negligible for Ta and Nb and is limited to W and Co (Roser et al., 2003; Martin et al., 2013). Powders were dried at 110°C for 2.5 hours and subsequently heated to 900°C for 2.5 – 3 hours to determine loss of ignition (LOI). For major oxide determination, X-ray flux (mixtures of lithium tetraborate: lithium metaborate in proportion 47:53 or 12:22) was added to the oxidized samples in a 10:1 ratio. Samples were then fused to produce glass discs using an XRF Scientific xrFuse 2 electrical furnace. XRF analysis of all samples employed a 1 kW Bruker Tiger S8 Series 2 WD-XRF spectrometer at Massey University in Palmerston North, New Zealand. Interference-corrected spectra intensities were converted to oxide concentrations using calibration curves consisting of natural standards closely approximating the mafic matrix of our samples. The long-term reproducibility of Oreas 24c reference material is better than ±1% relative (1 sigma) for all elements except MnO, for which it is better than ±1.5% relative.

5.5.3 Whole-rock trace element analysis

Trace element measurements were obtained on the fused XRF beads using a Resolution-SE Compact 193 nm excimer laser ablation (LA) system in tandem with an Agilent 8900 Inductively Coupled Plasma – Mass Spectrometer (ICP-MS) at Waikato University in Hamilton, New Zealand (**Appendix B1**). Analyses were conducted by pulsing the laser at 10 Hz with a 100 µm spot size and an energy density of 5 J/cm² for 45 seconds. Ultra-high purity helium was used as the carrier gas to deliver the ablated sample from the LA system to the ICP-MS. The ICP-MS was optimized to maximum sensitivity daily. Background counts (gas background, measured with the laser off) were collected for 30 seconds between samples. NIST (National Institute of Standards and Technology) glass standards (610, 612) were analysed every 10 spots to account for any instrument drift. The GeoReM database (<http://georem.mpch-mainz.gwdg.de/>; Jochum et al., 2005) was utilized for NIST glass values. Data processing was performed using Iolite (v3.32; Paton et al. 2011). Background counts were subtracted from the raw data and all data were standardised to NIST 612 glass. NIST 610 glass was applied as a secondary standard. Iolite used the SiO₂ whole-rock compositions measured by the XRF for internal

standardization. Repeat analyses of standard NIST610 indicate precision of better than 5% (RSD) and for most elements, accuracy is within 10% at the 95% confidence level.

5.6 Results

5.6.1 Petrography

The vesicular pyroclasts sampled from the pumice- and lithic-dominated hyperconcentrated flow deposits exhibit a wide range of vesicularity and colour. Most scoriaceous clasts display grey, dark grey, whereas pumiceous clasts exhibit white, light grey and rarely yellow colour. They show moderate vesicularity (9-32 vol%) or micro-vesicularity. Clasts display porphyritic, fluidal and seriate textures. The groundmass is mostly hypocrySTALLINE with high proportions of microphenocrysts (<300 μm). Phenocrysts range in size from 300 μm to 3 mm and proportions typically range from 35 to 65%, with most crystals exhibiting euhedral and subhedral faces. The most abundant mineral phase is plagioclase (45-76 % on average), followed by clinopyroxene (19-37 %), Fe-oxides (2-4 %), hornblende (1-25 %) and rarely orthopyroxene and/or olivine. The groundmass consists of glass, plagioclase, clinopyroxene and Fe-oxides. Glomerocryst assemblages (**Fig. 5.2 A, B**) are moderately common and they generally include clinopyroxene + Fe-oxides + plagioclase + hornblende or some combination of these phases. Phenocryst modal proportions for each growth phase are given in **Appendix B1**.

5.6.2 Mineral compositions

Mineral compositions of selected samples from the three GP units were investigated in detail. Samples were chosen based on their whole-rock silica content (see their whole-rock compositional data in **Appendix B1**), which was categorized as primitive ($\text{SiO}_2 < 52$ wt.%), transitional (SiO_2 between 52 – 57 wt.%) or evolved ($\text{SiO}_2 > 57$ wt.%). For representative analytical results of phenocrysts, see the complete dataset in the **Appendix B1**.

Plagioclase

Core compositions range between An_{44-91} , whereas rims show a broader range of An_{36-91} (**Fig. 5.3**). The most calcic compositions are present in cores (An_{85-91}) while the lowest An contents (An_{36-50}) can be found within rims, both appearing in samples of GP1 and GP3. Moreover, GP3 plagioclases display the broadest compositional range of rims and

cores (**Fig. 5.3**). Further, GP2 unit plagioclase cores mainly group into two trends: (a) An_{50-65} and (b) An_{80-91} , respectively (**Fig. 5.3**).

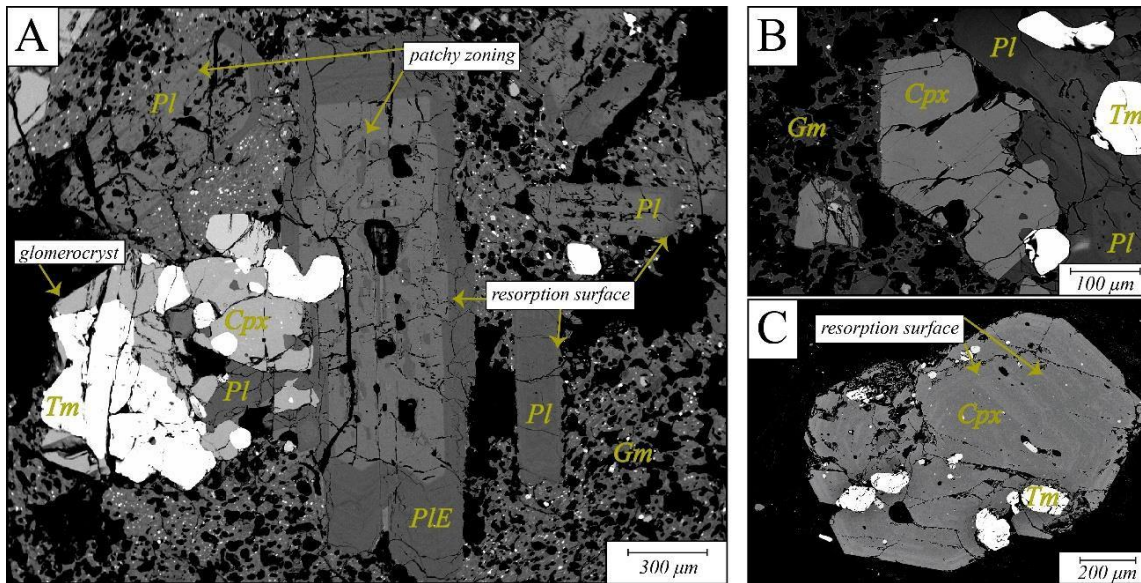


Fig. 5.2 **A:** Representative BSE image of an antecrystic, patchy zoned, resorbed plagioclase crystal (from GP2; sample *LB LHF5-6*; crystal *PIE*) interconnected with a glomerocryst consisting of titanomagnetite and clinopyroxene in a moderately vesicular microcrystalline groundmass. **B:** Glomerocryst consisting of clinopyroxene, plagioclase and titanomagnetite (from GP1; sample *KAUHF10-3*) emplaced within a moderately vesicular microcrystalline groundmass. **C:** Clinopyroxene antecryst exhibiting resorption surfaces and titanomagnetite inclusions (from GP2; *LBLHF2-10 16b*, crystal *PxA*). Gm: groundmass; Pl: plagioclase; Cpx: clinopyroxene; Tm: titanomagnetite.

Clinopyroxene

Clinopyroxenes of the GP units are dominated by augites and diopsides, with only two rims showing ferroaugite composition (**Fig. 5.4**). In general, compositions of analysed cores and rims display a range of $Wo_{25-50}En_{16-51}Fs_{10-46}$. The most magnesian contents (En_{49-51}) are present in rims of low-silica trachy-basaltic samples. The most ferrous compositions (Fs_{15-46}) appear in two rims of GP3 crystals. There are two clusters within the augite group of GP1. In general, GP1 cores and rims exhibit more dominant diopsidic compositions than those of GP2 and GP3.

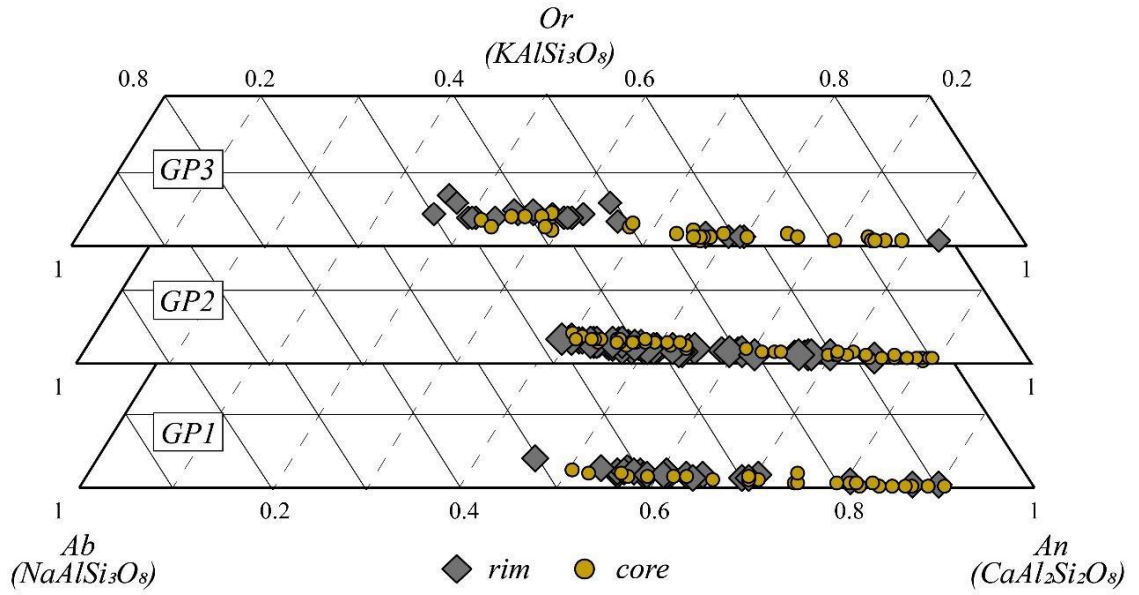


Fig. 5.3 Plagioclase core and rim compositions of the sampled Taranaki eruptives.

GP2 pyroxene rim contents display slightly broader values than those of GP1, of which pyroxenes partly are low-Ca augites (Fig. 5.4).

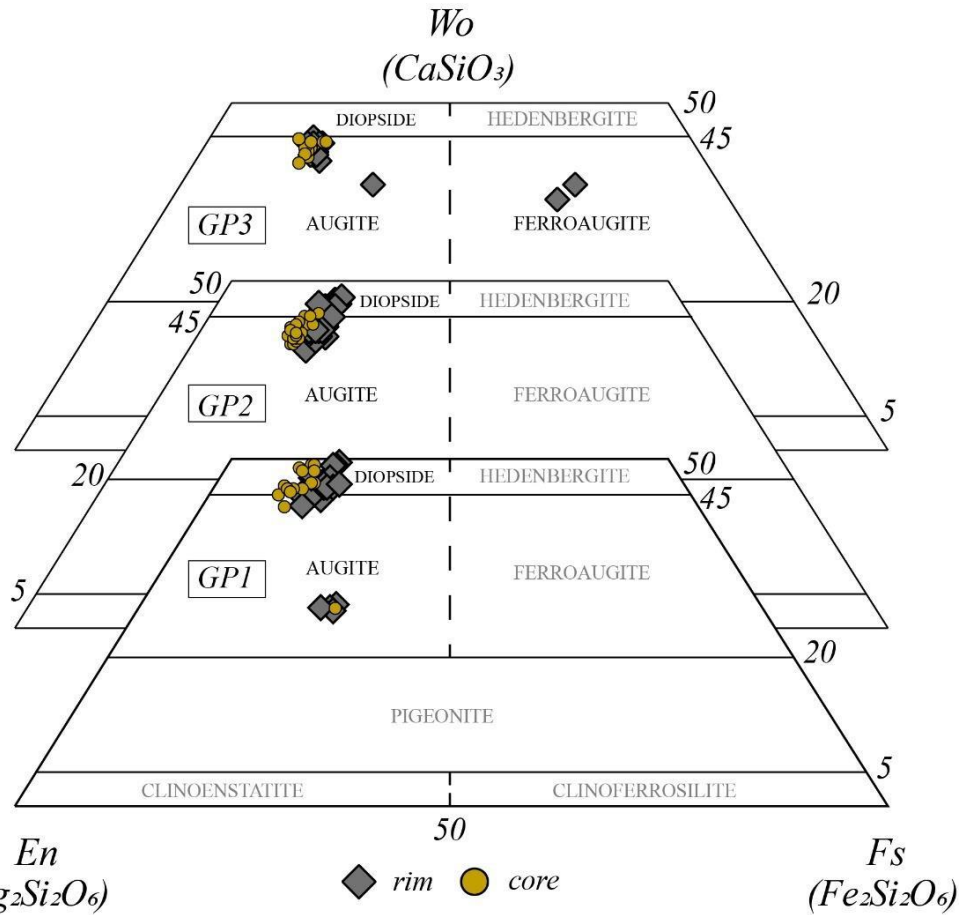


Fig. 5.4 Pyroxene compositional classification of the selected Taranaki eruptives.

5.6.3 Major and trace element geochemistry

In the classification of Le Bas et al. (1986), Taranaki rocks display basaltic, trachy-basaltic, basaltic trachy-andesitic and trachy-andesitic compositions on the TAS diagram with four sample plotting in the basaltic andesitic and one in the phono-tephritic region (**Fig. 5.5 A**). More than one third of the sampled rocks have basaltic compositions with variable K_2O wt.% concentrations. The analysed hyperconcentrated-flow clasts range in composition, using Gill's (1981) definitions, from medium-K, low-Si to high-K, high-Si basalts, trachy-basalts, basaltic trachy-andesites and trachy-andesites. The majority of samples plot in the fields of medium-K and high-K, low-Si basaltic trachy-andesites (**Fig. 5.5 B**).

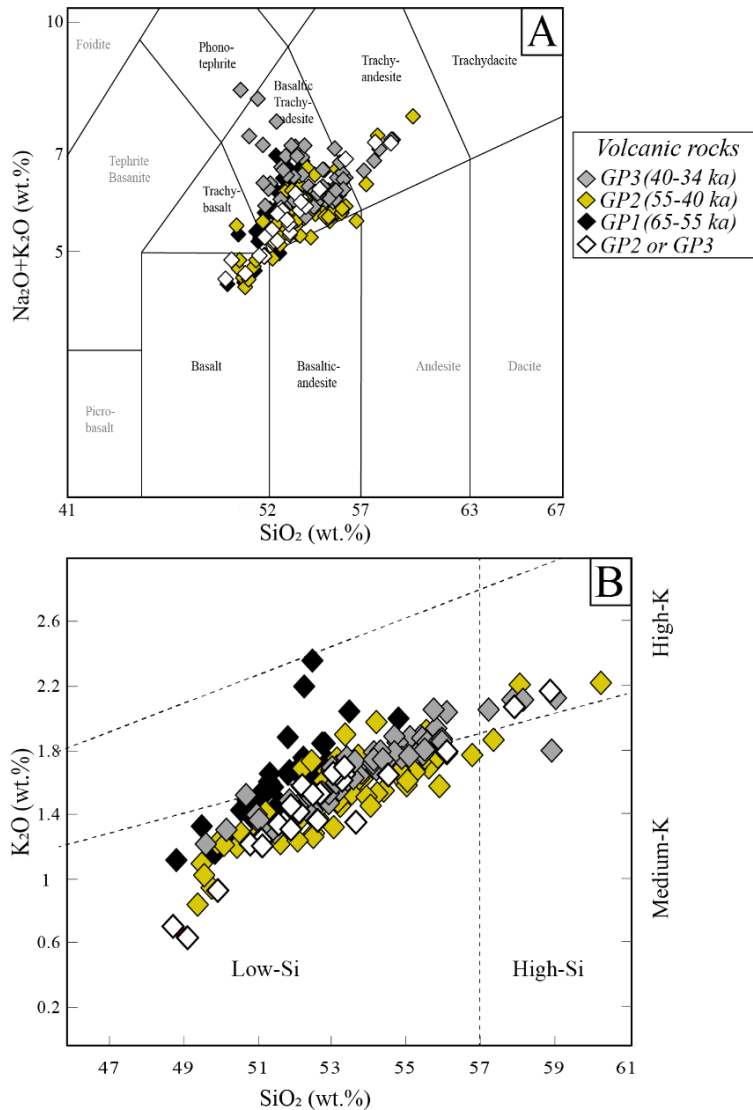


Fig. 5.5 A: Total alkali vs. silica classification representing the compositions of the volcanic rocks and groundmasses analysed by EMPA from the GP units. Nomenclature after Le Bas et al. (1986). **B:** K_2O vs. SiO_2 diagram following the classification of Gill (1981) for the mass flow deposit clasts from the three studied GP units.

Silica content varies from 49 wt.% for the most primitive to 60 wt.% for the most evolved rocks. All of the three chosen growth-phases (GP1, GP2, GP3 and the clasts of GP2 or GP3) display primitive compositions. However, the most primitive samples occur in GP1 and GP2. In general, GP2 and GP3 have higher proportions of andesite, which is accompanied by higher potassium contents. K₂O contents range from 0.6 wt.% to 2.3 wt.%. However, a temporal increase in K₂O, as described for the 200 kyr volcanic history (Zernack et al., 2012b), cannot be seen in the GP1 to GP3 sequence.

Selected major element variation diagrams are shown in **Fig. 5.6**. In general, MgO and CaO abundances decrease with increasing SiO₂ content, whereas Na₂O and K₂O (**Fig. 5.5 B**) values increase. However, major elements display different trends on the variation diagrams. Differences are most noticeable at low SiO₂ contents, namely in the case of CaO, MgO, Na₂O and Al₂O₃, which yield distinct trends towards endmember compositions. Moreover, at low SiO₂ contents (between 48 wt.% and 53 wt.%), Taranaki rocks represent a wide range of major element variability during edifice growths, independent of the time-period of the growth-phase. Three types of major element variations are observed, focusing on the most distinct unevolved melt compositions:

- (i) CaO and Na₂O contents show GP1 and GP2 plotting together and separately from GP3. In the case of CaO, GP1 and GP3 compositions are distinct while GP2 yields a wider range (8 – 10.5 CaO wt.%) at SiO₂ <53 wt.%. Na₂O contents at SiO₂ <53 wt.% show a wide range (from 3 to 6 wt.%), where GP3 values are the most variable and the highest concentrations (**Fig. 5.6**).
- (ii) Considering Al₂O₃ versus SiO₂, GP2 and GP3 plot together, sharing similar, higher Al₂O₃ values, distinct from GP1. Al₂O₃ wt.% abundances mirror two distinct trends at SiO₂ <53 wt.%, where GP1 compositions show low Al₂O₃ contents.
- (iii) For MgO versus SiO₂, all growth-phase units (GP1, GP2 and GP3) are to some extent distinguished showing individual clusters. MgO contents at SiO₂ <53 wt.% represent three distinct trends for the three different growth-phases, where GP2 has the lowest compositions (MgO <3.5 wt.%), GP1 the highest (MgO 3.1 - 6 wt.%) and GP3 displaying abundances in-between (MgO between 3 – 4.4 wt.%; **Fig. 5.6**).

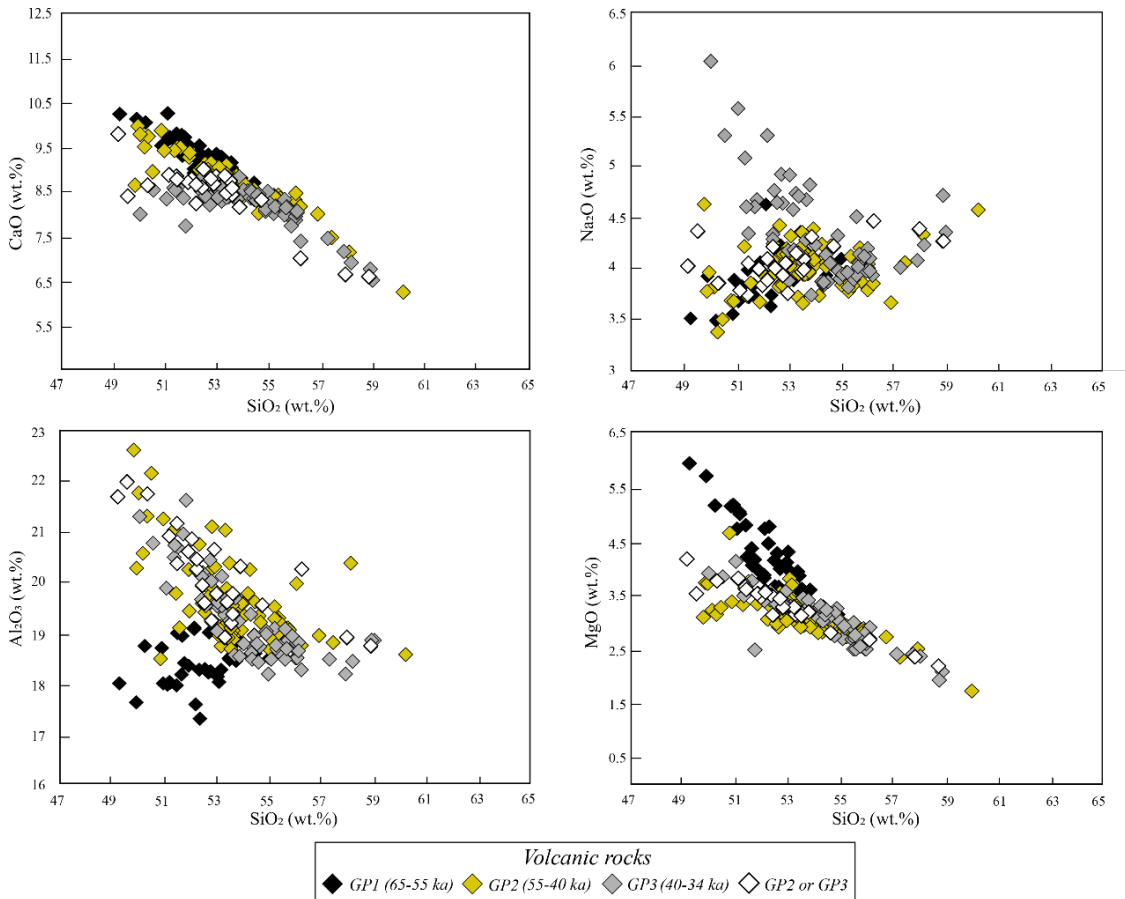


Fig. 5.6 Major element variation diagrams as a function of SiO_2 abundance (wt.%) for the analysed volcanic rocks of the Taranaki samples.

Trace element variability in comparison with SiO_2 is illustrated in **Fig. 5.7**. Again, showing three different variation patterns:

- (i) Vanadium versus SiO_2 has GP1 and GP2 plotting together, separately from GP3. Further, GP2 values are scattered, representing the widest range of vanadium abundance (**Fig. 5.7**). In general, vanadium abundances are negatively correlated with SiO_2 contents.
- (ii) Scandium, Zr and Rb vs. SiO_2 have GP2 and GP3 values clustering together, distinct from GP1. Zr abundances increase systematically with increasing SiO_2 content, with variation in these elements similar to that shown by K_2O . Hence, Zr values of GP2 and GP3 scatter at low (<53 wt.%) and high (>55 wt.%) SiO_2 , respectively. Abundance variability of Sc displays a systematic decrease with increasing SiO_2 , like the pattern shown by MgO, TiO_2 and FeO. GP1 values of Sc at less than 53 wt.% SiO_2 are scattered, producing a negative linear trend (**Fig. 5.7**).

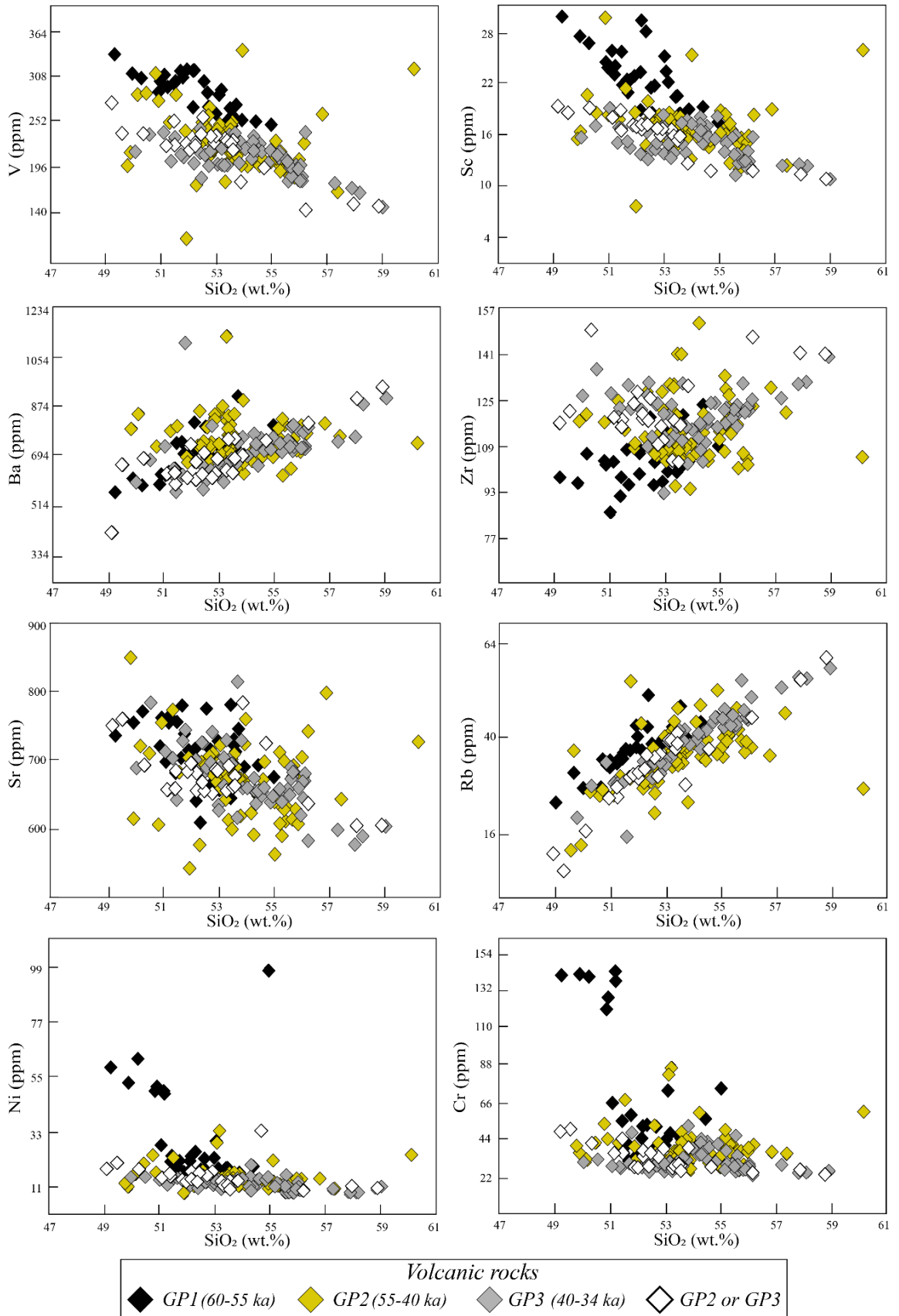


Fig. 5.7 Trace element variability (ppm) vs SiO₂ content (wt.%) of the sampled volcanic rocks from the GP units.

- (iii) Barium against SiO₂ has GP1 and GP3 clustering together, to some extent, separately from GP2. Ba contents of GP2 also indicate a wider range at low (<53 wt.%) SiO₂ (**Fig. 5.7**). However, Ba contents increase systematically with increasing SiO₂ content.

Nickel abundance is generally between 8 and 33 ppm, whereas Cr content ranges between 25 and 90 ppm (**Fig. 5.7**). Approximately 17% of GP1 samples display relatively high Ni (44 – 100 ppm) and Cr (120 – 150 ppm) compositions at low (<51.5 wt.%) SiO₂ abundances. In general, Ni and Cr compositions display a weak negative correlation with SiO₂ contents with the exception of GP1 samples with low silica abundances, for which Ni-Cr values are exceptionally high. However, Cr values are scattered at medium (52 – 54 wt.%) and low (<52 wt.%) SiO₂ abundances.

Primitive mantle normalized extended element patterns (**Fig. 5.8**) for the GP sample suites exhibit features characteristic of subduction-related volcanic rocks or continental crust (**Appendix B1**). These elemental patterns are expressed as enrichment of large ion lithophile elements (LILE) such as Ba, Rb and light rare earth elements (LREE) over heavy REE and Nb that is depleted relatively to K. Lead and, to a lesser extent, Sr is enriched relative to La and Ce. Samples of the GP units have scattered Rb abundances displaying narrower range over time. Lead abundances display a wide range, especially for GP1 and GP3 samples.

Chondrite-normalized REE patterns are characterized by enrichment in LREE relative to HREE, with (La/Yb)_n = 4.1 – 8.6 (**Fig. 5.8; Appendix B1**). GP2 samples exhibit the broadest REE elemental variations compared to GP3 with the narrowest compositional range. In general, samples are further characterised by moderately weak Eu anomalies (Eu/Eu* = 0.69-1.17; where Eu* is calculated as $Eu^* = \sqrt{Sm_N \cdot Gd_N}$). GP1 and GP3 samples display a narrower range (Eu/Eu* = 0.8-1), whereas GP2 exhibits a broader range of Eu/Eu* = 0.69-1.16. Positive Eu anomalies are rare but occur in all three GP units. The chondrite-normalized HREE abundances define a gentle decrease in normalized abundances from Gd to Ho and a relatively flat trace element profile from Er to Lu.

Groundmass

Representative analysis (i.e. random analysis obtained on the groundmass) of the groundmass glass in the collected GP samples display silica contents ranging from 62.9 to 65.9 wt.%, whereas compositions of glass inclusions in clinopyroxene and plagioclase

phenocrysts have bimodal composition of 47-54 and 64-67 wt.%, respectively. Al_2O_3 wt.% contents of groundmasses range between 16.8 – 27 wt.%, while melt inclusion Al_2O_3 wt.% compositions display a slightly wider range of 16.5 – 30.5 wt.% (see representative compositions in the **Appendix B1**).

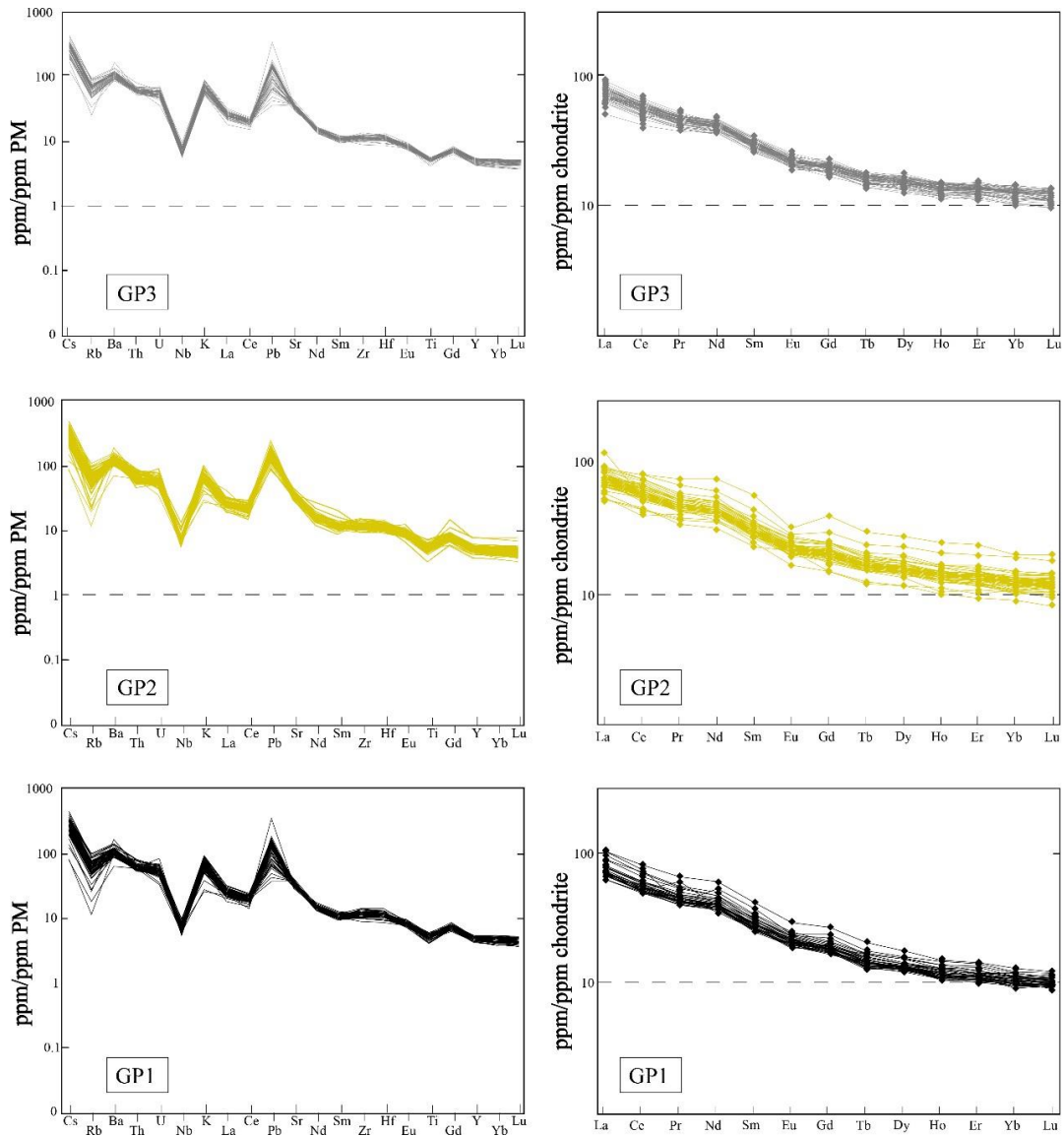


Fig. 5.8 Primitive mantle- (PM) and chondrite-normalized rare earth element patterns for volcanic rocks of the three studied growth cycles of Taranaki Volcano. Normalising values are from Sun and McDonough (1989).

5.6.4 Geochemical stratigraphy

GP1 samples were collected from pumice-dominated mass-flow deposits that are thought to represent one eruptive episode and thus, rapid successive mass-flow deposition over a short period of time with only a short break identified by the presence of reworked fluvial deposits within the sequence (see the sampled GP sequences in **Chapter 4**). Due

to this limitation, the time-dependent geochemical variability of this growth-phase cannot be determined. In contrast, GP2 and GP3 units offer several mass-flow sequences with interbedded paleosol accumulations providing an opportunity to examine the magmatic evolution during these periods of edifice growth in detail. Geochemical variation of the GP units in relation to the stratigraphy is presented in **Fig. 5.9**. On the basis of the geochemical variations (Section 6.3), the stratigraphically questionable mass-flow packages and their clast compositions have been assigned to GP2 (see question mark next to the mass-flow packages in the stratigraphic explanation in **Fig. 5.9**), thus are considered as older deposits than the Rama debris-avalanche deposits (DAD; ~40 ka; **Fig. 5.9**). Chemo-stratigraphic variability of the three studied growth-phases provides insights into the temporal changes in the magmatic evolution of the Taranaki volcanic system throughout several phases of edifice growth.

In general, there are significant differences between the GP units considering the temporal chemical variation of some elements. While GP1 displays the most primitive silica contents, all of the GP units have a variable range in SiO₂ wt.%. The chemical range of silica in the case of GP1 and GP2 increases throughout the strata, i.e. eruptives display more primitive and more evolved whole-rock compositions over time. GP3 overall shows a slight increase in SiO₂ wt.% over time (**Fig. 5.9**). In general, MgO and CaO, Fe₂O₃ (not shown) display the opposite patterns to those of the silica, while K₂O and total alkalis (not shown) mirror similar patterns. Al₂O₃ and Na₂O (not shown), the major oxides that are strongly partitioned into feldspars, exhibit dissimilar patterns to those of silica, with a remarkable difference in their concentration between GP1 and GP2/GP3 units (**Fig. 5.9**). The average Al₂O₃ contents of GP2 increase slightly, whereas as of GP3 decreases slightly over time. Incompatible trace elements such as Rb and Zr, REEs (not shown), display similar patterns to those in silica. Strontium and Ba (not shown), which partition strongly into feldspars, show a mirror image to the pattern of the SiO₂ and K₂O contents. Mg# of clinopyroxene rims in GP3 displays more mafic compositions, whereas in GP2 the Mg# range of cores and/or rims displays little variability. Anorthite contents of the plagioclase cores and rims exhibit broad, variable ranges. However, there is no particular link between stratigraphic position and Mg# or An content variability. Deposits display a shift to more primitive or evolved compositions following periods of quiescence as indicated by paleosol layers, however there is no link between chemical variability and breaks in volcanic activity.

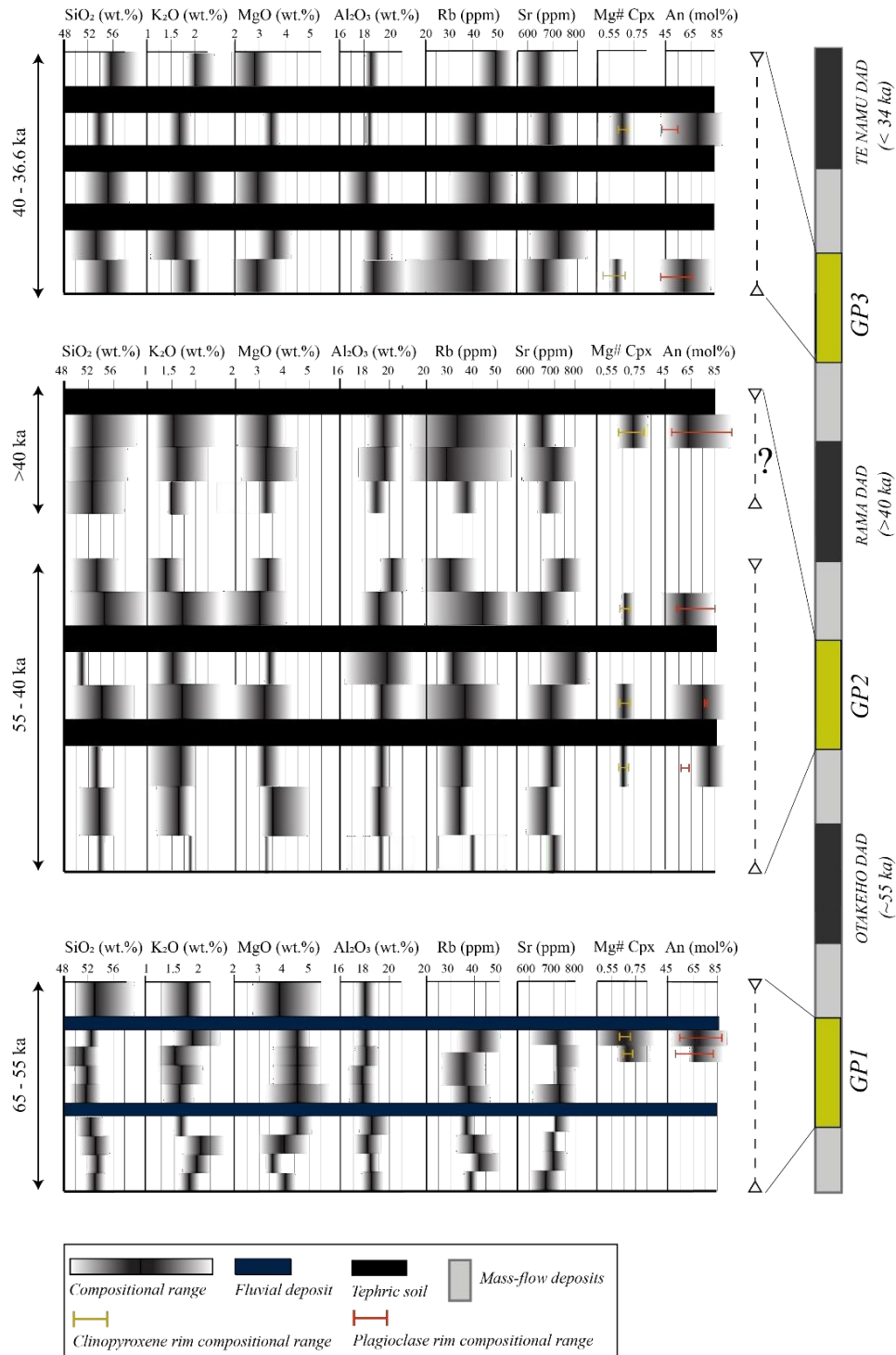


Fig. 5.9 Schematic illustration of the chemical stratigraphy of mass-flow packages within the time period c. 65-34 ka comprising the investigated three growth-phases (GP units) of Taranaki Volcano. Grey scales indicate the compositional variability of a measured element within a sampled mass-flow package. Mean values of element concentrations are indicated by the dark shades, whereas the lighter is the scale, the less frequent is the given composition. Note that the number of vesicular pyroclast samples of each mass-flow package is between 5 and 30, whereas the number of analysed crystals is between 5 and 20. Ages on the left of the stratigraphic columns are maxima based on the stratigraphic context of the sampled deposits. DAD marks the debris-avalanche deposits separating the GP sequences. It is important to note that the time between the deposition of the DADs and GP units cannot be determined, thus the right-side stratigraphic figure is presented for visualization purposes only, i.e. the thickness is not for scale. Question mark indicates the stratigraphically uncertain mass-flow packages and their selected clasts, that based on their major and trace element compositions ('GP2 or GP3' in Fig. 5, 6 and 7) were grouped to the GP2 sequence.

5.7 Discussion

5.7.1 The effect of edifice load on successive growth cycles

Several studies have investigated the possible relationships between pressurization, local stress and magma storage conditions beneath volcanic edifices using a range of analytical and numerical approaches (Pinel and Jaupart, 2000, 2003, 2005; Manconi et al., 2009; Pinel and Albino, 2013; Boudon et al., 2013; Roman and Jaupart, 2014; Karlstrom et al., 2015). On the other hand, petrological explorations have pointed out the complexity and variety of magma storage, transport and crystallization, thus emphasizing the concept of magma reservoirs that differs from the original concept and interpretation of a simple liquid magma chamber (Cashman and Blundy, 2013; Cashman et al., 2017). An edifice load establishes a departure from a lithostatic stress state in the underlying crust, the effect of which decreases with depth and becomes trivial at around three times the edifice radius (if the ratio of edifice radius to lithospheric elastic thickness is small; Pinel and Jaupart, 2005) resulting in its dominant effect on upper-crustal magma bodies in arc settings. Thus, the edifice load may affect the local stress field and influence magma chamber growth (Karlstrom, 2010; Gudmundsson, 2012) as well as aspects of dyke propagation (Pinel and Jaupart, 2000; Müller et al., 2001; Kervyn et al., 2009) and dyke formation (Pinel and Jaupart, 2005; Hurwitz et al., 2009; Roman and Jaupart, 2014), which are indispensable forerunners to eruption. Based on the analytical modelling of Pinel and Jaupart (2000, 2003), edifice growth is associated with an increasing eruption rate until a maximum rupture pressure (P_r) is reached, which then generates diminishing eruption rate subsequently (Pinel et al., 2010).

Considering the distinct growth cycles observed at Taranaki Volcano together with their mass-flow packages (**Fig. 5.9**), several compositional differences arise between individual cycles and individual eruptive periods. Such eruptive periods are represented by mass-flow packages separated by paleosol layers that formed during quiescence intervals. Statistically, the compositional shifts of individual eruptive periods are represented by the range and mean value of both the major and trace elemental compositions of the sampled vesicular pyroclasts (see average values and compositional ranges outlined in **Fig. 5.9**). Observations highlight that over time, the range in compositions increases in the case of GP1 and GP2. In the case of GP2, the depositional age range of three mass-flow packages are uncertain as illustrated in **Fig. 5.9** (indicated by question mark). Based on the chemical characteristics of these packages, they are

considered to be part of GP2. However, GP3 compositional ranges display an evolution towards more felsic compositions. In general, the ranges of SiO₂ content as well as K₂O and incompatible trace elements shift to higher values. The opposite can be observed in MgO, Al₂O₃ and compatible trace elemental compositions. Overall, there is no link between shifts in compositional range and quiescence intervals. However, compositional ranges widen over time, thus bulk rock compositions draw more primitive and more silicic chemical signatures towards the end a growth cycle, with the exception of the patterns displayed by GP3, which exhibit only more silicic temporal trend up through the growth cycle, while lacking more mafic endmembers. Within the time windows presented here, the data suggest that as the edifice rebuilds itself after a major collapse event, the upper-crustal reservoir exhibits broadening chemical variations during growth, as the edifice progresses closer to a subsequent sector collapse (**Fig. 5.9**). We suggest that the above chemostratigraphic compositional range broadening of the vesicular pyroclastic rocks may be the outcome of the edifice and reservoir co-development operating to affect the mid- to upper-crustal magmatic processes.

5.7.2 The 'mid-age' Taranaki magmatic system

Geochemical data from c. 65-34 kyr old volcanic clasts obtained from stratigraphically controlled medial volcanoclastic mass-flow sequences, that span a constrained stratigraphic interval, yields new insights into the periodic re-growth, eruptive and magmatic history of Taranaki Volcano. The compositionally variable porphyritic basalts, trachy-basalts, basaltic trachy-andesites and trachy-andesites exhibit complex resorbed surfaces of plagioclase and pyroxene crystals indicating non-equilibrium conditions (**Fig. 5.2 A, C**). Whole-rock major, minor and trace element variations of the individual GP units indicate different magmatic cycles in the individual growth-phases as indicated by different compositional trends on Harker diagrams (**Fig. 5.6** and **Fig. 5.7**). These chemical differences are mostly seen in the volcanic rocks of GP1, which comprises the most primitive, mafic compositions observed in major and trace elemental concentrations. Such chemical signatures of more mafic compositions have previously been interpreted to represent an increased supply of primitive, unmodified magma through the crust, without stalling or interaction with a more evolved, upper crustal reservoir (Stewart et al., 1996; Price et al., 2005; Gruender et al., 2010; Zernack et al., 2012b; Price et al., 2016). A mantle-derived primitive melt recharge control has also been adopted for the young

magmatic system of Taranaki Volcano by Turner et al. (2008a, 2011; The Curtis Ridge eruption episode, ~1800 yrs BP), at a time when the cone itself has already reached a pre-collapse state.

Additionally, the compositional chemical range of the analysed mass-flow sample suite shifted to more primitive compositions between 65-34 ka compared to the compositional trends of the older Taranaki rocks and the DAD clasts from the studied time period (Zernack et al., 2012b). The recognized chemical difference suggests distinctive geochemical features that are atypical of the older and younger Taranaki system. However, in contrast to the previous interpretative frameworks described above, the apparent compositional anomaly of the investigated Taranaki rocks will be shown (see **Section 5.7.3**) to imply that the more mafic GP whole-rock compositions are the outcome of an increase in the mush proportion relatively to the melt due to dominating magma-mush mixing processes.

5.7.3 Melt-phase interaction of Taranaki magmas

The new mass-flow samples analysed provide an opportunity to assess the main processes involved in the evolution of magmas throughout edifice re-growth cycles. For the investigation of processes such as magma mixing or FC-FCA-AFC (fractional crystallization; decoupled fractional crystallization and assimilation; and assimilation combined with fractional crystallization), the mixing equations after Powell (1984) were used in the modeler developed by Ersoy and Helvacı (2010). The relative ratio of assimilated material to crystallised material (r) and the “increments” value were chosen based on the arguments by Price et al. (2005, 2011, 2016). Two models were tested. For Model 1, an average value of the Median Batholith (MB), as the assimilant, was chosen after Price et al. (2016), as the representative composition for the plutonic rocks beneath Taranaki Volcano. Three basaltic ‘parental compositions’ have been used from the individual growth-phases, which represent primitive chemical concentrations. *KAUHF9-1* was sampled from a 65-55 ka pumice-dominated mass-flow deposit of GP1, while *LBLHF4-11* originates from a 55-40 ka lithic-dominated mass-flow deposit of GP2 and *TAULHF4-1* is a clast from a c. 40-36.9 ka lithic-dominated mass-flow deposit of GP3. The three basaltic samples show, to a certain extent a contrast in major (Al_2O_3 , Fe_2O_3 , MgO , K_2O) and trace elements (see **Appendix B1**). The calculated model could not

reproduce the trends expressed by the whole-rock compositions of the GP units (see parental, MB values in **Appendix B1** and modelling results in **Appendix B2**).

In the case of Model 2, modal phase proportion calculations of the basaltic volcanic rocks were used in order to estimate the melt (starting composition) and mush (assimilant) compositions of each growth cycle. This was accomplished by extracting the mineral and groundmass compositions from the whole-rock values of the three basaltic clasts mentioned above (see extracted mush and melt values of the GP units in **Appendix B1**). The computed mush concentrations exhibit primitive compositions of 47 – 47.7 SiO₂ wt.%, showing that throughout each growth cycle, these mushes were compositionally identical. The silica content of the GP unit groundmasses ranges between 56 and 58.5 wt.%, being compositionally similar during the growth phases. The calculated mush and melt compositions then have been attributed to the closest possible plutonic assimilants and rising melts from depth, respectively, playing an important role in the generation of the geochemical characteristics of the individual growth cycles. The results of the modelling are shown in **Fig. 5.10**. Additionally, calculated mush compositions are estimates for the assimilated material and might vary slightly due to (i) the diverse chemistry of mushes (or partly originating from the Median Batholith; see the variable compositional range of the Median Batholith in **Fig. 5.10**) and (ii) a variable proportion of mineral phases in the mush, allowing a minor degree of deviation in the generated slope of mixing lines (i.e. slightly variable compositional range of the mafic assimilant end-member).

Thus, the chemical signatures derived from mass-flow deposit clasts suggest an evolution controlled primarily by melt-mush mixing processes (e.g. Powell, 1984; Ersoy and Helvaci, 2010, Namur et al., 2020). The degree of mixing on average is between 20 – 65%, slightly varying within the individual growth cycles (GP1 25 – 65%; GP2 35-65%; GP3 10-60%). The overall results suggest that primarily trachyandesitic melts ascended from depth and upwelled into a primitive crystal cargo reservoir within the time-period 65-34 ka beneath Taranaki Volcano, where magma-mush mixing recycled compositionally primitive and discrete mush populations.

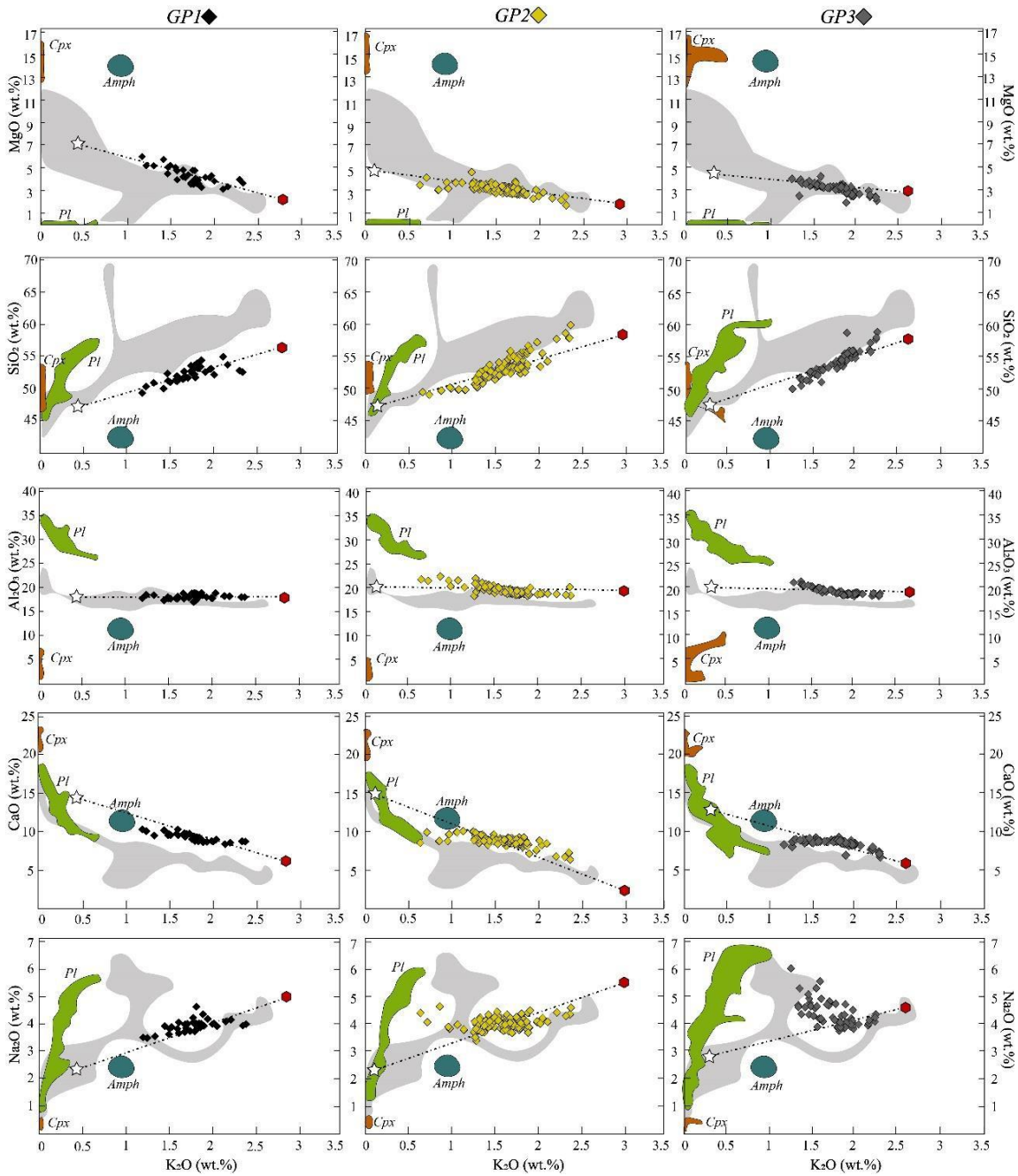


Fig. 5.10 Mixing modelling results of the GP sample suites represented by major element Harker diagrams. Red hexagon indicates the melt compositions, whereas white star represents the assimilated compositions in each plot. Dashed lines exhibit the mixing lines calculated by equations obtained from Powell (1984) and Ersoy and Helvaci (2010). Blue field represents amphibole compositions, orange field clinopyroxene compositions and green field plagioclase compositions. The grey shaded area highlights the Median Batholith compositions (gabbro, gabbro-diorite and diorite data from Mortimer et al., 1997; Price et al., 2011). Results are represented as the function of K_2O for better illustrative purposes.

Variable mixing proportions are seen within individual growth cycles, resulting in compositionally distinct volcanic rock suites. This is best shown by GP1 (*GP1*, **Fig. 5.10**), where whole-rock compositions display the most primitive compositions (**Fig. 5.6, 7**), leading to the conclusion that within the growth cycle GP1 (65-55 ka), the mush:melt

mixing proportion was on average higher than those of in GP2 and GP3 (see **Fig. 5.9** for additional mush:melt ratio stratigraphic variability). Accordingly, individual growth-phases exhibit different degrees of melt-mush mixing processes. This highlights the phenomena operating during the time-period of the mid-age Taranaki system (65-34 ka), trachyandesitic magmas were generated at depth and ascended to upper-crustal levels, where they remobilized an antecrystic (or in the case of the Median Batholith plutons, xenocrystic) mush zone. This is corroborated by the petrographic evidence of chemically complex, corroded or patchy-zoned, sieve-textured, partially resorbed plagioclase and clinopyroxene populations with variable melt inclusion compositions. These features are indicators of disequilibrium crystallization: such textures are the result of mixing processes (**Fig. 5.2**).

It has been proposed that conceivable outcomes of major collapse are the eruption of denser, less evolved magmas, or of magmas that exhibit signatures of a deeper, more mafic input (Manconi et al., 2009; Boulesteix et al., 2012) and a change in magma storage pressure (Rutherford and Devine, 2008; Pinel and Albino, 2013) as surface loading limits the ascent of denser mafic magmas inducing their stalling and storage in the upper crust (Pinel and Jaupart, 2004). Additionally, collapse events are accompanied by the reduction of magma chamber pressure (P_m ; Rutherford and Devine, 2008; Pinel and Albino, 2013), which triggers magma ascent from a deeper reservoir (Pinel et al., 2010). Consequently, sector collapse events are able to initiate heat and or volatile addition to the upper reservoir, which may lead to compositional changes in erupted magmas (Watt, 2019). Therefore, the dominant magma-modification process (i.e. magma-mush mixing) in each growth cycle may also be dependent, in addition to the edifice load factor, on the mantle-derived magma supply rate, which may then have contributed to the different degrees of mixing processes.

Overall, the calculated, dominantly intermediate ‘mid-age’ Taranaki melt compositions indicate that basaltic to trachyandesitic bulk rocks are generated by the incorporation of intermediate melts mixed with a compositionally primitive crystal cargo (amphibole, clinopyroxene, plagioclase) in mid-crustal magma reservoirs with the conceivable involvement of partially melted mid-crustal rocks (Stewart et al., 1996; Price et al., 2005; Reubi and Blundy, 2009; Stewart, 2010). In this case, some of these primitive, plutonic nodules may be part of the Median Batholith or represent other ancestral crystalline residues beneath Taranaki Volcano (Gruender et al., 2010; Price et al., 2011,

2016) or consanguineous plutonic precursors of the older Taranaki system. Their incorporation results from assimilation of plutonic rocks by ascending melts or incomplete separation of restitic fragments and residual melts during extraction from their source regions (Chappell and White, 2001; Dungan and Davidson, 2004).

5.7.4 Origin of the ascending intermediate melt

It is worth-while noting that mass-balance based estimations of matrix glass compositions have been more accurate compared to the conducted EMPA analysis, which gave higher values due to the presence of microlites within the groundmass (see description in Section 5.6.3). Representative Taranaki groundmass and melt inclusion analyses reveal basaltic and trachytic compositions (**Fig. 5.11**). Groundmass compositions display 56 – 58.5 SiO₂ wt.% based on the modal proportion calculations, whereas EMPA analysis yields 60 - 70 SiO₂ wt.%. Melt inclusions of plagioclase and clinopyroxene crystals display slightly broader ranges of 47 – 65 SiO₂ wt.% exhibiting bimodal, basaltic or trachytic melt compositions (**Fig. 5.11**). This is consistent with the conclusion made by Stewart (2010) that Quaternary andesite magma generation at Taranaki Volcano is the outcome of a complex interaction of magma-modification processes supported by the “hot zone” model (Annen et al., 2006) and the fact that andesites as liquids are unusual (Reubi and Blundy, 2009).

The representative melt inclusion data presented here supports the hypothesis that andesitic volcanoes contain dacitic to rhyolitic liquids (Reubi and Blundy, 2009). The majority of the melt inclusion compositions plot to the dacitic region, however, several inclusions plot in the basaltic field (**Fig. 5.11**). The mixing of these bimodal melt inclusion compositions may broadly explain the calculated trachyandesitic groundmass compositions of the mid-age Taranaki volcanic clasts (e.g. Cashman and Edmonds, 2019). Furthermore, melt inclusion compositions also corroborate to the conclusion supported by the Model 2 results (see section 7.3; **Fig. 5.10**) that the dominantly linear intermediate bulk-rock trends are mainly controlled by the incorporation of gabbroic crystal cargo into intermediate melts (for modelled mush and melt compositions, see **Appendix B1**).

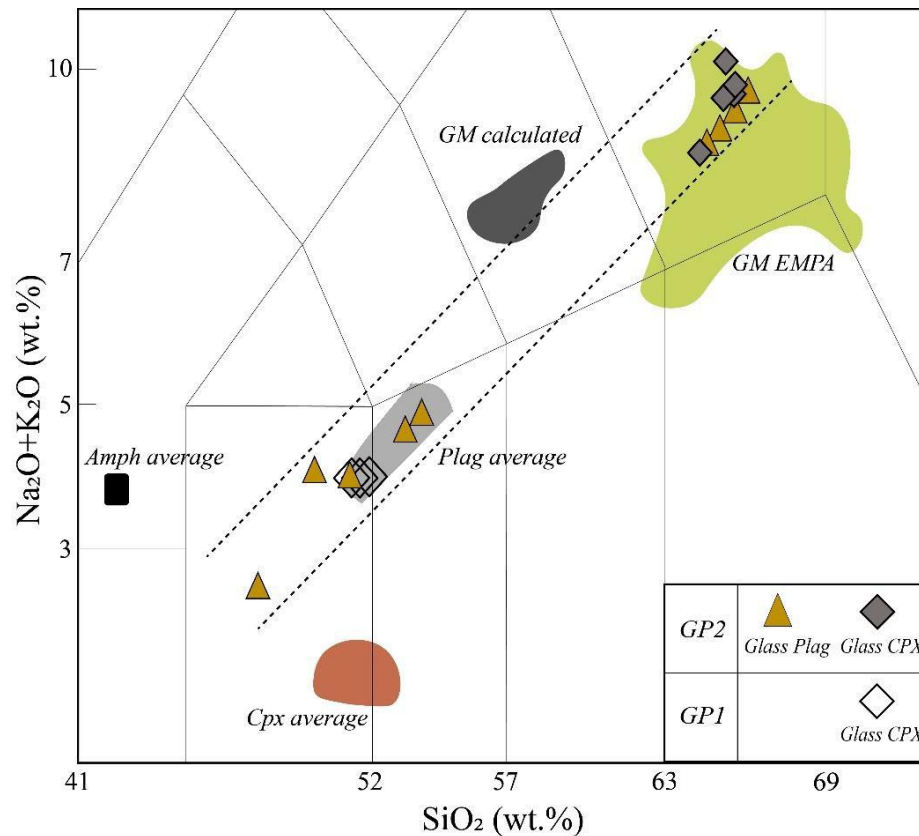
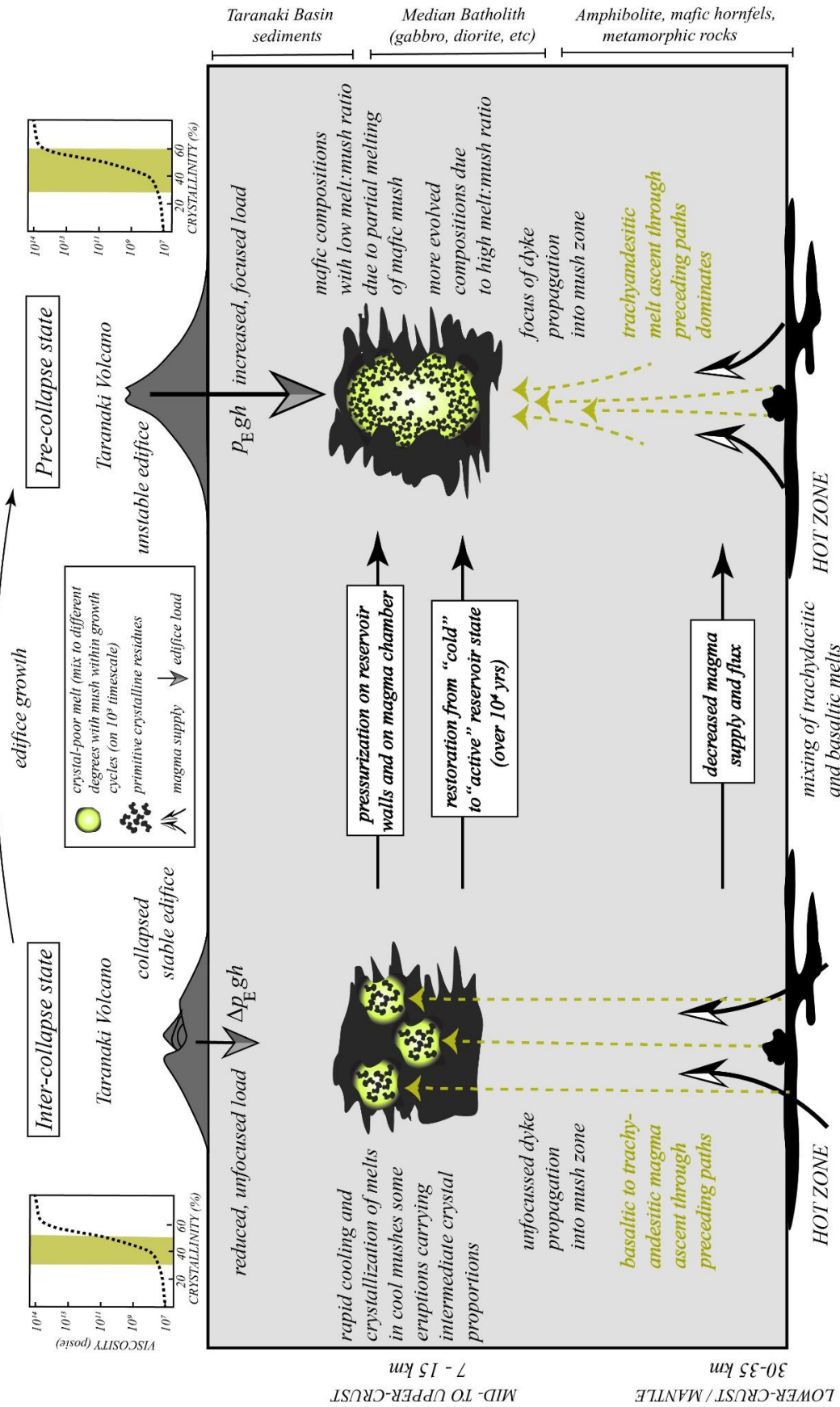


Fig. 5.11 Melt inclusion (clinopyroxene and plagioclase) and groundmass compositions measured by EMPA and groundmass compositions calculated by modal phase proportions of the GP sample suites represented by total alkalis as the function of SiO₂. Dashed lines indicate the possible compositional area of melt mixing. GM: Groundmass; Amph: Amphibole; Cpx: Clinopyroxene; Plag: Plagioclase.

5.7.5 Effects of edifice loading and unloading on the mid-age Taranaki plumbing system

The reduction in edifice load that accompanies edifice collapse generates a decrease in the magma chamber pressure and the stress on the reservoir walls (Pinel and Jaupart, 2005; Gudmundsson, 2012) favouring the ascent of higher density magmas. Over time, during a growth phase, the volcanic edifice establishes an increasing load at the surface modifying the stress field beneath. This results in the development of a density magma filter function affecting the petrological and thus, the chemical evolution of the mid- to upper- crustal magma reservoir (Pinel and Jaupart, 2000, 2005). An additional effect of the increasing edifice load over time is the focussing of magma transport beneath a volcano (Müller et al., 2001). The combination of these factors impacts the magmatic processes operating at mid- to shallow-crustal depths beneath a volcanic edifice, controlled by cyclic behaviour in arc settings (see Watt, 2019 and references therein).

The data of the present study provide insight into the andesitic magma evolution of Taranaki Volcano throughout three edifice growth cycles (65-34 ka), which are controlled by two main processes as visualized in **Fig. 5.12**:



◀**Fig. 5.12** Model of andesitic magma evolution and mid- to upper-crustal processes beneath Taranaki Volcano in relation to the influence of major collapse events. The “Inter-collapse” scenario is considered to follow a “post-collapse” end-member, as eruptives deposited immediately following collapse could not be sampled as part of this study. Edifice loading through time is building up to the pre-collapse scenario. The shaded area on the viscosity vs. crystallinity diagram (after Lejeune and Richet, 1995) indicates the viscosity range of the generated magmas at inter-collapse (crystallinity of sampled rocks between 35 – 60 vol%) and pre-collapse states. P_E : Edifice load from Watt (2019). Lower Crust – mantle boundary is from Sherburn and White (2005) and Stern et al. (2006). Rock types beneath the edifice after Mortimer et al. (1997), Gruender et al. (2010) and Price et al. (2011).

(i) Mid-crustal magma-mush mixing affected by depressurization

A deep-crustal hot zone (Stewart et al., 1996; Annen et al., 2006; Zernack et al., 2012b; Price et al., 2016) is generated by the interaction of mantle-derived magmas with the lower-crust, manifested as modification by fractional crystallization of new magmas, partial melting of previous intrusives and lower-crustal wall rock assimilation. Volcano collapse reduces edifice load and thus favours an increase in magma supply and magma flux from the lower-crust. Between 65-34 ka, the generated Taranaki trachyandesitic melts were likely mixtures of basaltic and trachy-dacitic primary melts (**Fig. 5.11**) supporting the phenomena of bimodal melt generation (Reubi and Blundy, 2009).

Volcano unloading depressurizes the upper-level storage system and affects its geometry, thus influencing the magmatic processes and crystallization conditions throughout edifice regrowth cycles. The reduced load following collapse leads to less focused magma ascent (Inter-collapse state; **Fig. 5.12**) and therefore to a colder, less active system directly below to vent, compared to pre-collapse when pressurization and dyke propagation is concentrated beneath the edifice (Müller et al., 2001). The produced intermediate melts enter the cool mush zone, where they crystallise rapidly, preventing crystal-poor melts from being erupted and limiting partial melting of the resident mush. Instead, new intermediate melts appear to mix with primitive crystalline residues within the ‘cold’ reservoir (on a $\sim 10^3$ year timescale; c.f. Watt, 2019 and references therein) and occasionally erupt. Mush-melt mixing ratios of eruptible melts are initially relatively invariable, resulting in magmas with c. 35-60% crystals and intermediate viscosity.

(ii) Mid-crustal magma-mush mixing response to edifice loading

Due to the gradual re-establishment of the volcano, melt transport is progressively focused beneath the growing edifice (Müller et al., 2001), initiating an increased influence of magma-modification processes (i.e. partial melting) within the reservoir. This contributes to a more significant mush remobilization within a more discrete, overall hotter plumbing system. Crystal-rich melts dominated by remobilized mafic mush may

thus erupt. On the other hand, erupted, more evolved compositions (i.e. magmas with high melt:mush ratio) are those that pass the upper crustal plumbing system with lesser assimilation of the mush, and do not crystallise rapidly due to the ambient heat of the active mush zone. This leads to more extended compositional ranges over time (**Fig. 5.9**) from inter-collapse state towards pre-collapse conditions, i.e. shifting to more evolved and more mafic endmembers. Progressive edifice growth and increased loading eventually promote more active upper-crustal processes over time (pre-collapse state; **Fig. 5.12**; on a $\sim 10^4$ year timescale; e.g. Watt, 2019). The increasing compositional range is thus seen as the outcome of the complex interplay between mid- to upper-crustal magmatic processes and the top-down physical effects of collapse events at Taranaki Volcano, manifesting as the resettling of the upper-level storage system over time (pre-collapse state; **Fig. 5.12**) expressed by the occurrence of more evolved erupted compositions (pre-collapse compositions of >53 SiO₂ wt.%), until the edifice reaches an unstable condition resulting in the next major collapse event.

5.7.6 Mid-age Taranaki in the context of the long-term evolution of its plumbing system

Based on the latest studies, Taranaki rocks exhibit a gradual evolution to more evolved and more potassic compositions over its ~ 200 kyr lifetime (Zernack et al., 2012b, Price et al., 2016). The accepted model for the Taranaki magmatic system postulates that repeated primitive melt injection into the lower crust generates a so-called “hot zone”, a model developed by Annen et al. (2006). Within this zone, mantle-derived magmas are trapped and modified by fractional crystallization and lower crustal wall rock assimilation processes. While the hot zone matures over time, significantly greater portions of the

lower crust are melted, generating progressively more K-rich and LILE-enriched compositional trends (Price et al., 2005; Gruender et al., 2010; Zernack et al., 2012b; Price et al., 2016). These magmas from the deep crust ascend to shallower depths and are initially stored in a multi-level magma storage system (Zernack et al., 2012b). Even though Taranaki Volcano is a well-studied edifice, the prehistoric volcanic record, and thus compositional information in particular of the older sequence is incomplete as the exposure of older deposits is limited due to periodic burial by collapse events and erosion/burial during growth-phases. Hence, it is not feasible to determine whether the unusually more mafic compositions of volcanics presented here are only characteristic within the studied time period (65-34 ka). We refer to the DAD clast chemistry of the

studied time span (65-34 ka) as ‘pre-collapse’ compositions as they represent the characteristic magmatic states prior to collapse. DAD clasts of the early Taranaki system (>105 ka; Okawa Fm. and >130 ka; Motunui Fm.; Zernack et al., 2012b) are referred to as “early system” and GP unit data are referred to as ‘inter-collapse’ compositions due to the uncertainty of the exact stratigraphical position of the sampled mass-flow deposits relatively to the following DAD deposit (e.g. collapse event) within the strata.

The comprehensive investigation of pre-collapse clasts (Zernack et al., 2012b) revealed different, more evolved compositions over the lifetime of Taranaki Volcano (**Fig. 5.13**), whereas the early-system DAD clasts show similar major element geochemical signatures to the GP clast compositions of this study (**Fig. 5.13**). However, there are significant compositional differences in trace elements between “early system” and “inter-collapse” magmas. As suggested by Zernack et al. (2012b), these oldest DAD clast assemblages might be the indicators of more primitive magmas that were able to ascend through the crust due to the absence of a well-developed upper-crustal reservoir exhibiting the early stage development of the Taranaki magmatic system. Therefore, there is an obvious connection between the early stages (>100 ka) and the mid-stages (65-34 ka) of the Taranaki magmatic system (**Fig. 5.13**), with the earlier expressed by the presence of a simpler and less active system and the absence of a dominant upper-crustal reservoir, but possibly contributing to the mafic mush zone involved in the compositional evolution of the mid-age system.

Overall, compositional trends indicate that pre-collapse magmas were further evolved by partial melting, fractional crystallization and mixing processes at shallow depths, superimposed on chemical signatures developed in the lower system (Smith et al., 1996; Stewart et al., 1996; Price et al., 1999; Turner et al., 2008a, b; Zernack et al., 2012b). In contrast, inter-collapse compositions seem to pass through the less active upper-crustal reservoir due to the edifice load and depressurization conditions after a major collapse. The dataset of the GP units presented here supports this hypothesis drawn from the chemical differences in magma compositions compared to the pre-collapse chemistry (**Fig. 5.13**). Pre- and inter-collapse rocks span different ranges in both major and trace element contents, where magmas of the GP units are more mafic than pre-collapse equivalents.

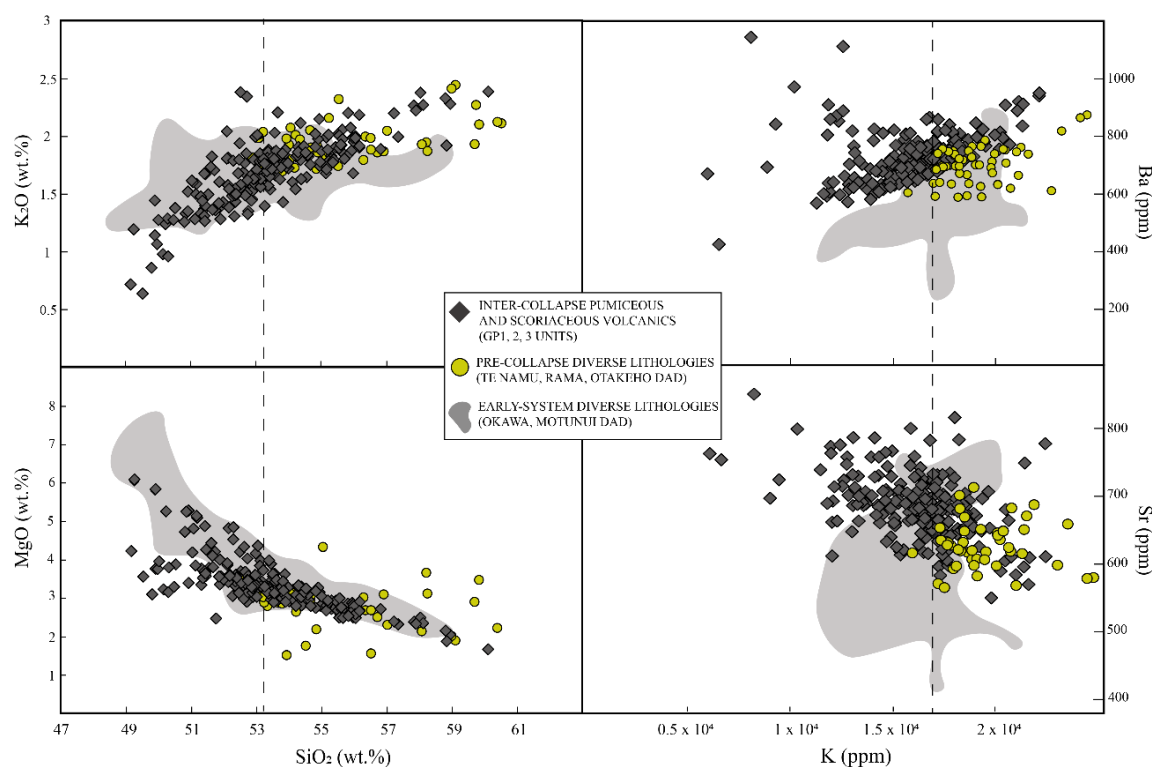


Fig. 5.13 Major and trace elemental comparison of inter-collapse (clasts of the GP units; 65-34 ka), pre-collapse (clasts of Te Namu DAD ~34 ka, Rama DAD ~40 ka and Otakeho DAD ~55 ka) and early-system (clasts of Okawa and Motunui DAD; >105 ka) compositions as a function of SiO₂ and K, respectively (pre-collapse and early-system composition data from Zernack et al., 2012b). Dashed lines indicate the SiO₂ (for major elements) and K (for trace elements) compositional boundary between pre- and inter-collapse chemistry.

However, there is a general overlap among pre- and inter-collapse (i.e. clast bulk rock compositions that are stratigraphically relatively closer to collapse) chemical compositions, with the majority ranging between ~53-57 SiO₂ wt.% (**Fig. 5.13**). This chemical range might be the indicator of the onset of a more active upper-level reservoir acting on the ascending magmas from mid-crustal depths.

5.8 Conclusions

1. The volcanic rocks of the mid-stage Taranaki system display basaltic to trachy-andesitic compositions. Variations in major and trace elements exist between the individual GP units. Mineral textural observations highlight the evidence of mixing expressed by antecrystic plagioclase and clinopyroxene resorption surfaces and partially resorbed cores.
2. Results using the model developed by Ersoy and Helvacı (2010) provide evidence of melt-mush mixing processes, where the mafic end-member is represented by a primitive mush (assimilant) and the felsic end-member by a

trachy-andesitic melt. The degree of melt-mush mixing (20 – 65%) and the assimilant compositions varied within individual growth-phases, resulting in the compositionally different bulk rock dataset.

3. Melt inclusion data reveal bimodal (basaltic or trachytic) melts possibly generated in the lower crust, which may be the source for the trachy-andesitic melts that ascended and mixed with the primitive mush.
4. Chemostratigraphic variability represents more mafic and more evolved compositional ranges over time, which are thought to be the outcome of variably mixed melt-mush ratios controlled by the co-development of edifice load and upper-crustal processes affected by major collapses.
5. The overall compositional difference between pre-collapse and inter-collapse volcanics are the result of the top-down control of edifice load operating on the “cold” upper-crustal reservoir over time, which then becomes more active leading to chemical diversification and thus, more mafic and more evolved compositions. This behaviour is seen to be cyclic through the frequently occurring edifice growth and collapse episodes at Taranaki Volcano.
6. Early-system (>105 ka) major element compositions are similar to the inter-collapse chemistry, suggesting the presence of a “colder”, less active mid- to upper-crustal reservoir in the early stage of the Taranaki system.

CHAPTER 6**MID-AGE TARANAKI ERUPTIVES (NEW ZEALAND) FED BY A COMPLEX
MAGMA PLUMBING SYSTEM: INSIGHTS FROM
GEO-THERMOBAROMETRY AND CRYSTAL ZONATION**

This chapter is planned to be subdivided into two articles and to be submitted to the Contributions of Mineralogy and Petrology journal and to the Geochimica et Cosmochimica Acta journal.

Supplementary Data for this Chapter can be found in **Appendix C**.

Chapter Contributions:

- ◆ **Aliz Zemeny** (Massey University, New Zealand): Conceptualization, Sampling, Formal analysis, Investigation, Methodology, Resources, Supervision, Visualization, Writing (original draft), Writing (review & editing)
- ◆ **Georg F. Zellmer** (Massey University, New Zealand): Methodology, Supervision, Writing (review & editing)
- ◆ **Teresa Ubide** (The University of Queensland, Australia) Methodology, Formal analysis (EMPA; LAICPMS), Resources, Supervision, Writing (review & editing)
- ◆ **John Caulfield** (The University of Queensland, Australia) Methodology, Formal analysis (LAICPMS), Resources, Supervision, Writing (review & editing)
- ◆ **Al-Tamini Tapu** (The University of Queensland, Australia): Formal analysis (EMPA), Data processing, Image production (BSE)
- ◆ **Jonathan Procter** (Massey University, New Zealand): Funding acquisition, Project administration, Resources, Supervision
- ◆ **Károly Németh** (Massey University, New Zealand): Writing (proofreading)

Abstract

Andesites are thought to be compound liquid-crystal mixtures of fractionated mantle basalts, evolved partial melts originating from the lower crust, underplated cumulates along with crustal recycled/cumulate crystals. Mid-age eruptives of individual growth phases (between c. 65-34 ka) from Taranaki Volcano are basaltic to trachyandesitic in composition. They consist of chemically and texturally complex mineral phases that are neither in equilibrium with their host whole-rock compositions nor trachyandesitic glass and trachytic or basaltic melt inclusions. Thus, their crystal cargo is considered to be of antecrystic origin. Thermobarometry and hygrometry modeling has been undertaken based on the mineral chemistry of clinopyroxenes, plagioclases and amphiboles, to determine crystal rim equilibration conditions and to constrain ascending melt and mush zone characteristics. Results suggest that within individual cone growth-phases, distinct melts ascended to different parts of the mid- to lower-crustal crystal-rich regions where they mixed with primitive cumulates. For the detailed investigation of mineral phases, the crystal pattern classification (CPC) method is developed, outlining the differences and similarities between different crystal regions and intra-crystal elemental distributions. Thermobarometry estimations exhibit clinopyroxene rim equilibration depths of 26-12 km outlining the mid- to lower-crustal regions. Hygrometry modeling revealed that individual growth cycles are characterised by melts with various water contents, possibly affecting the melt migration and crystallisation processes. Overall, chemical zonation patterns and textural complexities of the mineral phases indicate that Taranaki intermediate magmas are generated by melt-mush mixing involving multiple magma injection and crystal convection processes that modify the antecrystic cargo through time, while late-stage processes result in vertically extensive polybaric rim crystallization.

Keywords: Taranaki Volcano/Egmont, back-arc, crystal stratigraphy, geothermobarometry, crystal zonation, plumbing system

6.1 Introduction

Processes of crystallization and magmatic differentiation play an important role in understanding the nature of magmatic systems. In the early 20th century, fractional crystallization became widely accepted as the principal driver of magma differentiation based on the seminal work of Bowen (1928). Since then, several agents of magma differentiation beneath arc volcanoes have been identified, including magma mixing, crystal fractionation and crustal anatexis (Kent, 2010; Lee and Bachmann, 2014). As magma crystallises under a range of conditions (i.e. temperature, pressure, cooling rate, volatile contents), the main factors that influence magmatic evolution are temperature decrease (isobaric cooling or due to magma ascent into the cooler, upper crust), magma degassing (Brophy et al., 1999; Hawkesworth et al., 2000), and chemical modification during crustal assimilation and wall-rock assimilation or magma mixing (Grove et al., 1988, 1997; Müssewhite et al., 1989; DePaolo et al., 1992).

Volcanic plumbing systems are controlled by several dynamic processes including the progressive crystallization of parental magmas producing crystal mushes, magma - host / wall rock interactions, magma recharge into pre-established storage reservoirs, magma ascent to the surface, and eruptive events (Bachmann and Bergantz, 2008; Annen et al., 2015; Arienzo et al., 2016; Petrelli et al., 2018). These factors acting in a volcanic plumbing system result in a diverse environment where processes such as convection, resorption and crystal growth may be operating at the same time (Ruprecht and Wörner, 2007). The compositions and textures of minerals document these physiochemical conditions and processes occurring within magmatic systems (Vance, 1965; Meyer and Shibata, 1990; Ginibre et al., 2002; Pan and Batiza, 2002; Pietranik et al., 2006; Ridley et al., 2006; Ginibre and Wörner, 2007; Hellevang and Pedersen, 2008; Viccaro et al., 2010; Cashman and Blundy, 2013; Neave et al., 2014; Bouvet de Maisonneuve et al., 2016; Shane and Coote, 2018; Bennett et al., 2019). The currently estimated intrusive:extrusive magmatism ratios within magma plumbing systems in subduction zones are high ranging between 10:1 to 2:1 (White et al., 2006). Subsequent studies (Zellmer et al., 2019) also stressed that the present-day approximations are underestimated on regional scales, as these ratios might vary significantly through time. Thus, plutonism might be a significantly more dominant process in subduction settings than it was previously assumed and therefore, the nature of plumbing systems of individual arc volcanoes may be strongly affected by this phenomenon.

Compositional zonations in igneous minerals provide insights into the dynamics of the magmatic plumbing system leading up to volcanic eruptions (Davidson et al., 2007; Putirka, 2008; Costa and Morgan, 2010; Ganne et al., 2018; Ubide and Kamber, 2018; Ubide et al., 2019). Investigating the textural and chemical variations within crystals thus may provide decisive information on pre-eruptive processes, and the development and construction of the magmatic system (Blundy and Cashman, 2008). Moreover, crystal zonations may provide insights into magma mixing, differentiation, timescales of magma ascent, and magmatic volatile contents (Humphreys et al., 2006; Blundy and Cashman, 2008; Arienzo et al., 2010; Masotta et al., 2013; Ubide et al., 2014; Ubide and Kamber, 2018).

Clinopyroxene is a suitable mineral phase to discover pre-eruptive processes as it is characterised by relatively slow lattice or elemental diffusion (Van Orman et al., 2001; Costa and Morgan, 2011; Mueller et al., 2013) holding a prolonged record of magmatic histories and dynamic processes (Ubide and Kamber, 2018). Clinopyroxenes provide the ability to track recharge events of mafic magma into plumbing systems (through enrichment in MgO and transition-metals), to constrain the effectiveness of magma recharge as an eruption trigger and to calculate typical time windows from recharge to eruption (Ubide and Kamber, 2018; Petrone et al., 2018). Further, clinopyroxenes are common early crystallizing minerals in basaltic to intermediate magmas across a wide range of pressures and water contents (Armienti et al., 2007, 2013; Putirka, 2008) and their compositions are sensitive to pressure, temperature, water content and magma composition (e.g. Putirka, 2008; Perinelli et al., 2016; Mollo et al., 2015a, b; 2018). Therefore, they are also capable of providing estimates of crystallization conditions.

Further, the potential of plagioclase feldspars has long been recognized (Blundy and Shimizu, 1991; Singer et al., 1995; Tepley et al., 2000; Ginibre et al., 2002), because they are useful magmatic recorders as an abundant phase in a wide range of geotectonic settings including arc systems (Ginibre et al., 2002; Cashman and Blundy, 2013). In andesitic systems, the compositional and textural complexity of plagioclase crystals and their occurrence in volcanic rocks are well-documented due to their potential to crystallise over a wide range of magmatic conditions, which provides the opportunity to use them as tools in order to predict and determine magmatic storage, ascent rates and eruptive processes (Singer et al., 1995; Tepley et al., 2000; Stewart and Fowler, 2001; Couch et al., 2003; Zellmer et al., 2003; Landi et al., 2004; Blundy et al., 2006; Ginibre and Wörner,

2007; Ruprecht and Wörner, 2007; Shea and Hammer, 2013). Further, plagioclase crystals are characterized by slow major elemental diffusion rates preserving the magmatic conditions during the growth of the crystal. The slow inter-diffusion of CaAl – NaSi prevents equilibration of adjacent compositional zones (Morse, 1984; Holland and Powell, 1992). Therefore, this slow diffusion preserves textures over long timescales, providing an observable record of the processes operating within the magmatic system.

The present study focuses on the possible effects of edifice growth phases of Taranaki Volcano on its magmatic plumbing system through an investigation of the crystal cargo of samples deposited between c. 65-34 ka, a time-period here referred to as the ‘mid-age’ Taranaki system (see **Chapter 5** for further details). Taranaki Volcano provides mass-flow deposits within its volcanic apron, developed during edifice building phases terminated by edifice collapse events. Therefore, the nature of the magmatic system and its behaviour along with the characterisation of the crystal mush can be unravelled in detail by exploring the eruptive material from unique mass-flow deposits. Clinopyroxene and plagioclase phenocrysts of basaltic, basaltic-andesitic and basaltic trachy-andesitic rocks from these lithic- and pumice-dominated mass-flow deposits are suitable for this challenge as their phenocrysts provide repository of information on the magmatic histories of the studied ‘mid-age’ Taranaki magmatic and plumbing system.

6.2. Geological background

The Pacific Plate is subducted under North Island (New Zealand) into the mantle with a depth of 100 km below the approximately 40 km thick continental crust beneath Mt. Ruapehu (Reyners et al., 2006). Beneath the Taranaki Peninsula (western part of North Island; **Fig. 6.1 A**), the depth to the top of the subducting slab is c. 250 km (Boddington et al., 2004; Reyners et al., 2006). The Taranaki Region (or Taranaki Peninsula) is the onshore component of the Taranaki Basin, consisting of Cenozoic sedimentary rocks, including coal, limestone, silt- and sandstone, covered by volcanoclastic deposits of the Taranaki Volcanic Lineament (TVL) that trends northwest-southeast (**Fig. 6.1 B**; King and Thrasher, 1996; Neall, 1979; Neall et al., 1986; Neall, 2003). TVL volcanoes are located about 400 km west of the trench, c. 250 km above the Wadati–Benioff zone (Adams and Ware, 1977; Boddington et al., 2004; Reyners et al., 2006) and overlie 25 – 35 km thick continental crust (Stern, 1987). Taranaki Volcano (2518 m) is an andesitic atypical arc stratovolcano, the southernmost and youngest member of the TVL, which is

an expression of the Quaternary volcanism in the western part of the North-Island (**Fig. 6.1 B**).

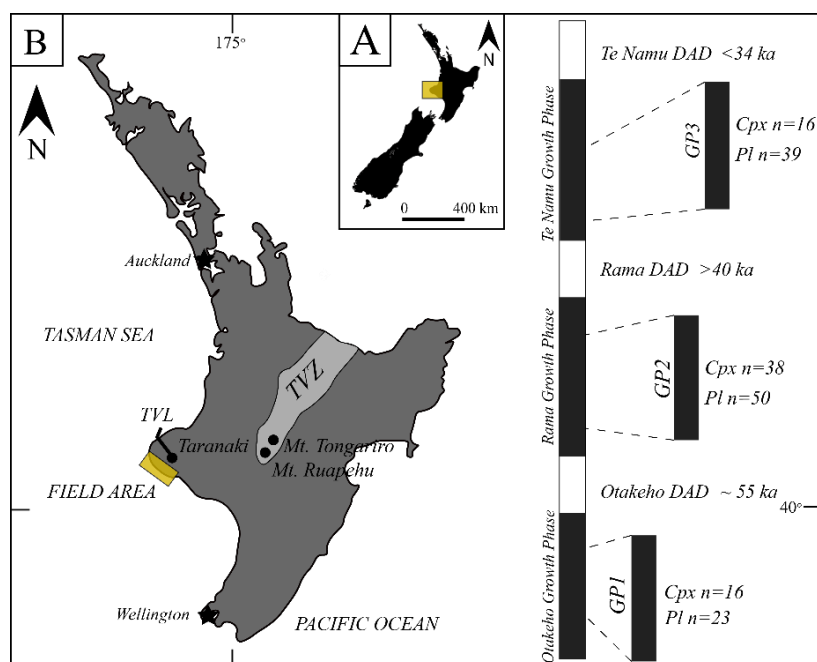


Fig. 6.1 A: Map of New Zealand indicating the Taranaki Peninsula (yellow rectangle) as the focus area of the study. **B:** The North Island indicating the Taupo Volcanic Zone (TVZ), the Taranaki Volcanic Lineament (TVL) and the location of the field area (yellow rectangle) within the south and southwestern part of the ring plain. Stratigraphic context of the three investigated growth-phases (GP) is represented with the illustrative position of the sampled GP sites along with the investigated number of clinopyroxene (Cpx) and plagioclase (Pl) crystals. The debris-avalanche deposits are indicated in-between the growth cycles (DAD) outlining the collapse events within the time period 65-34 ka.

The modern Taranaki edifice is an almost perfectly shaped cone made up of lavas and pyroclastic deposits younger than 14 ka (Neall, 1979; Turner et al., 2011), where the last known eruption occurred between 1785 and 1860 A.D. (Platz et al., 2012). The eruption history of the present-day cone (Neall et al., 1986) is represented by sub-Plinian eruptions with intercalated effusive events (Alloway et al., 1995) comprising alternating layers of pyroxene-andesite and hornblende-andesite lavas and fragmental volcanic deposits including tephra-fall units, scoria-rich pyroclastic-flow deposits and juvenile-lithic-rich block-and-ash-flow deposits. The cone is enclosed by $> 150 \text{ km}^3$ volcanic apron, characterised by debris avalanche and volcanoclastic mass flow deposits and fluvial materials (Neall et al., 1986; Procter et al., 2009; Zernack et al., 2009, 2011) surrounding the edifice and covering an area of nearly 1000 km^2 . The eruptive products within the ring-plain record more than 90% of the volcanic history of Taranaki Volcano (Neall,

1979; Neall et al., 1986), where the oldest materials are estimated to have been deposited c. 200 ka ago (Zernack et al., 2011).

6.3. Petrology of Taranaki rocks

Geochemically, Taranaki eruptives are classified as high-K, low-Si andesites (Gill, 1981). Over time, Taranaki magmas become progressively enriched in potassium and silica (Stewart et al., 1996; Price et al., 1999, 2005, 2016) and are highly evolved based on their low Mg# (<53) and low whole-rock Cr and Ni contents (Price et al., 1999). Trace elements are characterised by significant enrichment of large ion lithophile elements (LILE; e.g. Rb, Sr, Cs, Ba) and light rare elements (LREE) compared to high field strength elements (HFSE; e.g. Ta, Nb, Zr; Price et al., 1992, 1999, 2007).

Lavas from the young cone and clasts from debris-avalanche deposits are mostly hornblende-bearing high-K, porphyritic (25 – 55% phenocrysts) basaltic andesites (Neall et al., 1986; Stewart et al., 1996; Price et al., 1999; Zernack et al., 2012b) that are dominated by plagioclase with lesser amount of clinopyroxene and amphibole. Taranaki rocks have trace element characteristics typical of subduction-related igneous rocks (Keleman et al., 2005) or continental-crust (Rudnick and Gao, 2005), represented by (1) enrichment of Rb, K and light rare earth elements (LREE) relative to Zr, Y and heavy rare elements (HREE); (2) depletion of Nb relative to K and La, and (3) enrichment of Pb and Sr relative to Ce (Price et al., 1999; Zernack et al., 2012b). These signatures are considered as characteristic features of low-degree partial melts of a depleted mantle (Price et al., 1999).

Taranaki andesites vary from 46-60 wt.% SiO₂ (Graham et al., 1995) displaying coherent trends of decreasing MgO, FeO, CaO and increasing K₂O and Na₂O with increasing silica content. Al₂O₃ shows initial increase up to 57 wt.% silica, then decreases due to plagioclase crystallization at shallow depths (Price et al., 2005). Although these trends have been taken to indicate crystal fractionation and accumulation (Gamble et al., 1990), trace element variations, xenolith compositions, olivine and amphibole mineral chemistry, along with the melt inclusion chemistry suggest a more complex interplay of and a range of petrogenetic processes (Graham et al., 1995; Stewart et al., 1996; Platz et al., 2007a; Turner et al., 2008a, b; Gruender et al., 2010; Stewart, 2010; Price et al., 2016).

Based on the collaborative studies of Taranaki Volcano carried out over the years, the latest petrogenetic concepts have evolved to support the hypothesis that Taranaki andesites are multicomponent mixtures of silica-rich partial melts from the lower crust,

residual melts from underplated mantle basalts, and antecryst crystal populations, rather than the products of differentiation controlled by single FC and AFC processes (Stewart, 2010). The commonly accepted model is that magmas forming the late Quaternary andesites of Taranaki Volcano rise from a “hot-zone” (Price et al., 2005, 2016; Annen et al., 2006; Gruender et al., 2010) and are stored at about 10 km depth within the upper crust, undergoing recharge by melts forming at the crust-mantle boundary (Reubi and Blundy, 2009).

6.4. Methodology

6.4.1 Material

Based on the whole-rock compositional dataset provided by the study in **Chapter 5**, nine porphyritic and variably vesicular pyroclasts were selected from the growth phase (GP) units (stratigraphic position of sampled clasts can be found in **Appendix B3**; see field area in **Fig. 6.1 B**; **Table 6.1**) within the time-period of c. 65-34 ka (Otakeho, Rama and Te Namu Growth Phase; **Fig. 6.1 C**). The growth phases are referred to as GP1 (65-55 ka), GP2 (55-40 ka) and GP3 (40-34 ka; after **Chapter 5**), respectively. Representative minerals were investigated on petrographic thin sections (50 – 100 μm). Eighteen pyroxene and seventeen plagioclase crystals were chosen for full mapping analysis based on the whole-rock SiO_2 content of the host samples grouped into primitive (P; $\text{SiO}_2 < 52$ wt.%), transitional (T; SiO_2 between 52 – 57 wt.%) and evolved (E; $\text{SiO}_2 > 57$ wt.%; **Chapter 5**; **Table 6.1**; **Appendix C1**). A further forty-three pyroxenes and plagioclases were examined using transect mapping. Petrographic analyses and Scanning Electron Microscopy (SEM) data advised the selection of crystals for mapping based on the crystal size, habit, texture and the Mg-Fe zonation in clinopyroxenes and Ca-Na zonation in plagioclases. Clinopyroxene crystals range in size from 100 μm to <1000 μm and usually make up 19-37 vol. % of the rock fragments (for modal distributions see **Appendix C1**). They display euhedral or rarely subhedral morphologies and often are present within glomerocrysts. Fe-oxides often can be found as inclusions within the investigated clinopyroxene phenocrysts. Plagioclase phenocrysts range in size between 100 and 3000 μm , being the most dominant mineral phase in the sampled volcanic rocks (45-76 surf%). The crystals are subhedral, euhedral or resorbed and they often occur in glomerocrysts. Fe-Ti oxides can be found mainly in plagioclase rims.

<i>Growth phase</i>	<i>Sample name</i>	<i>Whole-rock SiO₂ wt.%</i>	<i>Group</i>	<i>Number of mapped</i>	<i>Number of mapped</i>	<i>Number of transects</i>	
				<i>Cpx phenocrysts</i>	<i>Pl phenocrysts</i>	<i>Cpx</i>	<i>Pl</i>
GP1	HF9-3	51.67	P	2	2	2	2
	HF10-3	51.64	P	3	2	-	-
GP2	LB LHF2-16B	53.37	T	1	1	5	5
	LB LHF4-12	50.17	P	2	2	-	-
	LHF5-6	53.44	T	2	2	2	4
	TAU IIFO-5	50.33	P	2	2	-	-
GP3	TAU LHF1-20	58.86	E	3	3	3	3
	TAU LHF2-17	51.06	P	2	2	3	5
	TAU LHF4-5	53.64	T	1	1	2	7
<i>SUM:</i>				18	17	17	26

Table 6.1 Number of mapped clinopyroxene (Cpx) and plagioclase (Pl) crystals from the selected volcanic rocks of the three studied growth phases (GP1, GP2, GP3). P: primitive; T: transitional; E: evolved. Whole-rock compositions after **Chapter 5**.

6.4.2 Scanning electron microscope analysis (SEM)

SEM was performed on carbon-coated thick-sections. A FEI Quanta 200 Environmental Scanning Electron Microscope (Hillsboro) was used at Massey University, Palmerston North, in order to select and locate the clinopyroxene crystals within the thick sections using an accelerating voltage of 20kV using a range of resolutions. Backscattered electron (BSE) images provided details on the relevant petrographic features and mineral zoning of the Taranaki vesicular pyroclasts samples.

6.4.3 Electron Microprobe Analysis (EMPA)

Mineral major element analyses were focused on plagioclases and clinopyroxenes, with additional analysis of Fe-Ti oxides, orthopyroxenes and amphiboles from the three studied growth phases (GP1, GP2, GP3). Electron Microprobe Analysis was performed at the Centre for Microscopy and Microanalysis (CMM) of The University of Queensland, Brisbane, Australia using a JEOL JXA 8200 electron microprobe equipped with five wavelength-dispersive spectrometers (WDS). Analytical data (raw data is provided in **Appendix C4**) were collected using a fully focused beam (ca. 2×2 μm interaction surface), accelerating voltage of 15 kV, beam current of 15 nA and counting time for all elements of 10 s on the peak and ±5 s on each of two background positions. The ZAF method was used for matrix correction. Calibration standards were wollastonite (Si-TAP and Ca-PET), orthoclase (K-PET), albite (Na-TAP and Al-TAP), chromite (Fe-LIF and Cr-PET), spessartine garnet (Mn-LIF), Durango F-apatite (P-PET), rutile (Ti-PET), P140 olivine (Mg-TAP) and Ni-olivine (Ni-LIF). Precision for major elements

ranges between 1 – 5% and accuracy of 1 to 3%. Precision for minor elements displays 2 to 9% and accuracy of 4 to 13%. Secondary standards Springwater olivine, Kakanui augite, Lake Co feldspar, and VG2 glass were measured to monitor accuracy and precision. Major elements are expressed as oxides and are reported in weight per cent (wt.%). Plagioclase and pyroxene data can be found in **Appendix C1** and BSE images with the analysed spots of crystals are given in **Appendix C2**.

6.4.4 Laser Ablation Inductively Coupled Plasma Mass Spectrometry (LA-ICP-MS) Analysis

High-resolution trace element mapping of eighteen clinopyroxene and seventeen plagioclase crystals was carried out in March – April 2019 via Laser Ablation Inductively Coupled Plasma Mass Spectrometry at The University of Queensland Centre for Geoanalytical Mass Spectrometry, Radiogenic Isotope Facility (UQ RIF-lab) in Brisbane, Australia (selected crystals and their location within the thin sections are shown in **Appendix C3**). Analysis was implemented on polished thick sections (~100 μm) prepared from one-half of the clasts (the other half was previously used for XRF analysis; **Chapter 5**), following the line rastering technique after Ubide et al. (2015). An ASI RESolution 193 nm excimer UV ArF laser ablation system with a dual-volume Laurin Technic ablation cell and GeoStar Norris software was used, coupled to a Thermo iCap RQ quadruple mass spectrometer with Qtegra software. Ablation was carried out in ultrapure He to which Ar make-up gas with a trace amount of N_2 was added for efficient transport and to aid ionisation. We used a 30 μm square spot, scan speed of 3 $\mu\text{m/s}$, repetition rate of 10 Hz and fluence of 3 J / cm^2 . The ICP-MS was tuned with scans on NIST612 glass reference material. Elemental maps were built with Iolite (v2.5; Paton et al., 2011) in quantitative mode, using NIST610 glass reference material as the calibration standard and Ca (pyroxene) and Si (plagioclase) concentrations previously obtained by EMPA (**Chapter 5**; see CaO and SiO_2 concentrations used for internal standardization of pyroxenes and plagioclases in **Appendix C1**). Accuracy and precision were monitored using BHVO-2G, BCR-2G and BIR-1G glass reference materials as secondary standards (GeoReM database: <http://georem.mpch-mainz.gwdg.de/>; Jochum et al., 2005). Precision was better than 5-10% and accuracy was better than 5-15%. Multi-element maps and transects were created using ‘Images from selections’ and CellSpace (Paul et al., 2012). The Monocle add-on for Iolite (Petrus et al., 2017) was used to extract average high-

precision compositions for crystal zones (regions of interest; ROIs) from the LA-ICP-MS maps.

6.4.5 Crystal Pattern Classification (CPC)

Here we develop a crystal pattern classification (general CPC, cf. **Table 6.2**) scheme that considers both the chemical and textural features of the crystals. During transect measurements (either by EMPA or LA-ICP-MS mapping), crystal map interpretations or BSE image evaluations, the following definitions are used:

Plagioclase and pyroxene crystal regions are categorized as rims (R), where outermost (R_1) and inner (R_2) rim regions were defined, the latter representing the last pre-eruptive processes affecting the crystal, whereas the former is in direct contact with the melt indicating the conditions at the onset and during eruption. Spot analyses of crystal rims typically reflect the composition of the inner rim, while the outermost rim can only be determined by detailed geochemical mapping. Mantles (M) are characterised as intermediate zones. Cores (C) are specified as the innermost part of a crystal and may therefore not always be seen in crystal sections. These regions (R, M, C) are defined by distinct chemical (major, minor or trace elemental) or textural (resorption surface, sieve texture, etc.) changes. Subscript numbers after the main crystal regions refer to the number of that particular region from the rim towards the core, i.e. M_1 and M_2 indicates that there are two regions within the mantle with different patterns. In order to minimize misinterpretation, the determination of the main regions (R, M, C) require at least two major and two trace elemental analyses. When the inner part of a crystal exhibits patchy zoning or is corroded, it is considered as a core (C) region, and mantle regions may or may not be present around this core. When the innermost part of the crystal is not patchy zoned or corroded, but obviously surrounded by a chemically or texturally distinct region, it is considered as a mantle (M) region, because the actual core may not have been intersected. While it is possible that this innermost part is in fact the actual core, this is simply a notation issue.

Therefore, the designation of terms is based on the observations made on the crystals, which can be influenced by the orientation of the cut, the textural or chemical changes or a combination of these. The classification considers three main patterns, namely (1) zonation, (2) texture and (3) concentration. These main patterns exhibit several sub-patterns, each having a code (see **Table 6.2**).

CRYSTAL REGION

R₁ - OUTERMOST RIM

R₂ - INNER RIM

M_X - MANTLE

C - CORE

CONCENTRATION

PATTERN	ZONATION	REMARK	EXPRESSED PROCESS	APPEARANCE
	(no) PATCHY	Anoehoid, irregular shaped patched surfaces surrounded by plagioclase with different An content.	Irregular shape due to resorption resulting in, to a vary of extent, crystallographic alignment and elongated forms. Diffuse zoned cores may result by temperature fluctuation.	
	(no) NORMAL	Increase in compatible elements and increase in incompatible elements towards rims.	Non-disturbed crystal growth.	
	(re) REVERSE	Increase in compatible elements and decrease in incompatible elements towards rims.	An-poor core and constant An content increase from core to rim indicates change in temperature within the system.	
	(os) OSCILLATORY	An composition frequently changes from core to rim creating concentric compositional zonation within the plagioclase.	Near-equilibrium conditions resulting in repeatedly-occurring destruction of the crystal-melt boundary taking new melt to the crystal-melt interface.	
	(se) SECTOR	Hour-glass form that can be seen based on the orientation of the thin section cut.	Low-degree of undercooling at near-equilibrium conditions.	
	(un) UNZONED	There are no compositional patterns observed.	The crystal experienced non-disturbed crystallization.	
TEXTURE	(ir) INTERNAL RESORPTION	Resorbed surfaces within core, mantle or rim zones that may differ in intensity to a varying degrees.	Periods of crystallization following initial disequilibrium conditions generate the resorption interfaces that were resorbed due to magma mixing and/or decompression during further ascent.	
	(er) EXTERNAL RESORPTION	Resorbed surfaces in the outer parts of core, mantle or rim zones that may differ in intensity to a varying degrees.	Extreme resorptional conditions indicating decompression probably under H ₂ O-saturated conditions.	
	(co) CORROSION	The crystal region surface has lost its euhedral or subhedral shape.	Reheating process contributes to the entrapment of glass due to rapid crystallisation.	
	(si) SIEVE	Voids filled with trapped melt is often associated with resorbed interfaces.	The crystal underwent no texturally destructive process.	
	(fl) FLAT	There are no textural patterns observed within the crystal surface.	Relative enrichment and depletion are indicators for certain processes depending on the characteristics of the element that is analyzed.	
CONCENTRATION	(en) ENRICHED	Relative enrichment of one zone in a certain element within the crystal.		
	(de) DEPLETED	Relative depletion of one zone in a certain element within the crystal.		

CRYSTAL PATTERN CLASSIFICATION (CPC)

Table 6.2 Crystal pattern classification (CPC) of the analysed plagioclase and clinopyroxene crystals of the GP units. Arrows indicate the order of classification, i.e. from rim to core and from zonation to concentration patterns.

Consequently, crystals can be classified focusing on a single element (major, minor or trace) using the nomenclature in order (from zonation patterns to concentration patterns), characterising a crystal from rim to core, based on the patterns observed. Thus, for example in the case of the element magnesium, $R_l(ex,en)M(re)C(pa,ex)$ specifies a crystal which has an externally resorbed, Mg enriched outermost rim, a reversely zoned mantle and a patchy zoned, externally resorbed core. Several elements may behave similarly and can be grouped to define a specific crystal pattern cluster.

Plagioclase and pyroxene BSE images (**Appendix C2**) were classified by their textural and major element characteristics and LA-ICP-MS crystal maps were used to classify the trace element distribution characteristics and occasionally the major and minor element distribution characteristics. Individual plagioclase and pyroxene crystals were defined as phenocrysts $> 300 \mu\text{m}$ and microcrysts $< 300 \mu\text{m}$ and were classified based on the crystal habit (see **Appendix C1**). Crystal habits have been identified as tabular, subhedral or resorbed for plagioclases and euhedral, subhedral or resorbed for pyroxenes. Plagioclase and clinopyroxene crystals have large variations in growth textures and major and trace element geochemical zonations within and between samples. The categorized patterns presented here are representative for the sample set analysed. The crystals may exhibit more than one characteristic pattern, and the sum of the patterns defines the type of crystal along with the complexity of magmatic conditions that individual pyroxene or plagioclase crystals experienced. Sieve textures are considered as the presence of copious trapped melt within partially resorbed zones (Tepley et al., 2000; Stewart and Fowler, 2001; Landi et al., 2004).

6.5 Results

In the following, the most significant crystal patterns (textural and chemical) are highlighted using the CPC scheme to provide insights into the processes occurring within the plumbing system of Taranaki Volcano during the 65-34 kyr period. Summary tables of plagioclase and pyroxene classification can be found in the **Appendix C1**.

6.5.1 Petrography and crystal cargo record

The vesicular pyroclasts of the GP units have variable crystallinity (25-65 vol.%; **Chapter 5**) with a moderately vesicular microcrystalline groundmass. Overall, the mineral assemblages consist in descending order of abundance of plagioclase (45-76%),

clinopyroxene (19-37 %), amphibole (1-25 vol%), Fe-Ti oxides (2-5 vol. %), and rarely orthopyroxene or olivine. The textures of GP3 samples are similar to GP1 and GP2 with the exception of one sample (*TAU LHF1-20*) having microvesicular groundmass and relatively small sized plagioclase and pyroxene crystals. The plagioclase phenocrysts range in size from 300 μm up to 3 mm, while pyroxenes exhibit sizes from 100 to 300 μm (microcrysts) and from 300 μm to 1 mm (phenocrysts).

6.5.2 Mineral textures coupled with major element oxide chemistry

6.5.2.1 Plagioclase

The investigated plagioclase phenocrysts ($n = 112$) from the GP unit samples exhibit complex compositional and textural variations, which are mirrored in the broad range of compositions from An_{13-91} . Crystals display complex compositional zoning characterized by corroded or patchy cores and multiple mantles and overgrowth rims. Normal, reverse, oscillatory and patchy zoning is present (for general plagioclase classification and description, see **Chapter 5**). The following crystal patterns were recognized that occurred individually or combined within the crystals:

- Patchy [Pattern C(pa)] (**Fig. 6.2 E**) or non-patchy [Pattern C(un)] (**Fig. 6.2 F**) zoned cores or patchy zoned mantles [Pattern M(pa)] (**Fig. 6.2 D, F**).

Patchy zoning is the most common type of zonation (77.5% of the investigated plagioclases display patch zoning; **Appendix C1**) within the crystals typically accompanied by irregular blebs of melt and occasionally associated with microinclusions of pyroxene or Fe-Ti oxides. Patchy zoned plagioclases usually show, variable extents of resorption. Amoeboid patchy zoning is common in individual plagioclases, often exhibiting a degree of crystallographic alignment (**Fig. 6.2 E**). In general, An contents within patchy zoned cores range between 42 – 91 mol%. Patches in individual crystals can display higher or lower An than the surrounding plagioclase (**Fig. 6.3**).

- Zonation (10 – 50 μm) of normal [Pattern R/M(no)], reverse [Pattern R/M(re)] or oscillatory [Pattern R/M(os)] type (**Fig. 6.2 C**).

The compositional changes within zones are between 35 – 92 An mol%. In most of the observed cases, individual plagioclase crystals exhibit complex zonation. Less than 4% of the analysed plagioclases are unzoned, whereas 15% display only one type of zoning and 82% exhibit multiple types of zoning (two or three types of zonation; **Appendix C1**). Overall, 47% of the plagioclases is oscillatory zoned and reverse-zoned, while 40% show

normal zoning. Where plagioclase displays one type of zoning, normal and reverse zoning is characteristic. In plagioclases exhibiting multiple types of zoning, patchy zoning is the most common followed by oscillatory and reverse zoning. Plagioclases from GP1 have mostly two types of zoning, whereas GP2 crystals exhibit multiple zonation, specifically half of the crystals have two and the other half of the crystals have three types of zonation, respectively (**Appendix C1**). GP3 plagioclases display similar zonation type proportions to those of GP2.

- Large-scale (50 – 100 μm ; **Fig. 6.2 G**) to small-scale (10 – 50 μm) single or multiple resorption interfaces [Pattern R/M/C(in,ex)] of rims, mantles or cores.

Resorption surfaces display An contents ranging from 39 – 69 mol%. They are often associated with voids and occasionally sieve-textures (Pattern R/M/C(si)). Amoeboid inclusions are found in crystals that exhibit resorption patterns. The majority of plagioclase crystals display resorption, which can be expressed as internally or externally resorbed crystal habits, cores, mantles or rims and/or partially resorbed interfaces/surfaces within the crystals. Individual plagioclases may express more than one resorbed surface (**Fig. 6.2 H**). A resorbed core interface is the most common type followed by mantle and rim resorption patterns. In general, 8% of the observed crystals show no evidence of resorption, whereas 52% exhibit one resorption pattern and 40% display multiple zonation surfaces (of which those with two-resorption surfaces are in majority; **Appendix C1**). GP1 plagioclases show one or two resorption events, while GP2 crystals largely exhibit multiple resorption events. GP3 plagioclases show mainly one resorption event (**Appendix C1**).

- Flat, texture free profiles of crystals [Pattern R/M/C(fl)], in size mostly smaller than 500 μm showing only minimal textural patterns (**Fig. 6.2 A, B**).

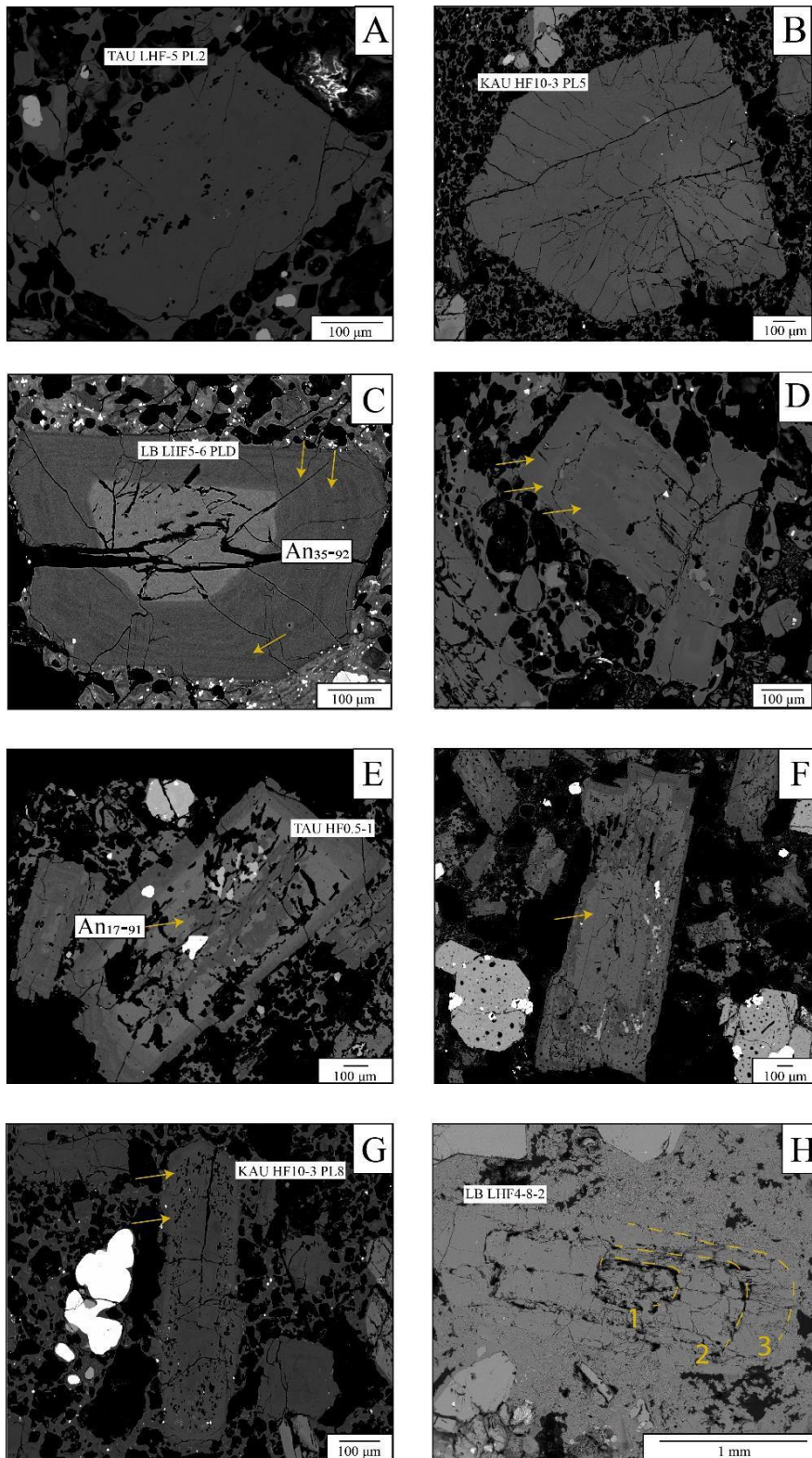


Fig. 6.2 Main textural and compositional features of plagioclases of the pumiceous and scoriaceous samples from GP1, 2, 3. **A:** Flat profiles. **B:** Small-scale oscillatory zoning and discordancy oscillatory zoning indicated by the arrow. The average anorthite (An) contents of oscillatory zones are also indicated. **C:** Patchy-textured core with resorption/dissolution textured mantle. The average An content of cores are indicated by the arrow. **D:** Large-scale sieve-textured mantle. The average sieve-texture compositions as indicated. **E:** Multiple sieve-textured resorption surfaces. Numbers indicate the order of resorption events. Yellow dashed lines highlight the resorption surfaces.

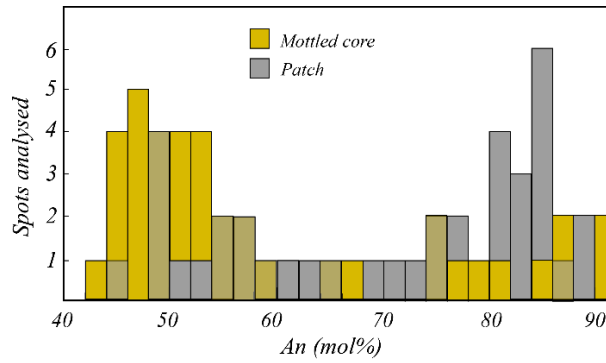


Fig. 6.3 Anorthite content of plagioclase mottled cores and patches analysed from the GP units.

The investigated plagioclase phenocrysts exhibit variable NaSi-CaAl zoning in cores, rims and/or sieve-textured mantles. The rims of the observed plagioclase crystals display fine oscillatory zoning or flat profiles. In most cases, they are free of melt inclusions, dissolution or partial resorption zones along with pyroxene or Fe-Ti oxides which occur rarely within rims. The majority of samples have cores with An₅₀₋₉₀, while mantles and rims yield An₃₅₋₇₀ (see histogram in **Fig. 6.4**). GP1 plagioclases show a narrower range of An contents in general, while GP2 core An contents represent bimodal variations (An₄₅₋₅₅ and An₇₅₋₈₈). GP3 unit plagioclases display the largest variability of compositions in cores, mantles and rims.

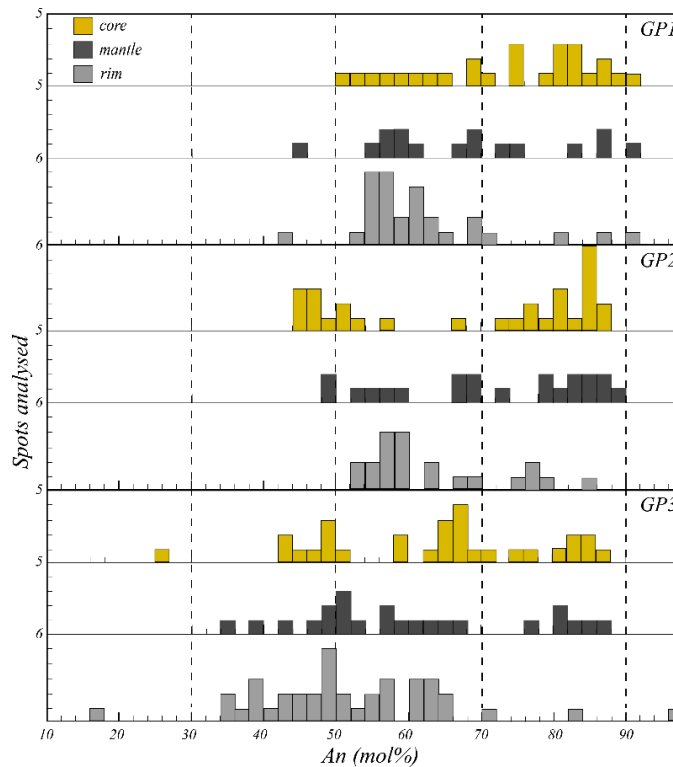


Fig. 6.4 Core, mantle and rim anorthite compositions of each GP unit plagioclase analysis.

6.5.2.2 Clinopyroxene

In general, compositions of analysed cores, mantles and rims are within the range $W_{0.25-0.50}En_{16-51}Fs_{10-46}$ and the investigated clinopyroxenes ($n = 70$) display mostly primitive compositions based on SiO_2 of 41-54 wt.% and Mg# as of 0.5-0.74. The phenocrysts ($> 300 \mu m$) display complex zoning within the cores, mantles and rims, whereas small crystals ($< 300 \mu m$) show unzoned or slight oscillatory zonation in rims. However, some large crystals are unzoned, and some small crystals may show compositional zonation. Normal, reverse and oscillatory zoning both occur. In most cases, clinopyroxenes from the GP units display distinctive, yet complex textural-compositional variations, ranging in size from $200 \mu m$ up to 1 mm. The characteristic patterns can be described as follows:

- Patchy [Pattern C(pa)] (**Fig. 6.5 A**) or non-patchy zoned cores [Pattern C(un)]. Clinopyroxenes show to a varying extent, a degree of resorption. The cores display distinct (Mg# < 0.65 or Mg# > 0.65) compositions. Patchy zoning, while not the most common type of zonation (27% of the investigated pyroxenes display patchy zoning) within the crystals, is typically accompanied by irregular blebs of melt and occasionally associated with inclusions of pyroxene or Fe-Ti oxides.
- Thin ($10 \mu m$) or thick ($10 - 50 \mu m$) normal [Pattern R/M(no)], reverse [Pattern R/M(re)] or oscillatory [Pattern R/M(os)] (**Fig. 6.5 B**) zonation.

In most cases, individual pyroxene crystals show complex zonation. Less than 9% of the analysed pyroxenes are unzoned, whereas 41% display only one type of zoning and 50% exhibit multiple types of zoning (two, three or four types of zonation; **Appendix C1**). Overall, the most common type of zoning is oscillatory zonation (50% of the studied crystals), while 41% display normal and 39% show reverse zonation. Less than 12% of the investigated pyroxenes have sector zonation. Where pyroxenes display one type of zoning, normal and oscillatory zonation is characteristic. In crystals exhibiting multiple types of zoning, oscillatory zoning is the most common followed by normal and reverse zonation. Oscillatory zonation is often associated with resorption patterns. Pyroxenes from GP1 show mostly multiple zonation, whereas GP2 crystals exhibit single and multiple zonation, specifically half of the crystals have one and the other half of the crystals have three types of zonation, respectively (**Appendix C1**). GP3 crystals exhibit mainly single and multiple zonations.

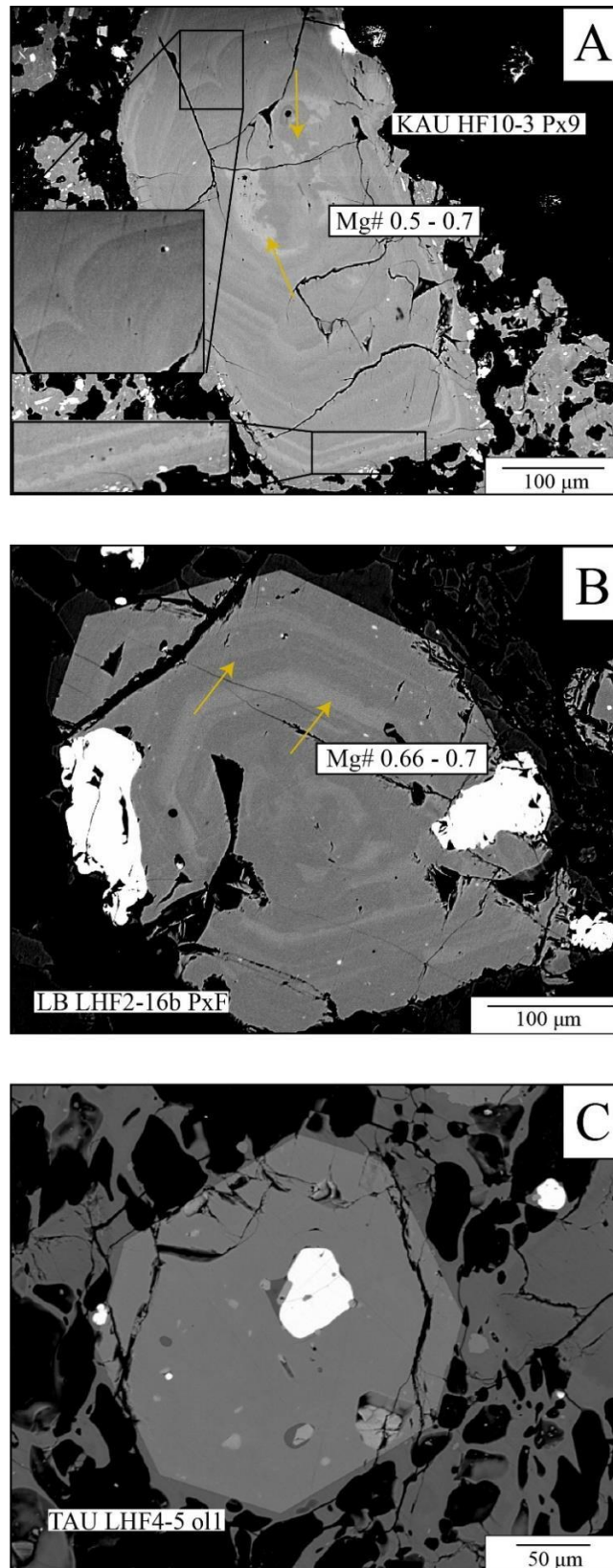


Fig. 6.5 Pyroxene crystals representing the main textural characteristics. **A:** Patchy-zoned cores outlined by the yellow arrows along with the Mg# value range. **B:** Thin and thick oscillatory zoning indicated by the arrows. Mg# content range of Mg#-rich mantles as indicated. **C:** Flat profiles with Fe-Ti oxide association.

- Internal or external resorption/dissolution surfaces [Pattern R/M(ir,er)] of mantle and rim regions forming resorbed, rounded bands connected to Fe-Mg and additional Al₂O₃ compositional variations.

45% of the observed clinopyroxenes exhibits resorbed (single or multiple) zones either in rims or mantles (**Appendix C1**) that are expressed as rounded, jagged bands in the crystal texture (**Fig. 6.5 A** insets).

- Innermost mantles and or outermost rims display high Mg# values (>66). Therefore, they are referred to as *Mg# - rich mantles* [Pattern M(en)] and *Mg# - rich rims* [Pattern R(en)].

Compositional changes within individual clinopyroxene crystals are significant, as expressed here by Mg# variations from the cores, through the mantles to the rims. This chemical complexity represented by single or multiple compositional changes within the individual crystals is most evident in the Mg# number differences within the mantle. The range of Mg# diversity of core-mantle-rim is between 0.03 – 0.1 within individual phenocrysts and in extreme cases, reaching Mg# differences of 0.2 (**Fig. 6.6**). These compositional variations within the individual crystals are independent of crystal size or GP unit origin as shown in **Fig. 6.6**. Overall, core compositions range between Mg# 0.50 – 0.70, while mantles range in a broader range of Mg# 0.50 – 0.74 and rims within Mg# 0.16 – 0.70 (see histogram in **Fig. 6.6**). The majority of core compositions are enriched within the range of Mg# 0.65 – 0.70 (at SiO₂ of 51 – 54 wt.%), while mantle and rim compositions dominate in the Mg# range of 0.62 – 0.70 (for general pyroxene classification and description, see **Chapter 5**).

- Unzoned profiles – usually between crystal sizes of 100 – 300 μm – without any or minimal oscillatory zonation [Pattern R/M/C(un)] (**Fig. 6.5 C**) and with occasional Fe-Ti oxides and melt inclusions.

Less than 9% of the investigated pyroxenes display no zonation. Fe-Ti oxide inclusions occur often within clinopyroxene phenocrysts (**Fig. 6.5 B, C**). Clinopyroxenes form glomerocrysts with titanomagnetite accompanied by plagioclase and rarely amphibole phenocrysts. Major element maps reveal that the analysed clinopyroxene crystals display homogeneity in major elements such as Ca. However, several crystals show sharp, oscillatory zonation in minor elements, such as Al and in a few cases, oscillatory or sector-zonation in Na (**Fig. 6.7**). 55% of the pyroxenes show no resorption surfaces.

Where resorption is present, 30% of the crystals exhibit one resorption event. Resorbed cores are the most characteristic, followed by mantle resorption surfaces.

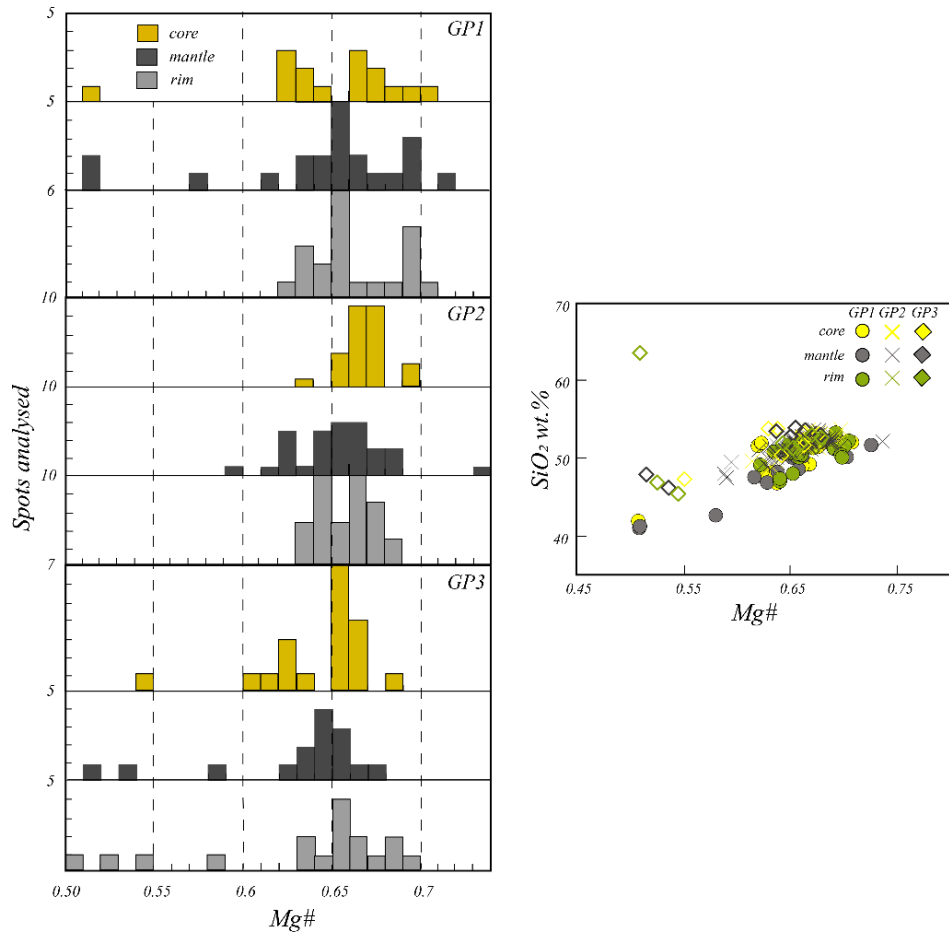


Fig. 6.6 Mg# compositions for core, mantle and rim of each GP unit clinopyroxene analyses. *Inset:* General Cpx SiO₂ wt.% compositions as a function of Mg#.

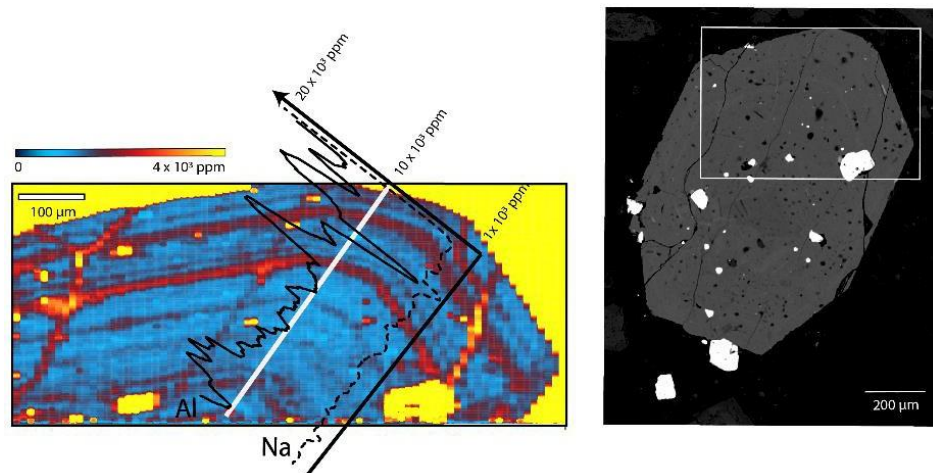


Fig. 6.7 Minor element (Al-Na) zonation within a clinopyroxene phenocryst. White line indicates the path of data extraction from the crystal map using CellSpace.

6.5.2.3 Titanomagnetite

Titanomagnetite is a ubiquitous Fe-Ti oxide in Taranaki rocks and is microphenocrystic (< 1 mm), commonly forming glomerocrysts with clinopyroxene ± plagioclase. Pyroxenes are typically accompanied by titanomagnetites (**Fig. 6.5 B, C**), usually both euhedral and subhedral (resorbed) grains are incorporated within the silica host mantles or rims. Cores also contain mostly resorbed titanomagnetites, but they are not as common as in mantles or in rims. Plagioclase mantles and rims may contain euhedral or subhedral titanomagnetites, whereas cores occasionally include titanomagnetites, filling up voids in the form of the crystallographic alignment. Representative titanomagnetite analyses display TiO₂ contents ranging between 5.74 – 10.04 wt.%. GP1 titanomagnetites represent the lowest TiO₂ contents with an average of ~ 6.24 wt.%, whereas GP2 titanomagnetites yield to the highest TiO₂ contents of >8.5 wt.%. MgO compositions range between 1.5 – 4 wt.% (see representative analyses in **Appendix C1**). The MgO contents of the GP1 titanomagnetites do not correlate, whereas GP2 titanomagnetite MgO contents correlate slightly and GP3 titanomagnetites contents correlate well with variations in the whole-rock compositions of the same eruptive products (see **Appendix C1**). Some titanomagnetites of GP3 exhibit the lowest MgO contents and an intermediate range of TiO₂.

6.5.2.4 Amphibole

Amphiboles are a common (1-25 %) mineral phase in the samples. The representative analysis displays amphiboles that are classified as Ti-rich pargasites (Hawthorne et al., 2012; Locock, 2014). They can contain titanomagnetite grains and/or blebs of melt. Textural zoning is not pronounced. There are two types of amphibole phenocrysts present in the investigated volcanic rocks: (i) flat or patchy/oscillatory zoned profiles without decompression rims (**Fig. 6.8 A**) and (ii) flat profiles with decompression rims (**Fig. 6.8 B**). These decompression rims (~100 µm) are thought to be developed due to the pressure drops during magma ascent at the onset of eruption, bringing the crystal out of its stability field (Rutherford and Hill, 1993; Browne and Gardner, 2006). This type of amphibole has been reported before in Taranaki rocks (Platz et al., 2007a, 2012; Turner et al., 2008a), but such crystals are rare within the investigated volcanic rocks.

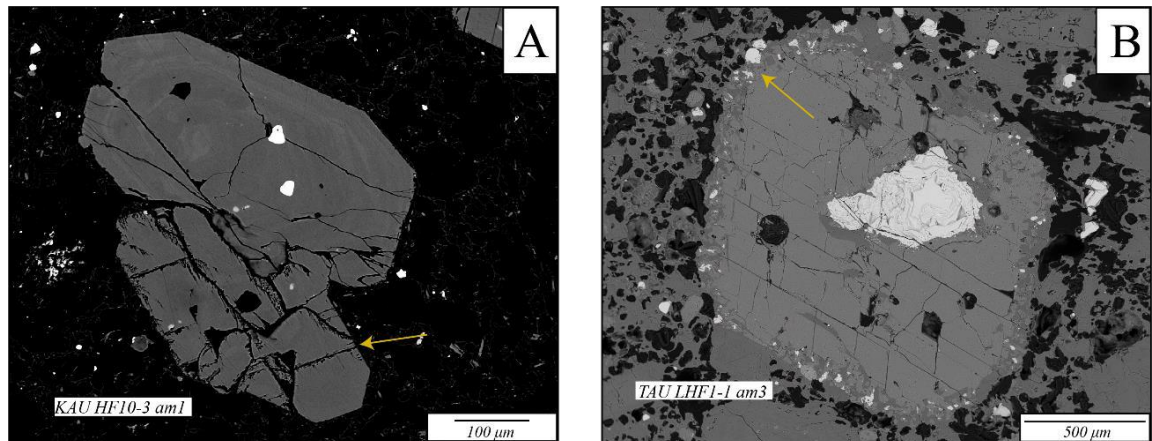


Fig 6.8 A: Amphibole (outlined by yellow arrow) with patchy zoning forming a glomerocryst with a clinopyroxene. **B:** Amphibole with decompression rim (indicated by the arrow) accompanied by titanomagnetite.

Representative amphibole analyses yield Mg# ranges of 0.54 – 0.56, whereas Al₂O₃ contents range from 10.9 to 11.7 wt.% (for representative analyses, see **Appendix C1**).

6.5.3 Mineral trace element chemical zonation

6.5.3.1 Plagioclases

Chemical variability in the investigated plagioclase crystals unravelled by the LA-ICP-MS mapping method is pronounced. In general, homogeneous or corroded cores are surrounded by zoned or patchy mantles and flat or oscillatory zoned rims. Mantles and rims represent enrichment in Li, La, Sr, Ba and Ce coupled with Na, rarely with Mg. Several crystals display relatively low Ce, La and rarely low Ba concentration in rims and mantles. Unique trace element distributional patterns within the plagioclase crystals can be categorized as the following:

- (i) Oscillatory zonation [Pattern R₂(os)] or relative enrichment in the outermost rims [Pattern R₁(en)] in Li accompanied by enrichment in Ba or occasionally in Sr (**Fig. 6.9**).
- (ii) Oscillatory zonation within rims [Pattern R₂(os)] or in the outer rims [Pattern R₁(os)] (**Fig. 6.9**) enriched in Ba, occasionally coupled with variations in major and or minor element concentrations (Ca, Na, Fe or Mg).

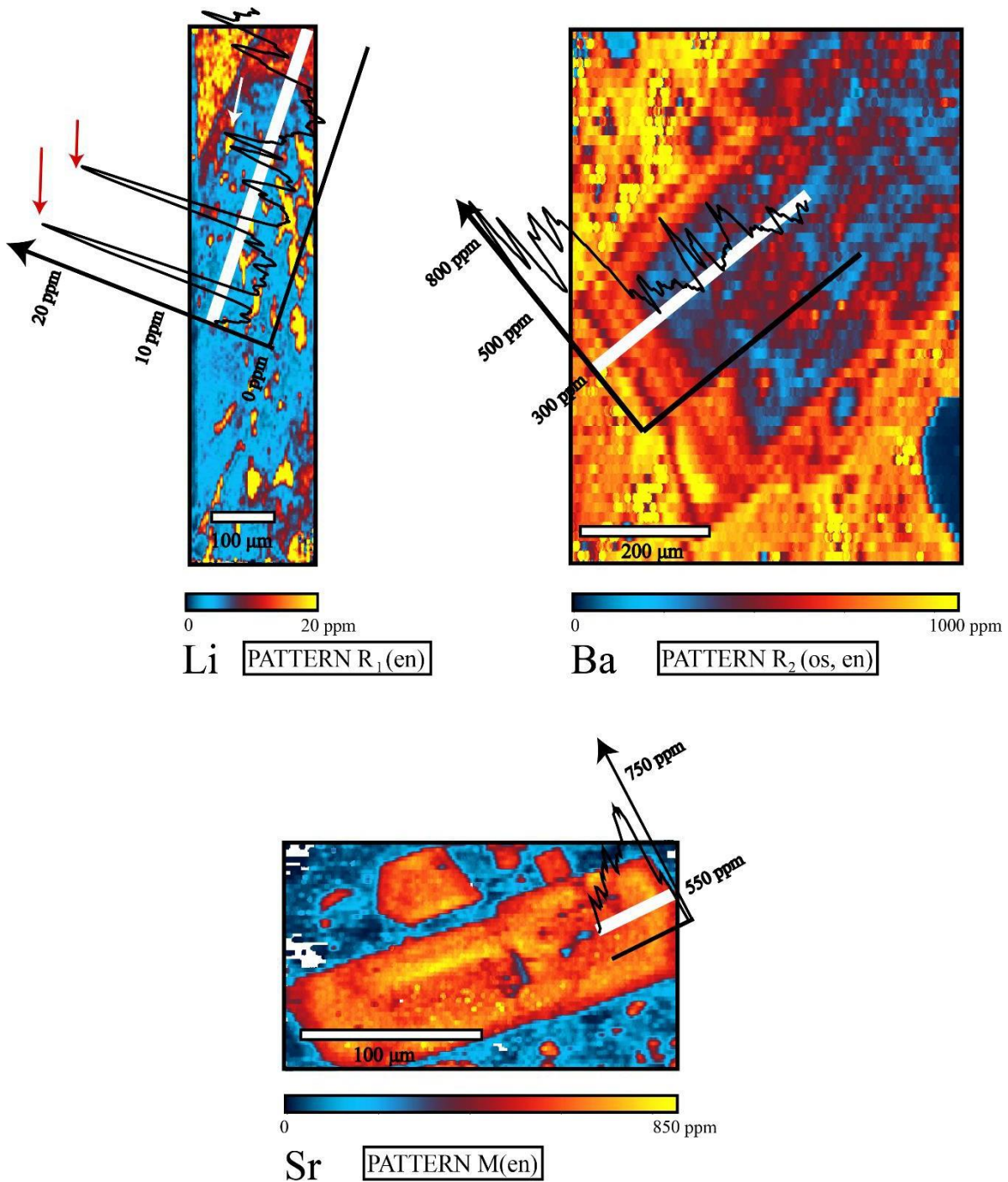


Fig. 6.9 The main types of trace elemental distributions within plagioclase phenocrysts. Type 1: Li enrichment within rims. Sample from GP1: *KAUHF10-3_2PL*. Type 2: Ba enrichment within rims. Sample from GP3: *TAULHF4-5_plA*. Type 3: Sr enrichment in the mantle region. Sample from GP3: *TAULHF1-20_plA*. White lines indicate the path of data extraction from the crystal map by CellSpace. Red arrows indicate data extraction from resorbed surfaces.

- (i) Unzoned profiles in trace element compositions [Pattern (un)].
- (ii) Normal or reverse zonation [Pattern (no) or (re)] or Sr-enriched mantles [Pattern M(en)] (**Fig. 6.9**).

6.5.3.2 Clinopyroxenes

LA-ICP-MS trace element maps expose marked chemical complexity within the clinopyroxene crystals. The examined trace elemental features can be subdivided into the following patterns (**Fig. 6.10**):

- (i) Corroded Cr-rich cores [Pattern C(co,en)] accompanied by enrichment in compatible transition metals (Ni, Sc).

They are either overgrown by oscillatory or sector zoned mantle and rim or by rims slightly enriched in mildly incompatible elements.

- (ii) Cr-enriched mantles [Pattern M(en)] with relative enrichment in Nd, Ni and Sc.

These mantles are often coupled with oscillatory or sector zonation. Zones rich in Cr for instance, are also enriched in other compatible metals, e.g. Ni and or Sc and are relatively depleted in incompatible elements such as La, Nd, Zr or Nb.

- (iii) Zonation of oscillatory or sector type [Pattern R/M(os,se)] with trace element enrichment of compatible metals and mildly incompatible elements (Ni, Sc, Zr, La, Ti, V).

Oscillatory trace elemental zonation characterises the majority of samples. Oscillatory zoned mantles and rims typically display enrichment in both minor and trace elements such as Al, Na and Zr, Ti, Nd, Sr and Li. Pyroxene crystals exhibit sector zonation (>12%; **Appendix C1**) in certain minor and trace elements, such as Al, mildly incompatible elements including La, Nd, Zr, and in Ti and or V. Overall, zonation patterns are occasionally coupled with minor (Al, Na) element enrichment or rim enrichment in mildly incompatible elements (i.e. La, Nd, Zr).

- (iv) Slight oscillatory zonation of mantles [Pattern M(os)] and or rims [Pattern R₂(os)] or enrichment in certain elements [Pattern M(en)] as Zr, La, Sc and or Nd seen within otherwise flat major and minor element profiles.

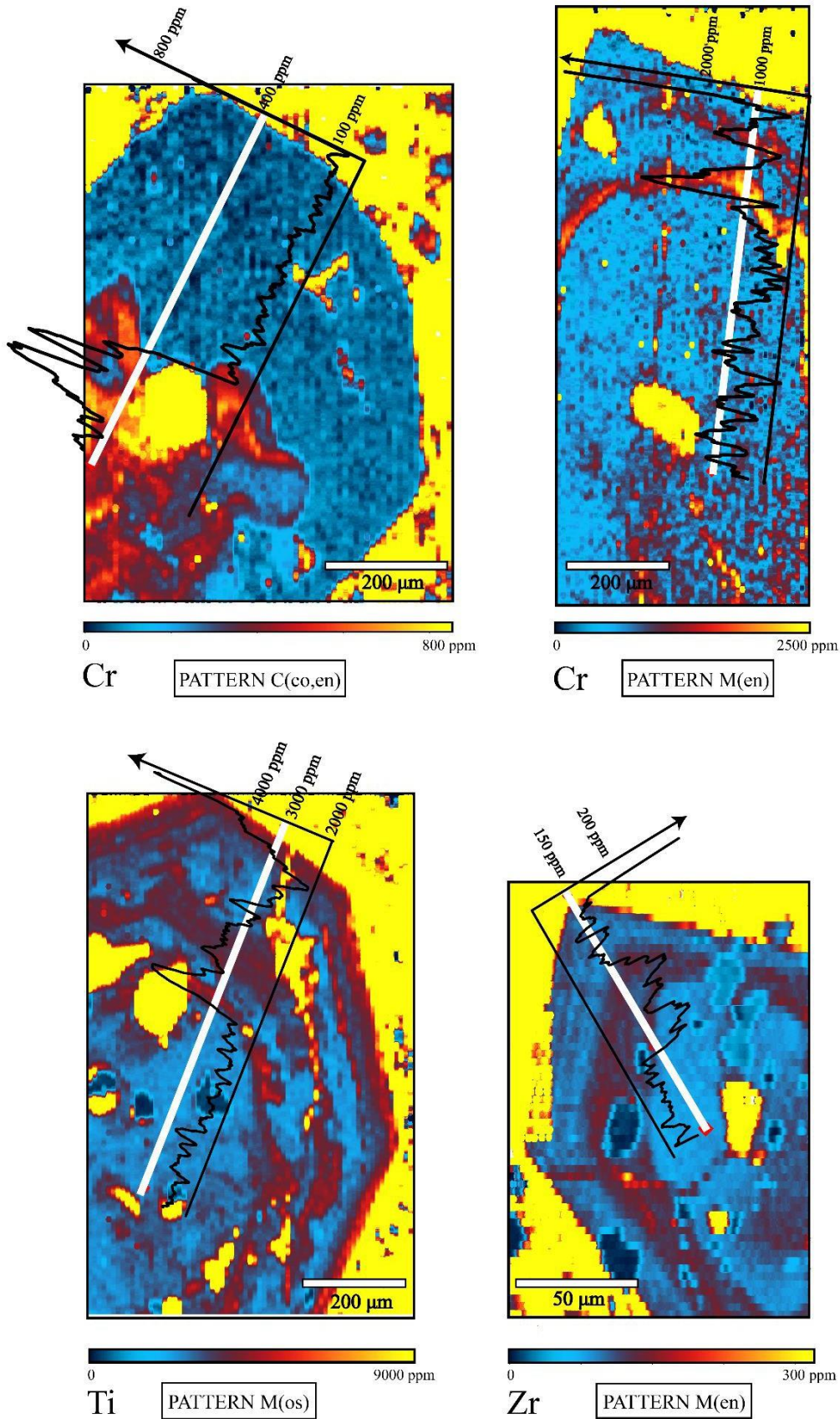


Fig. 6.10 Representative trace element zonation types of clinopyroxenes showing the most characteristic trace elemental compositional distribution patterns. Type 1: Cr-rich cores. Type 2: Oscillatory zonation of trace elements. Type 3: Cr-rich mantle. Type 4: Minor oscillatory zoned rims slightly enriched in mildly incompatible elements. White lines indicate the path of data extraction from the crystal maps by CellSpace.

6.6 Discussion

Petrological and geochemical data from volcanic clasts, c. 65-34 ka in age, obtained from volcanoclastic mass-flow sequences exposed at the south and southwestern sector of the ring-plain provide new insights into the ‘mid-age’ magmatic plumbing system and the mush zone characteristics beneath Taranaki Volcano. The studied volcanic rocks display diverse whole-rock major element compositions. However, the crystal populations seen are independent of the major element composition of the selected rocks.

6.6.1 Physical setting of crystallization and the ascending melts

6.6.1.1 Distinguishing magmas of the growth cycles between c. 65-34 ka

Titanomagnetites are a common phase in Taranaki rocks. Taranaki titanomagnetite analyses have been used for tephra (<30 ka) investigation and proved to be useful for distinguishing and correlation tephra sequences (Damaschke et al., 2017a, b). Titanomagnetites are thought to indicate surrounding magma compositions and their changes (Tomiya and Takahashi, 2005). TiO₂ contents within titanomagnetites reflect temperature and/or fO_2 changes of the surrounding environment, while MgO contents are related to silica activity, thus to the temperature and composition of the surrounding melts they crystallised from (Hill and Roeder, 1974; Lindsley et al., 1991). The above-mentioned method of this study using volcanoclastic mass-flow deposits provided the basis for the geochemical characterisation of the growth cycles. However, due to the medial ring-plain conditions of Taranaki Volcano, the exact stratigraphic position of several mass-flow deposit packages could not have been exactly determined, which made the interpretation of the geochemical evolution of Taranaki eruptives complex (**Chapter 5**). Therefore, to confirm the stratigraphic position of these mass-flow packages, we used the method that builds on the coupling of the major oxide chemistry (**Chapter 5**) to the titanomagnetite chemistry (see general description in **Chapter 5**, Section 5.2.3) of the GP unit clasts in order to correlate the mass-flow packages to the proper growth phases.

Differences in titanomagnetite chemistry of GP1 eruptives compared to GP2 and GP3 are likely related to characteristic temperature- fO_2 conditions of magmas (**Fig. 6.11**; Buddington and Lindsley, 1964; Devine et al., 2003) within 65-55 ka, as MgO contents of the whole-rock compositions do not correlate with the titanomagnetite MgO contents.

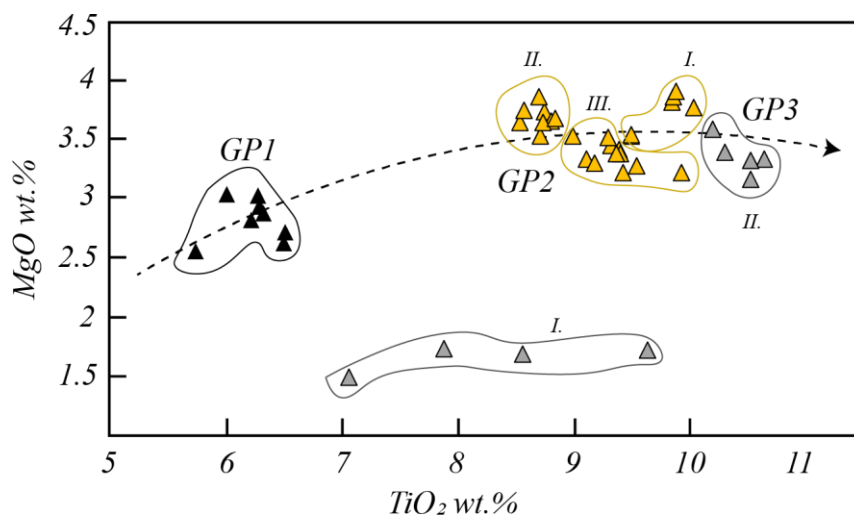


FIG 6.11 Titanomagnetite MgO wt.% compositions of the GP unit clasts as a function of TiO₂ wt.% showing different magmas of the growth cycles. Three distinct groups in GP2 (I., II., III.) and two separate groups within GP3 (I. and II.) can be identified. Dashed arrow indicates time. The numerals I. – III. indicate mass-flow packages from older to younger.

However, titanomagnetites mainly exhibit constant MgO contents, while TiO₂ compositions increase over time between 65–34 ka. Based on the titanomagnetite chemistry of GP2 and the stratigraphic position of the sampled eruptive products, three magmas are distinguishable based on variations in TiO₂ content (**Fig. 6.11**; GP2 I., II., III.). GP3 differs in a way that it partly shares the same MgO ranges as GP2, however some titanomagnetite compositions plot to a low-MgO and to a wide TiO₂ range, suggesting at least two different sources of these crystals within the time period 40–34 ka. This may indicate that the older GP3 I. magma was trapped and stalled, thus representing evolved compositions and possible higher oxygen fugacity, whereas GP3 II. magma represents an individual and different younger “batch” extruded at a later stage. In addition, these two distinct magmas of GP3 may explain the scattered major element variations, especially in the case of Na₂O vs SiO₂ (**Chapter 5**, Section 5.7.3), where the modelled mixing line represents mainly the GP3 I. magma batch, whilst the scattered Na₂O compositions at low silica content might be representative of GP3 II., respectively.

Overall, titanomagnetite chemistry provides a means of distinguishing between GP2 (55–40 ka) and GP3 (40–34 ka) samples, and thus aids in the classification of stratigraphically uncertain volcanoclastic mass-flow deposit clasts (see **Chapter 5**, section 5.6.3 and 5.6.4) to GP2 III. (for representative titanomagnetite chemistry, see **Appendix C1**). Therefore, this technique proved to be suitable when dealing with volcanoclastic mass-flow deposit correlation to the appropriate growth cycles in medial ring-plain settings. Thus, this additional method is recommended to be applied when correlation,

based on the stratigraphy and on the whole-rock compositions, is not sufficient to distinguish mass-flow deposits in the ring-plain stratigraphy.

6.6.1.2 Geothermobarometric conditions of the investigated mush domain

Mineral chemistry can provide thermobarometric constraints on the petrogenesis of volcanic rocks (Putirka, 2008). Although pressure estimates are subject to significant uncertainties, aluminium contents of amphiboles can deliver information on pressure (Hollister et al., 1987; Schmidt, 1992). Both natural and experimental data were used by Ridolfi et al. (2010) and Putirka (2016) in order to further develop independent amphibole compositional relationships that can be used to estimate temperature, pressure, f_{O_2} and melt water content in mafic, intermediate and felsic igneous rocks. Thermobarometric equations based on clinopyroxenes, such as the incorporation of jadeite ($NaAlSi_2O_6$; Jd) into clinopyroxene, pressure-dependent Jd-liquid reaction (Putirka et al., 1996), temperature-dependent Jd into diopside-hedenbergite (DiHd) and calcium Tschermak's component (CaTs) into DiHd exchange reactions have been subsequently reformulated and refined by Putirka et al. (2003) and Putirka (2008) providing extensive usage for clinopyroxene-liquid thermobarometry. Subsequent experiments established a more reliable Jd-in-clinopyroxene barometer by Neave and Putirka (2017) which is calibrated for ultramafic to intermediate rocks between 0.001-20 kbar and within the temperature range of 950-1400 °C for both hydrous and anhydrous compositions and is thus suitable for investigating andesitic rocks. Pyroxenes are common phenocryst phases in Taranaki eruptives, providing potential for the evaluation of crystallization temperatures (e.g. Lindsley, 1983; Putirka et al., 2003). In the investigated Taranaki rocks collected from mass-flow deposits, the opaque oxides are generally titanomagnetites, thus iron oxides cannot be used for geothermometry. However, clinopyroxenes and amphiboles are suitable phases for further examination.

Mineral/melt equilibria between clinopyroxene/liquid and amphibole/liquid can be obtained using experimentally derived values to test the equilibrium conditions. One of the most widely used tests for equilibrium is the Fe-Mg exchange coefficient or K_D ($Fe-Mg$)^{cp_x-liq} of the clinopyroxenes with an equilibrium range value is determined to be 0.28 ± 0.08 (Putirka, 2008), whereas in the case of amphibole, the K_D ($Fe-Mg$)^{amp-liq} is expected to be 0.28 ± 0.11 (Putirka, 2016), respectively. However, filtering for Fe-Mg equilibrium in itself may be insufficient in systems where mixing is prevalent due to the

fact that even if a system establishes Fe-Mg equilibria, pressure-dependent NaAl-CaMg exchange of the equilibration may not be guaranteed and different components may equilibrate at different rates (Neave and Putirka, 2017). Therefore, another option for testing is to compare predicted and measured multiple clinopyroxene components, such as diopside + hedenbergite ($\Delta DiHd$ of Putirka, 1999; Mollo et al., 2013). Furthermore, testing clinopyroxene-melt partition coefficients between clinopyroxene and melt is also reasonable (D_{Na} and D_{Ti} components; Blundy et al., 1995; Hill et al., 2011).

The measured and predicted values for the mineral-melt tests carried out in this study corroborate the reliability of the clinopyroxene-melt and amphibole-melt P-T-H₂O estimations (see mineral-melt tests in **Appendix C2**). Applying the partition coefficients to the investigated Taranaki phases, rim compositions of GP1 and GP2 clinopyroxenes exhibit calculated Mg#s higher (70-85 of GP2; 75-85 of GP1) than those of the host whole rocks (see **Appendix C1** and **C2**). On the contrary, GP3 clinopyroxene rims could have equilibrated with a melt having the composition of the host whole rock based on the well-correlated values of Mg# clinopyroxene/liquid, respectively. Overall, the major element dataset on clinopyroxene rims and amphibole cores/mantles/rims obtained from sampled clasts from selected mass-flow deposits combined with calculated melt compositions (**Appendix C1**) were applied to explore temperature, depth, fO_2 and melt water content conditions, from which the investigated phenocrysts crystallised.

Clinopyroxene P-T

Pressure and temperature estimates of the clinopyroxene rims (n = 75) using the Putirka (2008), Neave and Putirka (2017) for geothermobarometry coupled with the hygrometer model of Waters and Lange (2015) obtained from plagioclase rims, are compared in **Table 6.3**. Results indicate rim growth due to the injected melt into the mush and their equilibration.

The results are further illustrated graphically in **Fig. 6.12**, where the calculated pressure and melt water contents, respectively, are presented as a function of temperature. The maximum estimated temperature difference of equilibration on clinopyroxene rims calculated from Putirka (2008) and Neave and Putirka (2017) is 22 °C, showing an overall reliable correspondence for the estimated temperatures.

GROWTH-PHASE	SAMPLE	ROCK TYPE	Clinopyroxene	T °C	T °C	P (MPa)	P (MPa)	Depth (km)			
				(Putirka, 2008)	(Neave & Putirka, 2017)	(Putirka, 2008)	(Neave & Putirka, 2017)				
GP2	LB LHF2-16	B T-A	LB LHF 2 16b Px C-4	922.43	942.27	624.60	515.90	23.57 19.47			
			LB LHF 2 16b Px C-5	930.74	949.31	719.68	601.84	27.16 22.71			
			LB LHF 2 16b Px B-4	900.31	919.93	533.09	397.60	20.12 15.00			
			LB LHF 2 16b Px B-5	920.92	939.46	689.29	559.61	26.01 21.12			
			LB LHF 2 16b Px B-6	932.72	952.54	690.82	589.32	26.07 22.24			
			LB LHF 2 16b Px F-7	923.80	945.32	568.00	479.45	21.43 18.09			
			LB LHF 2 16b Px D-4	938.47	958.56	728.47	633.97	27.49 23.92			
			LB LHF 2 16b Px D-6	903.40	926.86	373.93	290.26	14.11 10.95			
			LB LHF 2 16b Px D-7	915.11	933.37	677.21	537.36	25.56 20.29			
			LB LHF 2 16b Px D-10	926.83	949.65	538.92	468.12	20.34 17.66			
			LB LHF 2 16b Px D-13	928.35	947.78	674.53	564.91	25.45 21.32			
			LB LHF 2 16b Px D-14	939.13	960.77	681.10	604.83	25.70 22.82			
			LB LHF 2 16b Px E-4	913.07	934.36	517.48	416.37	19.53 15.71			
			LB LHF 2 16b Px E-5	928.86	948.93	648.97	547.94	24.49 20.68			
			LB LHF 2 16b Px A-8	922.59	941.98	669.37	551.38	25.26 20.81			
			GP2	LB LHF5-6	B T-A	LB LHF 5 6 Px C-4	938.74	957.92	763.73	638.48	28.82 24.85
						LB LHF 5 6 Px C-5	930.02	950.97	659.35	566.39	24.88 21.37
						LB LHF 5 6 Px C-6	926.89	946.63	660.30	552.55	24.92 20.85
						LB LHF 5 6 Px D-5	927.38	946.64	700.23	585.18	26.42 22.08
						LB LHF 5 6 Px D-6	925.67	946.28	620.20	521.82	23.40 19.69
LB LHF 5 6 Px B1-3	941.82	960.91				767.99	666.18	28.98 25.14			
LB LHF 5 6 Px B1-4	918.73	940.27				550.98	457.00	20.79 17.25			
LB LHF 5 6 Px B2-4	919.37	941.61				515.97	431.90	19.47 16.30			
LB LHF 5 6 Px B2-5	916.18	939.31				465.17	388.62	17.55 14.67			
LB LHF 5 6 Px E-3	929.92	950.66				645.67	552.19	24.37 20.84			
LB LHF 5 6 Px E-4	914.47	936.87				497.61	409.67	18.78 15.46			
LB LHF 5 6 Px E-7	921.21	941.88				595.52	493.58	22.47 18.63			
LB LHF 5 6 Px F-4	913.47	932.91				639.81	511.76	24.14 19.31			
LB LHF 5 6 Px F-5	925.37	945.74				619.86	519.06	23.39 19.59			
LB LHF 5 6 OIA-3	928.39	948.15				700.10	590.78	26.42 22.29			
LB LHF 5 6 OIA-4	923.45	942.63				683.74	563.84	25.80 21.28			
GP2	LB LHF4-12	B				LB LHF 4 12 Px1-5	924.62	943.93	687.81	570.38	25.96 21.52
						LB LHF 4 12 Px1-6	937.83	956.99	733.60	629.92	27.68 23.77
						LB LHF 4 12 Px7-3	929.27	947.48	748.00	622.05	28.23 23.47
						LB LHF 4 12 Px7-4	925.69	945.06	669.72	556.15	25.27 20.99
			LB LHF 4 12 Px8-4	921.21	940.24	683.91	559.39	25.81 21.11			
			LB LHF 4 12 Px8-6	922.41	939.83	741.10	598.66	27.97 22.59			
			LB LHF 4 12 Px8-7	941.49	960.93	785.69	684.43	29.65 25.83			
			LB LHF 4 12 Px9-3	942.55	961.94	758.46	661.23	28.62 24.95			
			LB LHF 4 12 Px9-4	941.17	960.31	756.64	635.42	28.55 24.73			
			GP2	TAU HFO 5	TB	TAU HF 5 Px3-4	930.93	950.78	684.58	581.32	25.83 21.94
TAU HF 5 Px4-4	930.00	950.02				663.91	562.69	25.05 21.23			
TAU HF 5 Px5-4	913.98	935.85				511.13	416.82	19.29 15.73			
TAU HF 5 Px5-5	913.24	932.53				642.23	512.28	24.23 19.33			
TAU HF 5 Px C-4	904.41	924.78				609.94	479.62	23.02 18.10			
GP2	TAU HFO 5	TB				LB HF 5 Px D-5	913.34	935.43	487.08	395.82	18.38 14.94
			LB HF 5 Px E-3	909.74	931.17	487.03	385.13	18.38 14.53			
			LB HF 5 Px F-4	919.21	938.86	614.65	499.24	23.19 18.84			
			LB HF 5 Px E-6	897.94	919.30	462.32	345.29	17.45 13.03			
GP1	KAU HF9-3	TB	KAU HF 93 Px2-4	983.23	1001.03	513.50	415.28	19.38 15.67			
			KAU HF 93 Px3-3	960.03	979.35	421.68	308.29	15.91 11.63			
			KAU HF 93 Px3-4	970.72	989.27	507.88	397.29	19.17 14.99			
			KAU HF 93 Px3-6	964.94	983.74	453.22	340.50	17.10 12.85			
			KAU HF 93 Px4-4	990.58	1008.52	544.43	455.64	20.54 17.19			
			KAU HF 93 Px4-5	988.30	1004.82	594.46	487.60	22.43 18.40			
			KAU HF 93 Px5-4	995.47	1012.66	626.35	532.56	23.64 20.10			
			KAU HF 93 Px5-6	1005.93	1023.80	635.57	561.69	23.98 21.20			
			KAU HF 93 Px5-8	980.08	998.60	481.55	386.58	18.17 14.59			
			KAU HF 93 Px7-4	995.88	1011.49	680.66	570.99	25.69 21.55			
			KAU HF 93 Px5-9	997.91	1011.50	779.53	648.73	29.42 24.48			
			GP1	KAU HF10-3	TB	KAU HF 10 3 Px1-4	981.12	997.77	578.42	463.00	21.83 17.47
						KAU HF 10 3 Px1-6	992.93	1010.51	578.34	487.62	21.82 18.40
						KAU HF 10 3 Px1-5	1002.61	1019.73	668.76	581.61	25.24 21.95
KAU HF 10 3 Px5-3	980.70	998.46				503.02	401.63	18.98 15.16			
KAU HF 10 3 Px5-4	999.66	1017.65				605.22	525.39	22.84 19.83			
KAU HF 10 3 Px6-4	973.49	991.46				491.54	382.01	18.55 14.42			
KAU HF 10 3 Px6-6	973.98	992.53				488.85	384.39	18.45 14.51			
KAU HF 10 3 Px7-3	992.35	1008.31				643.09	533.95	24.27 20.15			
GP3	TAU LH4-5	B T-A	Tau LHF 4 5 Px2-5	1003.43	1014.32	480.79	346.68	18.14 13.08			
			Tau LHF 4 5 Px2-6	1006.69	1020.49	417.79	315.47	15.77 11.90			
			Tau LHF 4 5 Px2-7	1030.41	1043.13	538.45	451.12	20.32 17.02			
			Tau LHF 4 5 oII-3	1022.24	1034.37	517.67	416.45	19.53 15.71			
			Tau LHF 4 5 oII-3	1024.03	1034.37	517.67	416.45	19.53 15.71			
GP3	TAU LHF1-20	TA	TAU LHF 1 20 Px3-3	1024.03	1034.37	517.67	416.45	24.01			

Table 6.3 Clinopyroxene geothermobarometry for GP (1,2,3) igneous rocks of Taranaki Volcano. B T-A: Basaltic trachy-andesite; B: Basalt; TB: Trachy basalt; TA: Trachy andesite. Depth calculated on the basis of the continental pressure gradient of 26.5 MPa/km.

However, the thermobarometric results based on the Putirka (2008) estimations carry much larger uncertainties, particularly regarding barometric constraints, and are therefore not further considered (see estimated P-T-H₂O estimations illustrated in Appendix C2).

Equilibration temperatures calculated for Taranaki clinopyroxene rims range between 919-1043 °C (Neave and Putirka, 2017; **Appendix C1**). Based on the Neave and Putirka (2017) geothermometry, equilibration temperatures of the individual growth-phases display different ranges (**Fig 6.12 A**). The highest temperatures have been obtained from GP3 and vary between 1020-1043 °C in trachy-andesitic and basaltic trachy-andesitic rocks, whereas GP2 exhibits the lowest temperature ranges of 919-961 °C in basalts, trachy-basalts and basaltic trachy-andesites (**Table 6.3**).

Pressure estimates obtained from clinopyroxene geobarometers vary significantly in the investigated Taranaki rocks. The pressure range of the growth-phases, after Neave and Putirka (2017), is 290-685 MPa (**Appendix C1**). The widest pressure ranges of 290-685 MPa are obtained from GP2, where the lowest value (290 MPa) is obtained from a basaltic trachy-andesite (*LB LHF2-16b*) and the highest value (685 MPa) from a basalt (*LB LHF4-12*), respectively (**Table 6.3**). However, due to the uncertainties of given pressures, the estimations may overlap, and pressure ranges cannot be distinguished individually.

Amphibole P-T

Subsequent studies pointed out that Taranaki amphiboles equilibrated with host magmas over a wide range of conditions leading to variable pressures (190-870 MPa) and temperatures (890-1150 °C; Price et al., 2016) with oxygen fugacity above the NNO buffer. Amphibole is a moderately common phase in the Taranaki volcanic rocks of the studied growth-phases (1-25 vol.%). Therefore, the amphibole geothermobarometers developed by Ridolfi et al. (2010) and Putirka (2016) were applied on the representative dataset of the GP1 and GP3 amphiboles (n = 24) coupled with the hygrometer model developed by Waters and Lange (2015) using plagioclase rims. Modelling results indicate temperatures between 899-1017 °C after the Ridolfi et al. (2010) and 900-981 °C after the Putirka (2016) geothermometer (**Table 6.4; Appendix C1**), exhibiting similar temperature ranges. Temperature estimation differences of the amphiboles between the two geothermometers are at most 36 °C and on average 11 °C, respectively. Results corroborate the estimated temperature and pressure conditions of amphibole equilibration of Price et al. (2016), based on an earlier dataset (**Fig. 6.12 A**).

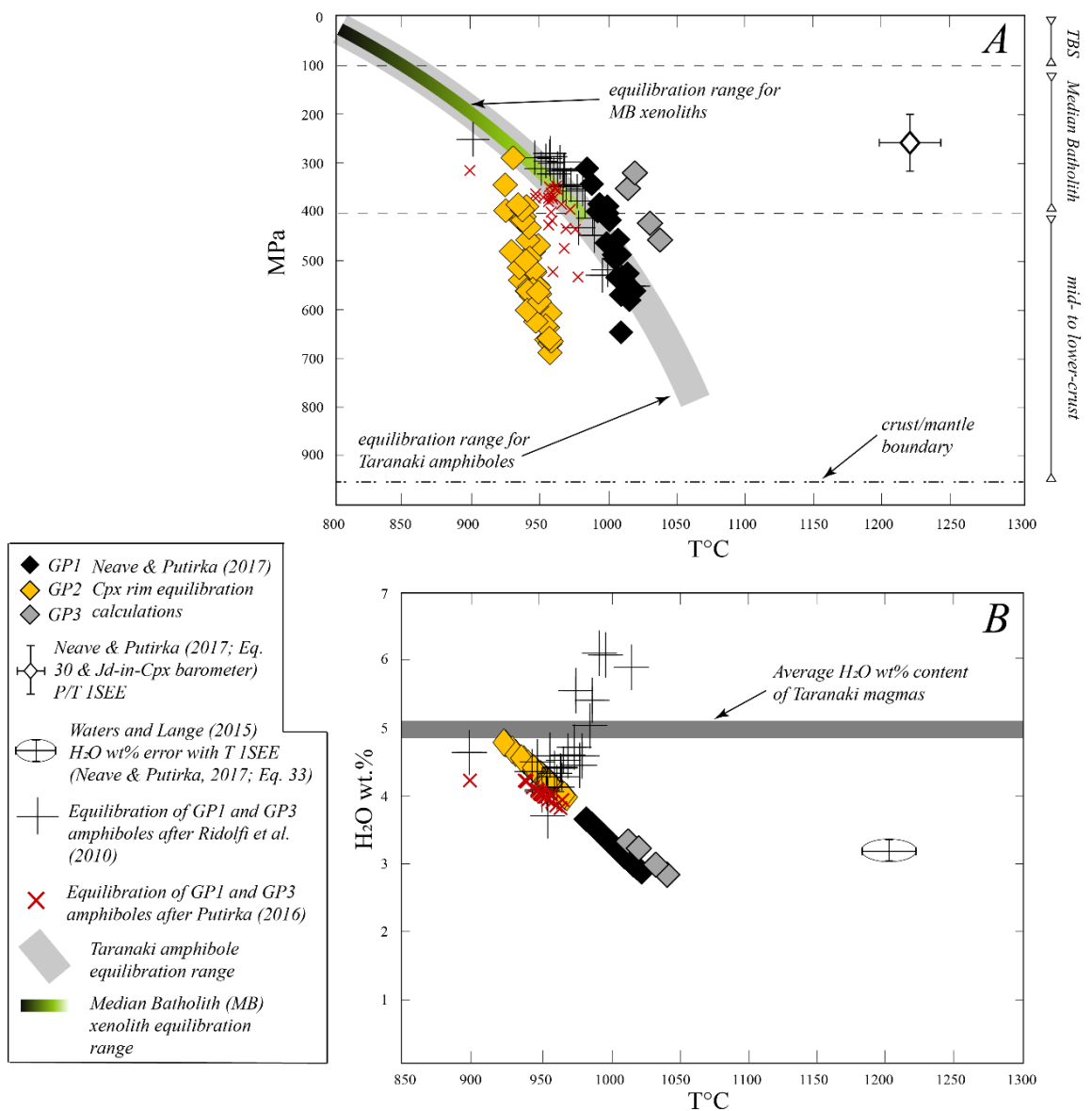


Fig. 6.12 A: Pressure - temperature equilibration for amphiboles and clinopyroxenes from the GP volcanic rocks of Taranaki Volcano based on the Putirka (2016), Neave and Putirka (2017), Ridolfi et al. (2010) geothermobarometers. For amphiboles, geobarometer uncertainty with respect to temperature is ± 22 °C, for pressure is a maximum of ± 61 MPa and for H₂O wt.%, is an average of ± 0.7 (Ridolfi et al., 2010). Maximum and average uncertainties are indicated by the length of the cross signs, respectively. Neave and Putirka (2017) geothermobarometer 1SEE for T is ± 42 °C (Eq. 33; Putirka, 2008) and for P is ± 0.96 kbar (Neave and Putirka, 2017; Jd-in-clinopyroxene barometer), respectively. See all geothermobarometer uncertainties summarized in **Chapter 3, Section 3.5**. Equilibration range for amphiboles of Taranaki volcanics and xenoliths after Price et al. (2016). Equilibration range for xenoliths of MB after Gruender et al. (2010) and Gründer et al. (2006). TBS: Sediments of the Taranaki Basin. Dashed lines indicate the transition between TBS-Median Batholith and Median-Batholith – mid- to lower-crust. Crust/mantle boundary is from Sherburn and White (2005) and Stern et al. (2006). **B:** Calculated H₂O wt.% melt contents for amphiboles and clinopyroxenes using the hygrometer of Waters and Lange (2015). Melt water content 1SEE is 0.35 wt.% coupled with T 1SEE of ± 42 °C after Neave and Putirka (2017; Eq. 33). Average H₂O wt.% for Taranaki magmas after Price et al. (2016).

Estimated pressures of GP1 and GP3 obtained from amphibole geobarometers vary between 251-552 MPa (Ridolfi et al. 2010) and 390-620 MPa (Putirka, 2016), the former displaying a wider range to lower and the latter to higher pressures (**Fig. 6.12 A**; **Appendix C1**). The representative results of GP3 in general exhibit a narrow range. In the most evolved, trachy-andesitic sample (*TAU LHF1-20*) of GP3, the pressure estimate based on amphibole compositions provides the lowest value by both geobarometers (250 and 390 MPa; **Table 6.4**).

The amphibole geothermobarometer has been applied previously to amphiboles from xenoliths that are thought to originate from the Median Batholith (MB; Gruender et al., 2010). The volcanic rocks obtained from the MB are gneisses, granodiorites and granites containing quartz and, in many cases, high amounts of biotite. Mineral chemical data obtained from Gruender et al. (2010) and Gründer (2006) exhibit temperature estimates of 710-970 °C and pressures of 45-370 MPa (**Fig. 6.12 A**). These values significantly overlap with the equilibration temperatures and pressures of the investigated GP1 and GP3 amphiboles, contributing to the hypothesis that the possible origin of the GP unit amphiboles is similar to the Median Batholith beneath Taranaki Volcano (**Fig. 6.12 A**). This scenario has been also postulated considering that the GP volcanic rocks may have been generated by melt:mush mixing processes at mid-crustal depths involving conceivable assimilants of the MB (see assimilant calculations and mixing modeling results in **Chapter 5**). However, isotopic analyses on the crystals in question would be required in order to determine whether they exhibit an antecrystic, xenocrystic or a mixed origin connected to the Median Batholith and underlying plutons.

Oxygen fugacity and H₂O wt.%

Oxygen fugacity estimations using the Ridolfi et al. (2010) geobarometer obtained from amphibole compositions display values of NNO+0.3 to NNO+0.8 (**Table 6.5**), showing that amphibole crystallization conditions occurred above the NNO buffer.

Water contents of GP1 and GP3 melts have been estimated using the combination of the Ridolfi et al. (2010) and Putirka (2016) geobarometers, the Putirka (2008) and Neave and Putirka (2017) geothermometers, the Waters and Lange (2015) hygrometer, and the amphibole and plagioclase rim compositions of certain volcanic rocks: (1) Amphibole compositions of GP1 and GP3 were used to estimate water contents of melts with which the amphiboles have been equilibrated (Ridolfi et al., 2010).

GROWTH-PHASE	SAMPLE	ROCK TYPE	Amphibole	T °C (Ridolfi et al. 2010)	T °C mean (Putirka 2016)	P (MPa) (Ridolfi et al. 2010)	P (Mpa) (Putirka 2016)	Depth (km)
GP1	HF10-3	TB	KAU HF 10 3 Amp1-1	966.05	954.82	314.07	440.00	11.85-16.60
			KAU HF 10 3 Amp1-2	970.67	968.07	344.71	450.00	13.01-16.98
			KAU HF 10 3 Amp1-3	948.98	949.48	310.35	440.00	11.71-16.60
			KAU HF 10 3 Amp1-4	967.40	961.19	348.22	510.00	13.14-19.25
			KAU HF 10 3 Amp1-5	975.46	960.58	357.98	460.00	13.51-17.36
			KAU HF 10 3 Px8b-1	965.44	961.35	316.50	440.00	11.94-16.60
			KAU HF 10 3 Px8b-2	961.04	960.99	309.95	430.00	11.70-16.23
			KAU HF 10 3 Px8b-3	962.82	964.74	297.86	420.00	11.24-15.85
			KAU HF 10 3 Px8b-4	979.49	974.69	353.64	470.00	13.34-17.74
			KAU HF 10 3 Px3-4	958.00	958.87	320.95	440.00	12.11-16.60
			KAU HF 10 3 Px3-5	955.09	959.25	287.20	430.00	10.84-16.23
			KAU HF 10 3 Px3-6	955.47	963.41	290.87	440.00	10.98-16.60
			KAU HF 10 3 Px3-1	976.72	947.47	432.26	540.00	16.31-20.38
			KAU HF 10 3 Px3-2	993.33	958.80	528.99	620.00	19.96-23.40
			KAU HF 10 3 Px3-3	997.81	962.00	519.17	580.00	19.59-21.89
GP1	HF9-3	TB	KAU HF 93 PxA-1	965.03	958.64	345.95	530.00	13.05-20.00
			KAU HF 93 Px6-4	986.54	971.55	413.69	490.00	15.61-18.49
			KAU HF 93 PxA-3	952.23	961.81	294.57	480.00	11.12-18.11
			KAU HF 93 PxA-4	956.05	958.46	299.93	480.00	11.32-18.11
			KAU HF 93 Px6-1	981.16	978.92	378.27	540.00	14.27-20.38
			KAU HF 93 Px6-2	944.75	949.32	289.68	450.00	10.93-16.98
			KAU HF 93 Px6-3	956.12	966.00	280.06	460.00	10.57-17.36
			KAU HF 93 PxA-2	988.18	970.59	447.40	540.00	16.88-20.38
GP3	TAU LHF4-5	B T-A	Tau LHF 4 5 Gmpx-3	1016.46	980.39	551.55	590.00	20.81-22.26
GP3	TAU LHF1-20	TA	TAU LHF 1 20 Px1-1	899.31	900.43	251.12	390.00	9.48- 14.72

Table 6.4 Amphibole geothermobarometry for GP (1,3) igneous rocks of Taranaki Volcano. TB: Trachy basalt; B T-A: Basaltic trachy-andesite; TA: Trachy andesite. Depth calculated on the basis of the continental pressure gradient of 26.5 MPa/km. Temperature means after Putirka (2016) is calculated using equation 5 and 6.

(2) Average plagioclase rim compositions coupled with the amphibole and clinopyroxene geothermobarometry P-T estimations (Putirka, 2008, 2016; Neave and Putirka, 2017) have been used for the hygrometry model of Waters and Lange (2015) to estimate the water contents of the final melts that remobilized the crystals. Results of the two approaches to Taranaki mineral compositions are compared in **Table 6.5** and are illustrated in **Fig. 6.12 B**.

Using approach (1), H₂O contents of GP1 and GP3 melts based on the amphibole compositions have been estimated to occur between 4-6 wt.% (Ridolfi et al., 2010), whereas using approach (2), melt water contents based on the Putirka (2016) thermobarometers combined with the Waters and Lange (2015) hygrometer yield values of a significantly narrower range between 3.7-4.3 wt.% (**Table 6.5**). Additionally, melt water content estimations based on the clinopyroxene geothermobarometers display differences in the case of GP1 and GP3 estimations compared to GP2. H₂O estimations of GP1/GP3 melts based on the Neave and Putirka (2017) geothermometry exhibit lower values (2.9 -3.7 wt.%) than those of GP2 (3.9-4.8 wt.%; **Fig. 6.12 B**). Compared to the water contents calculated by Putirka (2008), results show higher ranges of 3-4.1 wt.% for GP1/GP3 and 4.3-5.2 wt.% for GP2, respectively (**Table 6.5**).

Additionally, based on both the amphibole compositions (approach 1 and 2) and on the clinopyroxene compositions, water contents of the melts that interacted with the crystal cargo during the growth cycles are estimated to be between the expected values of 3.5-8.5 wt.% (Price et al., 2016) excluding the estimations using the Neave and Putirka (2017) geothermometer for GP1 and GP3, which gave lower H₂O wt.% estimates (**Fig. 6.12 B**).

SAMPLE	ROCK TYPE	Mineral	ANNO	APPROACH (1)		APPROACH (2)			
				H ₂ O wt% Ridolfi et al. (2010)	H ₂ O wt% Putirka (2008)	H ₂ O wt% Putirka (2016)	H ₂ O wt% Putirka (2017)		
GPI	HF10-3	TB	KAU HF 10 3 Amp1-1	0.7	4.12		4.14		
			KAU HF 10 3 Amp1-2	0.6	4.51		3.88		
		KAU HF 10 3 Amp1-3	0.7	4.39		4.25			
		KAU HF 10 3 Amp1-4	0.6	4.42		4.02			
		KAU HF 10 3 Amp1-5	0.7	4.65		4.02			
		KAU HF 10 3 Ps8b-1	0.7	4.28		4.02			
		KAU HF 10 3 Ps8b-2	0.8	4.18		4.03			
		KAU HF 10 3 Ps8b-3	0.7	3.94		3.94			
		KAU HF 10 3 Ps8b-4	0.6	4.33		3.76			
		KAU HF 10 3 Ps3-4	0.7	4.49		4.07			
		KAU HF 10 3 Ps3-5	0.7	3.89		4.05			
		KAU HF 10 3 Ps3-6	0.7	3.93		3.99			
		KAU HF 93 Ps6-4	0.6	5.04		3.84			
		KAU HF 10 3 Ps3-1	0.6	5.66		4.28			
	KAU HF 10 3 Ps3-2	0.4	6.32		4.08				
	KAU HF 10 3 Ps3-3	0.5	6.29		4.00				
	HF9-3	TB	KAU HF 93 PsA-1	0.4	4.29		4.09		
			KAU HF 93 PsA-2	0.5	3.88		4.09		
			KAU HF 93 PsA-3	0.6	3.86		4.09		
			KAU HF 93 Ps1-4	0.3	4.49		3.71		
			KAU HF 93 Ps6-1	0.6	4.22		4.27		
			KAU HF 93 Ps6-2	0.8	3.43		3.94		
	HF10-3	TB	KAU HF 10 3 Ps1-4			3.70		3.34	
			KAU HF 10 3 Ps1-5			3.49		3.73	
			KAU HF 10 3 Ps1-6			3.32		3.55	
			KAU HF 10 3 Ps3-3			3.71		3.63	
			KAU HF 10 3 Ps3-4			3.37		3.21	
KAU HF 10 3 Ps6-4					3.84		3.27		
KAU HF 10 3 Ps6-6					3.83		3.14		
KAU HF 10 3 Ps7-3					3.50		2.95		
KAU HF 10 3 Ps7-4					3.56		3.38		
KAU HF 10 3 Ps8a-4					3.38		3.16		
KAU HF 10 3 Ps8a-5					3.41		3.16		
HF9-3			TB	KAU HF 93 Ps2-4			3.66		3.40
				KAU HF 93 Ps3-3			4.09		3.17
				KAU HF 93 Ps3-4			3.89		3.02
				KAU HF 93 Ps3-6			4.00		3.38
				KAU HF 93 Ps4-4			3.53		3.05
	KAU HF 93 Ps4-5				3.57		3.51		
	KAU HF 93 Ps5-4				3.44		3.49		
	KAU HF 93 Ps5-6				3.26		3.21		
	KAU HF 93 Ps5-8				3.72		3.76		
KAU HF 93 Ps7-4			3.44		3.09				
KAU HF 93 Ps5-9			3.40		3.12				
GP2	LB LHF2-16	B T-A	LB LHF 2 16b PsC-4			4.69			
			LB LHF 2 16b PsC-5			4.34		4.18	
			LB LHF 2 16b PsB-4			3.16		4.75	
			LB LHF 2 16b PsB-5			4.74		4.37	
			LB LHF 2 16b PsB-6			4.50		4.11	
			LB LHF 2 16b PsF-7			4.68		4.25	
			LB LHF 2 16b PsD-4			4.39		4.00	
			LB LHF 2 16b PsD-6			5.09		4.61	
			LB LHF 2 16b PsD-7			4.86		4.49	
			LB LHF 2 16b PsD-10			4.62		4.17	
			LB LHF 2 16b PsD-13			4.59		4.20	
			LB LHF 2 16b PsD-14			4.38		3.96	
			LB LHF 2 16b PsE-4			4.89		4.46	
			LB LHF 2 16b PsE-5			4.58		4.18	
			LB LHF 2 16b PsA-8			4.70		4.32	
			LB LHF 5 6 PsC-4			4.39		4.01	
			LB LHF 5 6 PsC-5			4.36		4.14	
			LB LHF 5 6 PsC-6			4.62		4.23	
	LB LHF 5 6 PsD-5			4.61		4.23			
	LB LHF 5 6 PsD-6			4.64		4.23			
	LB LHF 5 6 PsB1-3			4.33		3.96			
	LB LHF 5 6 PsB1-4			4.78		4.33			
	LB LHF 5 6 PsB2-4			4.77		4.32			
	LB LHF 5 6 PsB2-5			4.83		4.37			
	LB LHF 5 6 PsE-3			4.56		4.15			
	LB LHF 5 6 PsE-4			4.87		4.41			
	LB LHF 5 6 PsE-7			4.73		4.32			
	LB LHF 5 6 PsF-4			4.89		4.49			
	LB LHF 5 6 PsF-5			4.65		4.24			
	LB LHF 5 6 OIA-3			4.59		4.20			
	LB LHF 5 6 OIA-4			4.69		4.30			
	LB LHF4-12	B	LB LHF 4 12 Ps1-5			4.66		4.28	
			LB LHF 4 12 Ps1-6			4.40		4.03	
			LB LHF 4 12 Ps7-3			4.57		4.21	
			LB LHF 4 12 Ps7-4			4.64		4.26	
			LB LHF 4 12 Ps8-4			4.73		4.35	
LB LHF 4 12 Ps8-6					4.71		4.36		
LB LHF 4 12 Ps8-7					4.33		3.96		
LB LHF 4 12 Ps9-3					4.31		3.94		
LB LHF 4 12 Ps9-4					4.34		3.97		
TAU HFO 5			TB	TAU HF 5 Ps3-4			4.54		4.15
TAU HF 5 PsA-4						4.56		4.16	
TAU HF 5 Ps5-4						4.88		4.43	
TAU HF 5 Ps5-5				4.89		4.50			
TAU HF 5 PsC-4				5.08		4.66			
TAU HF 5 PsD-5				4.89		4.44			
TAU HFO 5	TB	LB HF 5 PsE-3			4.96		4.53		
		LB HF 5 PsE-4			4.77		4.38		
		LB HF 5 PsE-6			5.21		4.76		
GP3	TAU LHF4-5	B T-A	Tau LHF 4 5 Gmpx-3	0.8	6.07		3.88		
			TAU LHF 1 20 Ps1-1	0.7	4.55		4.25		
	TAU LHF4-5	B T-A	Tau LHF 4 5 Ps2-5			3.54		3.35	
			Tau LHF 4 5 Ps2-6			3.48		3.24	
			Tau LHF 4 5 Ps2-7			3.07		2.86	
	TAU LHF1-20	TA	Tau LHF 4 5 oII-3			3.21		3.00	
TAU LHF 1 20 Ps3-3					3.19		3.03		

Table 6.5 H₂O wt.% estimations based on the hygrometer developed by Waters and Lange (2015) using average plagioclase rim compositions within each GP along with the clinopyroxene and amphibole geothermobarometers. TB: trachy basalt; B T-A: Basaltic trachy-andesite; B: Basalt; TA: trachy andesite.

Geothermobarometry and hygrometry comparison of the growth cycles

Geothermobarometry and hygrometry estimations have been applied to GP1 and GP3 amphiboles and clinopyroxenes. Thus, both temperature/pressure and H₂O wt.% estimates based on the two mineral phases are comparable within these growth cycles (**Table 6.6**). Considering both the geobarometers based on the amphibole compositions (Ridolfi et al., 2010; Putirka, 2016) and the geothermometers based on the clinopyroxene compositions (Putirka, 2008; Neave and Putirka, 2017, temperature estimates in general are higher in GP3 compared to GP1. Overall, amphibole compositions display a lower and narrower range of temperatures, whereas melt water contents have higher and narrower range for both GP1 and GP3.

The range of pressures is variable within and between the individual growth cycles. Thus, taking into account the uncertainties, estimated pressures are indistinguishable between the GP units. Therefore, considering pressure range approximations based on both amphibole and clinopyroxene compositions, they exhibit mid- to lower-crustal depths from 26.5±7.5 to 11.3±7.5 km (based on 2SEE after Neave and Putirka, 2017) suggesting (1) melts contributed partly to the crystallization of the MB, and (2) possibly polybaric melt-clinopyroxene rim equilibration environments that may have involved the MB.

	<i>GP1</i>	<i>GP3</i>	<i>GP1</i>	<i>GP3</i>	<i>GP1</i>	<i>GP3</i>
	<i>T</i>		<i>P</i>		<i>H₂O wt%</i>	
<i>PUTIRKA (2008)</i>	960-1006	1006-1031	421-780	417-637	3.2-4.1	2.9-3.8
<i>RIDOLFI ET AL. (2010)</i>	944-998	899-1017	280-529	251-552	3.4-6.3	3.7-4.3
<i>PUTIRKA (2016)</i>	947-979	900-981	420-620	390-590	4.5-6	3.8-4.3
<i>NEAVE & PUTIRKA (2017)</i>	979-1024	1020-1044	308-649	315-452	3-3.6	2.8-3.4

Table 6.6 GP1 and GP3 P-T-H₂O comparison based on the clinopyroxene and amphibole compositions, the geothermobarometers (Putirka, 2008, 2016; Neave and Putirka, 2017; Ridolfi et al., 2010; Ridolfi and Renzulli, 2012) and the hygrometer by Waters and Lange (2015).

The temporal variation of equilibration conditions

Based on the clinopyroxene rim equilibration results, the temporal changes of crystallization conditions were investigated for GP2 (c. 55-40 ka) based on four sampled volcanoclastic mass-flow packages (**Fig. 6.13**; P-T conditions after modeling results using the thermobarometer by Neave and Putirka, 2017). Results show overlapping clinopyroxene rim equilibration temperatures over time (i.e. from LBLHF5 towards TAUHF0 mass-flow packages) without any consistency. Further, crystallization depths exhibit similar patterns to the temperature ranges, however, overlapping is characteristic,

and thus there is no consistency between clinopyroxene equilibration depths and stratigraphic position of the mass-flow packages.

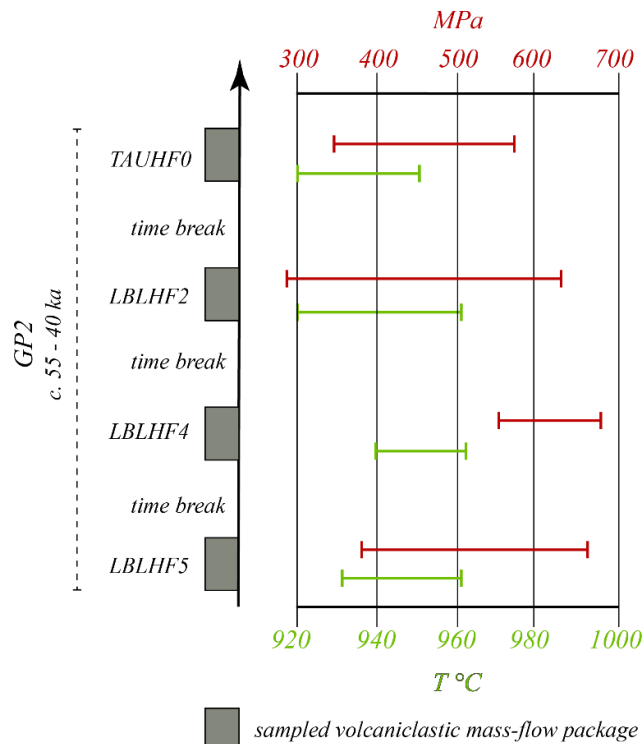


Fig. 6.13 Temporal stratigraphic illustration of the GP2 volcanoclastic mass-flow packages and the clinopyroxene rim equilibration conditions of their sampled pyroclasts (results after the thermobarometer by Neave and Putirka, 2017). Black arrow indicates time. Time break corresponds to the presence of paleosol between the volcanoclastic deposits. The age-range is considered as a maximum for GP2.

6.6.1.3 Aspects of the ascending melts

Crystal mush generation and recycling are well-linked processes. Compared to the characteristics of fully solidified plutons, mush zones are rheologically transient magmatic bodies that are able to defrost due to reheating episodes (Burgisser and Bergantz, 2011) or to the influx of new hot, volatile-rich magma resulting in gas sparging (Bachmann and Bergantz, 2006), and thus can incur significant amounts of partial melting by defrosting the crystal cargo (Huber et al., 2010).

Based on the thermobarometric and hygrometric estimates introduced in **Section 6.1.2**, the behaviour of ascending melts and the affected mush zone can be characterised from a temporal, kinematic and chemical perspective. An overall proposition is that the temperature and water content of the rising melts and the equilibration conditions of antecrystic (in this study they are considered as antecrysts) clinopyroxene rims observed in this study are distinct within the individual growth cycles of Taranaki Volcano

considering the time period of 65-34 ka. Thus, within each growth-phase, different regions of the vertically extended mush domain within the mid-crust are affected by ascending magmas with various properties.

The thermobarometric estimates (Ridolfi et al. 2010; Putirka, 2016) based on the amphibole compositions indicate that the amphiboles are representative of the affected mush zone. Additionally, comparing the results to Taranaki amphibole and xenolith thermobarometry calculations (Price et al., 2016; Gruender et al., 2010), they also suggest that the studied crystal cargo may involve components of the Median Batholith (**Fig. 6.12 A**). Hygrometry results based on the amphibole compositions corroborate this statement, exhibiting melt water contents at the mush zone ranging between 3.8 – 6.2 wt.% (considering both geothermometer results combined with the hygrometer after Ridolfi et al., 2010; Waters and Lange, 2015; Putirka, 2016) and relatively low temperatures (**Fig. 6.12 B**).

GP1 and GP3 melts that equilibrated with the clinopyroxene rims exhibit higher temperatures and lower water contents (2.9-3.7 wt.%; **Fig. 6.14 A**) suggesting that these are hotter magmas due to their less hydrous nature. Thus, they are less viscous (crystallinity of collected vesicular pyroclasts ~30-45 vol.%; **Appendix C1**) and ascended to and crystallised at shallower levels. This suggests that these magmas probably were less likely to stall in the subvolcanic magma storage system.

In contrast, GP2 melts are more hydrous (3.9-4.8 wt.%; Waters and Lange, 2015; Neave and Putirka, 2017) and display lower temperature ranges (**Fig. 6.12 B**), which may be overlapped (considering the uncertainty values) with the mush zone amphibole representatives (**Fig. 6.12 A, B**) leading to the conclusion that GP2 liquids share similarities with magmas that made up the mush domain and possibly parts of the Median Batholith. For these ascending GP2 hydrous magmas, water saturation and exsolution would have occur at greater depths (**Fig. 6.14 A**; e.g. Zellmer et al., 2016), thus degassing at depth will induce an increasing viscosity controlled by crystallinity, volumetric proportions of exsolved gas and the characteristics of the residual melt (Whittington et al., 2009; Pistone et al., 2013). These factors might lead to the undercooling of these magmas (Hammer and Rutherford, 2002; Pistone et al., 2016) promoting efficient crystallization (Pistone et al., 2016).

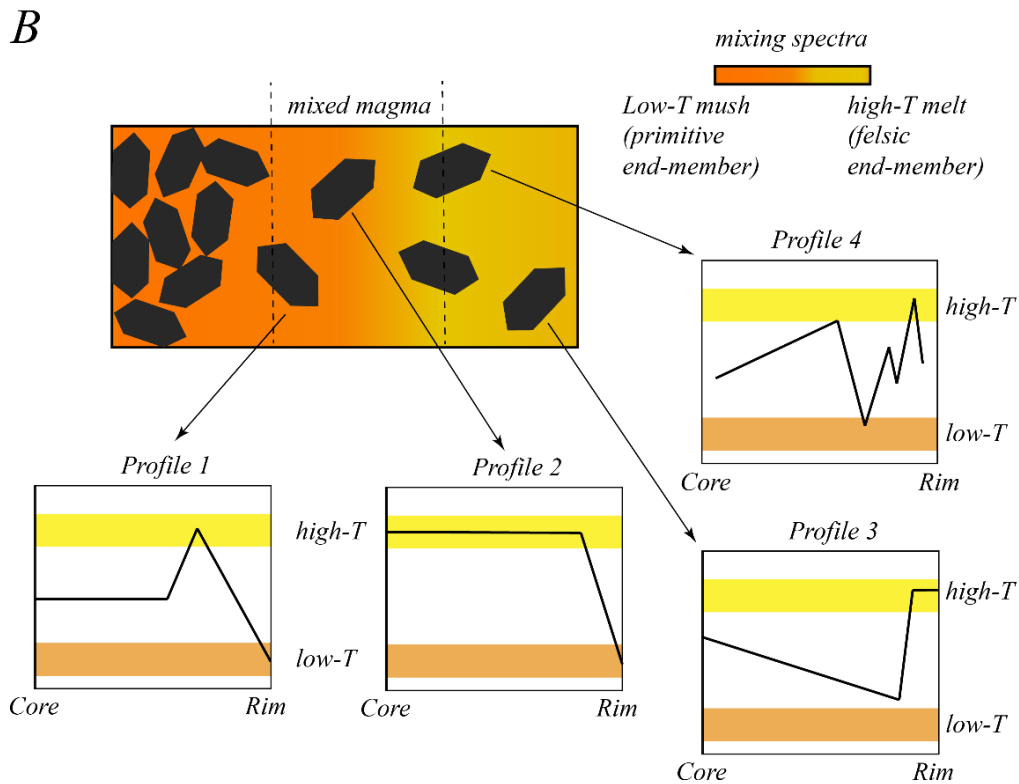
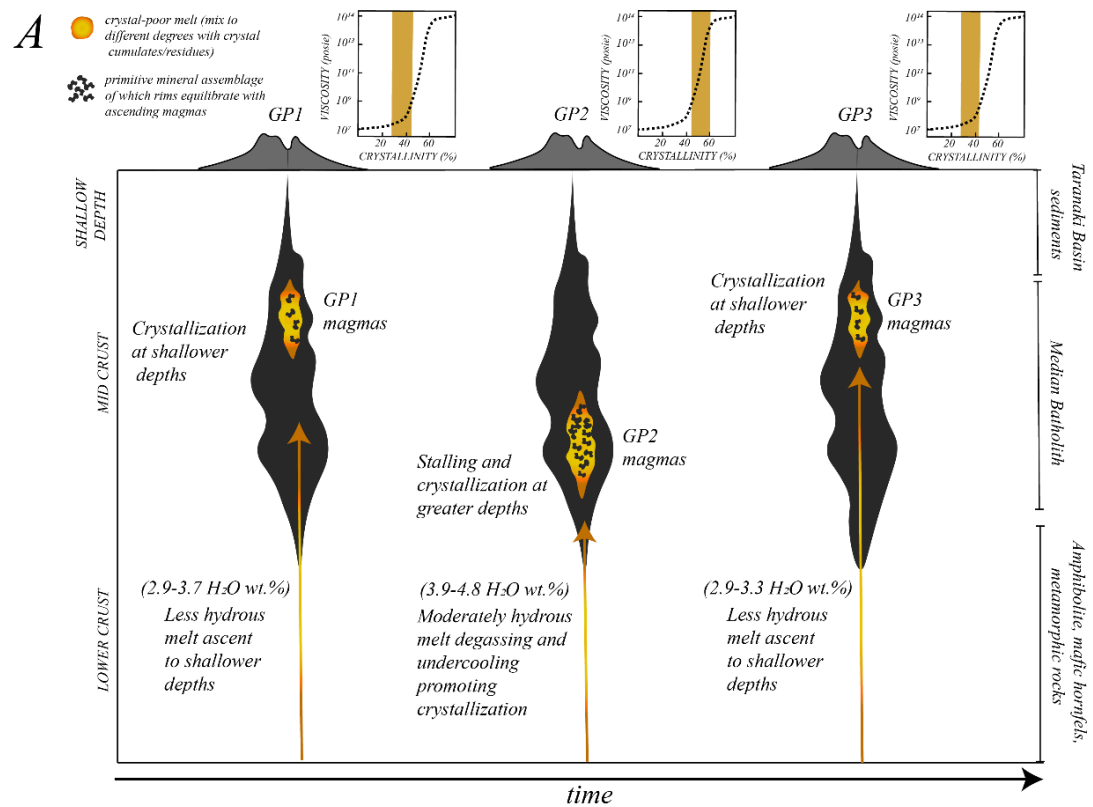
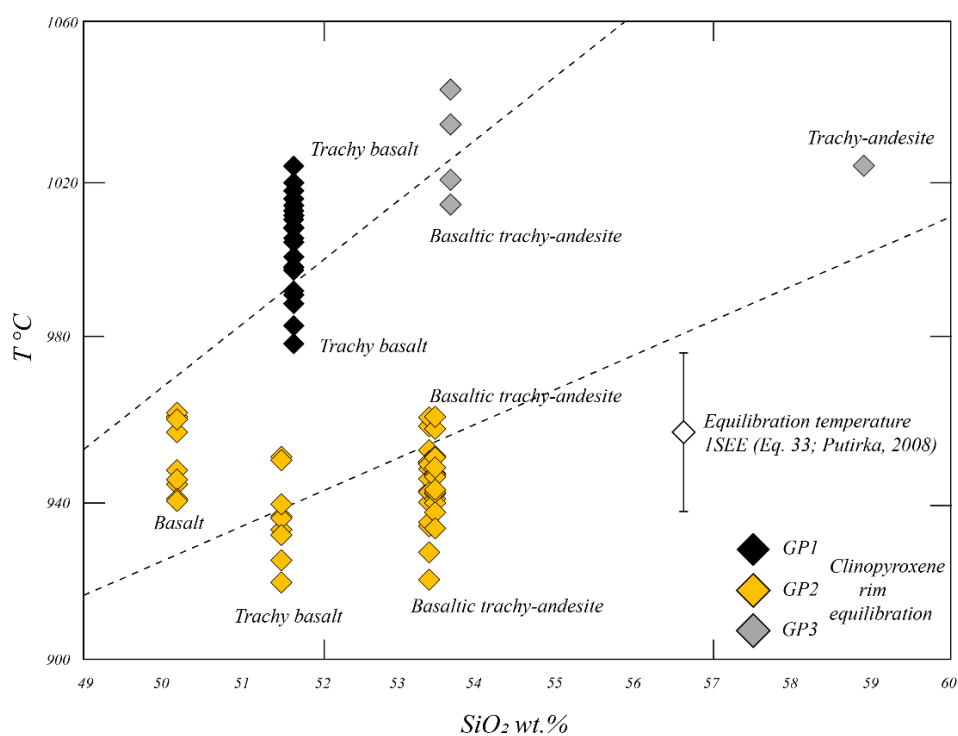


Fig. 6.14 A: Schematic representing the different ascending magmas of GP1, GP2 and GP3 over time (indicated by black arrow) based on the hygrometry (after Neave and Putirka, 2017) and geothermobarometry P-T-H₂O estimations (for details see **Section 6.1**). Viscosity vs crystallinity after Lejeune and Richet (1995) indicating the viscosity ranges of generated magmas during edifice growth cycles. Arrows show trachyandesitic melt ascent with water contents as indicated. **B:** Zoomed in spatial illustration of the melt-mush interface and the generated Mg# zoning profiles of clinopyroxenes due to the low-T mush incorporation into high-T melts.

Therefore, H₂O degassing-induced crystallization exerts a primary control on the stalling of magmas that are similar to GP2 and make up the mush domain. During ascent, degassing-induced crystallization further promotes slow cooling and phenocryst growth, which may clog melt migration pathways. However, GP2 magmas, with crystallinity of ~50-61 vol%, that are more likely to stall within the plumbing system (see crystallinity proportion calculations of GP2 volcanics in **Appendix C1**), did ultimately erupt. This may be the results of the edifice load influence on mid-crustal processes (see **Chapter 5, Section 5.7**) in cooperation with wall rock erosion during magma ascent, widening existing ascent paths and creating new ones (Bouilhol et al., 2015).

Overall, considering the thermobarometry and hygrometry results and the viscosity differences of GP1/3 and GP2, it is apparent that more felsic rocks containing the analysed clinopyroxenes exhibit higher rim-equilibration temperatures, while more mafic rocks display rim-equilibration at lower temperatures (**Fig. 6.15**). This corroborates our finding that more mafic rocks contain higher amount of antecrysts resulting from the low melt:mush mixing ratio and therefore lower rim equilibration temperatures (see **Chapter 5**). In contrast, more felsic rocks are comprised of lower amounts of antecrysts, but due to the melt characteristics these magmas were likely to stall by degassing induced crystallization, resulting in higher rim-equilibration temperatures (**Fig. 6.15**) and higher melt:mush mixing ratios.



◀**Fig. 6.15** Clinopyroxene rim equilibration estimations (Neave and Putirka, 2017) as the function of SiO₂ wt.% of the whole rocks. Dashed lines indicate a representative range of increasing T with increasing SiO₂ considering the rock types of the volcanics, i.e. from basaltic to trachytic compositions. Neave and Putirka (2017) geothermobarometer 1SEE for T is ± 42 °C (Eq. 33; Putirka, 2008). Collected samples as the following: Basalt: *LB LHF4-12*; Trachy-basalt: *KAUHF9-3*, *KAUHF10-3*, *TAUHFO.5*; Basaltic trachy-andesite: *LBLHF2-16b*, *LBLHF5-6*, *TAULHF2-17*; Trachy andesite: *TAULHF1-20*.

6.6.2 Crystal cargo characteristics outlined by the CPC

6.6.2.1 Interpretation of crystal patterns

Andesitic stratovolcanoes erupt similar crystal-rich andesite over thousands of years, suggesting periodic recharge of their magma system with new material from depth (Eichelberger et al., 2006). Mingling and mixing textures are common in andesites suggesting more complex magma systems (Price et al., 2005). The recharge supply may be basaltic magma derived from partial melting of the mantle wedge according to high-Mg-basalts (Grove, 2002), modified basalt, andesite derived from a combination of crystallization of the primary basalt (Grove et al., 2002) and or melting crustal rocks within the lower crust or upper mantle (Price et al., 2005). At Taranaki Volcano, periodic recharge has been estimated approximately on a 1.4 kyr timescale. Additionally, shorter period recharge events are also present at intervals of 0.4-0.5 kyr (Turner et al., 2008a, b). Recharging melts may involve trachyandesitic/trachydacitic compositions at Taranaki Volcano during the growth cycles (see details in **Chapter 5**). The investigated mineral phases of the pumiceous and scoriaceous samples from the GP units elucidate a complex, spatially, geochemically and temporally variable vertical plumbing system, with its magmatic processes recorded by its crystal populations. In the following, the most common crystal patterns and textures observed in plagioclase and clinopyroxene crystals are interpreted (see CPC coding in **Table 6.2**):

Plagioclase crystal patterns

- [Pattern C(pa)]: Patchy zoning of cores suggests growth at depth, which were partially resorbed during ascent (Humphreys et al., 2006; Price et al., 2005, Turner et al., 2008a).
- [Pattern M(os)]: Oscillatory zonation of mantles reflects near equilibrium conditions and diffusion-controlled mantle growth (Anderson and Bass, 1984; Pierce and Kolisnik, 1990; Pearce and Parkinson, 1993) and connected minor resorption surfaces might mirror minimal thermal and compositional fluctuation (<5 An mol%; Ginibre et al., 2002). On the other hand, major compositional

oscillations (>10 mol%) with minor wavy dissolution (i.e. resorption) surfaces are produced by crystal convection along minor thermal and compositional gradients (Pierce and Kolisnik, 1990; Giuffrida and Viccaro, 2017). However, such types of zoning within the rims denote late-stage dynamic conditions of the magmatic system or stalling at shallow depths (Viccaro et al., 2010, 2014).

- [Pattern (in,ex)]: Single or multiple, internal or external resorption surfaces are formed due to changes of the surrounding melt caused by changes in temperature, pressure, volatile content or composition (Pierce and Kolisnik, 1990; Singer et al., 1995).
- [Pattern (un,fl)]: There are no chemical zonations or textural identifiers observed reflecting non-disturbed crystallization connected to stable magmatic chemical and physical parameters, or indicating long term residence leading to complete diffusional equilibration.
- [Pattern R₁(en)] or [Pattern R₂(os)]: Rim enrichment in Li and Ba is connected to shallow depth processes prior to eruption (Berlo et al., 2004; Kent et al., 2007, Charlier and Grove, 2012).

Clinopyroxene crystal patterns

- [Pattern C(pa)]: Patchy zoning is most likely generated either due to (i) re-equilibration through Fe-Mg diffusion or (ii) to partial dissolution (Welsch et al., 2016; Shane and Coote, 2018). The latter would be accompanied by sharp Cr content change from core to mantle.
- [Pattern C(co,en)]: Corroded, Cr-rich cores indicate an origin from a mafic, high-T magma, because Cr concentration in clinopyroxenes are mainly controlled by the melt composition rather than by diffusion. The pattern also indicates dramatic changes in pressure and temperature affecting the core habitus, thus the pattern can be attributed to magma decompression.
- [Pattern M(en)]: Cr-enriched mantles suggest sudden temperature change due to the crystal interaction with a hotter, Cr-rich incoming melt (cf. Feng and Zhu, 2019a, b). Relatively Mg#-rich mantles with often occurring resorption surfaces are caused by thermal erosion due to higher-T magma interaction with the mush zone or by magma decompression (Zhu and Ogasawara, 2004; Zhu et al., 2012; Feng and Zhu, 2018).

- [Pattern R/M(os)]: Thin oscillatory zonation (<10 μm) can be explained by small-scale crystallization kinetic effects at the crystal-melt boundary or repeated changes in growth conditions influenced by external factors (Ginibre et al., 2002; Elardo and Shearer, 2014). Thick oscillatory zonation (>10 μm) likely reflects significant changes in growth conditions rather than only the effects of crystallization kinetics (Feng and Zhu, 2019a, b). This is supported by the jagged or rounded oscillatory bands observed within the crystals that can be attributed to resorption (**Fig. 6.5 A**).
- [Pattern R/M(se)]: Sector zoning develops under near-equilibrium conditions at slow growth rates and at relatively low undercooling (Ubide et al., 2019). A certain amount of undercooling refers to the temperature difference between the liquidus and the system (Mollo and Hammer, 2017).
- [Pattern R/M/C(un,fl)]: Lack of zonation in analysed elements and textural non-disturbance correspond to stable magmatic conditions such as composition, temperature, pressure or volatile content, or indicating long term residence leading to complete diffusional equilibration.

6.6.2.2 Overview of the clinopyroxene crystal patterns

The CPC contributed to distinguish between textural and chemical patterns of certain crystal regions such as cores, mantles and rims of the plagioclase and pyroxene crystals. These patterns could then be connected to specific magmatic processes. Therefore, the CPC method minimizes misinterpretations of crystal regions and sub-pattern identifications. The use of this method allows a description and analysis of complex crystal populations focusing on multiple elemental distributions. On the other hand, the classification can be applied worldwide to characterize complex mineral phases analysed by different instruments (EMPA, LA-ICP-MS, etc.) focusing on numerous elemental distributions or textural features and/or the connection of these.

The investigated crystal patterns of the individually examined clinopyroxene rims, mantles and cores are summarized in **Appendix C1**. The investigated elements are major elements (Ca), minor elements (Na, Al), compatible metals (Cr, Ni, Sc), incompatible elements (La, Nd, Zr) and mildly incompatible elements (Ti, V). The aim of the investigation of certain crystal regions and their connection to each other was to find recurrent crystal pattern characteristics. They are referred to as ‘crystal pattern clusters’

representing certain magmatic processes. Thus, they assist to identify repeatedly occurring magmatic histories within the Taranaki crystal cargo. They are grouped and interpreted as follows:

(i) Rim crystal pattern clusters

Major element (Ca) distributions exhibit unzoned, flat textures of pyroxene rims mainly coupled with oscillatory, sector zonation in minor elements (Na, Al) and diverse crystal patterns of compatible metals (Cr, Ni, Sc) such as oscillatory, sector zonation, depletion, enrichment or unzoned textures (**Appendix C1**). Rims mainly exhibit unzoned profiles in Cr that are characteristic for incompatible elemental patterns as well.

Interpretation: Crystal pattern clusters characterising the clinopyroxene rims of the individual growth cycles display diverse magmatic processes. However, there are no specific patterns occurring regularly, thus, the diversity of crystal pattern clusters suggests variable magmatic conditions and interaction of diverse magmas in the different segments of the plumbing system prior to eruption.

(ii) Mantle crystal pattern clusters

Major elemental distribution patterns of clinopyroxene mantles show unzoned profiles similarly to rims. Minor and incompatible elements on the other hand show occurring oscillatory and or sector zonation (**Appendix C1**). Additionally, GP1 clinopyroxene mantles exhibit more complex patterns such as patchy zoning with external resorption or enriched zones especially in the case of compatible metals and incompatible elements. Cr and Ni enrichment in mantles is characteristic within all GPs.

Interpretation: Similarly, to the clinopyroxene rim formation, mantle crystal patterns tend to suggest diverse magmatic processes within different segments of the plumbing system connected to chemically different magmas. There is no consistency between crystal pattern clusters and individual growth phases suggesting that observed phenocryst mantles characterise the overall spatial, temporal and chemical variability of the mush domain beneath Taranaki Volcano.

(iii) Core crystal pattern clusters

The majority of clinopyroxene cores display external resorption and corroded textures and textural patterns that are also connected to enrichment in Cr, patchy or less commonly sector zoning of most of the analysed elements excluding Ca (**Appendix C1**).

Interpretation: Clinopyroxene cores of the GP units texturally and chemically exhibit antecrystic origins, with crystals possibly originating from depth and picked-up by ascending melts.

6.6.2.3 Transect profiles elucidating spatial relationships of the melt-mush interface

Calc-alkaline rocks often exhibit petrological and chemical evidence of magma mixing indicating that mixing is one of the main process responsible for the generation of calc-alkaline andesite magmas (Kay and Kay, 1985; Sakuyama, 1981; Streck et al., 2007). Observed crystal patterns of the mush zone beneath Taranaki Volcano corroborate andesite generation by melt-mush mixing. Studied clinopyroxene phenocrysts record subtle geochemical variations, particularly that of Mg-number accompanied by Al₂O₃ variability (**Fig. 6.16**).

Independently from GP unit origin, certain types of Mg# zoning patterns are present within the investigated clinopyroxene population. Additionally, the various degree of resorption of cores may indicate thermal erosion prior to mantle growth (Nakagawa et al., 2002). On the other hand, Cr-rich corroded cores of antecrysts may indicate that the crystals were attacked by new melt injection or drastic pressure / temperature change in the system, suggesting that the crystals of the volcanic rocks have an antecrystic origin. The clinopyroxene cores are surrounded by oscillatory-, normal-, reverse-zoned mantles and rims with variable and complex chemical zonations and resorption surfaces. The observed phenocrysts exhibit specific Mg# - Al₂O₃ zoning profiles:

1. Mg#-rich mantles [Pattern C/M(en)] (**Fig. 6.16 A**)
2. Mg#-rich cores with low Mg# rims [Pattern C(en)] (**Fig. 6.16 F**)
3. Mg#-rich rims [Pattern R(en)] (**Fig. 6.16 C, B, E**)
4. Oscillating Mg# of mantles/rims [Pattern M/R(os)] (**Fig. 6.16 D**)

Profile 1 clinopyroxenes exhibit relatively higher Mg# (>0.68) within their mantles compared to the core and rim values (0.62-0.64) suggesting an interaction event with a higher-T magma. *Profile 2* was observed within clinopyroxene microcrysts (<200 μm) and shows that these pyroxenes crystallised from the high-T melt (i.e. from the felsic end-member; **Fig. 6.14 B**). This is also corroborated by the similar values of Mg# (67-68) of clinopyroxene phenocryst rims and the microcryst cores indicating that they crystallised due to the high-T melt:low-T mush mixing.

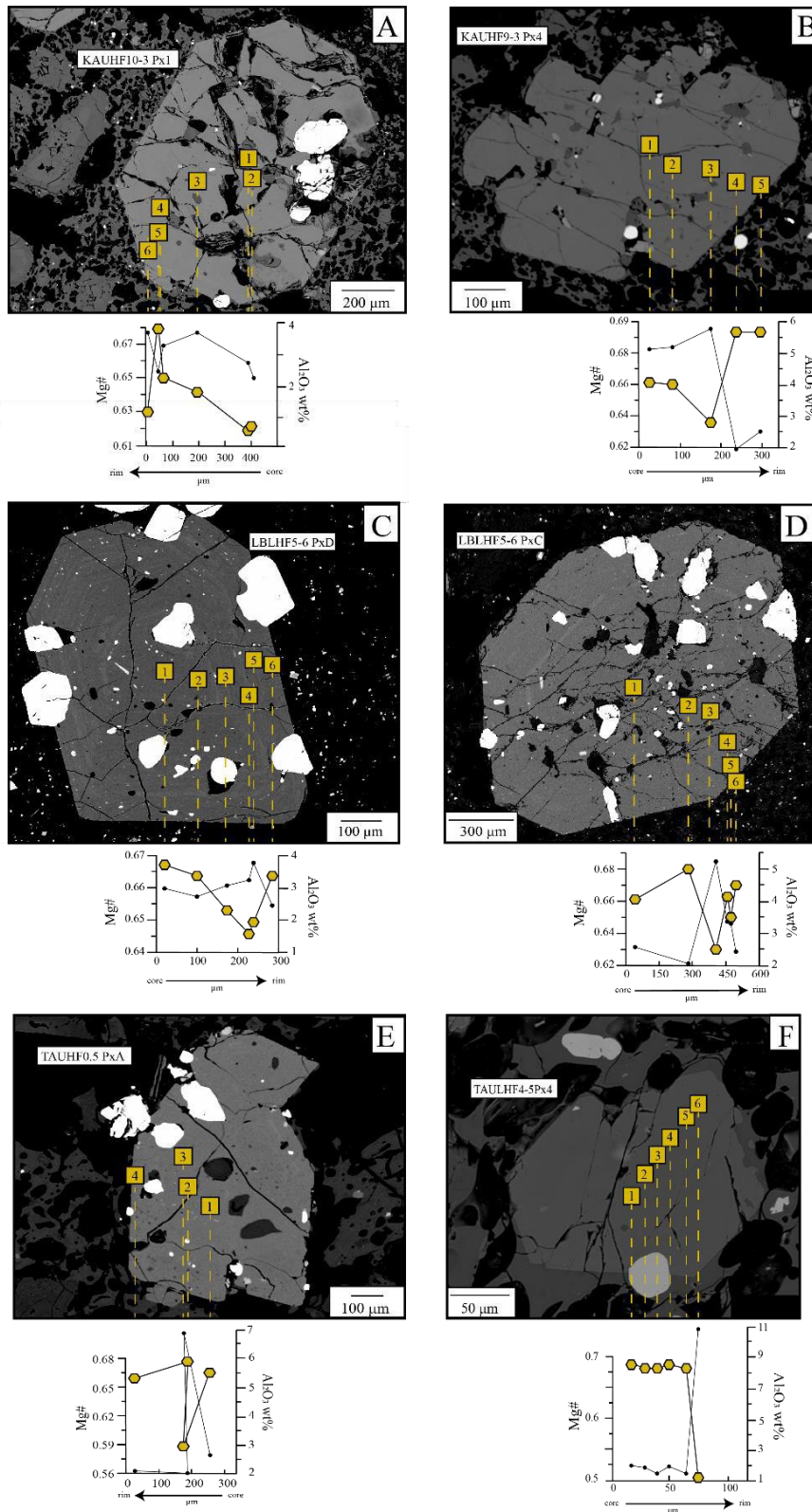


Fig. 6.16 Mg# and Al₂O₃ variation transects within individual crystals of GP the units. Mg# indicated by yellow circles; Al₂O₃ content highlighted by black circles. **A, B:** Normal and reverse zoned pyroxene phenocrysts from two different samples (*KAUHF10-3* and *KAUHF9-3*) of *GP1* unit. **C, D:** Single (C) and multiple (D) Mg# change within clinopyroxene phenocrysts towards the rims. The crystals are originated from the same pumiceous rock sample of *GP2* (*LBLHF5-6*). **E:** *GP2* clinopyroxene phenocryst (*TAUHF0.5 PxA*) with a flat profile outlining a significant Mg# change within its mantle. **F:** Small size clinopyroxene from a *GP3* sample (*TAULHF4-5*) with flat profiles representing noteworthy Mg# decrease within its inner rim.

Profile 3 suggests that clinopyroxene rims crystallised from a relatively hotter magma than their cores and mantles. It is coupled with Al_2O_3 decrease within the rims, which is expected from An-rich plagioclase crystallization that has depleted the surrounding melt in Al_2O_3 (Humphreys et al., 2006). The crystallization of An-rich plagioclase may be the result of an increase in magmatic temperature (Tepley et al., 2000; Stewart and Fowler, 2001; Zellmer et al., 2003) or during the decompression ascent of an H_2O -saturated magma (Humphreys et al., 2006). Further, high-Mg# and low-Al contents of clinopyroxene rims of the GP units are indicators of a recharge-induced temperature and $f\text{O}_2$ increase (Tepley et al., 2000). *Profile 4* clinopyroxenes exhibit oscillating bands of Mg# and also Al_2O_3 signifying that during the crystallization of mantles and rims, these crystals were emplaced on the boundary of the mixed magma and the high-T melt (**Fig. 6.14 B**) and/or may have been crystallised due to convection.

In general, these Mg# changes in clinopyroxenes may reflect temperature and $f\text{O}_2$ fluctuations during crystallization, with the increase of Mg# resulting from increases in temperature and $f\text{O}_2$ (Nakagawa et al., 2002). Mantles surrounding resorbed or non-resorbed cores, especially with specific compositional zonation patterns such as enrichment in Cr [Pattern C(co,en)] coupled with relative enrichment in compatible low-charge transition metals (Ni, Sc), may be related to recharge and magma mixing processes at depth (Ubide and Kamber, 2018). Moreover, repeated reverse zonations observed in clinopyroxene mantles (**Fig. 6.16 D; Appendix C1**) may be indicative of intermittent high-T magma injection processes (Nakagawa et al., 1999).

All zonation profiles occur in each of the three growth phases investigated. They mirror the melt-mush mixing processes operating at different depths within the mush zone in the individual growth cycles due to the various ascending melt characteristics, such as the water content and thus, the viscosity (**Fig. 6.13 A**). It is important to note that the clinopyroxene zoning profiles were generated frequently within the plumbing system of Taranaki Volcano for c. 30 kyr, implying the similar nature of melt-mush mixing processes within the mush domain. The Mg#-Al zonation patterns point to both single and multiple melt-mush mixing events based on the single or multiple resorption surfaces (40% of the investigated clinopyroxenes exhibit resorption surfaces; see **Appendix C1**) of the crystals, indicating that crystals may have been eroded thermally before further growth. Additionally, the majority of crystals display significant Mg# differences within core-mantle-rims (Mg# difference of 0.2 – 0.05; **Fig. 6.16**) implying that the low-T mush

domain was crystal-rich and may be considered as a plutonic assemblage, into which the higher-T melts were injected between c. 65-34 ka beneath Taranaki Volcano.

6.6.2.4 The mid-age Taranaki magmatic plumbing system

Petrological investigations and thermobarometric modelling suggest a multi-level magma plumbing system beneath Taranaki Volcano, which frequently recycles antecrystic material both from spatially and temporally different regions of the mush domain (**Fig. 6.17**). Possible intermediate melts (trachyandesitic; see **Chapter 5** for details) moved up to mid-crustal levels, where they interacted with different portions of the mush domain containing plutonic, gabbroic cumulates, i.e. primitive crystalline residues. Between the time-period c. 65-34 ka, eruptives were generated by high-T melt – low-T mush mixing processes in the mush zone and rim equilibration processes took place at variable depths of the mid- to lower-crust (**Fig. 6.12 A**) due to the different ascending melt characteristics during individual edifice growth cycles, such as water content and temperature (**Fig. 6.14 A**).

As fractional crystallization in a closed system cannot explain the complex mantle-rim zonation patterns and disequilibrium textures, repeated magma supply and injection containing hot magmas (i.e. hotter intermediate magmas than the cooler mush domain; see **Chapter 5** for calculated ascending melt compositions) into the different regions of the mush domain played a dominant role in the late stage magmatic processes acting on the entrained crystal cargo. Numbers below refer to **Fig. 6.17** with outlined crystal patterns:

- (1) The overall plagioclase, clinopyroxene and titanomagnetite textural and chemical results reflect certain crystallization conditions at depth, with crystal populations then ascending into and stored in the different segments of the mid- to upper-level storage system due to the different ascending melt characteristics. Observed core crystal patterns were produced by decompression due to ascent, such as the high abundance of patchy-zoned plagioclase cores [Patterns C(pa)], patchy-zoned clinopyroxene cores [Patterns C(pa)], Cr-enriched and corroded clinopyroxene cores [Pattern C(co,en)] or resorbed titanomagnetite inclusions.
- (2) In the mid- to upper-level system, different segments of the mush zone populations underwent different textural and chemical evolution due to the variable melt:mush mixing events within the individual growth cycles, leading to

a high diversity of mantle and rim crystal region patterns: (i) plagioclase and clinopyroxene populations with patterns of unzoned, flat profiles [Pattern C/M(un,fl)] or weak enrichment in certain trace elements [Pattern M(en)] presenting slightly affected storage regions with constant magmatic conditions; (ii) diverse zonations as [C/M(no/se)] showing near-constant and/or near-equilibrium conditions; (iii) crystals that were adjacent to these intruding melts would be captured and incorporated to the high-T melts, causing the formation of Mg# and Cr-rich mantles or specific Mg#-Al₂O₃ profiles (**Fig. 6.14 B**). The connected textures as jagged or resorbed bands [Pattern R/M(ir,er)] were produced by magma ascent induced decompression to shallower levels.

- (3) The repeated magma injection events in the individual growth cycles within different parts of the mush domain lead to possible thermal convection with the residing magmas and the incorporated crystal cargo. Clinopyroxene crystals were affected by minor temperature and compositional gradients due to the convection processes, producing thin oscillatory zones [Pattern R/M(os)], whereas thick oscillatory zonation with significant resorption surfaces might be formed as a result of crystal convection in differentially cooling, chemically heterogeneous, small melt-rich reservoir regions [Pattern R/M(os,ir,ex)]. Oscillatory zonation of plagioclase crystals also indicates new melt arriving and interaction with the crystals, whereas reheating events cause sieve-textures. Moreover, additional euhedral titanomagnetites crystallised from the residing melts, and thus remained unaffected by magma recharge events.
- (4) The already complex plagioclase crystals formed in different ways, in different spatial parts of the system exhibit enrichment in specific elements (Li, Ba) within the rims [Pattern R(en)] suggesting shallow, possibly syneruptive magmatic processes beneath Taranaki Volcano.

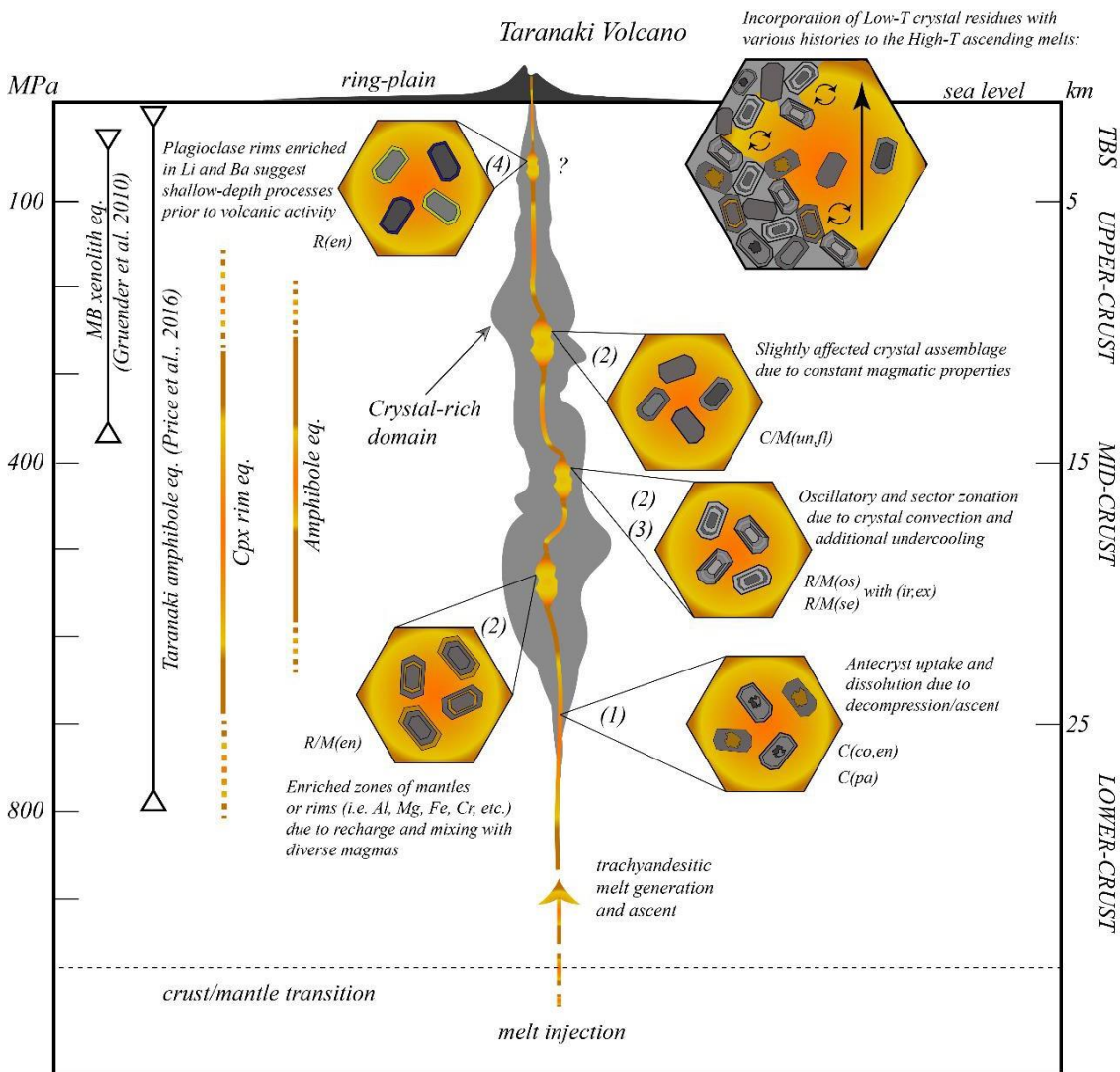


Fig. 6.17 Schematic illustration of the vertical plumbing system architecture at Taranaki Volcano in post-collapse state. MB: Median Batholith. Eq.: Equilibration. Cpx rim eq.: Clinopyroxene rim equilibration values by this study with dashed lines indicating the error (1SEE) after Neave and Putirka (2017). Amphibole eq.: Amphibole equilibration values by this study. Dashed lines show error (1SEE) after Ridolfi et al. (2010). TBS: Taranaki Basin Sediments. Crust/mantle boundary is from Sherburn and White (2005) and Stern et al. (2006). Hexagons indicate incorporated crystal residues and their crystal patterns (CPs) observed by the CPC in this study. Note that the vertical representation of different CPs is only illustrative to highlight that both spatial and temporal factors acted on the investigated crystal cargo within different segments of the plumbing system. Thus, the emplacement of CP hexagons may vary due to the different ascending melt characteristics (see Fig. 13 A for different melt emplacement depths). Inset of hexagon shows the general concept of crystal incorporation to ascending melts (black arrow) by melt:mush mixing.

6.7 Conclusions

The textural and chemical investigation of mineral assemblages from individual growth phases of Taranaki Volcano highlighted several aspects connected to ascending melt characteristics, crystal cargo features and connected crystallization settings between c. 65-34 ka. Thermobarometric calculations using amphiboles revealed that most likely they are representative of the basement plutonic residues beneath Taranaki Volcano, partly involving the Median Batholith. Moreover, both amphibole and clinopyroxene analyses indicate that within the studied growth cycles, ascending melts of GP2 exhibit initially significantly higher water contents compared to those of GP1 and GP3, resulting in higher viscosity of GP2 melts due to greater amounts of degassing-induced crystallisation. Thermobarometry approximations provided information on clinopyroxene rim equilibration conditions, suggesting depths of approximately 26-12 km (± 7.5), which outline mainly the mid- to lower-crustal regions and further indicate polybaric rim crystallization processes.

The CPC method was developed here as a useful approach to describe texturally and chemically complex mineral phases, focussing on multiple elemental distributions (major, minor and trace elements) using several instrumental techniques (i.e. EMPA transects or LA-ICP-MS mapping). CPC allowed for the detailed observations of the complex plagioclase and clinopyroxene crystals that constituting the subvolcanic crystal mush zone. Results suggest that crystal cores originate from greater depths and/or hotter regions, from which the intermediate melts were transported into mid-crustal levels within the mush zone. The diverse crystal patterns of plagioclase and clinopyroxene mantles and rims imply spatially, chemically and temporally highly variable magmatic conditions and significant antecryst recycling within different parts of the mush domain. However, specific textural features and zonation patterns signal that melt-mush mixing, crystal convection and magma injection were the main, repeatedly occurring phenomena within the individual growth cycles of Taranaki Volcano between c. 65-34 ka.

Considering the temporal variations of clinopyroxene rim equilibration temperatures and pressures within GP2 (c. 55-40 ka), results indicate that there is no temporal regulation or pattern connected to polybaric crystallization conditions from inter-collapse (i.e. edifice growth after a collapse) towards pre-collapse states. This consequently suggests that the scavenged crystal assemblages that had been erupted after a collapse during edifice growth exhibit no chemical and/or textural signatures or crystallization

conditions that would indicate collapse connected effects that led to eruption. In addition, the observed textural and chemical variations within the clinopyroxene and plagioclase crystals of GP2 (i.e. during c. 10 kyr of edifice growth) and the calculated equilibration conditions display no patterns, or any consistency that would suggest connection to edifice loading, such as changes in rim crystallization depth ranges or temperature ranges over time towards pre-collapse states. Ultimately, results outline that during a growth cycle, recycled crystals equilibrated in various depths with the rising melts and the reason of eruptions probably occurred due to the ascending melt properties and additional external factors, such as the plumbing system geometry, the connected stress regime, the dyke propagation paths and/or frequently occurring magma recharge events.

CHAPTER 7

TEMPORAL ASPECTS OF THE CRYSTAL-MUSH DOMINATED TARANAKI MAGMATIC SYSTEM DURING SUCCESSIVE GROWTH CYCLES

This chapter is planned to be structured as a manuscript and be submitted to Geology.

Supplementary Data for this Chapter can be found in **Appendix D**.

Chapter Contributions:

- ◆ **Aliz Zemeny:** Conceptualisation, Visualisation, Writing (original draft), Writing (review & editing)
- ◆ **Georg F. Zellmer** Writing (review & editing)
- ◆ **Jonathan Procter:** Supervision, Writing (review & editing)
- ◆ **Anke V. Zernack:** Writing (review & editing)

This chapter highlights recently established fieldwork-related techniques on how to gain information of short-term magmatic responses to volcano collapse and growth cycles. Furthermore, it aims to provide a discussion on the newly developed petrogenetic model and its integration into the current models of Taranaki Volcano as well as on the relationship and the magmatic behaviour of the long- and short-term transcrustal Taranaki magmatic system.

The overall results derived from whole-rock geochemical, thermobarometric and crystal stratigraphic studies (**Chapter 5** and **6**) indicated that the Taranaki transcrustal magmatic system is dominated by a crystal-rich mush domain, which reacts to repeated depressurisation (as a result of collapse events) that punctuate edifice growth. Results further confirmed that the mid-age Taranaki magmas are generated by melt-mush mixing, and that ascending intermediate melts scavenge the mobile parts of the mush domain.

7.1 Volcaniclastic mass-flow deposits as tools: From subaerial to subvolcanic processes

Long-lived stratovolcanoes across all tectonic settings are prone to architectural instability, which can lead to catastrophic edifice collapse events generating debris avalanches (destruction phases; Ui, 1983; Siebert, 1984). These structural failures followed by edifice re-growth cycles (construction) may be frequently recurring phenomena within the lifespan of individual stratovolcanoes (e.g. Zernack and Procter, 2021). The outcome of such a cyclic physical process is recorded across the surrounding region that is identified as the volcanic apron or ring-plain (Davidson De Silva, 2000; Donoghue and Neall, 2001; Borgia and van Wyk de Vries, 2003), in the form of (i) debris-avalanche deposits (DADs) as the indicators of flank or sector collapses (Voight et al., 1981; Ui et al., 1986b; Vallance et al., 1995; Capra et al., 2002; Concha-Dimas et al., 2005; Shea et al., 2008; Zernack et al., 2009; Coello-Bravo et al., 2020, Zernack, 2021; Zernack and Procter, 2021) and (ii) primary and secondary volcaniclastic mass-flow deposits as the principal sedimentary agents of volcano construction (Smith, 1991; Davidson de Silva, 2000; Borgia and van Wyk de Vries, 2003; Németh and Martin, 2007; Zernack and Procter, 2021).

The identified frequency of collapse event, which ranges from 0.1-1 kyr (Begét and Kienle, 1992; Belousov et al., 1999; Tibaldi, 2001) through 1-10 kyr (Scott et al., 1995; Zernack et al., 2012a; Tost et al., 2014) to 10-100 kyr (Moore et al., 1989, 1994;

Carracedo et al., 1999; Oehler et al., 2008) evidently governs the duration of edifice growth intervals. As frequent eruptions and continuous edifice growth and destruction occur at active volcanoes, the burial and/or erosion of older sequences and/or the cone becomes more prevalent, often limiting the preservation of deposits to the Holocene record (usually in the form of lava flows, pyroclastics and tephras near/on the young cone). The consequence of the lack of a proximal volcano-sedimentary record representing a complete time-window into the history of a volcano is that the overall processes of long-term edifice growth cycles are hard to capture, especially when dealing with long-lived stratovolcanoes whose life span extend well beyond the Holocene.

The solution to this problem lies in the exploration and recognition of well-exposed successions that integrate a detailed, near-continuous volcanic and sedimentary record of a volcano and provide temporal resolutions at which past subaerial and subvolcanic processes can be reconstructed. Therefore, the careful selection of specific volcanoclastic mass-flow deposit sequences in ring-plain settings is critical for interpreting maximum frequencies of eruptive periods and connected magmatic processes. The medial regions of the south and southwest Taranaki ring-plain sectors are exposed by the contemporary coastal erosion of the uplifted cliff sections, revealing processes and events connected to growth cycles. The spatiotemporal dimensions of these coastal volcanoclastic successions exhibit a near-continuous stratigraphic record within the time period between c. 65-34 ka. This exposed time window yields three edifice growth cycles interspersed by three collapse-generated DADs. These inter-collapse cycles, which have not been studied in detail before, provide an opportunity to decipher sedimentological and geochemical aspects of successive stratovolcano regrowth in a back-arc setting.

The targeted stratigraphically constrained, (i) widely distributed lithic-dominated and (ii) channelised pumice-dominated monolithologic hyperconcentrated-flow deposits are thought to represent rapidly remobilised eruptive products (**Chapter 4**). They provide not only sedimentological information on mass-flow transport and emplacement mechanisms, but their lithological properties furthermore indicate that they represent deposits that are connected to eruptive periods of Taranaki Volcano. Given the lack of equivalent proximal sites closer to the edifice, these medial volcanoclastic mass-flow deposits provide an opportunity to gain geochemical insights into the c. 65-34 ka time-window of growth cycles. Based on mass-flow frequency estimates, the maximum temporal resolution range of these stratigraphic records connected to volcanic activity are

within c. 3.5 – 10 kyr, which may be considered as the fine-scale resolution limit of what mass-flow deposits can provide on past volcanic processes at Taranaki Volcano. However, this stratigraphic resolution is exceptional when considering the fact that the present study deals with a long-lived atypical back-arc stratovolcano (>200 ka; Zernack et al., 2011, 2012a) and focuses on a time-period which extends back to c. 65 kyr by exploring the volcanoclastics in medial sectors (25-30 km) of its ring-plain system.

From a global perspective, eruptive compositions acquired from pre-collapse and post- or inter-collapse volcanic sequences typically have limited age constraints, and thus low stratigraphic resolutions covering 10-20 kyr intervals with fine-scale resolution frameworks of <10 kyr being uncommon (e.g. Hora et al., 2009; Cassidy et al., 2012, 2015; Boudon et al., 2013; Vezzoli et al., 2014; Watt, 2019). However, the exposed medial ring-plain succession of Taranaki Volcano provided the means to develop a volcanoclastic mass-flow deposit classification framework (**Chapter 4**), which may be helpful to identify specific deposits that can be used for the reconstruction of the temporal magmatic behaviour and its connection to collapse and construction phases in ring-plain settings of stratovolcanoes that lack such well-exposed successions. Such geochemical investigations can provide further knowledge on edifice growth and magmatic system interactions.

Taking advantage of the above-mentioned stratigraphic resolution of the Taranaki medial ring-plain, the temporal behaviour of the Taranaki magmatic system can be examined during three growth cycles by selecting pumiceous and scoriaceous clasts from the specific volcanoclastic mass-flow deposits, with clasts corresponding to eruptive primary material produced by volcanic activity (**Chapter 4**). Investigation of primary clasts from volcanoclastic mass-flow deposits provides information on the magmatic evolution as well as the characteristics of mineral assemblages, the melt and the magma plumbing system over time in the light of repeatedly occurring edifice growth cycles (**Chapter 5**).

7.2 Integration of the Taranaki petrogenetic models

The crystal mush concept

Arc stratovolcanoes are active foci for examining the generation and evolution of intermediate magmas that are fed from the complex assemblage of the crystal cargo containing pheno-, ante- and xenocrysts that are recycled during the lifetime of a

magmatic system (Miller et al., 2007; Claiborne et al., 2010; Ruprecht et al., 2012; Klemetti and Clyne, 2014; Pack et al., 2016). The traditional view of large-scale, long-lived, liquid-dominated magma chambers has now changed to concepts in which melts exist mainly as small pockets within a framework dominated by crystal cumulates and/or residues (Hildreth, 2004; Annen et al., 2015; Bachmann and Huber, 2016; Cashman et al., 2017; Lissenberg et al., 2019; Edmonds et al., 2019; MacLennan, 2019; Caracciolo et al., 2020; van Gerve et al., 2020). Due to these mush models, eruptible magmas are seen as transient features that develop from physical and chemical transport processes and phase change reactions within a crystal mush (Cooper and Kent, 2014), where crystals may experience vertical transport and storage at multiple levels in space and time within the crust (Metrich and Deloule, 2014; Stock et al., 2018; Tucker et al., 2019). These interconnected concepts have evolved to incorporate the entire crustal region, which can be expressed as the transcrustal magmatic system (TCMS; Cashman et al., 2017), that is viewed to be dominated by crystal mush. Magma mixing, recycling of remnant material and cycling of crystals in this semi-rigid framework affect both the chemical compositions of erupted magmas and the compositions of unerupted parts of the reservoir (Cashman and Blundy, 2013), which then may interact with subsequent batches of magmas over time and/or freeze. Therefore, the full incorporation of geochemical data of andesitic magmas along with detailed analyses of their crystal cargoes and phase equilibria studies (e.g. Browne et al., 2006; Botcharnikov et al., 2008; Streck et al., 2008; Kent et al., 2010; Ruprecht et al., 2012; Parat et al., 2014; Higgins et al., 2015; Melekhova et al., 2015; Wanke et al., 2019; Namur et al., 2020; Di Stefano et al., 2020) is key to improving our understanding of subduction zone volcanoes and their magmatic plumbing systems.

The petrogenetic model for inter-collapse states proposed by this study

The geochemical investigation of medial ring-plain volcanoclastics revealed that the “mid-age” Taranaki magmatic system (**Chapter 5**, Section **7.2**) exhibits a different behaviour to what has been proposed by earlier studies, which explained the petrogenetic evolution of Taranaki rocks as being dominated by fractional crystallisation (FC) and assimilation and fractional crystallisation (AFC) processes within the crust (Price et al., 2005; Zernack et al., 2012b; Damaschke et al., 2017a). These differences are reflected in (1) the main processes that produced the mid-age Taranaki magmas, (2) discrepancies

between inter-collapse and pre-collapse whole-rock chemistry during the 65-34 ka time-period and (3) the similarity of the early (>105 ka; Zernack et al., 2012b) and mid-age Taranaki magmatic system.

In contrast to previously suggested concepts of FC and AFC, mid-age Taranaki eruptive products appear to exhibit geochemical signatures that can be reproduced through mixing (Ersoy and Helvacı, 2010). To test this hypothesis and develop an underpinning model, modal phase proportions were calculated to estimate mineral phase and melt compositions of selected clasts, which then served as assimilant and melt endmember compositions. The results revealed that mid-age Taranaki magmas originated from the mixing of primitive crystals with ascending trachyandesitic melts and that the mixing ratio between crystals and melt influences the overall whole-rock compositions of the clasts, with mixing ratios varying between individual growth cycles (**Chapter 5**). The developed model also explains the effect of edifice loading on the mid- to upper-crustal magma evolution, which is predominantly reflected in progressive widening of compositional ranges over time in each growth cycle and eruption of more mafic and more felsic bulk rock compositions as the growing edifice reaches a pre-collapse state. This coupling between edifice growth and the subvolcanic plumbing system has been globally recognised in the form of cyclicity of mafic to more evolved volcanism, which has been interpreted as evidence for the re-establishment of a mid- to upper-crustal magma storage system following collapse events (e.g. Hall et al., 1999; Boudon et al., 2013; Cassidy et al., 2015).

The new mid-age Taranaki model (**Chapter 5**; see the illustrated model in **Fig. 7.1 A**) signifies the dominant process of ascending intermediate (trachyandesitic) melts mixing with a diverse, primitive crystal cargo during successive edifice growth cycles. In addition, the observed differences between inter-collapse and pre-collapse rock compositions indicate reactivation of the mid to upper crustal storage system within approximately 10 kyr during each studied growth cycle, following temporary cessation due to recurring collapse events between 65-34 ka (**Chapter 5**, Section **7.6**). This reactivation is thought to be generated due to the influence of increasing edifice loading towards pre-collapse states as the volcano rebuilt itself, which affected the dynamics of ascending melts and their focus beneath the edifice. Thus, an reduced edifice load (i.e. depressurisation) stimulates unfocussed magmatic processes during inter-collapse states, where ascending melts arrive to a colder mush zone and generate small dispersed melt

pockets; whereas at pre-collapse state the increased edifice loading focusses melts to create more active and spatially more restricted reservoir regions within the crystal mush space (**Fig. 7.1 A**; see details in **Chapter 5**, Section 7.5).

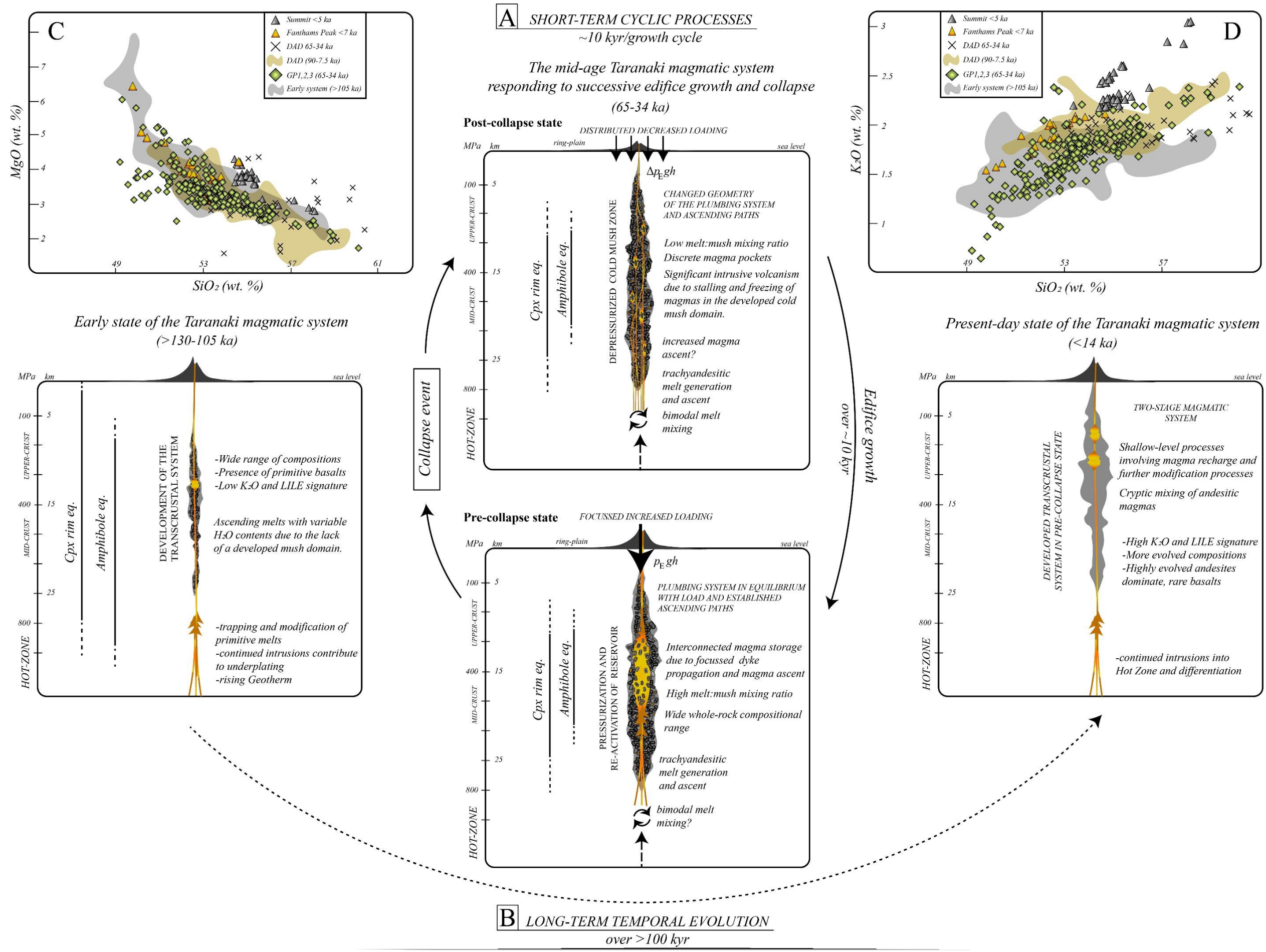
Supplementing the current Taranaki model

The proposed model of this study is consistent with the “hot-zone” hypothesis of Annen et al. (2006) in that the ascending recharging melts are thought to be originating from the crust-mantle boundary (Reubi and Blundy, 2009). The results, derived from the representative melt inclusion analysis support the paradigm of melt bimodality in the lower crust, with the presence of a mafic and a felsic melt endmember. Both of these components have been enclosed by the mid-age Taranaki clinopyroxene and plagioclase phenocrysts in the form of melt inclusions (**Chapter 5**, Section 7.4), which may provide evidence for the generation of trachyandesitic compositions of the ascending melts by melt mixing (e.g. Reubi and Blundy, 2009; Stewart et al., 2010).

The accepted concept for the long-term evolution of the Taranaki magmatic system, in agreement with the hot-zone model, shows a gradual evolution to more evolved and more potassic compositions over its lifetime, where compositions are affected by partial melting and fractional crystallisation at shallow depths (**Fig. 7.1 B, D**; Stewart et al., 1996; Price et al., 1999, 2005; Gruender et al., 2010; Zernack et al., 2012b; Price et al., 2016). This temporal evolution of Taranaki Volcano is explained by the progressive evolution of the hot zone, and thus the continuous interaction of partially remelted, underplated mafic material and the fractionating mantle-derived magmas (Price et al., 2005; Annen et al., 2006; Gruender et al., 2010; Zernack et al., 2012b). However, the long-term evolutionary trend evident in the debris-avalanche chemistry (Zernack et al., 2012b; **Fig. 7.1 D**) over the c. 200 kyr volcanic history of Taranaki Volcano was not observed between 65-34 ka, with no gradual K₂O and LILE enrichment recognised from GP1 to GP3. Instead, the new results indicate that on short timescales (i.e. 10 kyr long edifice regrowth cycles), Taranaki Volcano displays a “more mafic to more evolved” compositional petrogenetic trend over time within individual growth cycles. This behaviour is interpreted as a response to depressurisation of the magma plumbing system and its following gradual reactivation, where melt-mush mixing is the dominant process producing the eruptible magmas (**Fig. 7.1 A**). The inter-collapse petrogenetic model

detecting no gradual increase in K_2O or LILE evolution of the time period c. 65-34 ka, can be attributed to multiple factors:

- The relatively short time-window (c. 30 kyr) of this study, which may be insufficient to detect the broad trends recognised by the long-term model.
- The possible explanation is not only depending on the short timescales of the studied growth cycles (c. 10 kyr), but also on the depressurisation influenced and physically modified condition of the Taranaki TCMS and the melt-mush mixing processes producing the mid-age magmas. Moreover, surface loading over time will act on these processes, thus whole-rock compositions of mid-age eruptives closer to pre-collapse states will share similarities with DAD clasts (compositional overlapping above 53 SiO_2 wt.%; **Chapter 5**, Section **7.6**). However, their trace-elemental variations mainly differ with minimal overlapping (**Chapter 5**, Section **7.6**), indicating heterogeneities, i.e. diverse evolutions of the ascending melts carrying various trace elemental signatures.
- Additionally, studies stressed that sector collapses are thought to be able to initiate magma ascent, i.e. heat and/or volatile addition to the upper reservoirs (e.g. Pinel and Albino, 2013; Watt, 2019). This hypothesis essentially promotes the possibility of transportation of magmas in inter-collapse states lacking the temporal K_2O and LILE signatures that can be seen in pre-collapse eruptives over long timescales. Therefore, volatile content-based future investigation of crystal-hosted melt inclusions of pre- and inter-collapse eruptives would be beneficial in order to test this discrepancy, as they may give insights into melt evolution and modification processes at depth.



◀ **Fig. 7.1** Integrated petrogenetic model of Taranaki Volcano considering timescales and cyclic edifice growth and collapse induced magmatic response. **A:** Inter-collapse petrogenetic model proposed by this study and its inclusion in the combined model (see details in **Chapter 5** and **6**). **B:** The long-term temporal evolution model after Zernack et al. (2012b) and Turner et al. (2008a) in agreement with the hot zone model of Annen et al. (2006). **C:** MgO vs SiO₂ and **D:** K₂O vs SiO₂ of the analysed Taranaki volcanic rocks indicating significant differences over time. Fanthams Peak and Summit/Staircase data after Stewart et al. (1996); DAD and early system data after Zernack (2008) and Zernack et al. (2012b); GP1,2,3 data after this study. Datasets provided in **Appendix D1**.

Finally, recent studies emphasised that the relatively high collapse frequency indicates a high magma flux and thus, edifice growth rate for Taranaki Volcano (Zernack et al. 2012a, Zernack and Procter 2021). A high magma flux has been described elsewhere to control the interaction between edifice loading and the upper-crustal storage system, leading to an outpace of edifice growth over crustal response (Watt, 2019). However, this study reveals that the mid-age Taranaki magmatic system indeed corresponds to the surface load during the investigated growth cycles leading to a widening chemostratigraphic pattern exhibited by the investigated volcanoclastic mass-flow deposit clasts (**Chapter 5**). Furthermore, there are clear major and trace element geochemical differences between pre-collapse and inter-collapse magmas of the three examined volcanic cycles, implying that the upper-crustal plumbing system gradually becomes more active towards pre-collapse states. Overall this study shows that despite the lack of primary deposits overlying debris-avalanche deposits in the ring-plain succession of the studied time-period, specific volcanoclastic mass-flow deposits can be used instead to reveal the geochemical trends over c. 10 kyr-long edifice growth timescales of Taranaki Volcano, which have not been detected by previous long-term models.

7.3 The recycled Taranaki crystal cargo: Antecrystic, xenocrystic or a mixture?

Considering that melt-mush mixing processes dominate the generation of the mid-age Taranaki eruptives, an important question arises in relation to the properties of the crystal mush; what kind of ascending melts scavenge mineral assemblages over space and time (i.e. during growth cycles)? Recent research provides insights into andesitic magma generation processes supporting the paradigm that andesitic rocks represent the eruptive products of the mobile part of mush zones (Bachmann & Bergantz, 2004; Bachmann et al., 2007; Burgisser & Bergantz, 2011; Kent et al., 2010; Cooper & Kent, 2014; Annen et al., 2015; Lissenberg et al., 2019; Namur et al., 2020). Therefore, the crystal mush synthesis has become a modern solution to explain complex magmatic processes of igneous systems. While bulk magma compositions are commonly used to track magma

evolution by crystal fractionation, and/or assimilation (Lee and Bachmann, 2014; Turner and Langmuir, 2015; Keller et al., 2015), growing evidence suggests that these methods do not provide sufficient information to properly characterise magmatic systems, which is also the case for the mid-age Taranaki magmatic system (Section 7.3). A possible alternative approach to determine magma storage conditions is to study the compositions and textures of the components within the erupted material, i.e. the mineral assemblages.

This study used crystal stratigraphic mapping coupled with EMPA spot analyses and textural observations on plagioclase, clinopyroxene and amphibole crystals to investigate the mid-age Taranaki crystal cargo (**Chapter 6**), which represents the mafic endmember in the melt-mush mixing process. To characterise the key properties of the crystal mush beneath Taranaki Volcano, the first step was to analyse the interconnection of the crystal cargo and the ascending melts by textural and chemical observations. Therefore, the Crystal Pattern Classification (CPC) framework was developed, which is suitable for multiple elemental analysis and for identifying textural patterns within the crystal regions of complex individual crystals (**Chapter 6**, Section 4.5). This technique allowed linking certain elements to specific textures within the main crystal regions (i.e. rim, mantle, core).

The textural analyses of crystals confirmed that mid-age Taranaki eruptives contain crystals exhibiting disequilibrium petrographic characteristics (i.e. signs of mixing), such as resorption surfaces, partially resorbed cores or corroded crystal habits. These textural patterns coupled with chemical zonations within the crystals allowed the identification of specific, repeatedly occurring crystal patterns within the crystal cargo (**Chapter 6**, Section 5.2 and 5.3). These crystal patterns indicated an antecrystic origin for the majority of clinopyroxene, plagioclase and amphibole crystals. Furthermore, neighbouring crystals within individual samples displayed diverse pre-eruptive histories, suggesting that they were assembled from different sections of the Taranaki TCMS (**Chapter 6**, Section 6.2.4; c.f. Ginibre et al., 2002; Wallace and Bergantz, 2004; Berlo et al., 2007; Andrews et al., 2008; Cashman and Blundy, 2013). These observations indicated that these crystals may have been derived from cooler regions (c.f. Reubi and Blundy, 2009; Saunders et al., 2010; Kilgour et al., 2013) or from deeper and hotter parts of the TCMS (c.f. Sides et al., 2014; Edmonds et al., 2016).

While these observations have confirmed the antecrystic nature of the studied mineral assemblages, they do not explain their origin. To date, petrological and geochemical

studies at Taranaki Volcano have not focussed on the origin and subvolcanic emplacement of its recycled crystal cargo (Gruender et al., 2010; Price et al., 2016, Damaschke et al., 2017a). Therefore, an important question remains: could they be xenocrystic and have they been sourced from the plutonic Median Batholith beneath Taranaki Volcano? Potential future studies on isotopic and trace elemental variations within and between individual crystals and their chemical zonations, using the developed CPC method, may shed new light on the magmatic processes and melt heterogeneities within the Taranaki magmatic plumbing system, and thus provide answers to this question by characterising the plutonic assemblages in greater detail.

7.4 The spatiotemporal evolution of the Taranaki transcrustal magmatic system

Thermobarometry and hygrometry estimates have been obtained on the mineral phases of the mid-age Taranaki magmatic system to characterise rim equilibration conditions and ascending melt properties. Overall thermobarometry results suggest clinopyroxene rim equilibration depths of 26-12 (± 7.5) km indicating mid- to lower-crustal regions and polybaric rim crystallisation (**Chapter 6**, Section **6.1**). This is consistent with the accepted view on ascending melts in arc environments, namely that they commonly accumulate in the mid-crust (Sisson et al., 2014; Ward et al., 2014; Edmonds et al., 2016) and also with the growing evidence for mid-crustal magma intrusion and storage (Nichols et al., 2011; Kiser et al., 2016; White and McCausland, 2016). Hygrometric modelling, corresponding to the amphibole chemistry, reveals ascending melts with H₂O contents characteristic for the average Taranaki magmas that show similar P-T features as the Median Batholith (**Chapter 6**, Section **6.1**; Gruender et al., 2010; Price et al., 2016). On the other hand, the clinopyroxene hygrometry exposed that GP2 melts had higher H₂O contents compared to GP1 and GP3, suggesting that GP2 melts shared similar properties to the crystal mush, occupying the mid- to lower-crustal region beneath Taranaki Volcano, and that these magmas likely stalled due to early degassing-induced crystallisation.

These findings initiated the idea of comparing the early (>130-105 ka) and mid-age (65-34 ka) Taranaki system on the basis of crystallisation (P-T-H₂O) conditions using clinopyroxene, plagioclase rim and amphibole compositions (mid-age data provided in **Appendix C1** and early system data in **Appendix D1**). An important point to note is that there are no significant whole-rock trace-elemental signature differences between basaltic

and trachyandesitic mid-age Taranaki eruptives that would indicate involvement of primitive magmas, but instead the data supports the melt-mush mixing ratio hypothesis as predominant control for determining whole-rock compositions. However, previous studies reported basaltic debris-avalanche clasts (from the >105 ka Okawa DAD and >130 ka Motunui DAD; Zernack et al., 2011, 2012b) with subduction signatures that have been attributed to magmas that were able to ascend through the crustal region without any significant modification, thus representing primitive magmas (Zernack et al., 2012b). Therefore, thermobarometry and hygrometry estimations have been applied to early system (>105 ka) mineral phases from DAD clasts (**Appendix D1**) in order to reveal the physical settings of crystallisation and ascending melt characteristics and their evolution towards mid-age system conditions (**Fig. 7.2**). The modelling calculations have been obtained using the same procedures as specified in **Chapter 3** (Section 3.5).

The results reveal that the early Taranaki system (based on both the Okawa and Motunui DAD samples) was characterised by polybaric clinopyroxene rim ($n = 19$) crystallisation exhibiting equilibration pressures of 33-789 MPa and temperatures of 885-1023 °C (Neave and Putirka, 2017). Amphibole ($n = 148$) estimated pressures vary between 193-873 MPa, whereas modelling results indicate temperatures between 887-1045 °C (Ridolfi et al., 2010), confirming that early Taranaki amphiboles equilibrated with magmas over a wide range of conditions. Comparing the early and mid-age system results shows that the early Taranaki plumbing system was characterised by more diverse host magmas and that the clinopyroxene equilibration took place over a wider depth range (**Fig. 7.2 A**). Water contents (Ridolfi et al., 2010) based on amphibole compositions also exhibit diverse early system melts with 4-8 wt.% H₂O. In addition, H₂O content estimations, using the clinopyroxene geothermobarometer coupled with the plagioclase hygrometry model (Waters and Lange, 2015; Neave and Putirka, 2017), yield similar ranges of 2.2-7.9 wt.%, which correspond to the minimum and maximum water contents of the melts that interacted with the crystal cargo (**Fig. 7.2 B**). In comparison, mid-age Taranaki melts are characterised by significantly narrower water content ranges, based on the clinopyroxene and amphibole hygrometry approximations (**Fig. 7.2 B**; see details in **Chapter 6**, Section 6.1).

It is important to note that there is a minimum age difference of 40 kyr between the early and mid-age Taranaki system. Estimated modelling results expose an important phenomenon occurring during this time gap, which is expressed by the decreasing range

of both equilibration depths and water-saturation of ascending melts towards the younger Taranaki system over time (**Fig. 7.2**; i.e. from early to mid-age conditions). This evolution is revealed by the amphibole-based barometry calculations, which show the restriction of the equilibration ranges over time. These observations are also mirrored by the clinopyroxene-based thermobarometry results, where the mid-age system converges in equilibration depths compared to the early system equivalents.

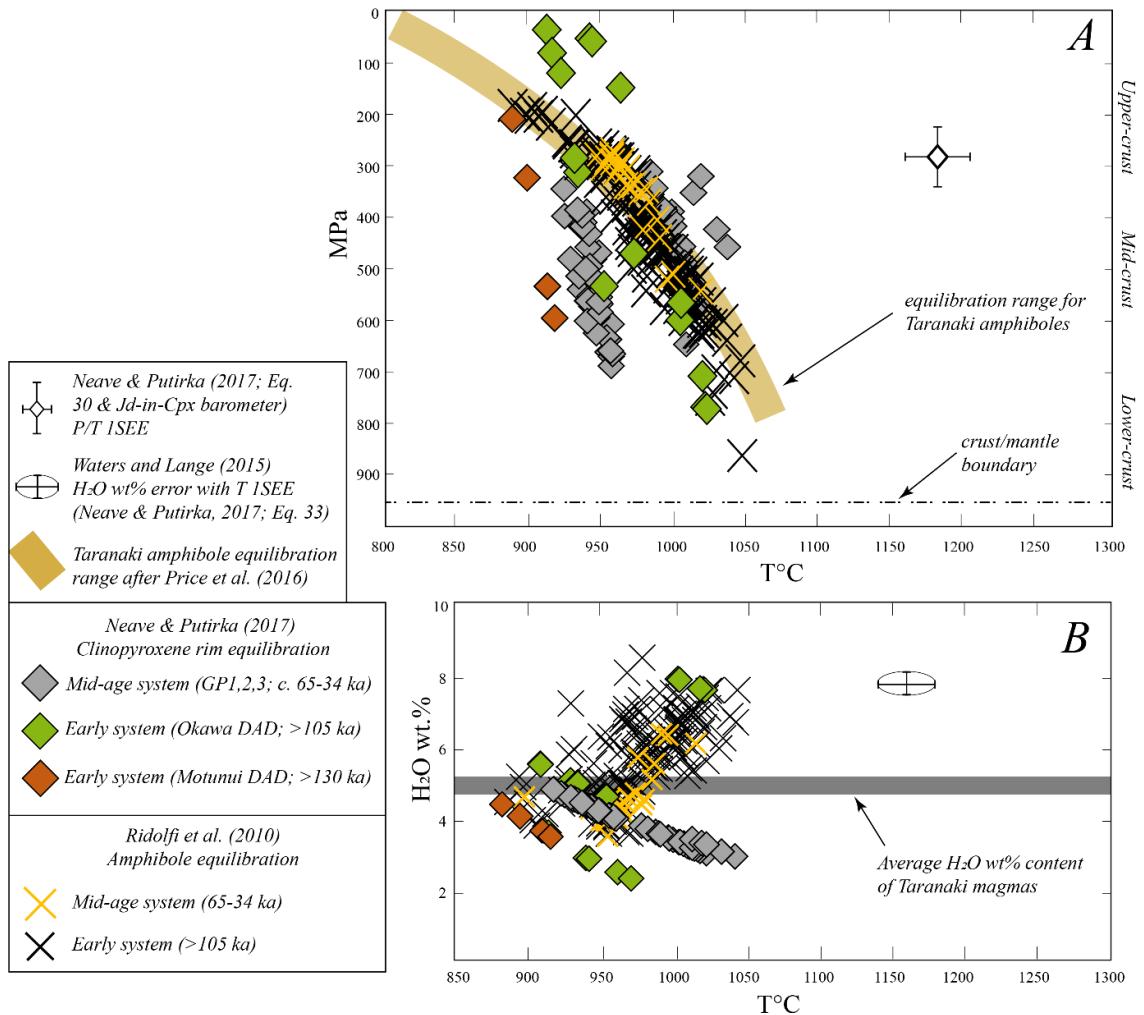


Fig. 7.2 A: Amphibole and clinopyroxene pressure and temperature equilibration estimates based on early (debris-avalanche deposit clasts) and mid-age system (pumice and scoria clasts) volcanics of Taranaki Volcano. Thermobarometry models after Ridolfi et al. (2010) and Neave and Putirka (2017) and hygrometry model of Waters and Lange (2015) were used. Amphibole geobarometer 1SEE is ± 22 °C, for pressure is ± 61 MPa and for H₂O wt.% is an average of ± 0.7 (Ridolfi et al., 2010). Clinopyroxene thermobarometer 1SEE for T is ± 42 °C (Eq. 33; Putirka 2008) and for P is ± 0.96 kbar (Neave and Putirka, 2017). **B:** Calculated H₂O wt.% melt contents for amphiboles and clinopyroxenes using the hygrometer of Waters and Lange (2015). Melt water content 1SEE is 0.35 wt.% coupled with T 1SEE of ± 42 °C after Neave & Putirka (2017; Eq. 33). Average H₂O wt.% for Taranaki magmas after Price et al. (2016). Early system clinopyroxene (n=19), plagioclase and amphibole (n=148) compositions after Zernack et al. (2012b). Equilibration range for amphiboles of Taranaki volcanics after Price et al. (2016). Crust/mantle boundary is from Sherburn and White (2005) and Stern et al. (2006). Uncertainties (1SEE) are indicated by the length of the cross signs.

Moreover, these results corroborate the hygrometry approximations, for both amphibole and clinopyroxene modelling. They indicate that the early Taranaki system was characterised by an extremely wide range of mainly hydrous melts. In contrast, these melts were limited in the mid-age system probably due to stalling and crystallisation, thus significantly contributing to the plutonic processes beneath Taranaki Volcano rather than being erupted as observed in the early system (**Fig. 7.2 B**). These findings support the hot-zone Taranaki model (Zernack et al., 2012b), stating that the hot-zone was developed over the first 100 kyr of volcanism at Taranaki Volcano (200-100 ka) and evolved over time by continuous intrusion and crystallisation of mantle-derived hydrous magmas in the lower crust. These processes assisted to the thickening of the underplated zone and the rising of the geothermal gradient, resulting in the entrapment and thus the modification and evolution of mantle-derived melts over time. The absence (or potentially weak development) of a mush domain in the early system (together with a relatively thin and cold hot zone prior to ~105 ka) provides an additional mechanism for the existence of the basaltic debris-avalanche clasts that were interpreted to represent primitive magmas without significant crustal modification (c.f. Zernack et al. 2012b).

The proposed mid-age Taranaki model (Section 7.3) states that as the edifice develops toward pre-collapse states, the mid- to upper-crustal system becomes active, thus trapping and modifying the ascending magmas. However, early system basaltic debris-avalanche clasts provide no evidence for modification in the mid- to upper-crust (Zernack et al., 2012b), nor for melt-mush mixing dependent whole-rock composition. An explanation may be that over the first 100 kyr (200-100 ka), the Taranaki magmatic system involved a colder, less complex crust that lacked a well-developed transcrustal magmatic system as reflected in the early system debris-avalanche clast compositions and the thermobarometry and hygrometry calculations presented here (**Fig. 7.1** and **7.2**). These conditions (represented by the early system clasts) allowed melts with diverse properties and with high water contents to ascend and initially erupt. Over timescales of tens of thousands of years, significant intrusive volcanism resulted in the development of the mush zone by c. 65 ka (**Fig. 7.1 A**), providing an additional filtering function in relation to the hot-zone derived migrating magmas and the mid-age Taranaki mineral phase equilibration depths (**Fig. 7.2**).

Altogether, these results characterise the temporal evolution of the Taranaki transcrustal system between c. >130 and 34 ka, indicating that over at least 100 kyr, the

magmatic plumbing system continued to mature due to ongoing significant intrusive volcanism into the mid- to upper crust, developing a crystal-rich mush zone (**Fig. 7.1**). Consequently, this well-established transcrustal magmatic system controls the magmatic processes occurring during the subsequent mid-age volcanic phase of Taranaki Volcano by trapping/homogenising the compositions of ascending melts, which then incorporate parts of the primitive crystal domain by melt-mush mixing processes, which is signified by the mid-age Taranaki model developed in the present study for the time period of c. 65-34 ka (**Fig. 7.1 A; Chapter 5**).

7.5 Global applications based on insights from the Taranaki magmatic system

Andesitic volcanism is typically found in continental settings as long-lived arc volcanoes (Rudnick, 1995), which exhibit a cyclic pattern of edifice growth and collapse that influences the chemical, physical and temporal development of magma reservoirs and their associated magmatic processes at depth (see references in **Chapter 1**, Section **1.1.1**). The relationship between plutonic and volcanic rocks is essential for gaining an in-depth understanding of the formation and evolution of these magmatic systems. Furthermore, the knowledge of andesite petrogenesis is fundamental for understanding volcanic and differentiation processes and TCMS characteristics.

From a global standpoint, geochemical and petrogenetic investigations have been conducted on individual arc systems in the light of cyclic behaviour, confirming the effect of sector collapse on volcano-magmatic regimes and associated post-collapse (i.e. inter-collapse) volcanic activity. These studies highlight various magmatic responses at different volcanoes as well as at the same volcano during consecutive collapse events but also stratigraphic limitations (**Chapter 1**, Section **1.1.1**). Some of the geochemical patterns and/or magmatic responses observed at other arc volcanoes exhibit similarities to the mid-age Taranaki system. These examples partially involve (but are not restricted to):

- Post-collapse magmas following the 8.8 ± 0.5 ka Parinacota DAD at Parinacota Volcano involving more mafic compositions that reflect less crustal modification and negligible upper-crustal storage compared to pre-collapse compositions (Hora et al., 2007, 2009; Jicha et al., 2015).
- Significantly more evolved shoshonites at Stromboli Volcano being erupted during the Neostromboli period towards pre-collapse state (6 ka), indicating re-

establishment of an upper crustal storage system over time (Tibaldi, 2001,2004; Romagnoli et al., 2009; Vezzoli et al., 2014); followed by the Secche di Lazzaro deposits (<6 ka), which display a shift to more mafic compositions due to the influence of collapse-induced decompression on the shallow reservoir (Tibaldi, 2001; Petrone et al., 2009; Vezzoli et al., 2014).

- A strong shift to more mafic, Mg-rich compositions following a significant sector-collapse of the Basal Edifice (65-60 ka) at Chimborazo Volcano, which remained constant during the post-collapse period (Samaniego et al., 2012).

Most studies to date, lack continuous volcanic and sedimentary sequences and/or volcanic deposits representative of inter-collapse states (i.e. growth cycles) with stratigraphic resolutions higher than 10-20 kyr (**Table 7.1**). However, increased temporal resolution is required for gaining insights into short-term (<10 kyr) chemical and physical controls on magma plumbing systems, temporal characteristics of melt-mush interactions, storage system features and the response of magma reservoirs to depressurisation following collapse. The present sedimentological and geochemical study of Taranaki Volcano revealed several new aspects connected to andesitic volcanism and its response to edifice growth following surface mass redistribution (i.e. collapse) thanks to the unique exposures of inter-collapse volcanoclastic mass-flow sequences in the ring plain, providing unusually high stratigraphic resolutions of <10 kyr. The impact of cyclic edifice failure and subsequent regrowth on the subvolcanic magmatic system is reflected in the following signatures:

- A significant proportion of crystals displaying petrographic textures of disequilibrium;
- chemically bimodal melt inclusions trapped in minerals;
- the role of trachyandesitic melt in the melt-mush mixing process that produces the eruptible magmas;
- chemically and texturally diverse, recycled crystal populations;
- the polybaric rim equilibration of the clinopyroxene population;
- diverse ascending melt characteristics (i.e. H₂O contents); and
- the identified crystal-rich mush domain beneath Taranaki Volcano.

All of these petrochemical features confirmed that bulk-rock analyses of these petrologically complex andesites cannot explain in entirety the fundamental processes of

arc magmatism at Taranaki Volcano. However, the results of this study indicate that the produced whole-rock compositions are affected by melt-mush mixing ratios, with ratios varying within individual edifice growth cycles. The data further revealed that bulk-rock compositions temporally (on a c. 10 kyr scale) exhibit a widening geochemical composition range towards pre-collapse states, signifying the reactivation of the mid- to upper-crustal system due to edifice loading. Furthermore, results of this study confirm that the short-term (c. 10 kyr) petrogenetic model complements the temporal evolution model of Taranaki Volcano (based on c. 200 kyr timescale; Price et al., 1999, 2005, 2016; Zernack et al., 2012b), shedding new lights on the differences of short- and long-term magmatic processes and their interpretation in relation to growth and collapse. While the long-term model confirmed a temporal gradual evolution of magmas over c. 200 kyr, it lacks the fine-resolution information of the magmatic system, which is provided by the model proposed here.

<i>Arc Volcano</i>	<i>Number of DAD in the studied time period</i>	<i>[Age-range of inter-collapse deposits/volcanic units] (from older to younger) Number of sampled deposits/volcanic units within the time period</i>	<i>(DAD age)</i>	<i>References</i>
<i>Montagne Pelée</i>	<i>1</i>	<i>[>32 ka] - (~32 ka) - [32-27 ka] - [22.5 ka - 1929]</i> <i>1 1 1</i>		<i>Boudon et al. (2013)</i>
<i>Parinacota</i>	<i>1</i>	<i>[50-40 ka] - [32-27 ka] - [27-22 ka] - (~20-15 ka) - [10-0 ka]</i> <i>3 2 1 3</i>		<i>Hora et al. (2009)</i>
<i>Montserrat</i>	<i>1</i>	<i>[282-130 ka]- (~130 ka) - [128-130 ka] - [110-23 ka] - [1995-2010]</i> <i>1 1 1 1</i>		<i>Cassidy et al., (2015)</i>
<i>Stromboli</i>	<i>2</i>	<i>[>14 ka] - (14 ka) - [~8 ka] - [~7.5 ka] - [~7 ka] - (6 ka) - [<6 ka]</i> <i>1 2 2 1 1</i>		<i>Vezzoli et al. (2014)</i>
<i>Chimborazo</i>	<i>2</i>	<i>[~120-100 ka] - [95-65 ka] - (~65-60 ka) - [~60 ka] - [48-35 ka] - [35-14 ka] - (14-12 ka) - [8-1 ka]</i> <i>1 1 1 1 1 1</i>		<i>Samaniego et al. (2012)</i>
<i>Taranaki</i>	<i>3</i>	<i>[>55-50 ka] - (~55-50 ka) - [~50-40 ka] - (>40 ka) - [40-36.9 ka] - (<34ka)</i> <i>2 10 5</i>		<i>this study</i>

Table 7.1 Stratigraphic resolution of geochemically investigated deposits/volcanic units of selected arc volcanoes in relation to inter-collapse states (i.e. growth cycles). In comparison, the sampled Taranaki inter-collapse volcanoclastic mass-flow deposit packages are indicated for each studied time period outlining the achieved high stratigraphic resolution. DAD: Debris-avalanche deposit.

CHAPTER 8

CONCLUSIONS

8.1 Accomplished objectives

This research revealed new aspects of ring plain volcanoclastic sedimentation and andesitic magma genesis at Taranaki Volcano, New Zealand, connected to recurring edifice growth cycles in the time period of c. 65-34 ka. The investigated time span involved the Otakeho (>55-50 ka), the Rama (>40 ka) and the Te Namu (<34 ka) Growth Phases. Multiple lithic-dominated and pumice-dominated hyperconcentrated-flow deposits were targeted from each growth phase and were sampled. The sampling strategy focussed on collecting vesicular pyroclasts (i.e. pumice and scoria), representing eruptive periods of Taranaki Volcano. These volcanic rocks produced by explosive volcanic activity contained information on the subvolcanic Taranaki volcanic system, and thus provided an opportunity to track the magmatic processes operating at depth within the time-windows of edifice growth cycles. For the purpose of the subaerial and subvolcanic exploration of Taranaki Volcano, five objectives were established and achieved:

Objective 1: Investigating sedimentological, lithological and stratigraphic properties and relationships of volcanoclastic mass-flow deposits in the southwestern sector of the Taranaki ring plain.

Long-lived composite volcanoes are surrounded by volcanic aprons worldwide (e.g. Merapi, Indonesia; Cascade Range, USA; Börzsöny Mountains, Hungary). However, in most cases, their deposits are largely hidden, eroded, buried or are entirely inaccessible. The investigation of the volcanoclastic mass-flow deposits in the southwestern sector of the Taranaki ring plain provided significant insights into ring plain stratigraphy. The volcanosedimentological exploration highlighted the connection of sedimentary textures – lithologies – paleotopography emplacements of the volcanoclastic deposits, adding important aspects on the categorization and interpretation of volcanoclastics in ring plain settings. To this aim, the developed classification criteria provide a better understanding on mass-flow processes during edifice growth phases at Taranaki Volcano that also contributes to distinguishing volcanoclastic mass-flow deposits globally.

The field study further revealed two debris-flow deposits (Lizzie Bell and Taungatara DFD) that related to significant flank collapse events as inferred by their minimum estimated volumes of 0.02 – 0.1 km³ and on the minimum travelled distance of 25-27 km. The study revealed widely distributed lithic-dominated volcanoclastic mass-flow deposits

with periodically recurring frequencies of a minimum c. 3-5 events per 4-10 kyr period in each investigated growth cycle. This also is significant for hazard and risk management in the southwestern sector of the Taranaki ring plain. Furthermore, the newly established term of “rapidly remobilised” was suggested for specific lithic-dominated and pumice-dominated volcanoclastic mass-flow deposits that indicate eruption connected mass-flow events and deposition shortly after eruptive activity. Finally, the stratigraphic model development for the time-period 65-34 ka will be of benefit for future studies of the ring plain deposits at Taranaki Volcano.

Objective 2: Geochemical fingerprinting of consecutive Taranaki growth cycles based on the nearly continuous stratigraphic succession from c. 65-34 ka.

The nature of magmatic responses to sector collapse and following edifice growth at stratovolcanoes is a growing topic in volcanology. However, there are several problems complicating this developing area of research, of which the most important factor appears to be the coarse time resolution (10-20 kyr) or the incomplete stratigraphic records that being sampled and analysed. The investigated growth phases outlined in Objective 1 provided a nearly continuous stratigraphy, with higher temporal resolution (3.5-10 kyr) of deposition within the three growth cycles, from which vesicular pyroclasts were sampled.

The geochemical analyses obtained on the eruptive products of Taranaki growth cycles showed basaltic to trachyandesitic whole-rock compositions and further pointed out major and trace elemental differences between the growth phases. Investigations involved petrogenetic modelling, which revealed that the pyroclast compositions can be reproduced by mixing processes, where the mafic endmember is characterised by a primitive mush and the felsic endmember by a trachy-andesitic melt. This was confirmed by the textural petrographic observations of the mineral phases within the samples. Results further showed that the melt-mush mixing ratios differ in the individual growth cycles resulting in variable bulk rock compositions. Geochemical analyses further unravelled the bimodal basaltic and trachytic melt inclusion compositions within phenocrysts, suggesting the possibility of trachy-andesitic melt generation by the mixing of these two components at depth.

An important discovery was the increasing compositional range of pyroclast whole-rock compositions through the stratigraphy towards pre-collapse conditions, suggesting

the effect of increasing surface loading on the mid-upper crustal processes during edifice growth. Additionally, the geochemical difference between inter-collapse and pre-collapse volcanic rocks in the studied time period further confirmed the role of the upper-crustal storage reactivation closer to pre-collapse states within short growth cycle timescales (3.5-10 kyr).

Objective 3: Determining crystallisation conditions and characterising ascending melts during individual growth cycles.

The melt-mush mixing results (Objective 2) indicated that the primitive crystal mush (as the mafic end member in the mixing process) plays an important role in the production of Taranaki eruptives. In order to elucidate the conditions of Taranaki magmas, thermobarometry and hygrometry models were applied to amphibole, clinopyroxene and plagioclase crystals to estimate crystallization temperatures, pressures and additional melt water contents.

Results revealed that amphibole crystallization corresponds to and may be representative of the crystal mush that Taranaki Volcano is fed from. Further, thermobarometric modelling displayed polybaric clinopyroxene rim crystallization occurring within the depth range of 26-12 km (± 7.5), which corresponds to mid-lower crustal regions. Moreover, hygrometry modelling indicated that ascending melts have significant differences between the individual growth cycles and that melts with higher water contents (3.9-4.8 wt%) share similar properties with the amphiboles from the mush zone. Thus, they are indicative of greater degassing and crystallisation at depth making up the mush domain. However, they ultimately did erupt, suggesting the potential influence of depressurization (i.e. collapse event) on the mid-crustal processes creating ascent paths for more viscous magmas.

Objective 4: Crystal stratigraphy of texturally and chemically complex mineral phases to unravel recurring patterns within the Taranaki crystal cargo.

There has not been any crystal stratigraphy research on samples of crystals from Taranaki Volcano in the past. Thus, clinopyroxene and plagioclase phenocrysts were targeted to discover reoccurring (textural and chemical) crystal patterns that would supply the recycled crystal cargo paradigm for the produced Taranaki andesites. This hypothesis has been confirmed by the characterisation of complex and variable chemical and textural

crystal patterns. To this end, the Crystal Pattern Classification (CPC) method has been developed. Focussing separately on the rim-mantle-core crystal regions of individual crystals, even the most complex patterns were able to be deciphered and interpreted in the light of multiple major and/or trace elemental variations.

Results confirmed the antecrystic origin of most of the crystal cores. Mantle and rim crystal pattern investigations of clinopyroxenes elucidated specific Mg# - Al profiles highlighting the complex magmatic processes (such as convection, recharge) working at the interface of the crystal mush and the ascending melts. Plagioclase rim crystal patterns, that appeared in each individual growth cycle, further displayed Li enrichment, which may be indicative for shallow storage and syneruptive magmatic processes. Reoccurring similar crystal patterns of clinopyroxene and plagioclase crystals during the growth cycles confirmed that the Taranaki magmatic plumbing system has recycled primitive plutonic assemblages during the studied 30 kyr and that the majority of crystals were primarily affected by magma recharge, convection and mixing with ascending melts.

Objective 5: Temporal aspects of the Taranaki magmatic system and the development of an integrated model for inter-collapse states.

The overall data and knowledge gained by this research highlighted several aspects of the subaerial and subvolcanic processes of Taranaki Volcano and their properties, such as the importance of volcanoclastic mass-flow deposits in elucidating the evolution of the volcanic system. These successions are useful to characterise sedimentary processes and stratigraphic constraints in ring plain settings connected to eruptive histories. Furthermore, they provide opportunities to analyse the geochemical/magmatic priorities of older eruptive periods of the volcano in relation to magmatic rates and timescales.

The development of a petrogenetic model for inter-collapse states complemented the accepted conceptual model of the Taranaki magmatic system. The thermobarometry and hygrometry results of the crystal cargo initiated the idea to compare those data with the early system of Taranaki Volcano (>105 ka), which revealed the temporal development of the Taranaki transcrustal system over c. 100 kyr. In addition, comparison of results indicated the importance of intrusive volcanism beneath Taranaki Volcano and its evolution and effect on the magmatic processes over time. These results further suggest that a more detailed exploration of the magmatic processes of the Taranaki transcrustal system and its temporal variation is required, and that the investigation of the Taranaki crystal cargo needs more attention in the future.

8.2 Future research

While achieving the research objectives of this study, several further questions arose, which may be addressed through future work. These partially can be obtained based on the dataset produced by the present research connected to Taranaki Volcano or on newly collected, processed datasets. Conceivable future research options are connected to the already reached objectives of this study as follows:

Objective 1:

- a) The investigation of the matrix of the different types of volcanoclastic mass-flow deposits in the ring plain of Taranaki Volcano and their connection to lithology and lithofacies.
- b) Paleomagnetism techniques obtained on the widely distributed, lithic-dominated mass-flow deposits to elucidate flow properties during transport as well as to possibly provide better time constraints.

Objective 2:

- a) The geochemical investigation of the recycled lithics (i.e. lava fragments and dense, glassy clasts) comprising the lithic-dominated volcanoclastic mass-flow deposits.
- b) Isotopic and trace elemental variations of the Taranaki mineral phases to potentially answer the antecrystic vs. xenocrystic dilemma of the recycled crystal cargo and to gain crystallization ages for that purpose.
- c) The comprehensive analysis of melt inclusions enclosed by plagioclase, clinopyroxene and amphibole of Taranaki crystals to characterise the melt evolution and additional volatile properties over the lifetime of the volcano using samples from the early system (>105 ka), from the mid-age system (c. 65-34 ka), from the young system (<29 ka) and from the debris avalanche deposits over the last 200 kyr.
- d) The more detailed study of the minerals originating from the Median Batholith to gain insights into the plutonic/intrusive magmatism beneath Taranaki Volcano.

Objective 3:

- a) P-T-H₂O estimations of the modern edifice (<14 ka) and a more detailed thermodynamic modeling of the old system (>105 ka) obtained on pyroclasts.

- b) P-T-H₂O modeling of the melt inclusion data to gain more insights into the ascending melt characteristics over the lifetime of Taranaki Volcano.
- c) More detailed titanomagnetite analysis on the mid-age and old system Taranaki eruptives and their comparison to the young Taranaki titanomagnetite chemistry.
- d) Melt inclusion analysis of the mid-age Taranaki eruptives in order to characterise the nature of melts responding to successive edifice collapses and to find a potential explanation for eruption triggering processes.

Objective 4:

- a) Li-diffusion calculations to elucidate shallow-depth minimum estimates of ascent using plagioclase antecryst rims.
- b) Fe-Mg exchange: diffusion modelling using clinopyroxene crystals to decipher information on magma residence times.

8.3 Epilogue

Andesitic arc magma generation and evolution is an active topic in volcanology that poses several, yet unsolved phenomena, due to the insufficient chemostratigraphic record beyond the Holocene and the complexity of magma plumbing systems worldwide. However, progressively evolving global research on arc magmatism provides new paradigms that support the crystal mush concept and the transcrustal magmatic system scenario along with the significant effects of melt-mush mixing processes in the crust.

Altogether, the research presented here supports and reinforces the melt-mush mixing processes operating at mid- to lower-crustal depths and aimed for finding temporal (short timescale) chemical signatures of magmatic response to edifice growth. The results provided by this study contributed to fill knowledge gaps connected to the nature of the Taranaki magmatic system within c. 65-34 ka and its temporal aspects affected by growth and collapse, which will support the risk and hazard management of Taranaki Volcano in the future and will provide useful background information on how to mitigate subaerial and subvolcanic risks associated with stratovolcanoes throughout growth cycles.

REFERENCES

- Adams RD and Ware DE** (1977) Structural Earthquakes Beneath New Zealand: Location Determined with A Laterally Inhomogeneous Velocity Model – New Zealand Journal of Geology and Geophysics. **20**: 59-83.
- Alloway B, McComb P, Neall V, Vucetich C, Gibb J, Sherburn S, Stirling M** (2005) Stratigraphy, age, and correlation of voluminous debris avalanche events from an ancestral Egmont Volcano: Implications for coastal plain construction and regional hazard assessment. Journal of the Royal Society of New Zealand, **35**: 229-267.
- Alloway B, Neall VE, Vucetich CG** (1995) Late Quaternary (post-28,000 year BP) tephrostratigraphy of northeast and central Taranaki, New Zealand. – Journal of the Royal Society of New Zealand. **25**: 385–458.
- Anderson DL and Bass JD** (1984) Mineralogy and composition of the upper mantle. Geophysical Research Letters. **11**(7): 637-40.
- Andrews GD, Branney MJ, Bonnicksen B, McCurry M** (2008) Rhyolitic ignimbrites in the Rogerson Graben, southern Snake River Plain volcanic province: volcanic stratigraphy, eruption history and basin evolution. Bulletin of Volcanology. **70**(3): 269-91.
- Annen C, Blundy JD, Leuthold J, Sparks RSJ** (2015) Construction and evolution of igneous bodies: Towards an integrated perspective of crustal magmatism. – Lithos. **230**: 206–221. doi: 10.1016/j.lithos.2015.05.008
- Annen C, Blundy JD, Sparks RSJ** (2006) The Genesis of Intermediate and Silicic Magmas in Deep Crustal Hot Zones. – Journal of Petrology. **47**: 505–539.
- Arculus RJ and Powell R** (1986) Source component mixing in the regions of arc magma generation. J. Geophys. Res. **91**: 5913–5926.
- Arienzo I, Mazzeo FC, Moretti R, Cavallo A, D’Antonio M** (2016) Open system magma evolution and fluid transfer at Campi Flegrei caldera (southern Italy) during the past 5 ka as revealed by geochemical and isotopic data: the example of the Nisida eruption. Chem. Geol. **427**, 109–124.
- Arienzo I, Moretti R, Civetta L, Orsi G, Papale P** (2010) The feeding system of Agnano–Monte Spina eruption (Campi Flegrei, Italy): Dragging the past into present activity and future scenarios – Chemical Geology. **270**: 135-147.
- Armienti P, Perinelli C, Putirka KD** (2013) A new model to estimate deep-level magma ascent rates, with applications to Mt. Etna (Sicily, Italy) – J. Petrol. **54**: 795-813. 10.1093/petrology/egs085
- Armienti P, Tonarini S, Innocenti F, D’Orazio M** (2007) Mount Etna pyroxene as tracer of petrogenetic processes and dynamics of the feeding system – Geol. Soc. Am. Spec. Pap. **418**: 265-276. 10.1130/2007.2418(13)
- Arnold HC** (1959) The Sugar Loaf Intrusions Near New Plymouth – New Zealand Journal of Geology and Geophysics **2**: 735-745.
- Atherton MP and Petford N** (1993) Generation of Sodium-rich Magmas from Newly Underplated Basaltic Crust – Nature. **362**: 144–146.
- Bachmann O and Bergantz GW** (2004). On the origin of crystal-poor rhyolites: Extracted from batholithic crystal mushes. Journal of Petrology. **45**(8): 1565–1582. <https://doi.org/10.1093/petrology/egh019>
- Bachmann O and Bergantz GW** (2008) Rhyolites and their source mushes across tectonic settings. J. Petrol. **49**: 2277–2285.
- Bachmann O and Huber C** (2016) Silicic magma reservoirs in the Earth’s crust. American Mineralogist. **101**: 2377-2404.

- Bachmann O and Bergantz GW** (2006) Gas percolation in upper-crustal silicic crystal mushes as a mechanism for upward heat advection and rejuvenation of near-solidus magma bodies. *Journal of Volcanology and Geothermal research*. **149**(1-2): 85-102.
- Bachmann O, Miller CF, De Silva SL** (2007) The volcanic–plutonic connection as a stage for understanding crustal magmatism. *Journal of Volcanology and Geothermal Research*. **167**(1-4): 1-23.
- Bagnold RA** (1954) Experiments on A Gravity-Free Dispersion of Large Solid Spheres in A Newtonian Fluid Under Shear – *Proc. R. Soc., Ser. A*. **225**:49-63.
- Barclay J, Alexander J, Sus˘ Nik J** (2007) Rainfall-Induced Lahars in The Belham Valley, Montserrat, West Indies – *Journal of the Geological Society, London*. **164**: 815–827.
- Beavan JM, Moore M, Pearson C, Henderson M, Parsons B, Bourne S, England P, Walcott D, Blick G, Darby D, Hodgkinson K** (1999) Crustal Deformation During 1994-1998 Due To Oblique Continental Collision In The Central Southern Alps, New Zealand, And Implications For Seismic Potential Of The Alpine Fault – *Journal of Geophysical Research* **104**: 25,233-25,255
- Begét JE and Kienle J** (1992) Cyclic formation of debris avalanches at Mount St Augustine volcano. *Nature*. **356**(6371): 701-704.
- Belousov A, Belousova M, Voight B** (1999) Multiple edifice failures, debris avalanches and associated eruptions in the Holocene history of Shiveluch volcano, Kamchatka, Russia. *Bulletin of Volcanology*. **61**: 324–342.
- Bennett EN, Lissenberg CJ, Cashman KV** (2019). The significance of plagioclase textures in mid-ocean ridge basalt (Gakkel Ridge, Arctic Ocean). *Contrib. Mineral. Petr.* **174**: 49.
- Benvenuti M and Martini IP** (2002) Analysis of terrestrial hyperconcentrated flows and their deposits. *Spec. Publ. int. Ass. Sediment.*, **32**: 167-93.
- Berlo K, Blundy J, Turner S, Cashman K, Hawkesworth C, Black S** (2004) Geochemical precursors to volcanic activity at Mount St. Helens, USA. *Science*. **306**(5699): 1167-9.
- Berlo K, Blundy J, Turner S, Hawkesworth C** (2007) Textural and chemical variation in plagioclase phenocrysts from the 1980 eruptions of Mount St. Helens, USA. *Contributions to Mineralogy and Petrology*. **154**(3): 291-308.
- Beverage JP and Culbertson JK** (1964) Hyperconcentrations of suspended sediment. *American Society of Civil Engineers, Proceedings, Hydraulics Division Journal*, **90**, no. HY6: 117-128.
- Blundy J and Cashman KV** (2001) Ascent-Driven Crystallisation of Dacite Magmas at Mount St Helens, 1980–1986 – *Contributions to Mineralogy and Petrology*. **140**: 631–650.
- Blundy J and Cashman KV** (2008) Petrologic Reconstruction of Magmatic System Variables and Processes – *Rev Mineral Geochem*. **69**: 179–239.
- Blundy J and Shimizu N** (1991) Trace element evidence for plagioclase recycling in calc-alkaline magmas. – *Earth and Planetary Science Letters*. **102**: 178–197.
- Blundy J, Cashman K, Humphreys M** (2006) Magma Heating by Decompression-Driven Crystallisation Beneath Andesite Volcanoes – *Nature*. **443**: 76–79 doi: 10.1038/nature05100
- Blundy JD, Falloon TJ, Wood BJ, Dalton JA** (1995) Sodium partitioning between clinopyroxene and silicate melts. *Journal of Geophysical Research: Solid Earth*. **100**(B8): 15501-15.

- Boddington T, Parkin CJ, Gubbins D** (2004) Isolated deep earthquakes beneath the North Island of New Zealand, *Geophys. J. Int.* **158**: 972–982, doi:10.1111/j.1365-246X.2004.02340.x.
- Borgia A and Van Wyk De Vries B** (2003) The Volcano-Tectonic Evolution of Concepcion, Nicaragua – *Bulletin of Volcanology*. **65**: 248-266.
- Botcharnikov RE, Almeev RR, Koepke J, Holtz F** (2008) Phase relations and liquid lines of descent in hydrous ferrobasalt—implications for the Skaergaard intrusion and Columbia River flood basalts. *Journal of Petrology*. **49**(9): 1687-727.
- Boudon G, Villemant B, Le Friant A, Paterne M, Cortijo E** (2013) Role of Large Flankcollapse Events on Magma Evolution of Volcanoes. Insights from The Lesser Antilles Arc – *Journal of Volcanology and Geothermal Research*. **263**: 224-237.
- Bouilhol P, Schmidt MW, Burg JP** (2015) Magma transfer and evolution in channels within the arc crust: the pyroxenitic feeder pipes of Sapat (Kohistan, Pakistan). *Journal of Petrology*. **56**(7): 1309-42.
- Boulestex T, Hildenbrand A, Gillot PY, Soler V** (2012) Eruptive response of oceanic islands to giant landslides: New insights from the geomorphologic evolution of the Teide-Pico Viejo volcanic complex (Tenerife, Canary). *Geomorphology*. **138**: 61-73.
- Bouvet de Maisonneuve C, Costa F, Huber C, Vonlanthen P, Bachmann O, Dungan MA** (2016) How do olivines record magmatic events? Insights from major and trace element zoning. *Contrib. Mineral. Petrol.* **176**: 56.
- Bowen NL** (1928) *The Evolution of the Igneous Rocks*: Princeton, New Jersey, Princeton University Press, 332 p.
- Brophy JG, Whittington CS, Park Y-R** (1999) Sector-zoned augite megacrysts in Aleutian high alumina basalts: implications for the conditions of basalt crystallization. – *Contrib. Mineral. Petrol.* **125**: 277-290
- Browne BL and Gardner JE** (2006) The influence of magma ascent path on the texture, mineralogy, and formation of hornblende reaction rims. *Earth and Planetary Science Letters*. **246**(3-4): 161-76.
- Browne BL, Eichelberger JC, Patino LC, Vogel TA, Dehn J, Uto K, Hoshizumi H** (2006). Generation of porphyritic and equigranular mafic enclaves during magma recharge events at Unzen Volcano, Japan. *Journal of Petrology*. **47**(2): 301–328. <https://doi.org/10.1093/petrology/egi076>
- Buddington AF and Lindsley DH** (1964) Iron-titanium oxide minerals and synthetic equivalents. *Journal of petrology*. **5**(2): 310-57.
- Burgisser A and Bergantz GW** (2011) A rapid mechanism to remobilize and homogenize highly crystalline magma bodies. *Nature*. **471**(7337): 212-5.
- Capra L and Macias JL** (2000) Pleistocene cohesive debris flows at Nevado de Toluca volcano, central Mexico. *Journal of Volcanology and Geothermal Research*, **102**: 149–168.
- Capra L and Macias JL** (2002) The Cohesive Naranjo Debris-Flow Deposit (10 Km³): A Dam Breakout Flow Derived from The Pleistocene Debris-Avalanche Deposit of Nevado De Colima Volcano (México) – *Journal of Volcanology and Geothermal Research*. **117**: 213-235.
- Capra L, Macias JL, Scott KM** (2002) Debris avalanches and debris flows transformed from collapses in the Trans-Mexican volcanic belt, Mexico behaviour, and implications for hazard assessment. *Journal of Volcanology and Geothermal Research*, **113**: 81-110.

- Caracciolo A, Bali E, Guðfinnsson GH, Kahl M, Halldórsson SA, Hartley ME, Gunnarsson H.** (2020). Temporal evolution of magma and crystal mush storage conditions in the Bárðarbunga-Veiðivötn volcanic system, Iceland. *Lithos.* 352-353, 105234. <https://doi.org/10.1016/j.lithos.2019.105234>
- Carracedo JC** (1994) The Canary Islands: an example of structural control on the growth of large oceanic-island volcanoes. – *J Volcanol Geotherm Res.* **60**:225–241.
- Carracedo JC, Day SJ, Guillou H, Torrado FJ** (1999) Giant quaternary landslides in the evolution of La Palma and El Hierro, Canary Islands. *Journal of Volcanology and Geothermal Research.* **94**(1-4):169-90.
- Carracedo JC, Rodriguez, Badiola E, Guillou H, Paterne M, Scaillet S, Perez Torrado FJ, Paris R, Fra-Paleo U, Hansen A** (2007) Eruptive and structural history of Teide volcano and rift zones of Tenerife, Canary Islands - *GSA Bull.* **119**: 1027-1051.
- Cas R and Wright JV** (1987) *Volcanic Successions Ancient and Modern* – London, Allen and Unwin
- Cashman K and Blundy J** (2013) Petrological cannibalism: The chemical and textural consequences of incremental magma body growth. *Contrib. Mineral. Petrol.* **166**: 703–729. doi: 10.1007/s00410-013-0895-0
- Cashman KV and Edmonds M** (2019) Mafic glass compositions: a record of magma storage conditions, mixing and ascent. – *Phil. Trans. R. Soc. A.* **377**: 20180004. <http://dx.doi.org/10.1098/rsta.2018.0004>
- Cashman KV, Sparks RSJ, Blundy JD** (2017) Vertically extensive and unstable magmatic systems: a unified view of igneous processes. *Science* 355, eaag3055. doi:10.1126/science.aag3055
- Cassidy M, Edmonds M, Watt SFL, Palmer MR, Gernon TM** (2015) Origin of Basalts by Hybridization in Andesite-Dominated Arcs. – *Journal of Petrology.* **56**: 325-346.
- Cassidy M, Taylor RN, Palmer MR, Cooper RJ, Stenlake C, Trofimovs J** (2012) Tracking the magmatic evolution of island arc volcanism: Insights from a high-precision Pb isotope record of Montserrat, Lesser Antilles. *Geochemistry, Geophysics, Geosystems.* **13**(5).
- Chappell BW and White JR** (2001) Two Contrasting Granite Types: 25 Years Later – *Australian Journal of Earth Sciences.* **48**: 489–499.
- Charlier B and Grove TL** (2012) Experiments on liquid immiscibility along tholeiitic liquid lines of descent. *Contributions to Mineralogy and Petrology.* **164**(1): 27-44.
- Claiborne L, Miller C, Wooden J** (2010) Trace element composition of igneous zircon: a thermal and compositional record of the accumulation and evolution of a large silicic batholith, Spirit Mountain, Nevada. – *Contributions to Mineralogy and Petrology.* **160**: 511-531.
- Clynne, MA** (1999) A Complex Magma Mixing Origin for Rocks Erupted In 1915, Lassen Peak, California – *Journal of Petrology.* **40**: 105–132.
- Coello-Bravo JJ, Márquez Á, Herrera R, Huertas MJ, Ancochea E** (2020) Multiple related flank collapses on volcanic oceanic islands: Evidence from the debris avalanche deposits in the Orotava Valley water galleries (Tenerife, Canary Islands). *Journal of Volcanology and Geothermal Research.* **401**: 106980.
- Cole JW** (1979) Structure, Petrology and Genesis of Cenozoic Volcanism, Taupo Volcanic Zone, New Zealand: A Review – *New Zealand Journal of Geology and Geophysics* **22**: 631-657.

- Cole JW** (1982) Tonga-Kermadec-New Zealand. In: Thorpe RS (Ed.) *Andesites: Orogenic Andesites And Related Rocks* - Wiley, New York
- Cole JW** (1986) Distribution and Tectonic Setting of Late Cenozoic Volcanism in New Zealand. In: Smith IEM (Ed.) *Late Cenozoic Volcanism in New Zealand* – Bulletin of the Royal Society of New Zealand **23**: 7-20.
- Concha-Dimas A, Cerca M, Rodríguez SR, Watters RJ** (2005) Geomorphological evidence of the influence of pre-volcanic basement structure on emplacement and deformation of volcanic edifices at the Cofre de Perote-Pico de Orizaba chain and implications for avalanche generation. *Geomorphology*, **72**: 1-4.
- Cooper KM and Kent AJ** (2014) Rapid remobilization of magmatic crystals kept in cold storage. *Nature*. **506**(7489): 480-3.
- Costa F** (2000) The Petrology and Geochemistry of Diverse Crustal Xenoliths, Tatará-San Pedro Volcanic Complex, Chilean Andes – *Terre & Environment*. **19**: 120.
- Costa F and Chakraborty S** (2004) Decadal Time Gaps Between Mafic Intrusion and Silicic Eruption Obtained from Chemical Zoning Patterns in Olivine – *Earth Planet Sci Lett*. **227**: 517–530.
- Costa F and Morgan D** (2011) Time Constraints from Chemical Equilibration in Magmatic crystals – In: Dosseto, A., Turner, S.P., Van Orman, J.A. (Eds.), *Timescales of Magmatic Processes: From Core to Atmosphere*, 125–159 pp
- Costa F and Singer B** (2002) Evolution of Holocene Dacite and Compositionally Zoned Magma, Volcán San Pedro, Southern Volcanic Zone, Chile – *Journal of Petrology*. **43**: 1571-1593.
- Costa JE** (1984) Physical Geomorphology of Debris Flows – In: Costa JE, Fleischer PJ (Eds.) *Developments and applications of geomorphology*, Springer, Berlin, p. 269-317.
- Costa JE** (1988) Rheologic, Geomorphic, and Sedimentologic Differentiation of Water Floods, Hyperconcentrated Flows, and Debris Flows – In: V.R. Baker, R.C. Kochel and P.C. Patton (Editors), *Flood Geomorphology*. Wiley, New York, pp. 113-122.
- Costa JE and Schuster RL** (1988) The formation and failure of natural dams. *Geol. Soc. Am. Bull.*, **100**: 1054–1068.
- Couch S, Harford CL, Sparks RSJ, Carroll MJ** (2003) Experimental constraints on the conditions of formation of highly calcic plagioclase microlites at the Soufriere Hills Volcano, Montserrat. *J. Petrol.* **44**: 1455-1475.
- Coussot P and Meunier M** (1996) Recognition, classification and mechanical description of debris flows. *Earth Sci. Rev.*, **40**: 209-227.
- Crandell DR, Miller CD, Glicken HX, Christiansen RL, Newhall CG** (1984) Catastrophic debris avalanche from ancestral Mount Shasta Volcano, California. *Geology*, **12**: 143-146.
- Cronin SJ and Neall VE** (1997) A Late Quaternary Stratigraphic Framework for The Northeastern Ruapehu And Eastern Tongariro Ring Plains, New Zealand – *New Zealand Journal of Geology and Geophysics* **40**: 185-197.
- Cronin SJ, Hodgson KA, Neall VE, Palmer AS, Lecointre JA** (1997) 1995 Ruapehu lahars in relation to the late Holocene lahars of Whangaehu River, New Zealand. *NZ J. Geol. Geophys.*, **40**: 507-520.
- Cronin SJ, Lecointre JA, Palmer AS, Neall VE** (2000a) Transformation, Internal Stratification, and Depositional Processes within a Channelised, Multi-Peaked Lahar Flow – *New Zealand Journal of Geology and Geophysics*. **43**: 117-128.
- Cronin SJ, Neall VE, Lecointre JA, Palmer AS** (2000b) Dynamic Interactions Between Lahars and Stream Flow: A Case Study from Ruapehu Volcano, New Zealand:

- Discussion and Reply – Bulletin of the Geological Society of America. **112**: 1151-1152.
- Cronin SJ, Neall VE, Palmer AS** (1996) Geological History of The Northeastern Ring Plain of Ruapehu Volcano, New Zealand – Quaternary International. **35**: 21-28.
- Damaschke M, Cornin SJ, Holt KA, Bebbington MS, Hogg AG** (2017a) A 30,000 yr high-precision eruption history for the andesitic Mt Taranaki, North Island, New Zealand – Quat. Res. **87**: 1-23.
- Damaschke M, Cornin SJ, Torres-Orozco R, Wallace RC** (2017b) Unifying tephrostratigraphic approaches to redefine major Holocene marker tephras, Mt. Taranaki, New Zealand – J. Volcanol. Geotherm. Res. **337**: 29-43.
- Danišik M, Shane PAR, Schmitt AK, Hogg A, Santos GM, Storm S, Evans NJ** (2012) Re-anchoring the late Pleistocene tephrochronology of New Zealand based on concordant radiocarbon ages and combined $^{238}\text{U}/^{230}\text{Th}$ disequilibrium and (U-Th)/He zircon ages. Earth and Planetary Science Letters 349-350: 240-250.
- Davidson JP and De Silva S** (2000) Composite Volcanoes – In: Sigurdsson H, Houghton B, McNutt S, Rymer H, Stix J (Eds.) Encyclopedia of Volcanoes, Academic Press, San Diego, p. 663-681.
- Davidson JP, Hora JM, Garrison JM, Dungan MA** (2005) Crustal Forensics in Arc Magmas – Journal of Volcanology and Geothermal Research. **140**: 157–170.
- Davidson JP, Morgan DJ, Charlier BLA, Harlou R, Hora JM** (2007) Microsampling and isotopic analysis of igneous rocks: Implications for the study of magmatic systems. – Annu. Rev. Earth Planet. Sci. **35**: 273–311. doi: 10.1146/annurev.earth.35.031306.140211
- Davies JH, Stevenson DJ** (1992) Physical model of source region of subduction zone volcanics. – Journal of Geophysical Research. **97**: 2037-2070.
- Day S, Llanes P, Silver E, Hoffman G, Ward S, Driscoll N** (2015) Submarine Landslide Deposits of The Historical Lateral Collapse of Ritter Island, Papua New Guinea – Marine and Petroleum Geology. **67**: 419-438.
- Delcamp A, Troll VR, van Wyk de Vries B, Carracedo JC, Petronis MS, Pérez-Torrado FJ, Deegan FM** (2012) Dykes and structures of the NE rift of Tenerife, Canary Islands: a record of stabilisation and destabilisation of ocean island rift zones. Bull Volcanol. **74**: 963–980.
- DePaolo DJ** (1981) Trace-element and isotopic effects of combined wallrock assimilation and fractional crystallisation. – Earth and Planetary Science Letters. **53**: 189–202.
- DePaolo DJ, Perry FV, Baldrige WS** (1992) Crustal versus mantle sources of granitic magmas-a 2-parameter model based on Nd isotopic studies. Transactions of the Royal Society of Edinburgh – Earth Sciences. **83**: 439–446.
- Devine CY, Dollar TE, Munguia WJ, Schwarz E** (2003) inventors; Verizon Business Global LLC, assignee. Integrated proxy interface for web-based report requester tool set. United States patent US 6,631,402.
- Di Stefano F, Mollo S, Ubide T, Petrone CM, Caulfield J, Scarlato P, Nazzari M, Andronico D, Del Bello E.** (2020) Mush cannibalism and disruption recorded by clinopyroxene phenocrysts at Stromboli volcano: New insights from recent 2003–2017 activity. Lithos. **360**: 105-440.
- Donoghue SL and Neall VE** (2001) Late quaternary constructional history of the southeastern Ruapehu ring plain, New Zealand. New Zealand Journal of Geology and Geophysics, **44**: 439-466.

- Donoghue SL, Neall VE, Palmer AS** (1995) Stratigraphy and Chronology of Late Quaternary Andesitic Tephra Deposits, Tongariro Volcanic Centre, New Zealand – Royal Society of New Zealand Journal, v. **25**, p. 115–206.
- Dungan M, Wulff A, Thompson R** (2001) Eruptive Stratigraphy of The Tatara-San Pedro Complex, 36°S, Southern Volcanic Zone, Chilean Andes: Reconstruction Method and Implications for Magma Evolution at Long-Lived Arc Volcanic Centers – Journal of Petrology. **42**(3): 555-626.
- Dungan MA and Davidson J** (2004). Partial assimilative recycling of the mafic plutonic roots of arc volcanoes: an example from the Chilean Andes. – Geology. **32**: 773:776.
- Edmonds M, Cashman KV, Holness M, Jackson M** (2019) Architecture and dynamics of magma reservoirs. Phil. Trans. R. Soc. A 377, 20180298. (doi:10.1098/rsta.2018.0298)
- Edmonds M, Kohn SC, Hauri EH, Humphreys MC, Cassidy M** (2016) Extensive, water-rich magma reservoir beneath southern Montserrat. Lithos. **252**: 216-33.
- Eichelberger JC** (1978) Andesitic Volcanism and Crustal Evolution – Nature. **275**: 21-27.
- Eichelberger JC, Izbekov PE, Browne BL** (2006) Bulk chemical trends at arc volcanoes are not liquid lines of descent. Lithos. **87**(1-2): 135-54.
- Elardo SM and Shearer Jr CK** (2014) Magma chamber dynamics recorded by oscillatory zoning in pyroxene and olivine phenocrysts in basaltic lunar meteorite Northwest Africa 032. American Mineralogist. **99**(2-3): 355-68.
- Elburg M and Foden J** (1998) Temporal changes in arc magma geochemistry, northern Sulawesi, Indonesia – Earth and Planetary Science Letters. **163**: 381-398.
- Elkins-Tanton LT, Grove TL, Donnelly-Nolan J** (2001) Hot shallow melting under the Cascades volcanic arc. – Geology. **29**: 631–634.
- Ersoy Y and Helvaci C** (2010) FC–AFC–FCA and Mixing Modeler: A Microsoft® Excel© Spreadsheet Program for Modeling Geochemical Differentiation of Magma by Crystal Fractionation, Crustal Assimilation and Mixing – Computers and Geosciences. **36**: 383-390.
- Ewart A, Brothers RN, Mateen A** (1977) An Outline of the Geology and Geochemistry, and the Possible Petrogenetic Evolution of The Volcanic Rocks of The Tonga-Kermadec-New Zealand Island Arc – Journal of Volcanology and Geothermal Research **2**: 205-250
- Fairbanks RG, Mortlock RA, Chiu TC, Cao L, Kaplan A, Guilderson TP, Fairbanks TW, Bloom AL, Grootes PM, Nadeau MJ** (2005) Radiocarbon calibration curve spanning 0 to 50,000 years BP based on paired $^{230}\text{Th}/^{234}\text{U}/^{238}\text{U}$ and ^{14}C dates on pristine corals. Quaternary Science Reviews, **24**: 1781-1796.
- Feng W and Zhu Y** (2018) Decoding magma storage and pre-eruptive processes in the plumbing system beneath early Carboniferous arc volcanoes of southwestern Tianshan, Northwest China. Lithos. **322**: 362-75.
- Feng W and Zhu Y** (2019a) Petrogenesis and tectonic implications of the late Carboniferous calc-alkaline and shoshonitic magmatic rocks in the Awulale mountain, western Tianshan. Gondwana Research. **76**: 44-61.
- Feng W and Zhu Y** (2019b) Magmatic plumbing system beneath a fossil continental arc volcano in western Tianshan (NW China): Constraints from clinopyroxene and thermodynamic modelling. Lithos. **350**: 105221.
- Fisher RV** (1961) Proposed Classification of Volcaniclastic Sediments and Rocks – Geological Society of America Bulletin. **72**: 1409-1414.

- Fisher RV** (1966) Rocks composed of volcanic fragments and their classification – *Earth Science Reviews*. **1**: 287–298. doi: 10.1016/0012-8252(66)90010-9
- Fisher RV** (1983) Flow transformation in sediment gravity flows. *Geology*, **11**: 273-274.
- Fisher RV and Schmincke HU** (1984) *Pyroclastic Rocks* – Springer, Heidelberg, 472p
- Forneris JF, Holloway JR** (2003) Phase equilibria in subducting basaltic crust: implications for H₂O release from the slab. *Earth and Planetary Science Letters*. **214**: 187–201.
- Gaetani GA and Grove TL** (2003) Experimental constraints on melt generation in the mantle wedge: American Geophysical Union Geophysical Monograph 138, p. 107–134.
- Galipp K, Klugel A, Hansteen TH** (2006) Changing depths of magma fractionation and stagnation during the evolution of an oceanic island volcano: La Palma (Canary Islands). *J. Volcanol. Geotherm. Res.* **155**: 258–306.
- Gamble JA, Smith IE, Graham IJ, Kokelaar BP, Cole JW, Houghton BF, Wilson CJ** (1990) The petrology, phase relations and tectonic setting of basalts from the Taupo Volcanic Zone, New Zealand and the Kermadec Island Arc-Havre Trough, SW Pacific. *Journal of volcanology and geothermal research*. **43**(1-4): 253-70.
- Gamble JA, Wood CP, Price RC, Smith IEM, Stewart RB, Waight T** (1999) A Fifty-Year Perspective of Magmatic Evolution on Ruapehu Volcano, New Zealand; Verification of Open System Behaviour in an Arc Volcano – *Earth Planet. Sci. Lett.* **170**: 301– 314.
- Ganne J, Bachmann O, Feng X** (2018) Deep into Magma Plumbing Systems: Interrogating the Crystal Cargo of Volcanic Deposit – *Geology* 2018133 <https://doi.org/10.1130/G39857.1>
- Gaylord DR and Neall VE** (2012) Subedifice Collapse Of An Andesitic Stratovolcano: The Maitahi Formation, Taranaki Peninsula, New Zealand – *GSA Bulletin* **124**: 1-2, 181-199 <https://doi.org/10.1130/B30141.1>
- Gaylord DR, Neall VE, Palmer AS** (1993) The Maitahi Formation, A Mid-Pleistocene Volcanic Debris Avalanche Assemblage, Taranaki, New Zealand – Abstract in: *Volcanic activity and the environment, abstracts of the IAVCEI, Puerto Vallarta, Mexico 1997 General Assembly*. Gobierno de Jalisco, Unidad Editorial, Guadalajara, Mexico
- Geist D, White WM, Albarède F, Harpp K, Reynolds R, Blichert R, Toft Kurz M** (2002) Volcanic evolution in the Galapagos: The dissected shield of Volcan Ecuador – *Geochem. Geophys. Geosyst.* **3**: 1-32.
- Germa A, Quidelleu, X, Lahitte P, Labanieh S, Chauve C** (2011) The K/Ar Cassignol-Gillot Technique Applied to Western Martinique Lavas: A Record of Lesser Antilles Arc Activity From 2ma To Mount Pelée Volcanism – *Quaternary Geochronology*. **6**: 341-355.
- Gertisser R and Keller J** (2003) Temporal Variations in Magma Composition at Merapi Vol-Cano (Central Java, Indonesia): Magmatic Cycles During the Past 2000 Years of Ex-Plosive Activity – *Journal of Volcanology and Geothermal Research*. **123**: 1–23.
- Gill JB** (1981) *Orogenic Andesites and Plate Tectonics*, Springer-Verlag.
- Ginibre C and Wörner G** (2007) Variable parent magmas and recharge regimes of the Parinacota magma system (N. Chile) revealed by Fe, Mg and Sr zoning in plagioclase. *Lithos*. **98**(1–4):118–140.
- Ginibre C, Wörner G, Kronz A** (2007) Crystal Zoning as An Archive for Magma Evolution – *Elements*. **3**: 261-266.

- Ginibre C, Wörner G, Kronz A** (2002) Minor and trace element zoning in plagioclase: implications for magma chamber processes at Paríacota Volcano, N. Chile – *Contrib. Mineral. Petrol.* **143**: 300-315.
- Giordano G, De Rita D, Fabbri M, Rodani S** (2002) Facies associations of rain-generated versus crater lake-withdrawal lahar deposits from Quaternary Volcanoes, Central Italy. *J. Volcanol. Geotherm. Res.*, **118**: 145-160.
- Giuffrida M and Viccaro M** (2017) Three years (2011–2013) of eruptive activity at Mt. Etna: Working modes and timescales of the modern volcano plumbing system from micro-analytical studies of crystals. *Earth-Science Reviews.* **171**: 289-322.
- Glicken H** (1991) Sedimentary architecture of large volcanic debris avalanches. In: Fisher RV, Smith GA (Eds.) *Sedimentation in Volcanic Settings*. SEPM Special Publication, **45**: 99-106.
- Glicken H** (1996) Rockslide-debris avalanche of May 18, 1980, Mount St. Helens Volcano. Washington, US Geological Survey, Open File Report, 96-677, 90 p.
- Gorbach N, Portnyagin M and Tembrel I** (2013) Volcanic Structure and Composition of Old Shiveluch Volcano, Kamchatka – *Journal of Volcanology and Geothermal Research.* **263**: 193-208
- Gow AJ** (1968) Petrographic and Petrochemical Studies of Mt. Egmont Andesites – *New Zealand Journal of Geology and Geophysics* **11**: 166-190.
- Graham DW, Humphris SE, Jenkins WJ, Kurz MD** (1992) Helium Isotope Geochemistry of Some Volcanic Rocks from Saint Helena – *Earth Planet. Sci. Lett.* **110**: 121-131.
- Graham IJ and Hackett WR** (1987) Petrology of Calc-Alkaline Lavas from Ruapehu Volcano and Related Vents – *Journal of Petrology.* **28**: 531-567.
- Graham IJ, Cole JW, Briggs RM, Gamble JA, Smith IE** (1995) Petrology and petrogenesis of volcanic rocks from the Taupo Volcanic Zone: a review. *Journal of volcanology and geothermal research.* **68**(1-3): 59-87.
- Grant-Taylor TL** (1964a) Volcanic History of Western Taranaki – *New Zealand Journal of Geology and Geophysics* **7**: 78-86.
- Grant-Taylor TL** (1964b) Geology of Egmont National Park – In: Scanlan AB (ed) *Egmont National Park*. Egmont National Park Board, New Plymouth, p. 13-26.
- Grant-Taylor TL and Kear D** (1970) Geology. In: *Land Inventory Survey, Waimate West Country* – Department of Lands and Survey, Wellington, pp 20–33.
- Grant-Taylor TL and Rafter TA** (1963) New Zealand Natural Radiocarbon Measurements I-V. *Radiocarbon*, **5**: 118-162.
- Grove T, Parman S, Bowring S, Price R, Baker M** (2002) The role of an H₂O-rich fluid component in the generation of primitive basaltic andesites and andesites from the Mt. Shasta region, N California. *Contributions to Mineralogy and Petrology.* **142**(4): 375-96.
- Grove TL and Kinzler RJ** (1986) Petrogenesis of Andesites – *Annual Review of Earth and Planetary Sciences.* **14**: 417-454.
- Grove TL, Donnelly-Nolan JM, Housh T** (1997) Magmatic processes that generated the rhyolite of Glass Mountain, Medicine Lake volcano, N California. *Contributions to Mineralogy and Petrology.* **127**: 205-223.
- Grove TL, Elkins-Tanton LT, Parman SW, Chatterjee N, Muntener O, Gaetani GA** (2003) Fractional Crystallisation and Mantle-Melting Controls on Calc-Alkaline Differentiation Trends – *Contributions to Mineralogy and Petrology.* **145**: 515–533.
- Grove TL, Kinzler RJ, Baker MB, Donnelly-Nolan JM, Leshner CE** (1988) Assimilation of granite by basaltic magma at Burnt Lava Flow, Medicine Lake

- Volcano, Northern California—decoupling of heat and mass-transfer. *Contributions to Mineralogy and Petrology*. **99**: 320-343.
- Grove TL, Till CB, Crawczynski MJ** (2012) The role of H₂O in subduction zone magmatism - Annual Review of Earth and Planetary Sciences. **40**: 413-439.
- Gruender K, Stewart RB, Foley S** (2010) Xenoliths from The Sub-Volcanic Lithosphere of Mt Taranaki, New Zealand – *Journal of Volcanology and Geothermal Research*. **190**(1-2): 192-202.
- Gründer AL, Klemetti EW, Feeley TC, McKee CM** (2006) Eleven million years of arc volcanism at the Aucanquilcha Volcanic Cluster, northern Chilean Andes: implications for the life span and emplacement of plutons. *Earth and Environmental Science Transactions of the Royal Society of Edinburgh*. **97**(4): 415-36.
- Gudmundsson A** (2012) Magma chambers: Formation, local stresses, excess pressures, and compartments. *Journal of Volcanology and Geothermal Research*. **237**: 19-41.
- Hall ML, Robin C, Beate B, Mothes P, Monzier M** (1999) Tungurahua Volcano, Ecuador: structure, eruptive history and hazards. *Journal of Volcanology and Geothermal Research*. **91**(1): 1-21.
- Hammer JE, Rutherford MJ** (2002) An experimental study of the kinetics of decompression-induced crystallization in silicic melt. *Journal of Geophysical Research: Solid Earth*. **107**(B1): ECV-8.
- Hasegawa A and Nakajima J** (2004) Geophysical constraints on slab subduction and arc magmatism. In: Sparks, R. S. J. & Hawkesworth, C. J. (eds) *The State of the Planet: Frontiers and Challenges in Geophysics*. Washington, DC: American Geophysical Union, pp. 81-94.
- Hawkesworth CJ, Blake S, Evans P, Hughes R, Macdonald R, Thomas LE, Turner SP, Zellmer G** (2000). Time scales of crystal fractionation in magma chambers—integrating physical, isotopic and geochemical perspectives. *Journal of Petrology*. **41**: 991–1006.
- Hawkesworth CJ, Norry MJ, Roddick JC, Baker PE, Francis PW and Thorpe RS** (1979) ¹⁴³Nd/¹⁴⁴Nd, ⁸⁷Sr/⁸⁶Sr, incompatible element variations in calc-alkaline andesites and plateau lavas from South America. *Earth and Planetary Science Letters*. **42**: 45-57.
- Hawthorne FC, Oberti R, Harlow GE, Maresch WV, Martin RF, Schumacher JC, Welch MD** (2012) Nomenclature of the amphibole supergroup. *American Mineralogist*. **97**(11-12): 2031-48.
- Hay R** (1967) Sheet 7 Taranaki. Geological map of New Zealand 1:250,000. Department of Scientific and Industrial Research, Wellington, New Zealand.
- Heliker C** (1995) Inclusions in Mount St. Helens Dacite Erupted From 1980 Through 1983 – *Journal of Volcanology Geotherm. Res.* **66**: 115–135.
- Hellevang B and Pedersen RB** (2008) Magma ascent and crustal accretion at ultraslow-spreading ridges: constraints from plagioclase ultraphyric basalts from the Arctic Mid-Ocean Ridge – *Journal of Petrology*. **49**: 267-294.
- Higgins MD, Voos S, Vander Auwera J** (2015) Magmatic processes under Quizapu volcano, Chile, identified from geochemical and textural studies. *Contributions to Mineralogy and Petrology*. **170**(5-6): 51.
- Hildner E, Kluegel A and Hansteen TH** (2012), Barometry of lavas from the 1951 eruption of Fogo, Cape Verde Islands: Implications for historic and prehistoric magma plumbing systems, *J. Vol. Geotherm. Res.* **217–218**: 73–90, doi:10.1016/j.volgeo.2011.12.014.

- Hildreth W and Moorbath S** (1988) Crustal contribution to arc magmatism in the Andes of Central Chile. - *Contributions to Mineralogy and Petrology*. **98**: 455-489.
- Hildreth W** (2004). Volcanological perspectives on Long Valley, Mammoth Mountain, and mono craters: Several contiguous but discrete systems. *Journal of Volcanology and Geothermal Research*. **136**(3-4): 169–198. <https://doi.org/10.1016/j.jvolgeores.2004.05.019>
- Hill E, Blundy JD, Wood BJ** (2011) Clinopyroxene–melt trace element partitioning and the development of a predictive model for HFSE and Sc. *Contributions to Mineralogy and Petrology*. **161**(3): 423-38.
- Hill R and Roeder P** (1974) The crystallization of spinel from basaltic liquid as a function of oxygen fugacity. *The Journal of Geology*. **82**(6): 709-29.
- Hobden BJ, Houghton BF, Nairn IA** (2002) Growth of A Young, Frequently Active Composite Cone: Ngauruhoe Volcano, New Zealand – *Bull. Volcanol.* **64**:392–409 DOI 10.1007/s00445-002-0216-3
- Hochstein MP** (1995) Crustal Heat Transfer in The Taupo Volcanic Zone (New Zealand): Comparison with Other Volcanic Arcs and Explanatory Heat Source Models – *Journal of Volcanology and Geothermal Research* **68**: 117-151.
- Hodgson KA and Manville VR** (1999) Sedimentology and Flow Behaviour of a Rain-Triggered Lahar, Mangatoetoe Stream, Ruapehu Volcano, New Zealand – *Bulletin of the Geological Society of America*. **5**: 743-754.
- Holland T and Powell R** (1992) Plagioclase Feldspars: Activity-Composition Relations Based Upon Darken’s Quadratic Formalism and Landau Theory – *American Mineralogist*. **77**: 53–61.
- Hollister LS, Grissom GC, Peters EK, Stowell HH and Sisson VB** (1987) Confirmation of the empirical correlation of Al in hornblende with pressure of solidification of calc-alkaline plutons. - *American Mineralogist*. **72**: 231-239.
- Hora JM, Singer BS, Wörner G** (2007) Volcano Evolution and Eruptive Flux on The Thick Crust of The Andean Central Volcanic Zone: 40ar/39ar Constraints from Volcán Parinacota, Chile – *Geological Society of America Bulletin*. **119**: 343-362.
- Hora JM, Singer BS, Wörner G, Beard BL, Jicha BR, Johnson CM** (2009) Shallow and Deep Crustal Control on Differentiation of Calc-Alkaline and Tholeiitic Magma – *Earth and Planetary Science Letters*. **285**: 75-86.
- Huber C, Bachmann O, Manga M** (2010) Two competing effects of volatiles on heat transfer in crystal-rich magmas: thermal insulation vs defrosting. *Journal of Petrology*. **51**(4): 847-67.
- Humphreys MCS, Blundy JD, Sparks RSJ** (2006) Magma Evolution and Open-System Processes At Shiveluch Volcano: Insights From Phenocryst Zoning – *Journal of Petrology* 47:12-1 2303 2334 <https://doi.org/10.1093/petrology/egl045>
- Hurwitz DM, Long SM and Grosfils EB** (2009) The characteristics of magma reservoir failure beneath a volcanic edifice. *Journal of Volcanology and Geothermal Research*. **188**: 379-394.
- Infante-Paez L and Marfurt KJ** (2017) Seismic expression and geomorphology of igneous bodies: A Taranaki Basin, New Zealand, case study. *Interpretation*. **5**(3): SK121- SK140, doi:10.1190/INT-2016-0244.1.
- Isacks BL and Barazangi M** (1977) Geometry of Benioff Zones: Lateral Segmentation and Downwards Bending of The Subducted Lithosphere – In: Talwani M, Pittman III WC (eds.) *Island Arcs, Deep Sea Trenches and Back Arc Basins*. American Geophysical Union, Maurice Ewing Series 1, p. 94- 117.
- Iverson RM** (1997) The physics of debris flows. *Rev. Geophys.*, **35**: 245-296.

- Jackson JA, Mehl J and Neuendorf K** (2005) Glossary of Geology – American Geological Institute, Alexandria, Virginia. 800 pp.
- Jicha BR, Laabs BJC, Hora JM, Singer BS, Caffee MW** (2015) Early Holocene Collapse of Volcán Paríacota, Central Andes, Chile: Volcanological And Paleohydrological Consequences – Geological Society of America Bulletin. **127**: 1681-1688.
- Jochum KP, Nohl U, Herwig K, Lammel E, Stoll B and Hofmann AW** (2005) GeoReM: A new geochemical database for reference materials and isotopic standards. *Geostandards and Geoanalytical Research*. **29**: 333–338.
- Johnson AM** (1970) *Physical Processes in Geology*, W. H. Freeman, 557p
- Kamp PJ, Vonk AJ, Bland KJ, Hansen RJ, Hendy AJ, McIntyre AP, Ngatai M, Cartwright SJ, Hayton S, Nelson CS** (2004) Neogene stratigraphic architecture and tectonic evolution of Wanganui, King Country, and eastern Taranaki Basins, New Zealand. *New Zealand Journal of Geology and Geophysics*. **47**(4): 625-44.
- Karátson D, Sztanó O and Telbisz T** (2002) Preferred Clast Orientation in Volcaniclastic Mass-Flow Deposits: Application of a New Photo-Statistical Method – *Journal of Sedimentary Research*. **72**(6), 823-835.
- Karlstrom L, Dufek J, Manga M** (2010) Magma chamber stability in arc and continental crust. *Journal of Volcanology and Geothermal Research*. **190**: 249-270.
- Karlstrom L, Wright HM, Bacon CR** (2015) The effect of pressurized magma chamber growth on melt migration and pre-caldera vent locations through time at Mount Mazama, Crater Lake, Oregon. *Earth and Planetary Science Letters*. **412**: 209-219.
- Karstens J, Berndt C, Urlaub M, Watt SFL, Micallef A, Ray M, Klauke I, Klaeschen D, Kühn M, Roth T, Böttner C, Schramm B, Elger J, Brune S** (2019) From Gradual Spreading To Catastrophic Collapse – Reconstruction Of The 1888 Ritter Island Volcanic Sector Collapse From High-Resolution 3d Seismic Data – *Earth and Planetary Science Letters*, in press.
- Kay SM, Kay RW** (1985) Aleutian tholeiitic and calc-alkaline magma series I: the mafic phenocrysts. *Contributions to Mineralogy and Petrology*. **90**(2-3): 276-90.
- Keleman PB, Hanghoj K, Greene AR** (2005) One view of the geochemistry of subduction-related magmatic arcs, with an emphasis on primitive andesite and lower crust. In: Holland HD, Turekian KK eds. *Treatise on geochemistry*. Vol. 3: the crust. Oxford, Elsevier-Pergamon. Pp. 593–659.
- Keller CB, Schoene B, Barboni M, Samperton KM** (2015) Husson JM. Volcanic–plutonic parity and the differentiation of the continental crust. *Nature*. **523**(7560): 301-7.
- Kent AJ, Darr C, Koleszar AM, Salisbury MJ, Cooper KM** (2010) Preferential eruption of andesitic magmas through recharge filtering. *Nature geoscience*. **3**(9): 631-6.
- Kent BR, Giovanelli R, Haynes MP, Saintonge A, Stierwalt S, Balonek T, Brosch N, Catinella B, Koopmann RA, Momjian E, Spekkens K** (2007) Optically unseen HI detections toward the Virgo cluster detected in the Arecibo Legacy Fast ALFA survey. *The Astrophysical Journal Letters*. **665**(1): L15.
- Kervyn M, Ernst GGJ, van Wyk de Vries B, Mathieu L and Jacobs P** (2009) Volcano load control on dyke propagation and vent distribution: Insights from analogue modeling. - *Journal of Geophysical Research*. **114**: B03401.
- Kilgour G, Blundy J, Cashman K, Mader HM** (2013) Small volume andesite magmas and melt–mush interactions at Ruapehu, New Zealand: evidence from melt inclusions. *Contributions to Mineralogy and Petrology*. **166**(2): 371-92.

- Kilgour G, Manville V, Della Pasqua F, Graettinger A, Hodgson KA, Jolly GE** (2010) The 25 September 2007 eruption of Mount Ruapehu, New Zealand: directed ballistics, Surtseyan jets, and ice-slurry lahars – *J. Volcanol. Geotherm. Res.* **191**: 1-14.
- King PR** (1991) Physiographic Maps of The Taranaki Basin – Late Cretaceous to Recent. New Zealand Geological Survey report, G155
- King PR and Thrasher GP** (1996) Cretaceous–Cenozoic Geology and Petroleum Systems of The Taranaki Basin, New Zealand – I Institute of Geological and Nuclear Sciences Monograph 13, Institute of Geological and Nuclear Sciences Ltd, Lower Hutt, 243
- Kiser E, Palomeras I, Levander A, Zelt C, Harder S, Schmandt B, Hansen S, Creager K, Ulberg C** (2016) Magma reservoirs from the upper crust to the Moho inferred from high-resolution Vp and Vs models beneath Mount St. Helens, Washington State, USA. *Geology*. **44**(6): 411-4.
- Klemetti EW and Clynne MA** (2014) Localized rejuvenation of a crystal mush recorded in zircon temporal and compositional variation at the Lassen Volcanic Center, northern California. *PLoS One* **9**(12): e113157.
- Knox GJ** (1982) Taranaki Basin, Structural Style and Tectonic Setting - New Zealand Journal of Geology and Geophysics, **25**:2, 125-140, DOI: 10.1080/00288306.1982.10421405
- Landi P, Metrich N, Bertagnini A, Rosi M** (2004) Dynamics of magma mixing and degassing recorded in plagioclase at Stromboli (Aeolian Archipelago, Italy). *Contributions to Mineralogy and Petrology*. **147**(2): 213-27.
- Lange RA, Frey HM, Hector J** (2009). A thermodynamic model for the plagioclase-liquid hygrometer/thermometer – *American Mineralogist*. **94**: 494-506.
- Lavigne F and Thouret JC** (2002) Sediment Transportation and Deposition by Rain-Triggered Lahars at Merapi Volcano, Central Java, Indonesia – *Geomorphology*. **49**: 45-69.
- Le Bas MJ, Le Maitre RW, Streckeisen A, Zanettin B** (1986) A chemical classification of volcanic rocks based on the total alkali-silica diagram – *J. Petrol.* **27**: 445-450.
- Lee C-T A and Bachmann O** (2014) How important is the role of crystal fractionation in making intermediate magmas? Insights from Zr and P systematics. *Earth Planet. Sci. Lett.* **393**: 266–274. doi: 10.1016/j.epsl.2014.02.044
- Lejeune AM and Richet P** (1995) Rheology of crystal-bearing silicate melts: An experimental study at high viscosities. – *Journal of Geophysical Research*. **11**: 4215-4229.
- Lerner GA, Cronin SJ, Turner GM, Piispa EJ** (2019) Recognizing long runout pyroclastic flow deposits using paleomagnetism of ash. *Bull. Geol. Soc. Am.* <https://doi.org/10.1130/B35029.1>
- Lindsley DH** (1983) Pyroxene thermometry. *American Mineralogist*. **68**(5-6): 477-93.
- Lindsley DH, Frost BR, Ghiorso MS, Sack RO** (1991) Oxides lie: The Bishop Tuff did not erupt from a thermally zoned magma body. *EOS Transaction, American Geophysical Union*. **72**(17): 313.
- Lissenberg CJ, MacLeod CJ, Bennett EN** (2019) Consequences of a crystal mush-dominated magma plumbing system: a mid-ocean ridge perspective. *Phil. Trans. R. Soc. A* **377**, 20180014. doi:10.1098/rsta.2018.0014
- Locock AJ** (2014) An Excel spreadsheet to classify chemical analyses of amphiboles following the IMA 2012 recommendations. *Computers & Geosciences*. **62**: 1-1.

- Longpre´ M-A, Troll VR, Walter TR and Hansteen TH** (2009) Volcanic and geochemical evolution of the Teno massif, Tenerife, Canary Islands: some repercussions of giant landslides on ocean island magmatism. *Geochemistry, Geophysics, Geosystems*, **10**, Q12017.
- Lorenz V** (1974a) Studies of Surtsey Tephra Deposits – *Surtsey Res Prog Rep.* **7**: 72–79.
- Lorenz V** (1974b) Vesiculated Tuffs and Associated Features – *Sedimentology*. **21**: 273–291.
- Lowe DR** (1982) Sediment Gravity Flows: Ii. Depositional models With Special Reference to The Deposits of High-Density Turbidity Currents – *J. Sed. Petrol.* **52**:279-297.
- MacLennan J** (2019) Mafic tiers and transient mushes: evidence from Iceland. *Phil. Trans. R. Soc. A* **377**, 20180021. doi:10.1098/rsta.2018.0021
- Major JJ and Iverson RM** (1999) Debris-flow deposition: Effects of pore-fluid pressure and friction concentrated at flow margins. *Geol. Soc. Am. Bull.*, **111**: 1424-1434.
- Major JJ, Newhall CG** (1989) Snow and Ice Perturbation During Historical Volcanic Eruptions and The Formation of Lahars and Floods – *Bulletin of Volcanology*. **52**: 1-27.
- Major JJ, Pierson TC, Scott KM** (2005) Debris Flows at Mount St. Helens, Washington, Usa – In: Jakob M and Hungr O (Eds.) *Debris-flow hazards and related phenomena* – Springer Berlin Heidelberg 685-731.
- Manconi A, Longpré M-A, Walter TR, Troll VR, Hansteen TH** (2009) The effects of flank collapses on volcano plumbing systems – *Geology* **37**(12): 1099–1102. [http:// dx.doi.org/10.1130/G30104A.1](http://dx.doi.org/10.1130/G30104A.1).
- Manville V, Németh K, Kano K** (2009) Source to sink: a review of three decades of progress in the understanding of volcanoclastic processes, deposits, and hazards. *Sediment. Geol.* **220**(3–4): 136– 161.
- Manville V, White JDL, Hodgson KA** (2000) Dynamic Interactions Between Lahars and Stream Flow: A Case Study from Ruapehu Volcano, New Zealand: Discussion and Reply –*Bulletin of the Geological Society of America*. **112**: 1149-1151.
- Manville V and Cronin SJ** (2007) Break-out lahar from New Zealand's Crater Lake EOS Trans. AGU, **88**: 441-442.
- Marschall HR and Schumacher JC** (2012) Arc Magmas Sourced from Melange Diapirs Insubduction Zones – *Nature Geosciences*. **5**: 862–867.
- Martin AP, Cooper AF, Price RC** (2013) Petrogenesis of Cenozoic, alkalic volcanic lineages at Mount Morning, West Antarctica and their entrained lithospheric mantle xenoliths: lithospheric versus asthenospheric mantle sources. *Geochim. Cosmochim. Acta* **122**: 127–152.
- Masotta M, Mollo S, Freda C, Gaeta M, Moore G** (2013) Clinopyroxene–liquid thermometers and barometers specific to alkaline differentiated magmas – *Contributions to Mineralogy and Petrology*. **166**: 1545-1561.
- Masson DG, Watts AB, Gee MJR, Urgeles R, Mitchell NC, Le Bas TP, Canals M** (2002) Slope failures on the flanks of the western Canary Islands. *Earth Sci Rev.* **57**(1–2):1–35.
- McGlone MS, Neall VE, Pillans BJ** (1984) Inaha Terrace Deposits: A Late Quaternary Terrestrial Record in South Taranaki, New Zealand – *New Zealand Journal of Geology and Geophysics*. **27**: 35-49.
- McGuire WJ** (2003) Volcano instability and lateral collapse. – *Revista*. **1**:33–45.

- Mephie J, Doyle M and Allen R** (1993) Volcanic Textures A Guide to The Interpretation of Textures in Volcanic Rocks – Centre for Ore Deposit and Exploration Studies, University of Tasmania, Hobart, Tasmania. 198 pp
- Melekhova E, Blundy J, Robertson R, Humphreys MC** (2015) Experimental evidence for polybaric differentiation of primitive arc basalt beneath St. Vincent, Lesser Antilles. *Journal of Petrology*. **56**(1):161-92.
- Métrich N and Deloule E** (2014). Water content, δD and $\delta^{11}B$ tracking in the Vanuatu arc magmas (Aoba Island): Insights from olivine-hosted melt inclusions. *Lithos*. **206**: 400-408.
- Meyer PS and Shibata T** (1990) Complex zoning in plagioclase feldspars from ODP site 648. In: Detrick R, Honnorez J, Bryan WB, Juteau T et al (eds) Proceedings of ocean drilling program scientific results. **106/109**: 123–142.
- Middleton GV and Hampton MA** (1973) Sediment Gravity Flows: Mechanics of Flow and Deposition. Society of Economic Paleontologists and Mineralogists, Pacific Section, Los Angeles, CA, pp. 1-37.
- Miller JS, Matzel JP, Miller CF, Burgess SD, Miller RB** (2007) Zircon growth and recycling during the assembly of large, composite arc plutons: *Journal of Volcanology and Geothermal Research*. **167**: 282–299. doi: 10.1016/j.jvolgeores.2007.04.019.
- Minami Y, Ohba T, Hayashi S, Saito-Kokubu Y, Kataoka KS** (2019) Lahar record during the last 2500 years, Chokai Volcano, northeast Japan: Flow behavior, sourced volcanic activity, and hazard implications. *Journal of Volcanology and Geothermal Research*, 287.
- Mollo S, Blundy J, Scarlato P, De Cristofaro SP, Tecchiato V, Di Stefano F, Vetere F, Holtz F., Bachmann O** (2018) An Integrated P-T-H₂O-Lattice Strain Model To Quantify The Role Of Clinopyroxene Fractionation On Ree+Y And Hfse Patterns Of Mafic Alkaline Magmas: Application To Eruptions At Mt. Etna – *Earth Sci. Rev.* **185**: 32–56. <https://doi.org/10.1016/j.earscirev.2018.05.014>
- Mollo S, Giacomoni PP, Andronico D, Scarlato P** (2015a) Clinopyroxene and Titanomagnetite Cation Redistributions at Mt. Etna Volcano (Sicily, Italy): Footprints of the Final Solidification History of Lava Fountains and Lava Flows – *Chemical Geology*. **406**: 4554.
- Mollo S, Hammer JE** (2017) Dynamic crystallization in magmas. *EMU Notes in Mineralogy*. **16**: 373-418.
- Mollo S, Putirka K, Misiti V, Soligo M, Scarlato P** (2013) A new test for equilibrium based on clinopyroxene–melt pairs: Clues on the solidification temperatures of Etnean alkaline melts at post-eruptive conditions. *Chemical Geology*. **352**: 92-100.
- Mollo S, Giacomoni PP, Coltorti M, Ferlito C, Iezzi G, Scarlato P** (2015b) Reconstruction of magmatic variables governing recent Etnean eruptions: constraints from mineral chemistry and P-T-fO₂-H₂O modelling – *Lithos*. **212–215**: 311-320, 10.1016/j.lithos.2014.11.020
- Moore JG, Clague DA, Holcomb RT, Lipman PW, Normark WR, Torresan ME** (1989) Prodigious submarine landslides on the Hawaiian Ridge. *Journal of Geophysical Research: Solid Earth*. **94**(B12): 17465-84.
- Moore JG, Normark WR, Holcomb RT** (1994) Giant hawaiian landslides. *Annual Review of Earth and Planetary Sciences*. **22**: 119-44.
- Morris PA** (1995) Slab Melting as An Explanation of Quaternary Volcanism and Aseismicity In Southwest Japan – *Geology*. **23**: 395-8.
- Morse SA** (1984) Cation diffusion in plagioclase feldspar. – *Science*. **225**: 504-505.

- Mortimer N, Tulloch AJ, Ireland TR** (1997) Basement Geology of Taranaki And Wanganui Basins, New Zealand – *New Zealand Journal of Geology and Geophysics*. **40**: 223-236.
- Mortimer N, Tulloch AJ, Spark RN, Walker NW, Ladley E, Allibone A, Kimbrough DL** (1999) Overview of The Median Batholith, New Zealand: A New Interpretation of The Geology of The Median Tectonic Zone and Adjacent Rocks – *Journal of African Earth Sciences* **29**: 257-268.
- Muir RJ, Bradshaw JD, Weaver SD, Laird MG** (2000) The Influence of Basement Structure on The Evolution of The Taranaki Basin, New Zealand – *Journal of the Geological Society* **157** (6), 1179–1185.
- Mueller SB, Varley NR, Kueppers U, Lesage P, Reyes Davila GÁ, Dingwell DB** (2013) Quantification of magma ascent rate through rockfall monitoring at the growing/collapsing lava dome of Volcán de Colima, Mexico, *Solid Earth*. **4**: 201–213.
- Müller JR, Ito G, Martel SJ** (2001) Effects of volcano loading on dike propagation in an elastic half-space. *Journal of Geophysical Research*, **106**: 11101-11113.
- Müntener O, Kelemen PB, Grove TL** (2001) The role of H₂O during crystallisation of primitive arc magmas under uppermost mantle conditions and genesis of igneous pyroxenites: an experimental study. *Contributions to Mineralogy and Petrology* **141**: 643–658.
- Müsselwhite DS, De Paolo DJ, McCurry M** (1989) The evolution of a silicic magma system— isotopic and chemical evidence from the Woods Mountains Volcanic Center, Eastern California. *Contributions to Mineralogy and Petrology*. **101**: 19–29.
- Nairn IA, Wood CP, Hewson CAY** (1979) Phreatic eruptions of Ruapehu, April 1975 – *NZ J Geol Geophys*. **22**:155-173.
- Nakagawa M, Wada K, Thordarson T, Wood CP, Gamble JA** (1999) Petrologic investigations of the 1995 and 1996 eruptions of Ruapehu volcano, New Zealand: formation of discrete and small magma pockets and their intermittent discharge. *Bulletin of Volcanology*. **61**(1-2): 15-31.
- Nakagawa M, Wada K, Wood CP** (2002) Mixed magmas, mush chambers and eruption triggers: evidence from zoned clinopyroxene phenocrysts in andesitic scoria from the 1995 eruptions of Ruapehu volcano, New Zealand. *Journal of petrology*. **43**(12): 2279-303.
- Namur O, Montalbano S, Bolle O, Auwera JV** (2020) Petrology of the April 2015 eruption of Calbuco volcano, southern Chile – *Journal of Petrology*, ega084 <https://doi.org/10.1093/petrology/egaa084>
- Neall VE** (1976a) Lahars as Major Geological Hazards – *Bulletin of the International Association of Engineering Geology*. **14**: 233-240.
- Neall VE** (1976b) Lahars - Global Occurrence and Annotated Bibliography – Victoria University Wellington, New Zealand, Publication 5, 18.
- Neall VE** (1979) Sheets P19, P20 And P21 New Plymouth, Egmont And Manaia – *Geological Map of New Zealand 1:50,000*. 3 maps and notes, 36 p. New Zealand Department of Science and Industrial Research, Wellington
- Neall VE** (2003) The Volcanic History of Taranaki. Institute of Natural Resources - Massey University, Soil & Earth Sciences Occasional Publication No. 2
- Neall VE and Alloway BE** (2004) Quaternary Geological Map of Taranaki. Institute of Natural Resources – Massey University, soil & earth sciences occasional publication no. 4

- Neall VE, Stewart RB, Smith IEM** (1986) History and Petrology of The Taranaki Volcanoes – Royal Society of New Zealand Bulletin **23**: 251-263.
- Neave DA and Putirka KD** (2017) A New Clinopyroxene-Liquid Barometer, And Implications for Magma Storage Pressures Under Icelandic Rift Zones – Am. Mineral. **102**: 777-794.
- Neave DA, Maclennan J, Hartley ME, Edmonds M, Thordarson T** (2014) Crystal storage and transfer in basaltic systems: the Skuggafjöll eruption, Iceland – J. Petrol. **55**: 2311-2346.
- Németh K and Martin U** (2007) Practical Volcanology. Occasional Papers of the Geological Institute of Hungary, Budapest. **207**.
- Németh K, Riso C, Nullo F, Kereszturi G** (2011) The role of collapsing and cone rafting on eruption style changes and final cone morphology: Los Morados scoria cone, Mendoza, Argentina. – Central European J Geosci. **3**(2):102-118
- Németh, K. and Martin, U.** (2007) Practical Volcanology. Occasional Papers of the Geological Institute of Hungary, Budapest. **207**.
- Newhall CG** (1979) Temporal variation in the lavas of Mayon Volcano, Philippines. – J Geophys. Res. **6**: 61-83.
- Nichols IA and Ringwood AE** (1973) Effect of Water on Olivine Stability in Tholeiites and the Production of Silica-Saturated Magmas in the Island-Arc Environment – J. Geol. **81**: 285–300.
- Nichols ML, Malone SD, Moran SC, Thelen WA, Vidale JE** (2011) Deep long-period earthquakes beneath Washington and Oregon volcanoes. Journal of Volcanology and Geothermal Research. **200**(3-4): 116-28.
- Nicol A and Wallace LM** (2007) Temporal Stability of Deformation Rates: Comparison of Geological and Geodetic Observations, Hikurangi Subduction Margin, New Zealand – Earth and Planetary Science Letters **258**:3-4 397-413.
- Nicol A, Stagpoole V and Maslen G** (2004) Structure and Petroleum Potential of The Taranaki Fault Play – New Zealand Petroleum Conference Proceedings, 7–10.
- Oehler JF, Lénat JF, Labazuy P** (2008) Growth and collapse of the Reunion Island volcanoes. Bulletin of Volcanology. **70**(6):717-42.
- Oyan V, Keskin M, Lebedev VA, Chugaev AV, Sharkov EV** (2016) Magmatic Evolution of The Early Pliocene Etrusk Stratovolcano, Eastern Anatolia Collision Zone, Turkey – Lithos. **256–257**: 88–108.
- Pack B, Schmitt AK, Roberge J, Tenorio FG, Damiata BN** (2016) Zircon xenocryst resorption and magmatic regrowth at El Chichón volcano, Chiapas, Mexico – J. Volcanol. Geotherm. Res. **311**: 170-182.
- Palmer BA and Neall VE** (1989) The Murimotu Formation, 9500-year old deposits of a debris avalanche and associated lahars, Mount Ruapehu, North Island, New Zealand. New Zealand Journal of Geology and Geophysics, **32**: 477-486.
- Palmer BA and Neall VE** (1991) Contrasting lithofacies architecture in ring plain deposits related to edifice construction and destruction, the quaternary Stratford and Opunake formations, Egmont Volcano, New Zealand. – Sedimentary Geology. **74**: 71-88.
- Palmer BA and Walton AW** (1990) Accumulation of volcanoclastic aprons in the Mount Dutton Formation (Oligocene–Miocene), Marysvale volcanic field, Utah. Geological Society of America Bulletin, **102**: 734–748.
- Palmer BA, Alloway BV, Neall VE** (1991) Volcanic-Debris-Avalanche Deposits in New Zealand - Lithofacies Organisation in Unconfined, Wet-Avalanche Flows – In: Fisher RV, Smith GA (Eds.) Sedimentation in Volcanic Settings, SEPM Special Publication **45**: 89-98.

- Pan Y and Batiza R** (2002) Mid-ocean ridge magma chamber processes: Constraints from olivine zonation in lavas from the East Pacific Rise at 9°30'N and 10°30'N – *J. Geophys. Res.* **107**:10. 1029/2001JB000435
- Parat F, Streck MJ, Holtz F, Almeev R** (2014) Experimental study into the petrogenesis of crystal-rich basaltic to andesitic magmas at Arenal volcano. *Contributions to Mineralogy and Petrology.* **168**(2): 10-40.
- Pareschi MT, Favalli M, Giannini F, Sulpizio R, Zanchetta G, Santacroce R** (2000) May 5, 1998, Debris Flows in Circum-Vesuvian Areas (Southern Italy): Insights for Hazard Assessment – *Geology.* **28**: 639-642.
- Parson LM and Wright IC** (1996) The Lau-Havre-Taupo Back-Arc Basin: A Southward-Propagating, Multistage Evolution from Rifting to Spreading – *Tectonophysics* **263**: 1-22.
- Paton C, Hellstrom J, Paul B, Woodhead J and Hergt J** (2011) Iolite: Freeware for The Visualisation and Processing of Mass Spectrometric Data – *J. Anal. Atomic Spectrom.* **26**: 2508–2518. doi: 10.1039/c1ja10172b
- Paul B, Paton C, Norris A, Woodhead J, Hellstrom J, Hergt J, Greig A** (2012) CellSpace: a module for creating spatially registered laser ablation images within the Iolite freeware environment. *Journal of Analytical Atomic Spectrometry.* **27**(4): 700-6.
- Peacock SM, Rushmer T, Thompson AB** (1994) Partial Melting of Subducting Oceanic Crust – *Earth Planet Sci Lett.* **121**: 227-44.
- Pearce JA and Stern RJ** (2006) The origin of back-arc basin magmas: trace element and isotope perspectives D.M. Christie, C.R. Fisher, S. M. Lee, S. Givens (Eds.), *Back-arc Spreading Systems: Geological, Biological, Chemical and Physical Interactions*, American Geophysical Union Geophysical Monograph, **166**: 63-86.
- Pearce JA and Parkinson IJ** (1993) Trace element models for mantle melting: application to volcanic arc petrogenesis. *Geological Society, London, Special Publications.* **76**(1): 373-403.
- Pearce TH and Kolisnik AM** (1990) Observations of plagioclase zoning using interference imaging. *Earth-Science Reviews.* **29**(1-4): 9-26.
- Perinelli C, Mollo S, Gaeta M, DeCristofaro SP, Palladino DM, Armienti P, Scarlato P, Putirka KD** (2016) An improved clinopyroxene-based hygrometer for Etnean magmas and implications for eruption triggering mechanisms – *Am. Mineral.* **101**: 2774-2777, 10.2138/am-2016-5916
- Petrelli M, El Omari K, Spina L, Le Guer Y, La Spina G, Perugini D** (2018) Timescales of water accumulation in magmas and implications for short warning times of explosive eruptions. – *Nat. Commun.* 10.1038/s41467-018-02987-6
- Petrone CM, Braschi E, Francalanci L** (2009) Understanding the Collapse-Eruption Link at Stromboli, Italy: A Microanalytical Study on The Products of The Recent Secche Di Lazzaro Phreatomagmatic Activity – *Journal of Volcanology and Geothermal Research.* **188**: 315-332.
- Petrone CM, Braschi E, Francalanci L, Casalini M, Tommasini S** (2018) Rapid Mixing and Short Storage Timescale in The Magma Dynamics of a Steady-State Volcano – *Earth Planet. Sci. Lett.* **492**: 206–221.
- Petrus JA, Chew DM, Leybourne MI, and Kamber BS** (2017) A new approach to laser ablation inductively-coupled-plasma mass spectrometry (LAICP-MS) using the flexible map interrogation tool ‘Monocle’. *Chem. Geol.* **463**, 76–93. doi: 10.1016/j.chemgeo.2017.04.027

- Pierson TC** (1986) Flow behavior in channelized debris flows, Mount St. Helens, Washington. In: Abrahams AD (Ed.) Hillslope processes, Boston, Allen and Unwin, p. 269-296.
- Pierson TC** (2005) Hyperconcentrated Flow - Transitional Process Between Water Flow and Debris Flow – In: Jakob M, Hungr O (Eds.) Debris-flow Hazards and Related Phenomena, Springer, Heidelberg, p. 159-202.
- Pierson TC and Costa JE** (1987) A Rheologic Classification of Subaerial Sediment-Water Flows – Geological Society of America Reviews in Engineering Geology. **7**: 1-12.
- Pierson TC and Janda RJ** (1994) Volcanic Mixed Avalanches: A Distinct Eruption-Triggered Mass-Flow Process at Snow-Clad Volcanoes – Bulletin of the Geological Society of America. **106**: 1351-1358.
- Pierson TC and Scott KM** (1985) Downstream Dilution of a Lahar: Transition from Debris Flow to Hyperconcentrated Streamflow – Water Resource Research. **12**: 1511-1524.
- Pierson TC, Janda RJ, Thouret J-C, Borrero CA** (1990) Perturbation and Melting of Snow and Ice by the 13 November 1985 Eruption of Nevado Del Ruiz, Colombia And Consequent Mobilization, Flow and Deposition of Lahars – Journal of Volcanology and Geothermal Research. **41**: 17-66.
- Pierson TC, Wood NJ, Driedger CL** (2014) Reducing risk from lahar hazards: concepts, case studies, and roles for scientist. Journal of Applied Volcanology, **3**: 16.
- Pietranik A, Koepke J, Puziewicz J** (2006) Crystallization and resorption in plutonic plagioclase: implications on the evolution of granodiorite magma (Ge₂siniec granodiorite, Strzelin Crystalline Massif, SW Poland) – Lithos. **86**: 260-280.
- Pillans BJ** (1983) Upper Quaternary Marine Terrace Chronology and Deformation South Taranaki, New Zealand – Geology. **11**: 292-297.
- Pinel V and Albino F** (2013) Consequences of volcano sector collapse on magmatic storage zones: Insights from numerical modeling. Journal of Volcanology and Geothermal Research. **252**: 29-37.
- Pinel V and Jaupart C** (2000) The effect of edifice load on magma ascent beneath a volcano. Philosophical Transactions of the Royal Society of London A. **358**: 1515-1532.
- Pinel V and Jaupart C** (2003) Magma chamber behavior beneath a volcanic edifice. Journal of Geophysical Research. **108**: 2072.
- Pinel V and Jaupart C** (2005) Some consequences of volcanic edifice destruction for eruption conditions. Journal of Volcanology and Geothermal Research. **145**: 68-80.
- Pinel V, Jaupart C, Albino F** (2010) On the relationship between cycles of eruptive activity and growth of a volcanic edifice. Journal of Volcanology and Geothermal Research. **194**: 150-164.
- Pistone M, Caricchi L, Ulmer P, Reusser E, Ardia P** (2013) Rheology of volatile-bearing crystal mushes: mobilization vs. viscous death. Chemical Geology. **345**: 16-39.
- Pistone M, Cordonnier B, Ulmer P, Caricchi L** (2016) Rheological flow laws for multiphase magmas: an empirical approach. Journal of Volcanology and Geothermal Research. **321**: 158-70.
- Platz T, Cronin SJ, Cashman KV, Stewart RB, Smith IE** (2007a) Transition from effusive to explosive phases in andesite eruptions—A case-study from the AD1655 eruption of Mt. Taranaki, New Zealand. Journal of volcanology and geothermal research. **161**(1-2): 15-34.

- Platz T, Cronin SJ, Procter JE, Neall VE, Foley S** (2012) Non-Explosive, Dome-Forming Eruptions at Mt. Taranaki, New Zealand – *Geomorphology* **136**:1 15-30
- Powell R** (1984) Inversion of the assimilation and fractional crystallization (AFC) equations; characterization of contaminants from isotope and trace element relationships in volcanic suites - *Journal of the Geological Society*. **141**: 447-452.
- Price RC, Cronin SJ, Smith IEM, Ukstins IA, Zernack AV** (2020) Formation of crystal-rich, mixed, intermediate lavas at Pouakai Volcano and the evolution of the Taranaki volcanic lineament, western North Island, New Zealand – *Lithos*, in press.
- Price RC, Gamble JA, Smith IEM, Maas R, Waight T, Stewart RB, Woodhead J** (2012) The Anatomy of An Andesite Volcano: A Time-Stratigraphic Study of Andesite petrogenesis And Crustal Evolution at Ruapehu Volcano, New Zealand – *J. Petrol.* **53**(10): 2139–2189.
- Price RC, Gamble JA, Smith IEM, Stewart RB, Eggins S, Wright IC** (2005) An integrated model for the temporal evolution of andesites and rhyolites and crustal development in New Zealand’s North Island. - *Journal of Volcanology and Geothermal Research*. **140**: 1-24.
- Price RC, Mcculloch MT, Smith IEM, Stewart RB** (1992) Pb-Nd-Sr Isotopic Compositions and Trace Element Characteristics of Young Volcanic Rocks from Egmont Volcano and Comparisons with Basalts and Andesites from the Taupo Volcanic Zone, New Zealand – *Geochimica et Cosmochimica Acta*. **56**:3 941-953 [https://doi.org/10.1016/0016-7037\(92\)90038-K](https://doi.org/10.1016/0016-7037(92)90038-K)
- Price RC, Smith IEM, Stewart RB, Gamble JA, Gruender K, Maas R** (2016) High-K andesite petrogenesis and crustal evolution: Evidence from mafic and ultramafic xenoliths, Egmont Volcano (Mt. Taranaki) and comparisons with Ruapehu Volcano, North Island, New Zealand. *Geochimica et Cosmochimica Acta*, 185, 328–357. <https://doi.org/10.1016/j.gca.2015.12.009>
- Price RC, Spandler C, Arculus R, Reay A** (2011) The Longwood Igneous Complex, Southland, New Zealand. A Permo-Jurassic, intra-oceanic, subduction-related, I-type batholithic complex. – *Lithos*. **126**: 121.
- Price RC, Stewart RB, Woodhead JD, Smith IEM** (1999) Petrogenesis of High-K Arc Magmas: Evidence from Egmont Volcano, North Island, New Zealand. *Journal of Petrology*. **40**: 167-197.
- Price RC, Zernack AV, Smith IE, Gamble J, Stewart RB** (2007) Mantle source compositions for the basaltic component in North Island andesitic volcanoes - A lithospheric source for Taranaki andesites. *Geological Society of New Zealand Miscellaneous Publications A*. 2007;123:134.
- Procter JN, Cronin SJ, Zernack AV** (2009) Landscape and sedimentary response to catastrophic debris avalanches, western Taranaki, New Zealand. – *Sedimentary Geology*. **220**: 271-287.
- Putirka K** (1999) Clinopyroxene+liquid equilibria to 100 kbar and 2450 K. *Contributions to Mineralogy and Petrology*. **135**(2-3): 151-63.
- Putirka K** (2008) Thermometers and Barometers for Volcanic Systems – In: Putirka K, Tepley F (eds) *Minerals, inclusions and volcanic processes*, *Rev Mineral Geochem*. **69**: 61–120.
- Putirka K, Johnson M, Kinzler R, Walker D** (1996) Thermobarometry Of Mafic Igneous Rocks Based on Clinopyroxene-Liquid Equilibria, 0-30 kbar – *Contrib. Mineral. Petrol.* **123**: 92-108.

- Putirka K, Ryerson Fj, Mikaelian H** (2003) New Igneous Thermobarometers For Mafic and Evolved Lava Compositions, Based on Clinopyroxene + Liquid Equilibria – *Am. Mineral.* **88**: 1542-1554.
- Putirka KD** (2016) Amphibole Thermometers and Barometers for Igneous Systems and Some Implications for Eruption Mechanisms of Felsic Magmas at Arc Volcanoes – *Am. Mineral.* **101**(4): 841–858.
- Rapp RP and Watson EB** (1995) Dehydration Melting of Metabasalt at 8–32 Kbar—Implications for Continental Growth and Crust–Mantle Recycling – *Journal of Petrology.* **36**: 891–931.
- Rawson H, Keller T, Fontijn K, Pyle DM, Mather TA, Smith VC, Naranjo JA** (2016) Compositional variability in mafic arc magmas over short spatial and temporal scales: Evidence for the signature of mantle reactive melt channels. *Earth and Planetary Science Letters*, 456, 66–77. <https://doi.org/10.1016/j.epsl.2016.09.056>.
- Reid ME, Sisson TW, Brien DL** (2001) Volcano collapse promoted by hydrothermal alteration and edifice shape, Mount Rainier, Washington – *Geology.* **29**: 779-782.
- Reilly C, Nicol A, Walsh JJ, Seebeck H** (2015) Evolution of Faulting and Plate Boundary Deformation in The Southern Taranaki Basin, New Zealand – *Tectonophysics* **651-652** 1-18.
- Reubi O and Blundy J** (2009) A Dearth of Intermediate Melts at Subduction Zone Volcanoes and The Petrogenesis of Arc Andesites – *Nature.* **461**: 1269–1273 <https://doi.org/10.1038/nature08510>
- Reubi O and Nicholls IA** (2004) Magmatic evolution at Batur volcanic field, Bali, Indonesia: petrological evidence for polybaric fractional crystallization and implications for caldera-forming eruptions. *J. Volcanol. Geotherm. Res.* **138**: 345–369.
- Reyners M, Eberhart-Phillips D, Bannister S** (2011) Tracking repeated subduction of the Hikurangi Plateau beneath New Zealand. *Earth and Planetary Science Letters.* **311**: 165-171. doi: 10.1016/j.epsl.2011.09.011.
- Reyners M, Eberhart-Phillips D, Stuart G, Nishimura Y** (2006) Imaging subduction from the trench to 300 km depth beneath the central North Island, New Zealand, with Vp and Vp/Vs, *Geophys. J. Int.* **165**: 565 – 583.
- Ridley WI, Perfit MR, Smith MC, Fornari DJ** (2006) Magmatic processes in developing oceanic crust revealed in a cumulate xenolith collected at the East Pacific Rise, 9°50'N – *Geophys. Geochem. Geosyst.*, 7. [10.1029/2006GC001316](https://doi.org/10.1029/2006GC001316)
- Ridolfi F, Renzulli A, Puerini M** (2010) Stability and Chemical Equilibrium of Amphibole in Calc-Alkaline Magmas: An Overview, New Thermobarometric Formulations and Application to Subduction-Related Volcanoes – *Contrib. Mineral Petrol.* **160**: 45–66.
- Ringwood AE** (1974) Petrological evolution of island arc systems. – *Journal of the Geological Society, London.* **130**: 183-204.
- Rodin JD and Johnson AM** (1976) The Ability of Debris, Heavily Freighted with Coarse Clastic Material, To Flow on Gentle Slopes – *Sedimentology.* **23**: 213-234.
- Rodolfo KS** (1989) Origin and Early Evolution of Lahar Channel at Mabinit, Mayon Volcano, Philippines – *Bulletin of the Geological Society of America.* **101**: 414-426.
- Rogers G and Hawkesworth CJ** (1989) A Geochemical Traverse Across the North Chilean Andes—Evidence for Crust Generation from The Mantle Wedge – *Earth and Planetary Science Letters.* **91**: 271–285.

- Romagnoli C, Kokelaar P, Casalbore D, Chiocci FL** (2009) Lateral collapses and active sedimentary processes on the northwestern flank of Stromboli volcano, Italy. *Marine Geology*. **265**(3-4): 101-19.
- Roman A and Jaupart C** (2014) The impact of volcanic edifice on intrusive and eruptive activity - *Earth Planet. Sci. Lett.* **408**: 1-8.
- Roser B, Kimura JI, Sifeta K** (2003) Tantalum and niobium contamination from tungsten carbide ring mills: much ado about nothing. *Geosci Rep Shimane Univ.* **22**: 107–110.
- Rouchon V, Gillot PY, Quidelleur X, Chiesa S, Floris B** (2008) Temporal evolution of the Roccamonfina volcanic complex (Pleistocene), central Italy – *J. Volcanol. Geotherm. Res.* **177**: 500-514.
- Rowan CJ, and Roberts, AP** (2005) Tectonic and Geochronological Implications of Variably Timed Remagnetizations Carried by Authigenic Greigite In Fine-Grained Sediments from New Zealand – *Geology* **33**: 553–556, doi:10.1130/G21382.1.
- Rowland JV, Wilson CJ, Gravley DM** (2010) Spatial and temporal variations in magma-assisted rifting, Taupo Volcanic Zone, New Zealand. *Journal of Volcanology and Geothermal Research.* **190**(1-2): 89-108.
- Rudnick RL** (1995) Making continental crust. *Nature.* **378**(6557): 571-8.
- Rudnick RL and Gao S** (2005) Composition of the continental crust. In: Holland HD, Turekian KK eds. *Treatise on geochemistry. Vol 3: the crust.* Oxford, Elsevier-Pergamon. Pp. 1–64.
- Ruprecht P and Wörner G** (2007) Variable Regimes in Magma Systems Documented in Plagioclase Zoning Patterns: El Misti Stratovolcano and Andahua Monogenetic Cones – *J. Volcanol. Geotherm. Res.* **165**: 142–162.
- Ruprecht P, Bergantz GW, Cooper KM, Hildreth W** (2012) The crustal magma storage system of Volcán Quizapu, Chile, and the effects of magma mixing on magma diversity. *Journal of Petrology.* **53**(4): 801–840. <https://doi.org/10.1093/petrology/egs002>
- Rutherford MJ and Devine JD** (2003) Magmatic Conditions and Magma Ascent as Indicated by Hornblende Phase Equilibria and Reactions in the 1995–2002 Soufriere`Re Hills Magma – *Journal of Petrology.* **44**: 1433–1454.
- Rutherford MJ and Devine JD** (2008) Magmatic Conditions and Processes in the Storage Zone of the 2004-2006 Mount St. Helens Dacite. In: Sherrod, D.R., Scott, W.E., Stauffer, P.H. (Eds.), *A volcano rekindled: the renewed eruption of Mount St. Helens, 2004-2006.* US Geological Survey Professional Paper 1750, pp. 703-725.
- Rutherford MJ and Hill PM** (1993) Magma ascent rates from amphibole breakdown: an experimental study applied to the 1980–1986 Mount St. Helens eruptions. *Journal of Geophysical Research: Solid Earth.* **98**(B11): 19667-85.
- Sakuyama M** (1981) Petrological study of the Myoko and Kurohime volcanoes, Japan: crystallization sequence and evidence for magma mixing. *Journal of Petrology.* **22**(4): 553-83.
- Samaniego P, Barba D, Robin C, Fornari M, Bernard B** (2012) Eruptive History of Chimborazo Volcano (Ecuador): A Large, Ice-Capped and Hazardous Compound Volcano in The Northern Andes – *Journal of Volcanology and Geothermal Research.* **221**: 33-51.
- Saunders KE, Baker JA, Wysoczanski RJ** (2010) Microanalysis of large volume silicic magma in continental and oceanic arcs: Melt inclusions in Taupo Volcanic Zone

- and Kermadec Arc rocks, South West Pacific. *Journal of Volcanology and Geothermal Research*. **190**(1-2): 203-18.
- Schmid R** (1981) Descriptive Nomenclature and Classification of Pyroclastic Rocks and Fragments: Recommendations of the IUGS Subcommittee on the Systematics of Igneous Rocks – *Geology*. **9**: 41–43, doi: 10.1130/ 0091-7613 (1981) 941: DNACOP2.0.CO;2
- Schmidt MW** (1992) Amphibole composition in tonalite as a function of pressure: an experimental calibration of the Al-in-hornblende barometer. *Contributions to mineralogy and petrology*. **110**(2-3): 304-10.
- Schmidt MW and Poli S** (1998) Experimentally Based Water Budgets for Dehydrating Slabs and Consequences for Arc Magma Generation – *Earth and Planetary Science Letters*. **163**: 361-379.
- Schmincke HU** (1967) Graded lahars in the type sections of the Ellensburg Formation, South Central Washington. *J. Sedim. Petrol.*, **37**: 438-448.
- Schultz AW** (1984) Subaerial debris-flow deposition in the Upper Palaeozoic Cutler Formation, Western Colorado. *J sediment. Petrol.*, **54**: 759-772.
- Scott KM** (1988a) Origins, Behavior, and Sedimentology of Lahars and Lahar-Runout Flows in the Toutle-Cowlitz River System. US Geological Survey, Professional Paper, 1447-A.
- Scott KM** (1988b) Origin, behaviour, and sedimentology of prehistoric catastrophic lahars at Mount St. Helens, Washington. *Geological Society of America Special Paper*, **229**: 23-36.
- Scott KM, Vallance JW, Kerle N, Macías JL, Strauch W, Devoli G** (2005) Catastrophic Precipitation-triggered Lahar at Casita Volcano, Nicaragua: Occurrence, Bulking and Transformation – *Earth Surface Processes and Landforms*. **30**: 59-79.
- Scott KM, Vallance JW, Pringle PT** (1995) Sedimentology, Behaviour, And Hazards of Debris Flows at Mount Rainier, Washington – US Geological Survey Professional Paper 1547, 56.
- Scrivenor JB** (1929) The Mudstreams (“Lahars”) Of Gunong Keloet In Java - *Geological Magazine*
- Shane P and Coote A** (2018) Thermobarometry of Whangarei volcanic field lavas, New Zealand: Constraints on plumbing systems of small monogenetic basalt volcanoes. *Journal of Volcanology and Geothermal Research*. **354**: 130-9.
- Shea T and Hammer JE** (2013) Kinetics of decompression and cooling-induced crystallization of mafic-intermediate hydrous magmas – *J. Volcanol. Geotherm. Res.* **260**: 127-145.
- Shea T, de Vries BV, Pilato M** (2008) Emplacement mechanisms of contrasting debris avalanches at Volcán Mombacho (Nicaragua), provided by structural and facies analysis. *Bulletin of Volcanology*. **70**(8): 899.
- Sherburn S and White RS** (2005) Crustal seismicity in Taranaki, New Zealand using accurate hypocentres from a dense network. *Geophysical Journal International*. **162**: 494-506.
- Sherburn S and White RS** (2006) Tectonics of the Taranaki region, New Zealand: earthquake focal mechanisms and stress axes. *New Zealand Journal of Geology and Geophysics*. **49**: 269-279.
- Sides IR, Edmonds M, MacLennan J, Swanson DA, Houghton BF** (2014) Eruption style at Kīlauea Volcano in Hawai ‘i linked to primary melt composition. *Nature Geoscience*. **7**(6): 464-9.

- Siebert L** (1984) Large volcanic debris avalanches: Characteristics of source area, deposits, and associated eruptions. – *Journal of Volcanology and Geothermal Research*. **22**: 163-197.
- Siebert L, Glicken H, Ui T** (1987) Volcanic hazards from Bezymianny- and Bandai-type eruptions. *Bulletin of Volcanology*, **49**: 435-459.
- Siebert L, Begét JE, Glicken H** (1995) The 1883 and late-prehistoric eruptions of Augustine Volcano, Alaska – *J. Volcanol. Geotherm. Res.* **66**: 367-395.
- Silver E, Day S, Ward S, Hoffmann G, Llanes P, Driscoll N, Appelgate B, Saunders S** (2009) Volcano collapse and tsunami generation in the Bismarck Volcanic Arc, Papua New Guinea – *J. Volcanol. Geotherm. Res.* **186**: 210-222.
- Singer BS, Dungan MA, Layne GD** (1995) Textures and Sr, Ba, Mg, Fe, K, and Ti compositional profiles in volcanic plagioclase: clues to the dynamics of calc-alkaline magma chambers. *American Mineralogist*. **80**(7-8): 776-98.
- Sisson TW and Bronto S** (1998) Evidence for pressure-release melting beneath magmatic arcs from basalt at Galunggung, Indonesia. *Nature*. **391**: 883–886.
- Sisson TW, Salters VJ, Larson PB** (2014) Petrogenesis of Mount Rainier andesite: Magma flux and geologic controls on the contrasting differentiation styles at stratovolcanoes of the southern Washington Cascades. *Bulletin*. **126**(1-2): 122-44.
- Smith DJ** (2014) Clinopyroxene Precursors to Amphibole Sponge in Arc Crust – *Nature Communications* 5:6 doi:10.1038/ncomms5329
- Smith DR and Leeman WP** (1987). Petrogenesis Of Mount St. Helens Dacitic Magmas –*Journal of Geophysical Research*. **92**: 10313–10334
- Smith GA** (1986) Coarse-Grained Nonmarine Volcaniclastic Sediment: Terminology and Depositional Process – *Geol. Soc. Am. Bull.* **97**: 1-10.
- Smith GA** (1991) Facies Sequences and Geometries in Continental Volcaniclastic Settings. In: Fisher RV, Smith GA (Eds.) – *Sedimentation in Volcanic Settings*, SEPM Special Publication. **45**: 109-121.
- Smith GA and Lowe DR** (1991) Lahars: Volcano-Hydrologic Events and Deposition in The Debris Flowhyperconcentrated Flow Continuum – In: Fisher RV, Smith GA (Eds.) *Sedimentation in Volcanic Settings*. SEPM Special Publication. **45**: 60-70.
- Smith RD, Cameron KL, McDowell FW, Niemeyer S and Sampson DE** (1996) Generation of voluminous silicic magmas and formation of mid-Cenozoic crust beneath north–central Mexico: evidence from ignimbrites, associated lavas, deep crustal granulites, and mantle pyroxenites. - *Contributions to Mineralogy and Petrology*. **123**: 375-389.
- Smith DR and Leeman WP** (1987) Petrogenesis of the Mt. St. Helens dacitic magmas – *J. Geophys. Res.* **92**: 10313-10334.
- Sohn C and Sohn YK** (2019) Distinguishing Between Primary and Secondary Volcaniclastic Deposits *Sci Rep* **9**: 1242-125. doi:10.1038/s41598-019-48933-4
- Stamper CC, Blundy JD, Arculus RJ, Melekhova E** (2014) Petrology of Plutonic Xenoliths And Volcanic Rocks from Grenada, Lesser Antilles – *Journal of Petrology*. **55**: 1353–1387.
- Stern TA and Davey FJ** (1987) A Seismic Investigation of The Crustal and Upper Mantle Structure Within the Central Volcanic Region of New Zealand – *New Zealand Journal of Geology and Geophysics* **30**: 217–231.
- Stern TA, Stratford WR and Salmon ML** (2006) Subduction evolution and mantle dynamics at a continental margin: Central North Island, New Zealand. – *Rev. Geophys.* **44**, RG4002.

- Stewart ML and Fowler AD** (2001) The nature and occurrence of discrete zoning in plagioclase from recently erupted andesitic volcanic rocks, Montserrat. – *Journal of Volcanology and Geothermal Research*. **106**: 243–253.
- Stewart RB, Price RC, Smith IEM** (1996) Evolution of high-K arc magma, Egmont volcano, Taranaki, New Zealand: evidence from mineral chemistry. - *Journal of Volcanology and Geothermal Research*. **74**: 275-295.
- Stewart RB** (2010) Andesites as magmatic liquids or liquid-crystal mixtures: Insights from Egmont and Ruapehu Volcanoes, New Zealand Research Article – *Central European Journal of Geosciences*. **2**: 329 – 338. doi: 10.2478/v10085-010-0022-7.
- Stipp JJ** (1968) The Geochronology and Petrogenesis Of Cenozoic Volcanics Of the North Island, New Zealand – Unpublished PhD thesis, Australian National University, Canberra, 438
- Stock MJ, Bagnardi M, Neave DA, Maclellan J, Bernard B, Buisman I, Geist D** (2018) Integrated petrological and geophysical constraints on magma system architecture in the western Galápagos Archipelago: insights from Wolf volcano. *Geochemistry, Geophysics, Geosystems*. **19**(12): 4722-4743.
- Stoopes GR, Sheridan MF** (1992) Giant Debris Avalanches from The Colima Volcanic Complex, Mexico: Implication for Long-Runout Landslides (>100 KM) – *Geology*. **20**: 299-302.
- Straub S, Gomez-Tuena A, Stuart FM, Zellmer GF, Espinasa-Perena R, Cai Y, Iizuka Y** (2011) Formation of hybrid arc andesites beneath thick continental crust Earth and Planetary Science Letters. **303**: 337-347.
- Streck MJ, Broderick CA, Thornber CR, Clyne MA, Pallister JS.** (2008) Plagioclase populations and zoning in dacite of the 2004–2005 Mount St. Helens eruption: constraints for magma origin and dynamics. US Geological Survey Professional Paper 1750.
- Streck MJ, Leeman WP, Chesley JT** (2007) High-magnesian andesite from Mount Shasta: A product of magma mixing and contamination, not a primitive melt: COMMENT AND REPLY: REPLY. *Geology*. **35**(1): e148-.
- Sykes LR** (1966) The Seismicity and Deep Structure of Island Arcs – *Journal of Geophysical Research* **71**: 2981-3005
- Taddeucci J, Edmonds M, Houghton B, James MR, Vergnolle S** (2015). In H. Sigurdsson (Ed.) – *The Encyclopedia of Volcanoes (Second Edition)* (pp. 485-503). Amsterdam: Academic Press. <https://doi.org/10.1016/B978-0-12-385938-9.00027-4>
- Tatsumi Y and Eggins S** (1995). *Subduction Zone Magmatism* – Oxford: Blackwell Scientific
- Tatsumi Y, Hamilton DL and Nesbitt RW** (1986) Chemical characteristics of fluid phase from the subducted lithosphere: evidence from high-pressure experiments and natural rocks - *J. Volcanol. Geotherm. Res.* **29**: 293-309.
- Tepley FJ, Davidson JP, Tilling RI, Arth JG** (2000) Magma Mixing, Recharge and Eruption Histories Recorded in Plagioclase Phenocrysts From El Chichón Volcano, Mexico – *Journal of Petrology*. **41**(9-1): 1397–141.
- Tepper JH, Nelson BK, Bergantz GW, Irving AJ** (1993) Petrology of The Chiilwack Batholith, North Cascades, Washington. Generation of Calc-Alkaline Granitoids By Melting of Mafic Lower Crust with Variable Water Fugacity – *Contributions to Mineralogy and Petrology*. **113**: 333–351.

- Thouret JC** (2005) The Stratigraphy, Depositional Processes, And Environment of The Late Pleistocene Polallie-Period Deposits at Mount Hood Volcano, Oregon, Usa – *Geomorphology*. **70**: 12-32.
- Thouret JC, Abdurachman KE, Bourdier JL, Bronto S** (1998) Origin, Characteristics, And Behaviour of Lahars Following The 1990 Eruption of Kelud Volcano – *Bulletin of Volcanology*. **59**: 460-480.
- Tibaldi A** (2001) Multiple Sector Collapses at Stromboli Volcano, Italy: How They Work – *Bulletin of Volcanology*. **63**: 112-125.
- Tibaldi A** (2004) Major Changes in Volcano Behaviour after a Sector Collapse: Insights from Stromboli, Italy – *Terra Nova*. **16**: 2-8.
- Tinkler RJ** (2013) A High-Resolution Record of Late Quaternary Climatic and Environmental Change in Taranaki, New Zealand – Unpublished PhD thesis, Massey University, Palmerston North, New Zealand, 273 p.
- Tomiya A and Takahashi E** (2005) Evolution of the magma chamber beneath Usu Volcano since 1663: a natural laboratory for observing changing phenocryst compositions and textures. *Journal of Petrology*. **46**(12): 2395-426.
- Tormey D** (2010) Managing the Effects of Accelerated Glacial Melting on Volcanic Collapse and Debris Flows: Planchon-Peteroa Volcano, Southern Andes – *Global and Planetary Change*. **74**: 82-90.
- Torres-Orozco R, Cronin SJ, Damaschke M, Pardo N** (2017a) Diverse dynamics of Holocene mafic-intermediate Plinian eruptions at Mt. Taranaki (Egmont), New Zealand. *Bulletin of Volcanology*. **79**(11): 76.
- Torres-Orozco R, Cronin SJ, Pardo N, Palmer AS** (2017b) New insights into Holocene eruption episodes from proximal deposit sequences at Mt. Taranaki (Egmont), New Zealand. *Bulletin of Volcanology*. **79**(1): 3.
- Tost M, Cronin SJ, Procter JN** (2014) Transport and emplacement mechanisms of channelised long-runout debris avalanches, Ruapehu volcano, New Zealand. – *Bulletin of Volcanology*. **76**(12): 881.
- Tost M, Price RC, Cronin SJ, Smith IEM** (2016) New insights into the evolution of the magmatic system of a composite andesite volcano revealed by clasts from distal mass-fow deposits: Ruapehu volcano, New Zealand. *Bull. Volcanol.* **78**(5):38. doi:10.1007/s00445-016-1030-7.
- Tucker JM, Hauri EH, Pietruszka AJ, Garcia MO, Marske JP, Trusdell FA** (2019) A high carbon content of the Hawaiian mantle from olivine-hosted melt inclusions. *Geochimica et Cosmochimica Acta*. **254**: 156-72.
- Turner MB** (2008) Eruption Cycles and Magmatic Processes at A Reawakening Volcano, Mt. Taranaki, New Zealand – PhD Thesis, INR, Massey University, New Zealand
- Turner MB, Cronin SJ, Smith IE, Stewart RB, Neall VE** (2008a) Eruption episodes and magma recharge events in andesitic systems: Mt Taranaki, New Zealand. *Journal of Volcanology and Geothermal Research*. **177**(4): 1063-76.
- Turner MB, Cronin SJ, Bebbington MS, Platz T** (2008b) Developing a probabilistic eruption forecast for dormant volcanoes; a case study from Mt Taranaki, New Zealand. *Bulletin of Volcanology*. **70**: 507-515. DOI: 10.1007/s00445-007-0151-4.

- Turner MB, Cronin SJ, Bebbington MS, Smith IEM, Stewart RB** (2011) Integrating Records of Explosive and Effusive Activity from Proximal and Distal Sequences: Mt. Taranaki, New Zealand – *Quaternary International* **246**(1-2): 364-373. <https://doi.org/10.1016/j.quaint.2011.07.006>
- Turner S, Bourdon B, Gill J** (2003) Insights into Magma Genesis at Convergent Margins from U-Series Isotopes – *Reviews in Mineralogy and Geochemistry*. **52**: 255.
- Turner SJ and Langmuir CH** (2015) The global chemical systematics of arc front stratovolcanoes: Evaluating the role of crustal processes. *Earth and Planetary Science Letters*. **422**: 182-93.
- Ubide T and Kamber BS** (2018) Volcanic Crystals as Time Capsules of Eruption History – *Nat. Commun.* **9** (1): 1–12. <http://dx.doi.org/10.1038/s41467-017-02274-w>
- Ubide T, Mollo S, Zhao J, Nazzari M, Scarlato P** (2019) Sector-Zoned Clinopyroxene As A Recorder of Magma History, Eruption Triggers, And Ascent Rates – *Geochim Cosmochim Acta*. **251**: 265–283.
- Ubide T, Galé C, Arranz E, Lago M, Larrea P** (2014) Clinopyroxene and amphibole crystal populations in a lamprophyre sill from the Catalanian Coastal Ranges (NE Spain): a record of magma history and a window to mineral-melt partitioning – *Lithos*. **184–187**: 225-242. [10.1016/j.lithos.2013.10.029](https://doi.org/10.1016/j.lithos.2013.10.029)
- Ubide T, McKenna CA, Chew DM, Kamber BS** (2015) High-resolution LA-ICP-MS trace element mapping of igneous minerals: in search of magma histories – *Chem. Geol.* **409**: 157-168. [10.1016/j.chemgeo.2015.05.020](https://doi.org/10.1016/j.chemgeo.2015.05.020)
- Ui T** (1983) Volcanic dry avalanche deposits: Identifications and comparison with nonvolcanic debris stream deposits. *Journal of Volcanology and Geothermal Research*. **18**: 135-150.
- Ui T, Kawachi S, Neall VE** (1986a) Fragmentation of debris avalanche material during flowage - evidence from the Pungarehu Formation, Mount Egmont, New Zealand. *Journal of Volcanology and Geothermal Research*, **27**: 255-264.
- Ui T, Yamamoto H, Suzuki-Kamata K** (1986b) Characterisation of debris avalanche deposits in Japan. – *Journal of Volcanology and Geothermal Research*. **29**: 231-243.
- Ulmer P** (2001) Partial melting in the mantle wedge - the role of H₂O in the genesis of mantle-derived 'arc-related' magmas. *Physics of the Earth and Planetary Interiors*. **127**: 215–232.
- Vallance JW, Siebert L, Rose WI, Giron JR, Banks NG** (1995) Edifice collapse and related hazards in Guatemala. *Journal of Volcanology and Geothermal Research*. **66**: 337-355.
- Vallance JW** (2000) Lahars. In: Sigurdsson H, Houghton B, McNutt S, Rymer H, Stix J (Eds.) *Encyclopedia of Volcanoes*, Academic Press, San Diego, p. 601-616.
- Vallance JW and Iverson RM** (2015) Lahars and their deposits. In: Sigurdsson H, Houghton B, McNutt S, Rymer H, Stix O (eds) – *The Encyclopedia of volcanoes*, 2nd ed. Academic Press, Cambridge, pp 649–664.
- Vallance JW and Scott KM** (1997) The Osceola mudflow from Mount Rainier; sedimentology and hazard implications of a huge clay-rich debris flow. *Bulletin of the Geological Society of America*, **109**: 143-163.

- Van Dissen R and Yeats RS** (1991) Hope Fault, Jordan Thrust, And Uplift of The Seaward Kaikoura Range, New Zealand – *Geology* **19**: 393-396.
- van Gerve TD, Neave DA, Almeev R, Holtz F, Namur O** (2020). Zoned crystal records of transcrustal magma transport, storage and differentiation: insights from the Shatsky Rise oceanic plateau. *Journal of Petrology*.
- Van Orman JA, Grove TL, Shimizu N** (2001) Rare earth element diffusion in diopside: influence of temperature, pressure and ionic radius, and an elastic model for diffusion in silicates – *Contrib. Mineral. Petrol.* **141**: 687-703.
- Van Wyk De Vries B and Francis PW** (1997) Catastrophic collapse at stratovolcanoes induced by gradual volcano spreading. *Nature*, **387**: 387-390.
- Vance JA** (1965) Zoning in igneous plagioclase: patchy zoning – *J. Geol.*, **73**: 636-651
- Vandergoes MJ, Hogg AG, Lowe DJ, Newnham RM, Denton GH, Southon J, Blaauw M** (2013) A Revised Age for The Kawakawa/Oruanui Tephra, A Key Marker for The Last Glacial Maximum in New Zealand – *Quaternary Science Reviews*. **74**: 195-201.
- Vezzoli L, Renzulli A, Menna M** (2014) Growth After Collapse: The Volcanic and Magmatic History of The Neostromboli Lava Cone (Island of Stromboli, Italy) – *Bulletin of Volcanology*. **76**: 821.
- Viccaro M, Garozzo I, Cannata A, Di Grazia G, Gresta S** (2014) Gas burst vs. gas-rich magma recharge: a multidisciplinary study to reveal factors controlling triggering of the recent paroxysmal eruptions at Mt. Etna. *Journal of volcanology and geothermal research*. **278**: 1-3.
- Viccaro M, Giacomoni PP, Ferlito C, Cristofolini R** (2010) Dynamics of magma supply at Mt. Etna volcano (Southern Italy) as revealed by textural and compositional features of plagioclase phenocrysts. *Lithos*. **116**(1-2): 77-91.
- Voight B, Janda RJ, Glicken H, Douglass PM** (1981) Catastrophic rockslide avalanche of May 18. In: Lipman PW & Mullineaux DR (Eds.) *The 1980 eruptions of Mount St. Helens, Washington, US*. Geological Survey Professional Paper, **1250**: 347-377.
- Waite RB, Pierson Jr TC, MacLeod NS, Janda RJ, Voight B, Holcomb RT** (1983) Eruption-triggered avalanche, flood, and lahar at Mount St. Helens - Effects or winter snowpack. *Science*, **221**: 1394-1397.
- Walcott RI** (1987) Geodetic Strain and The Deformational History of The North Island of New Zealand During the Late Cainozoic – *Phil. Trans. Soc. Land*. **321** 163-181
- Wallace GS and Bergantz GW** (2005) Reconciling heterogeneity in crystal zoning data: An application of shared characteristic diagrams at Chaos Crags, Lassen Volcanic Center, California. *Contributions to Mineralogy and Petrology*. **149**(1): 98-112.
- Wallace LM, Beavan J, Mccaffrey R, Darby D** (2004) Subduction Zone Coupling and Tectonic Block Rotations in The North Island, New Zealand – *Journal of Geophysical Research* **109**: B12406, doi:10.1029/2004JB003241
- Walter TR and Schmincke HU** (2002) Rifting, Recurrent Landsliding And Miocene Structural Reorganization on Nw-Tenerife (Canary Islands) – *International Journal of Earth Sciences*. **91**: 615-628.
- Wanke M, Karakas O, Bachmann O** (2019) The genesis of arc dacites: the case of Mount St. Helens, WA. *Contributions to Mineralogy and Petrology*. **174**(1):7.
- Ward KM, Zandt G, Beck SL, Christensen DH, McFarlin H** (2014) Seismic imaging of the magmatic underpinnings beneath the Altiplano-Puna volcanic complex from the joint inversion of surface wave dispersion and receiver functions. *Earth and Planetary Science Letters*. **404**: 43-53.

- Waters LE and Lange RA** (2015) An Updated Calibration of The Plagioclase-Liquid Hygrometer-Thermometer Applicable to Basalts Through Rhyolites – *American Mineralogist*. **100**: 2172-2184.
- Watt SFL** (2019) The Evolution of Volcanic Systems Following Sector Collapse – *Journal of Volcanology and Geothermal Research*
- Watt SFL, Karstens J, Micallef A, Berndt C, Urlaub M, Ray M, Desai A, Sammartini M, Klauke I, Böttner C, Day S, Downes H, Kühn M, Elger J** (2019) From catastrophic collapse to multi-phase deposition: flow transformation, seafloor interaction and triggered eruption following a volcanic-island landslide. – *Earth and Planetary Science Letters*, revised.
- Watt SFL, Kerstens J, Berndt, C** (2020) Volcanic Island Lateral Collapse and Submarine Volcanic Debris Avalanche Deposits
- Watt SFL, Talling PJ, Vardy ME, Helle V, Huhnerbach V, Urlaub, Morelia, Sarkar, Sudipta, Masson DG, Henstock TJ, Minshull TA, Paulatto M, Le Friant A, Lebas E, Berndt C, Crutchley G, Karsten, J, Stinton A, Maeno F** (2012) Combinations Of Volcanic-Flank And Seafloor-Sediment Failure Offshore Montserrat, And Their Implications For Tsunami Generation. – *Earth Planet. Sci. Lett.* **319–320**: 228–240.
- Waythomas CF and Miller TP** (1999) Preliminary volcano-hazard assessment for Iliamna Volcano, Alaska. U.S. Geological Survey Open-File Report, 99-373, 31 pp.
- Waythomas CF and Wallace KL** (2002) Flank collapse at Mount Wrangell, Alaska, recorded by volcanic mass flow deposits in the copper river lowland. *Canadian Journal of Earth Sciences*, **39**: 1257-1279.
- Waythomas CF, Miller TP and Beget JE** (2000) Record of Late Holocene debris avalanche and lahars at Iliamna Volcano, Alaska, *J. Volcanol.*, **104**: 97–130.
- Welsch B, Hammer J, Baronnet A, Jacob S, Hellebrand E, Sinton J** (2016) Clinopyroxene in postshield Haleakala ankaramite: 2. Texture, compositional zoning and supersaturation in the magma. *Contributions to Mineralogy and Petrology*. **171**(1): 6.
- Wentworth CK** (1922) A scale of grade and class terms for clastic sediments. *Journal of Geology*, **30**, 377–392.
- White JDL and Houghton BF** (2006) Primary Volcaniclastic Rocks – *Geology*. **34**: 677-680.
- White R and McCausland W** (2016) Volcano-tectonic earthquakes: A new tool for estimating intrusive volumes and forecasting eruptions. *Journal of Volcanology and Geothermal Research*. **309**: 139-55.
- White SM, Crisp JA, Spera FJ** (2006) Long-term volumetric eruption rates and magma budgets: *Geochemistry, Geophysics, Geosystems*, **7**, p. Q03010, doi: 10.1029/2005GC001002.
- Whittington AG, Hellwig BM, Behrens H, Joachim B, Stechern A, Vetere F** (2009) The viscosity of hydrous dacitic liquids: implications for the rheology of evolving silicic magmas. *Bulletin of Volcanology*. **71**(2): 185-99.
- Wiens DA, Conder JA, Faul UH** (2008) The Seismic Structure and Dynamics of The Mantle Wedge – *Annu. Rev. Earth Planet. Sci.* **36**: 421–55.
- Wilson CJN, Gravley DM, Leonard GS, Rowland JV** (2009) Volcanism in The Central Taupo Volcanic Zone, New Zealand: Tempo, Styles and Controls. In: Thordarson, T., Self, S., Larsen, G., Rowland, S.K., Hoskuldsson, A. (Eds), *Studies in Volcanology: The Legacy of George Walker – Special Publications of IAVCEI (Geological Society, London)* **2**: 225-247.

- Wilson CJN, Houghton BF, McWilliams MO, Lanphere MA, Weaver SD, Briggs RM** (1995) Volcanic and Structural Evolution of Taupo Volcanic Zone, New Zealand: A Review – *Journal of Volcanology and Geothermal Research* **68**: 1-28.
- Zanchetta G, Sulpizio R, Di Vito Ma** (2004) The Role of Volcanic Activity and Climate in Alluvial Fan Growth at Volcanic Areas: An Example from Southern Campania (Italy) – *Sedimentary Geology*. **168**: 249-280.
- Zellmer GF, Pistone M, Iizuka Y, Andrews BJ, Gómez-Tuena A, Straub SM, Cottrell E** (2016) Petrogenesis of antecryst-bearing arc basalts from the Trans-Mexican Volcanic Belt: Insights into along-arc variations in magma-mush ponding depths, H₂O contents, and surface heat flux. *American Mineralogist*. **101**(11): 2405-2422.
- Zellmer GF, Sparks RSJ, Hawkesworth CJ, Wiedenbeck M** (2003) Magma Emplacement and Remobilization Timescales Beneath Montserrat: Insights from Sr and Ba zonation in Plagioclase Phenocrysts. – *J. Petrol.* **44**: 1413-1431.
- Zellmer GF, Chen K-X, Gung Y, Kuo B-Y, Yoshida T** (2019) Magma transfer processes in the NE Japan arc: insights from crustal ambient noise tomography combined with volcanic eruption records – *Front. Earth Sci.* **7**: 40. [10.3389/feart.2019.00040](https://doi.org/10.3389/feart.2019.00040)
- Zernack AV** (2008) A sedimentological and geochemical approach to understanding cycles of stratovolcano growth and collapse at Mt Taranaki, New Zealand: a thesis presented in partial fulfilment of the requirements for the degree of Doctor of Philosophy in Earth Science at Massey University, Palmerston North, New Zealand (Doctoral dissertation, Massey University).
- Zernack AV** (2021) Volcanic Debris-Avalanche Deposits in the Context of Volcaniclastic Ring Plain Successions—A Case Study from Mt. Taranaki. In: Roverato M., Dufresne A., Procter J. (eds) *Volcanic Debris Avalanches. Advances in Volcanology (An Official Book Series of the International Association of Volcanology and Chemistry of the Earth's Interior)*. Springer, Cham. https://doi.org/10.1007/978-3-030-57411-6_9
- Zernack AV and Procter JN** (2021) Cyclic Growth and Destruction of Volcanoes. In: Roverato M., Dufresne A., Procter J. (eds) *Volcanic Debris Avalanches. Advances in Volcanology (An Official Book Series of the International Association of Volcanology and Chemistry of the Earth's Interior)*. Springer, Cham. https://doi.org/10.1007/978-3-030-57411-6_9
- Zernack AV, Cronin SJ, Neall VE, Procter JN** (2011) A Medial to Distal Volcaniclastic Record of An Andesite Stratovolcano: Detailed Stratigraphy of The Ring-Plain Succession of South-West Taranaki, New Zealand – *International Journal of Earth Sciences*, **100**, 1937–1966.
- Zernack AV, Cronin SJ, Bebbington MS, Price RC, Smith IEM, Stewart RB, Procter JN** (2012a) Forecasting catastrophic stratovolcano collapse: A model based on Mount Taranaki, New Zealand – *Geology*. <http://dx.doi.org/10.1130/G33277.1>.
- Zernack AV, Cronin SJ, Bebbington M, Price R, Smith IEM, Stewart RB, Procter JN** (2012a) Forecasting catastrophic stratovolcano collapse: a model based on Mt. Taranaki. *New Zealand Geol* **40**:983–986
- Zernack AV, Price RC, Smith IEM, Cronin SJ, Stewart RB** (2012b) Temporal evolution of a high-K andesitic magmatic system: Taranaki Volcano, New Zealand – *Journal of Petrology*, **53**: 2-1, 325–363
<https://doi.org/10.1093/petrology/egr064>

- Zernack AV, Procter JN, Cronin SJ** (2009) Sedimentary signatures of cyclic growth and destruction of stratovolcanoes: a case study from Mt. Taranaki, New Zealand. *Sedimentary Geology*. **220**: 288-305.
- Zheng YF, Chen RX, Xu Z** (2016) The Transport of Water in Subduction Zones – *Sci China Earth Sci*. **59**: 651-82.
- Zhu DC, Zhao ZD, Niu Y, Dilek Y, Wang Q, Ji WH, Dong GC, Sui QL, Liu YS, Yuan HL, Mo XX** (2012) Cambrian bimodal volcanism in the Lhasa Terrane, southern Tibet: record of an early Paleozoic Andean-type magmatic arc in the Australian proto-Tethyan margin. *Chemical Geology*. **328**: 290-308.
- Zhu Y and Ogasawara Y** (2004) Clinopyroxene phenocrysts (with green salite cores) in trachybasalts: implications for two magma chambers under the Kokchetav UHP massif, North Kazakhstan. *Journal of Asian Earth Sciences*. **22**(5): 517-27.

APPENDIX A: Supplementary Data of **Chapter 4** can be found electronically at:

<https://drive.google.com/drive/folders/1XPeehWwOvj4YN4LTa5zNwa0AZ81op41R?usp=sharing>

CONTENTS:

Appendix A1: Used and presented data

Appendix A2: Figures connected to field work

APPENDIX B: Supplementary Data of **Chapter 5** can be found electronically at:

https://drive.google.com/drive/folders/1oqpIoniBc_0K1e7Wfa_06Wi_ByVc0x6j?usp=sharing

CONTENTS:

Appendix B1: Used and presented data

Appendix B2: Figure of Model 1

Appendix B3: Stratigraphic position of analysed samples

APPENDIX C: Supplementary Data of **Chapter 6** can be found electronically at:

<https://drive.google.com/drive/folders/1EVF7F-OXQr8qdGJNOK0jHNyAPNDDFhT?usp=sharing>

CONTENTS:

Appendix C1: Used and presented data

Appendix C2: Pictures of EMPA spot analysis and figures of Thermobarometry

Appendix C3: Images of mapped crystals and their location within the thin sections

Appendix C4: EMPA Raw Data

APPENDIX D: Supplementary Data of **Chapter 7** can be found electronically at:

https://drive.google.com/drive/folders/1Ndwtq1Fsh70VEuOQUpzBctG7OqcAmz_Z?usp=sharing

CONTENTS:

Appendix D1: Used and presented data

APPENDIX E: DRC16 Form

DRC 16



STATEMENT OF CONTRIBUTION DOCTORATE WITH PUBLICATIONS/MANUSCRIPTS

We, the candidate and the candidate's Primary Supervisor, certify that all co-authors have consented to their work being included in the thesis and they have accepted the candidate's contribution as indicated below in the *Statement of Originality*.

Name of candidate:	ALIZ ZEMENY	
Name/title of Primary Supervisor:	PROF. JONATHAN PROCTER	
Name of Research Output and full reference:		
Aliz Zemeny, Jonathan Procter, Kaiti Henrich, Dong P. Zhai, Anika V. Zemanek and Shane J. Connors (2020) Modelling Subaqueous Conduits from Volcaniclastic Mass Flow Deposits, The Māori King Place of Taranaki Volcano, New Zealand		
In which Chapter is the Manuscript /Published work:	CHAPTER 4	
Please indicate:		
<ul style="list-style-type: none"> The percentage of the manuscript/Published Work that was contributed by the candidate: 	90%	
and		
<ul style="list-style-type: none"> Describe the contribution that the candidate has made to the Manuscript/Published Work: 	Conceptualization, Formal analysis, Investigation, Methodology, Resources, Supervision, Visualization, Writing (original draft), Writing (review & editing)	
For manuscripts intended for publication please indicate target journal:		
SEDIMENTOLOGY		
Candidate's Signature:	Aliz Zemeny	Digitally signed by Aliz Zemeny Date: 2020.12.14 17:54:20 +13'00'
Date:	14.12.2020	
Primary Supervisor's Signature:	Jonathan Procter	Digitally signed by Jonathan Procter Date: 2020.12.23 08:24:16 +13'00'
Date:	23.12.2020	

(This form should appear at the end of each thesis chapter/section/appendix submitted as a manuscript/ publication or collected as an appendix at the end of the thesis)

GRS Version 4– January 2019